

# Towards understanding structure-property relations for the Kondo effect

**Dissertation**

with the aim to achieve a doctoral degree at the Faculty of Mathematics,  
Informatics and Natural Science  
Department of Chemistry  
University of Hamburg

Submitted by

**Marc Philipp Bahlke**

2019



The present work was carried out in the period from October 2015 to February 2019 in the Institute of Inorganic and Applied Chemistry at the University of Hamburg in the group of Prof. Dr. Carmen Herrmann.

Dissertation accepted on the recommendation of  
Prof. Dr. Carmen Herrmann  
Prof. Dr. A. I. Lichtenstein

Date of submission: 15.02.2019  
Date of oral defence: 05.04.2019  
Approval of dissertation: 05.04.2019



# Contents

<b>Abstract</b>	<b>v</b>
<b>Zusammenfassung</b>	<b>vii</b>
<b>I. List of abbreviations</b>	<b>xi</b>
<b>1. Introduction</b>	<b>1</b>
<b>2. Scope and aim of this work</b>	<b>4</b>
<b>3. Theory</b>	<b>6</b>
3.1. The Kondo effect . . . . .	6
3.2. Hartree–Fock theory . . . . .	9
3.3. Density functional theory (DFT) . . . . .	11
3.3.1. Broken-symmetry DFT . . . . .	12
3.4. Introduction to Green’s functions . . . . .	12
3.5. How to define “electron correlation”? . . . . .	16
3.6. Beyond DFT — explicit treatment of electron correlation . . . . .	18
3.6.1. The Coulomb interaction tensor . . . . .	19
3.6.2. DFT+U . . . . .	23
3.6.3. The Anderson impurity model as parameterized by DFT (DFT++) . . . . .	24
3.6.4. The energy window for the projection onto the impurity or- bitals . . . . .	27
3.7. The Continuous-time quantum Monte Carlo (CT-QMC) method . . . . .	28
3.7.1. Introduction . . . . .	28
3.7.2. The hybridization expansion . . . . .	29
3.7.3. Total energy within CT-QMC . . . . .	33
3.7.4. Magnetic properties of the impurity atom . . . . .	33
3.7.5. Fermi-liquid properties of the impurity atom . . . . .	34
3.7.6. From the imaginary to the real energy axis (Analytic con- tinuation) . . . . .	35
3.7.7. Comparison with other quantum Monte Carlo methods . . . . .	36

---

<b>4. Towards a conceptional understanding of the Kondo effect in terms of chemical bonding</b>	<b>38</b>
4.1. Introducing a local decomposition of hybridization functions . . . . .	40
4.2. A porphyrin ligand as a discrete electronic bath: Comparison with ligand field theory . . . . .	45
4.2.1. Computational methodology . . . . .	46
4.2.2. Fe subsystem $d$ energies and hybridization function as obtained from different projection windows . . . . .	47
4.3. H <sub>2</sub> dissociation — closed-shell to open-shell singlet transition . . . . .	52
4.3.1. Computational Methodology . . . . .	53
4.3.2. Hybridization functions and $S^2$ expectation values at different H-H bond distances . . . . .	53
4.4. From discrete energies to a continuous bath . . . . .	55
4.4.1. Computational methodology . . . . .	57
4.4.2. Helium coupled to a hydrogen chain . . . . .	58
4.4.3. Spin-up and spin-down hybridization of a spin-polarized adsorbate on a metallic surface . . . . .	62
<b>5. A Cobalt atom on Cu(001) - The interplay between strong correlation and adsorption distances</b>	<b>64</b>
5.1. Introduction . . . . .	64
5.2. Computational methodology . . . . .	65
5.3. Potential energy surface scan along the adsorption coordinate . . . . .	67
5.4. Electronic structure of Co/Cu(001) . . . . .	70
5.5. Conclusion . . . . .	76
<b>6. Kondo screening in Co on Cu(001) with full Coulomb interaction</b>	<b>78</b>
6.1. Introduction . . . . .	78
6.2. Computational methodology . . . . .	79
6.3. Fermi liquid properties of Co on Cu(001) . . . . .	81
6.4. Role of the coulomb interaction scheme onto the Fermi liquid properties of Co on Cu(001) . . . . .	83
6.5. k-grid dependence of the hybridization function and consequences for the Fermi liquid properties . . . . .	86
6.6. Conclusion . . . . .	87
<b>7. Co on Ag(001) at low <math>T</math>: A general problem with approximate Coulomb interaction for Co on metal surfaces?</b>	<b>90</b>
7.1. Introduction . . . . .	90
7.2. Computational methodology . . . . .	91
7.3. Excitation spectra of Co on Ag(001) and Fermi-liquid properties . . . . .	92

7.4. Conclusion . . . . .	94
<b>8. <math>\text{Co}(\text{CO})_n/\text{Cu}(001)</math>: Towards understanding chemical control of the Kondo effect</b>	<b>95</b>
8.1. Introduction . . . . .	95
8.2. Computational methodology . . . . .	96
8.3. Atomistic structure of $\text{Co}(\text{CO})_n$ on $\text{Cu}(001)$ . . . . .	98
8.3.1. $\text{Co}(\text{CO})_2/\text{Cu}(001)$ . . . . .	99
8.3.2. $\text{Co}(\text{CO})_3/\text{Cu}(001)$ . . . . .	99
8.3.3. $\text{Co}(\text{CO})_4/\text{Cu}(001)$ . . . . .	100
8.4. Kondo properties of $\text{Co}(\text{CO})_n/\text{Cu}(001)$ . . . . .	101
8.4.1. Spectral properties of $\text{Co}(\text{CO})_n/\text{Cu}(001)$ . . . . .	102
8.4.2. Fermi liquid properties of $\text{Co}(\text{CO})_n/\text{Cu}(001)$ . . . . .	103
8.4.2.1. Spin–spin correlation function at high temperatures: Is there a magnetic moment to be screened? . . . . .	103
8.4.2.2. Temperature dependence of $\chi(\beta/2)$ . . . . .	105
8.4.2.3. First Matsubara frequency rule . . . . .	107
8.4.2.4. Discussion . . . . .	107
8.4.3. Adsorbate-structure dependence of the local moment in $\text{Co}(\text{CO})_2$ on $\text{Cu}(001)$ . . . . .	109
8.4.3.1. $\text{Co}(\text{CO})_2/\text{Cu}(001)$ : C-Co-C angle analysis . . . . .	111
8.5. DFT-based analysis of the Kondo effect: What can we learn without solving the AIM? . . . . .	112
8.5.1. The effect of the CO–surface interaction on the Co $3d$ hy- bridization function . . . . .	115
8.6. Conclusion . . . . .	117
<b>9. <math>\text{Co}(\text{CO})_4</math> on <math>\text{Cu}(001)</math>: What can we learn from chemical concepts on the Kondo effect?</b>	<b>119</b>
9.1. Methodology . . . . .	120
9.2. Can a truncated cluster approach reproduce the hybridization func- tion of an approach using periodic boundary conditions ? . . . . .	121
9.3. The effect of the exchange–correlation functional onto the hybridiza- tion function in $\text{Co}(\text{CO})_4$ ( $C_{4v}$ ) on $\text{Cu}(001)$ . . . . .	124
9.4. Conclusion . . . . .	127
<b>10. Conclusion and perspective</b>	<b>128</b>
10.1. Summary . . . . .	128
10.2. Outlook . . . . .	132

---

<b>A. Additional data</b>	<b>134</b>
A.1. The H <sub>2</sub> bond breaking scenario . . . . .	134
A.2. Cobalt on Cu(001) . . . . .	136
A.2.1. Potential energy surface . . . . .	136
A.2.2. Hybridization functions . . . . .	138
A.2.3. Self-energies . . . . .	139
A.2.4. PBE results . . . . .	140
A.2.5. Configuration- and spin state probabilities . . . . .	141
A.2.6. Specification of the unit cell . . . . .	142
A.3. Co(CO) <sub>n</sub> /Cu(001) . . . . .	143
A.3.1. Information about the Co(CO) <sub>n</sub> /Cu(001) atomistic structures	143
A.3.2. Non-local correlation functional for structural optimization of Co(CO) <sub>4</sub> /Cu(001) . . . . .	145
A.3.3. Ligand flipping in Co(CO) <sub>4</sub> /Cu(001) ( <i>C</i> <sub>2v</sub> ) . . . . .	146
A.3.4. Spectral properties of Co(CO) <sub>3</sub> /Cu(001) and Co(CO) <sub>4</sub> /Cu(001) in <i>C</i> <sub>2v</sub> symmetry . . . . .	147
A.3.5. High temperature spin–spin correlation of Co(CO) <sub>3</sub> /Cu(001) and Co(CO) <sub>4</sub> /Cu(001) in <i>C</i> <sub>2v</sub> symmetry . . . . .	148
A.3.6. Dependence of the spin–spin correlation function on <i>U</i> and <i>J</i>	150
A.3.7. Molecular orbital diagram of CO . . . . .	152
<b>B. List of publications</b>	<b>153</b>
B.1. Published . . . . .	153
B.2. In preparation . . . . .	153
<b>C. List of chemicals</b>	<b>154</b>
<b>Acknowledgement</b>	<b>155</b>
<b>Bibliography</b>	<b>157</b>

# Abstract

In order to make molecules usable for electronic components, they often must be brought into contact with solid-state systems (by adsorption or as linkers between two electrodes). Here, the physical properties of the molecules can be strongly influenced by the interactions with the solid. One example of such an interaction is the so-called Kondo effect, where the spin of an adsorbate can be screened by the conduction band electrons of a metal below a certain temperature. This phenomena can be used to experimentally find an indication for the presence of spin polarization on adsorbates (which is not known a priori). In addition, this effect is interesting for information technology and computer science, as it is possible to monitor the magnetism of adsorbates when manipulating their chemical structures via the Kondo effect.

In this work, we obtained insights into the chemical and mechanical control of the Kondo effect, and proposed a conceptional scheme which allows for an interpretation in terms of local properties in line with chemical concepts such as partial charges. For the latter, we found that the results using a truncated cluster approach are qualitatively in agreement with those obtained by applying periodic boundary conditions. Combined with state-of-the-art calculations for Kondo systems such as DFT++, this concept could pave the way towards new insights for understanding the control of the Kondo effect.

The physical properties of a system depend often on its atomistic structure, which is why we studied the effect of structural changes on the DFT++ results at the examples of a single cobalt atom on Cu(001) and carbonyl cobalt complexes on Cu(001). At the same time, one observes structure–property relations for the Kondo effect (or electron correlation effects in general) by such an analysis. We found that increasing the adsorption distance of Co/Cu(001) significantly affects the self-energy of the singly occupied orbitals, i.e. they are getting more correlated, which one would expect to result in a lowering in the Kondo temperature. The same trend was found for Co(CO)<sub>2</sub>/Cu(001). For structural optimization of Kondo systems, one learns from this observation that an inadequate choice of the electronic structure method can have considerable consequences for quantities extracted from DFT++. To this end, we compared the minimum adsorption

---

distances as obtained from DFT, DFT++ and DFT+ $U$ . The DFT++ approach suggests larger values for Co/Cu(001) as compared to DFT, but the differences are of the same order as changing the exchange–correlation functional, which is why we believe that applying the more expensive DFT++ approach for structural optimizations is not necessary for adsorbates on surfaces. This assumption is also confirmed by the almost unaffected adsorption distances for different values of  $U$ , and the agreement of these distances between DFT+ $U$  and DFT++, because the explicit treatment of electron correlation (DFT++) on Co yields no further improvement compared with DFT+ $U$ .

More care should be taken in the treatment of the Coulomb part within the AIM at lower electronic temperatures ( $T < 116$  K). We have found for Co/Cu(001) and Co/Ag(001) that at such electronic temperatures, the physical properties observed by considering only density–density terms deviate from the results extracted from the more expensive Coulomb tensor with all its matrix elements. In contrast to this, the density–density approximation yields results for Co(CO)<sub>2</sub>/Cu(001) and Co(CO)<sub>4</sub>/Cu(001) ( $C_{4v}$ ) that are in agreement with experimental observations found by Wahl *et al.* [1]. According to this, one would conclude that this approximation fails in the special case of Co on metallic surfaces, but is sufficient for its molecular derivatives, which, however, requires further studies for a more general conclusion.

With the aim to study how the Kondo properties are affected by chemical modification, we investigated the effect of CO ligands onto the Kondo temperature at the example of carbonyl cobalt complexes by applying DFT++ using the density–density approximation. It could be shown that the Kondo temperature increases with the number of CO ligands attached to Co due to an increasing hybridization at the Fermi energy of the Kondo-relevant orbitals. Additionally, for Co(CO)<sub>2</sub>/Cu(001) sensitive changes in the magnetism on Co was found by changing the adsorption distance, which suggests that the Kondo properties of this system might be easily controlled mechanically. Using a truncated cluster approach combined with a chemistry-inspired local decomposition analysis, it was found that the CO ligands in case of Co(CO)<sub>4</sub>/Cu(001) ( $C_{4v}$ ) indirectly causes an increased hybridization due to CO–surface interaction. This observation could open the door for future applications, by focusing on the modification or substitution of ligands to indirectly increase the coupling of a magnetic atom (or molecular fragment) to the conduction band electrons of a metallic substrate.

# Zusammenfassung

Um Moleküle für elektronische Bauteile nutzbar zu machen, müssen diese mit Festkörpersystemen in Kontakt gebracht werden (durch Adsorption oder als Linker zwischen zwei Elektroden). Hierbei können die physikalischen Eigenschaften der Moleküle stark durch die Wechselwirkung mit den Festkörpern beeinflusst werden. Zum Beispiel wird bei dem sogenannten Kondo-Effekt der Spin eines Adsorbates durch die Leitungsbandelektronen eines Metalls unterhalb einer gewissen Temperatur abgeschirmt. Dieses Verhalten kann man sich zunutze machen, um experimentell ein Indiz für Existenz von Spinpolarisation auf Adsorbaten zu finden (was a priori nicht bekannt ist) oder auch um in spinpolarisierten Molekülbrücken herauszufinden, ob das ungepaarte Elektron im Transportweg liegt oder nicht. Zudem ist dieser Effekt für die Informationstechnologie und Informatik interessant, um den Magnetismus von Adsorbaten durch die Manipulation ihrer chemischen Struktur über den Kondo-Effekt zu steuern.

In dieser Arbeit haben wir Erkenntnisse über die chemische und mechanische Kontrolle des Kondo-Effekts erlangt und schlagen ein konzeptionelles Schema vor, welches eine Interpretation in Form von lokalen Eigenschaften im Einklang mit chemischen Konzepten wie Partialladungen ermöglicht. Für letzteres fanden wir heraus, dass die Ergebnisse mit Hilfe von einem abgeschnittenen Clusteransatz qualitativ in Übereinstimmung mit Ergebnissen unter periodischen Randbedingungen sind. Kombiniert mit State-of-the-Art Berechnungen für Kondosysteme wie dem DFT++ Ansatz, könnte dieses Konzept den Weg für ein tieferes Verständnis zur Kontrolle des Kondo-Effekts ebnen.

Die physikalischen Eigenschaften eines Systems hängen oft von seiner atomistischen Struktur ab, welche zum Beispiel häufig von der Wahl der Elektronenstrukturmethode signifikant beeinflusst werden. Aus diesem Grund ist es für uns erstrebenswert, die Auswirkungen der DFT++ Methode auf Strukturveränderungen zu untersuchen. Hierfür wurden als Beispiele ein einzelnes Cobaltatom auf Cu(001) und Carbonylcobalt-Komplexe auf Cu(001) ausgewählt. Zusätzlich wird dabei Einsicht in Struktur-Eigenschaftsbeziehungen erhalten, beispielsweise für den Kondo-Effekt oder Elektronenkorrelationseffekte im Allgemeinen. Wir haben beobachtet, dass eine Vergrößerung des Adsorptionsabstandes für Co/Cu(001) einen

---

empfindlichen Einfluss auf die Selbstenergie der einfach besetzten Co-Orbitale hat, was bedeutet, dass diese stärker korreliert werden und somit eine Erniedrigung der Kondotemperatur zu erwarten ist. Der selbe Trend konnte auch für  $\text{Co}(\text{CO})_2/\text{Cu}(001)$  beobachtet werden. Aus dieser Erkenntnis lernt man für Strukturoptimierungen von Kondosystemen, dass eine ungeeignete Wahl der Elektronenstrukturmethode einen beträchtlichen Einfluss auf die aus dem DFT++-Ansatz extrahierten Eigenschaften haben kann. Zu diesem Zweck haben wir die optimierten Adsorptionsabstände aus DFT, DFT++ und DFT+ $U$  miteinander verglichen. Der DFT++-Ansatz kommt dabei zu größeren Werten im Vergleich zu DFT, aber die Unterschiede sind von derselben Größenordnung wie sie von der Änderung des Austauschkorrelationsfunktional zu erwarten wären. Aus diesem Grund glauben wir, dass die teurere DFT++-Methode nicht notwendigerweise für Strukturoptimierungen von Adsorbaten angewendet werden muss. Diese Annahme wird auch durch den nahezu unbeeinflussten Adsorptionsabstand von  $\text{Co}/\text{Cu}(001)$  durch die Änderung des  $U$ -Wertes, und durch die Übereinstimmung dieses zwischen DFT++ und DFT+ $U$  bestätigt, da offensichtlich die explizite Behandlung der Elektronenkorrelation (DFT++) auf Co zu keiner Verbesserung gegenüber DFT+ $U$  führt.

Mit mehr Vorsicht sollte der Coulombteil im AIM behandelt werden. Wir haben herausgefunden, dass für  $\text{Co}/\text{Cu}(001)$  und  $\text{Co}/\text{Ag}(001)$  bei tiefen elektronischen Temperaturen die physikalischen Eigenschaften unter alleiniger Berücksichtigung der Dichte–Dichte-Terme des Coulomb-Tensors von denen abweichen, wie die beim Verwenden einer teureren Berechnung mit allen Matrixelementen zu erwarten wären. Für  $\text{Co}(\text{CO})_2$  auf  $\text{Cu}(001)$  und  $\text{Co}(\text{CO})_4$  auf  $\text{Cu}(001)$  ( $C_{4v}$ ) hingegen liefert die Dichte–Dichte-Näherung Ergebnisse, die mit experimentellen Beobachtungen von Wahl *et al.* [1] übereinstimmen. Hierbei könnte der Schluss gezogen werden, dass in dem besonderen Fall von Co auf metallischen Oberflächen diese Näherung versagt, aber ausreichend für seine molekularen Derivate ist. Dies bedarf allerdings weitere Studien, um ein generelles Fazit ziehen zu können.

Mit dem Ziel, den Effekt von chemischer Modifikation auf die Kondoeigenschaften zu studieren, haben wir unter Verwendung der Dichte–Dichte Näherung den Effekt von Liganden auf die Kondotemperatur am Beispiel von Carbonylcobalt-Komplexen untersucht. Es konnte gezeigt werden, dass die Kondotemperatur mit steigender Anzahl an CO-Liganden zunimmt, was auf eine vergrößerte Hybridisierung des Kondo-relevanten Orbitals an der Fermienergie zurückzuführen ist. Zusätzlich wurde für  $\text{Co}(\text{CO})_2/\text{Cu}(001)$  eine empfindliche Änderung des Magnetismus auf dem Co-Atom abhängig vom Adsorptionsabstand beobachtet. Dies könnte darauf hinweisen, dass die Kondoeigenschaften dieses Systems relativ einfach durch mechanische Einwirkungen kontrollierbar sind. Unter der Verwendung

eines abgeschnittenen Clusteransatzes kombiniert mit einer chemisch-motivierten lokalen Zerlegungsanalyse wurde gezeigt, dass die verstärkte Hybridisierung in  $\text{Co}(\text{CO})_4/\text{Cu}(001)$   $C_{4v}$  indirekt durch die CO-Oberflächen Wechselwirkung induziert wird. Diese Beobachtung könnte die Tür für zukünftige Anwendungen öffnen, bei denen der Fokus auf der Modifikation oder der Substitution von Liganden liegt, um die Kopplung eines magnetischen Atoms (oder eines Molekülfragmentes) an die Leitungsbandelektronen eines metallischen Substrats indirekt zu erhöhen.



# I. List of abbreviations

<b>AIM</b>	Anderson impurity model
<b>AMF</b>	around-mean-field
<b>CASSCF</b>	complete active space self-consistent field
<b>cDFT</b>	constrained density functional theory
<b>CI</b>	Configuration-Interaction
<b>cRPA</b>	constrained random-phase approximation
<b>CT-AUX</b>	Continuous-Time Auxiliary-Field Algorithm
<b>CT-INT</b>	Continuous-Time Quantum Monte Carlo in the interaction expansion
<b>CT-HYB</b>	Continuous-Time Quantum Monte Carlo in the hybridization expansion
<b>CT-QMC</b>	Continuous-Time Quantum Monte Carlo
<b>DC</b>	double-counting
<b>DFT</b>	density functional theory
<b>DFT++</b>	density functional theory plus Anderson impurity model
<b>DFT+<math>U</math></b>	density functional theory + $U$
<b>DMFT</b>	dynamical mean-field theory
<b>DOS</b>	density of states
<b>EXAFS</b>	extended X-ray absorption fine structure
<b>FCI</b>	full configuration interaction
<b>FLL</b>	fully localized limit
<b>FT</b>	Fourier transformation

---

<b>GF</b>	Green's function
<b>GGA</b>	general gradient approximation
<b>GMR</b>	giant magnetoresistance
<b>HF</b>	Hartree–Fock
<b>HF-QMC</b>	Hirsch–Fye Quantum Monte Carlo
<b>HOMO</b>	highest occupied molecular orbital
<b>KS</b>	Kohn–Sham
<b>KS-DFT</b>	Kohn–Sham density functional theory
<b>LDA</b>	local density approximation
<b>LDOS</b>	local density of states
<b>LGO</b>	ligand group orbital
<b>LUMO</b>	lowest unoccupied molecular orbital
<b>MO</b>	molecular orbital
<b>PAW</b>	projector augmented plane-wave
<b>PBC</b>	periodic boundary conditions
<b>PDOS</b>	projected density of states
<b>PES</b>	potential energy surface
<b>RHF</b>	restricted Hartree–Fock
<b>SCF</b>	self-consistent field
<b>STM</b>	scanning tunneling microscopy
<b>STS</b>	scanning tunneling spectroscopy
<b>UHF</b>	unrestricted Hartree–Fock
<b>QMC</b>	Quantum Monte Carlo
<b>VASP</b>	Vienna Ab initio Simulation Package

# 1. Introduction

In recent years, the quest for smaller and more diverse electronic components has intensified [2]. The ongoing miniaturization of electronic devices confronts physicists, chemists and materials scientists with new challenges. On the one hand, it must be possible to manufacture the components synthetically under well-controlled conditions, and on the other hand, the desired properties must be stable under operating conditions. In addition, there is the demand for low energy consumption that goes along with reducing heat production during operation [3].

Molecular electronics provides an interesting portfolio of possible systems which potentially can pave a way towards solving problems arising in nano-electronics [4,5]. This research field may also provide an exciting playground for fundamental science, since it allows insight into the behavior of molecules under extreme conditions (and how this behavior can be modified via their chemical structure). A fascinating approach that can help overcome the problem of heat production is to use the spin degree of freedom of an electron instead of its charge, which defines the field of molecular spintronics [6].

The idea of building electronic components based on atoms or molecules (bottom-up approach) was already proposed by von Hippel [7] in the fifties, which was the first mention of molecular electronics [8]. One of the first scientific works using monolayers of molecules as a “bridge” for electron transport between two electrodes was by Mann and Kuhn [9] in 1971. The breakthrough for molecular electronics, however, was paved by the work of Aviram and Ratner [10] on the theoretical description of rectification by a single organic molecule.

Already in 1936 Mott [11] postulated the influence of the electron spin on the mobility of electrons. The real breakthrough for spintronics came with the discovery of the giant magnetoresistance effect (GMR effect) by Grünberg [12] and Fert [13]. In this case, the electrical resistance depends on the magnetic orientation of two magnetic layers separated by a non-magnetic layer. Nowadays, this effect is used in almost every hard disk drive [14].

Motivated by the search for new applications, the idea developed to combine the advantages of spintronics with those of molecular electronics. This new field, called

---

“molecular spintronics”, is among others inspired by the experimental works of Dediu *et al.* [15] and Rocha *et al.* [16]. It includes not only the electron transport by spin-polarized molecules, but also the possibility to use the electron spin to store and transport information [17].

Devices in molecular electronics and spintronics are often realized by a combination of a bulky material acting as a surface or electrode for the adsorption of spin-polarized single atoms or molecules [18–21]. The physical properties of an adsorbate can strongly be influenced by the interaction with the substrate. For instance, if the singly occupied orbital of a spin-polarized molecule lies below the Fermi energy of the substrate, it might lose the spin polarization due to electron transfer from the substrate into this orbital, leading to a double occupation (for further details about adsorbate–surface interactions, see Reference [22]). If, however, the Coulomb repulsion on the singly occupied orbital is large enough to avoid such double occupation (or transfer of an electron to the substrate), the adsorbate will keep its spin polarization. In physics, this situation is often called to as a well-defined local moment [23].

In transition metal atoms or molecules that contain them, the Coulomb interaction on the  $d$  or  $f$  shell is often large enough to favor such local moment formation. Such systems belong to the class of so-called strongly correlated materials [24, 25]. If the substrate is metallic, the interaction of the conduction band electron with the local moment can result in a screening of the spin below a certain temperature, which is known as the Kondo effect [26]. It manifests itself in scanning tunneling spectroscopy (STS) experiments as an anomalous behavior at zero bias voltage (often called zero-bias anomaly) [27]. For this reason, the detection of a Kondo effect can act as an experimental indication for unpaired electrons on adsorbates [28, 29], which is a priori not known when a molecule is brought into contact with a substrate, but is essential for applications in spintronics. In addition, it is conceivable to use the Kondo effect as a probe for spin-polarized molecules in a molecular junction, which could explain in a combined theoretical and experimental investigation whether the unpaired electron is part of the tunneling pathway or not.

The focus on the Kondo effect has grown recently regarding the control of the magnetic state of a molecule or an atom which could be promising for information technology and computing [30, 31], realized by chemical modification [32–35], or modifying the environment [36]. At present, using the Kondo effect directly for practical applications in spintronics appears rather unpractical, because it is often manifested below temperatures of 100 K. Nevertheless, there is experimental evidence for molecules on surfaces with rather large temperatures ( $T \sim 200\text{--}280$  K) at which the Kondo effect appears [1, 32], which is promising for future work towards new applications in spintronics.

Another motivation for scientists to study the Kondo effect is its complex many-body nature, which is why this effect is still not entirely understood. A theoretical description is often difficult without significant approximations. It is exactly this complexity which makes the Kondo effect fascinating, and a more complete picture of it would be a big step towards understanding the correlation of electrons in a more general context.

## 2. Scope and aim of this work

For realistic atomic and molecular adsorbates, qualitative calculations of Kondo temperatures are parameter-dependent, and (qualitative) structure–property relationships are often not known. This is why considerable theoretical and experimental work will be necessary to contribute to its elucidation. This is the motivation behind this thesis, focusing on obtaining insights into structure–property relations, and to obtain a quantitative picture for this effect.

Historically, the Kondo effect has its origin in physics. From a theoretical point of view, several models have been developed for taking into account this many-body phenomenon to explain experimental observations. As already mentioned before, the attention to controlling the Kondo effect by modifying the chemical structure of spin-polarized molecules on surfaces has grown recently. This is also one of the reasons why this effect has moved in the focus of chemists. It appears likely that the experience of chemists with the qualitative and quantitative properties resulting from electron correlation can contribute to understanding this puzzling many-body phenomenon.

This thesis aims to obtain insights into the chemical and mechanical control of the Kondo effect. To this end, a conceptional scheme for a chemical analysis of the bonding between adsorbates and surfaces based on the hybridization function shall be established, which in combination with state-of-the-art calculations for the Kondo effect can contribute to the understanding of its control.

One of the commonly used numerical approaches to studying the Kondo effect is the so-called DFT++ [37] approach, which in our case is a combination of KS-DFT and the AIM<sup>1</sup>. This combination captures the electron correlation effects within a small sub-space explicitly, including the Kondo effect<sup>2</sup>. Since the DFT++ approach is in practice not entirely free from approximations, certain parameters

---

<sup>1</sup>DFT++ approaches can, e.g., also be a combination of DFT and dynamical mean-field theory (DMFT), but here we exclusively mean the combination of DFT+AIM.

<sup>2</sup>It should be mentioned that KS-DFT is in principle an exact method and should also account for ground-state properties of Kondo systems, if the exact exchange–correlation functional would be known.

entering this approach will be tested concerning their effect onto the Kondo properties. This requires knowledge about whether a Kondo effect in the systems under investigation is present or not above a certain temperature, for which experimental observations taken from the literature will act as a reference.

Furthermore, the focus of this work will be on translating the fundamentals used in solid state physics for describing the Kondo effect into a language that is in line with concepts and terminology known in chemistry. This should highlight common ground in Kondo physics and in chemical bonding and could make it easier to transfer ideas and methods between both communities. Wherever possible, examples from chemistry will be used to obtain further insight into the presented physical context.

## 3. Theory

In this chapter, we discuss the most important theoretical concepts that are necessary for understanding the results of this thesis. At first, we briefly introduce the Kondo effect and density functional theory. Afterwards, there will be an introduction on Green's functions in quantum chemistry, and a discussion about the different definitions of electron correlation in the community of physicists and chemists. Once the different definitions about electron correlation become clear and the basics of Green's functions are known, the Anderson impurity model will be introduced to take into account electron correlation explicitly within a given sub-space. This will be complemented by an introduction about the Continuous-Time Quantum Monte Carlo (CT-QMC) method, which will be used in this work to solve the AIM.

### 3.1. The Kondo effect

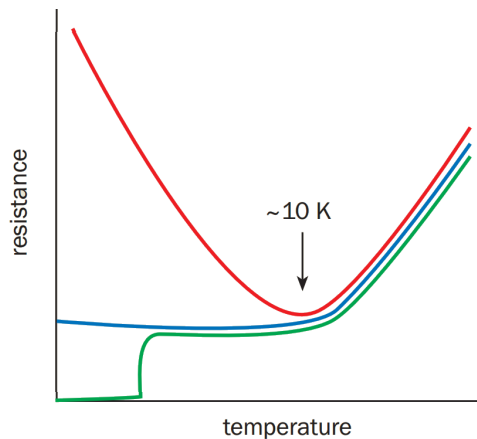


Figure 3.1.: Resistance vs. temperature curve for a metal (blue), a superconductor (green) and a metal with an impurity that shows the Kondo effect (red). Figure taken and adapted from Reference [26].

Imagine the task would be to measure the conductance of several metals like copper, gold, silver, etc. as a function of the temperature. Before doing so, one would think of what could be expected by these measurements, and would likely conclude that the resistance drops to a constant value as the temperature is lowered. This behavior is shown in blue in Figure 3.1, and is caused by getting rid of thermally induced lattice vibrations. It is clear that the observation of an increasing resistance of gold below a certain temperature was challenging to explain in 1934 [38]. Although it was believed to be caused by impurities, there was no plausible explanation for this observation. It took almost 30 years until Jun Kondo [39] found a theoretical explanation for the increased resistivity at low temperatures for impure metallic systems (red plot in Figure 3.1). He explained that this phenomenon is caused by the scattering of conduction band electrons by the localized magnetic moment of an impurity. Kondo showed that the interaction between the local magnetic moment of the impurity and the itinerant electrons of the metal is of antiferromagnetic nature [40], similar to what a chemist understands as an open-shell singlet state [41].

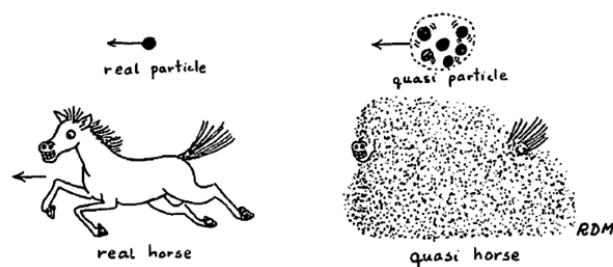


Figure 3.2.: Schematic representation of a quasi particle, at the example of the quasi horse. left: A horse without dust. right: The horse is dressed by dust and in the spirit of Landau would then be called a “quasi” horse. The “quasi” horse has in contrast to the “real” horse a renormalized mass, as a consequence of the clouding dust. Figure taken from Reference [42].

An important step towards understanding the Kondo effect was made by Nozières [43], who showed that the Kondo effect can conceptually be described as a local Fermi-liquid [40]. The basic idea of a Fermi-liquid is that the strong interaction between the local spin of the impurity and the conduction band electrons, leads to collective low-energy excitations close to the Fermisurface. Below a certain temperature, impurity electrons dressed by these excitations can behave as weakly interacting quasiparticles in the spirit of Landau’s phenomenological Fermi-liquid theory [44]. He argued that only the effective magnetic moment and the mass of

quasiparticles have to be renormalized<sup>1</sup>. A good illustration for the renormalized mass is depicted in Figure 3.2 if one considers the “real” horse as the non-interacting fermion which changes its mass when it runs through dry sand and swirls up dust dressing it to a “quasi” horse. In sum, the horse and the dressing cloud of dust has clearly a different mass as the “real” horse.

In the density of states, or the excitation spectrum, the Kondo effect can be seen as a resonance close to the Fermi energy which corresponds to these quasi particles [40] (see Section 3.6.3). The screening of the local moment due to a Kondo effect has also consequences for the local (impurity) spin susceptibility<sup>2</sup>  $\chi_{imp}^{\omega=0}$ . For an unscreened local moment, one expects the well-known Curie behavior,

$$\chi_{imp}^{\omega=0}(T) = \frac{1}{T}, \quad (3.1)$$

i.e., the susceptibility increases as the temperature  $T$  is decreased. For Kondo systems, this behaviour can only be observed above the Kondo temperature  $T_K$  where the local moment is unscreened. It gets modified below  $T_K$ , where the system shows Pauli paramagnetism ( $\chi_{imp}^{\omega=0}(T)$  constant in  $T$ ).

In the simplest case, which is one impurity orbital with a constant hybridization  $\Gamma$  to the conduction band electrons [40], the Kondo temperature can be estimated as

$$k_b T_K = \frac{\sqrt{\Gamma U}}{2} \exp\left(\frac{\pi \epsilon (\epsilon + U)}{\Gamma U}\right), \quad (3.2)$$

with  $\epsilon$  being the energy level of the impurity relative to the Fermi level,  $U$  the Coulomb interaction and  $k_b$  the Boltzmann constant. It will later get clear what a constant hybridization means in this context, but for now it is only important to know that one can learn some interesting properties for the Kondo effect from Equation 3.2: Lowering  $U$  or increasing  $\Gamma$  will shift  $T_K$  towards larger temperatures. As we will see in the later course of this work, the Kondo effect in realistic systems is much more difficult to understand than in this simple model, but these properties give at least a feeling of how it depends on these two parameters.

---

<sup>1</sup>This is only a very brief summary of the important Landau Fermi liquid theory, which in detail goes beyond the scope of this work. The reader is referred to the textbook of Coleman [44] for further details.

<sup>2</sup>The susceptibility is actually energy-dependent, e.g., if it is measured in response to an alternating magnetic field, rather than a constant ( $\omega = 0$ ) one. The  $\omega = 0$  susceptibility is often referred to as the physical susceptibility.

## 3.2. Hartree–Fock theory

Hartree–Fock (HF) theory is a quantum mechanic approach to calculate the electronic wave function of a many particle system. It is a so-called ab-initio method, which means that it is free of empirical parameters and only requires natural constants.

In this theory, one uses the exact many particle operator in the scope of the Born–Oppenheimer approximation which reads for  $N$  electrons in atomic units<sup>3</sup> [45],

$$\hat{H} = \sum_{i=1}^N \underbrace{\left[ -\frac{1}{2} \nabla_i^2 + V_i \right]}_{\hat{h}_i} + \underbrace{\sum_{i<j}^N \frac{1}{|\mathbf{r}_i - \mathbf{r}_j|}}_{V_{ee}}, \quad (3.3)$$

with  $\nabla$  being the Nabla operator,  $V_i$  the interaction between the electron  $i$  and the nuclei, and  $V_{ee}$  the interaction between electrons  $i$  and  $j$  at positions  $\mathbf{r}_{ij}$ .

The aim is to calculate the expectation value of the energy of a system,

$$\langle E \rangle = \langle \Psi | \hat{H} | \Psi \rangle \quad (3.4)$$

with  $\Psi$  being the electronic wave-function. One choice for  $\Psi$  is the so-called Slater determinant, which reads for  $N$  electrons [45]

$$\Phi = \frac{1}{\sqrt{N!}} \begin{vmatrix} \psi_1(1) & \psi_1(2) & \dots & \psi_1(N) \\ \psi_2(1) & \psi_2(2) & \dots & \psi_2(N) \\ \dots & \dots & \dots & \dots \\ \psi_N(1) & \psi_N(2) & \dots & \psi_N(N) \end{vmatrix}. \quad (3.5)$$

Here,  $\psi_k$  are single particle functions (spin orbitals).

A Slater determinant describes an electronic configuration in which one electron is located in  $\psi_1$ , another one in  $\psi_2$ , and so on (the electrons are indistinguishable). Furthermore, it fulfills the Pauli exclusion principle, which is the antisymmetric relation of the wave function with respect to the exchange of two identical particles (fermions). Expressing Equation (3.4) in terms of  $\Phi$  and using some simplifications, one ends at an effective single-particle equation (the Hartree-Fock equation) [45],

$$\hat{f}_i |\psi_i\rangle = \left( \hat{h}_i + \sum_{j=1}^N [\hat{J}_j - \hat{K}_j] \right) |\psi_i\rangle = \epsilon_i |\psi_i\rangle. \quad (3.6)$$

<sup>3</sup>This is actually the so-called electronic Hamilton operator after separation of the nuclei and electrons from the full Hamilton operator within the Born–Oppenheimer approximation.

Here,  $\hat{h}_i = -\frac{1}{2}\nabla_i^2 + V_i$  (as already introduced above), and  $\hat{J}_j$  and  $\hat{K}_j$  are the so-called Coulomb and exchange operators.  $\psi_i$  is the eigenfunction of the Fock operator  $\hat{f}_i$  with the corresponding eigenenergy  $\epsilon_i$ .

It turns out that in Equation (3.6) the electron–electron interaction (term in square brackets) simplifies to an effective potential in which the electron  $i$  interacts with the average of the remaining electrons. This is the so-called mean-field approximation and turns the HF theory from a many-particle theory into an effective one-particle one. The energy of a system then becomes,

$$E_{\text{HF}} = \sum_{i=1}^N \epsilon_i - \frac{1}{2} \sum_{i=1}^N \sum_{\substack{j=1 \\ j \neq i}}^N (\hat{J}_{ij} - \hat{K}_{ij}). \quad (3.7)$$

In Practice, one obtains  $E_{\text{HF}}$  by the so-called variational principle<sup>4</sup>, for which reason the total energy obtained within HF theory will always be above the true ground-state energy  $E_0$  of a system. The difference  $E_{\text{HF}} - E_0$  is then defined as the correlation energy  $E_{\text{cor}}$  [46], which is only a small contribution to the total energy of a system, but gives rise to many interesting phenomena observable in experiments. In Section 3.5 it will be discussed what types of electron correlation are known in physics and chemistry.

Several electronic structure methods have been proposed to overcome this drawback of the HF theory. For instance, the electronic wave-function can also be expanded as a linear combination of different Slater determinants (different electronic configurations) [47]

$$\Psi = \sum_i C_i \Phi_i, \quad (3.8)$$

with  $C_i$  being the coefficient of the Slater determinant  $\Phi_i$ . Including all excited determinants (usually one takes the HF ground-state configuration as reference) would yield the numerically exact solution to the electronic Schrödinger equation. However, in practice this is only possible for very small molecules, which is why one has to truncate the sum over the determinants appearing in Equation (3.8). Two examples commonly used in quantum chemistry applying such truncation are the Configuration-Interaction (CI), and complete active space self-consistent field (CASSCF) theories [47, 48].

<sup>4</sup>In HF theory, the functions  $\psi_i$  are approximated as a linear combination of atom centered basis functions  $\phi_k$  ( $\psi_i = \sum_k c_{ik} \phi_k$ ), for which the coefficients  $c_{ik}$  are varied to yield  $\psi_i$  which minimizes the energy of a system until a given convergence criteria is fulfilled.

### 3.3. Density functional theory (DFT)

Nowadays density functional theory (in the spirit of Kohn and Sham, see later) is probably the most widely used quantum mechanic method for electronic structure calculation. It is based on the proof of Hohenberg and Kohn [49], that there is a bijective relation of the external potential of a system with the ground-state density. This gives rise to the idea of calculating the energy of a system from the ground-state electron density, rather than the electronic wave function, resulting in the energy functional [45]

$$E = E[\rho]. \quad (3.9)$$

One choice for describing the energy functional of Equation (3.9), as proposed by Kohn and Sham, is

$$E[\rho] = T_s[\rho] + J[\rho] + E_{\text{XC}}[\rho] + \int V_{\text{ext}}(\mathbf{r})\rho(\mathbf{r})d\mathbf{r}. \quad (3.10)$$

Here,  $T_s[\rho]$  is the kinetic energy of a reference system of non-interacting fermions which have the same ground-state density as the real system. It is assumed that the difference between the kinetic energies of the reference system and the real system is small and can be included in the exchange-correlation functional  $E_{\text{XC}}[\rho]$ . The term  $J[\rho]$  captures the classical electron–electron interaction, and  $V_{\text{ext}}(\mathbf{r})$  is the external potential that arises due to the electron–nuclei interaction. Throughout the rest of the work, the abbreviation DFT is used for the Kohn–Sham formalism introduced above.

It is important to note that the Kohn–Sham formalism is in principle exact, if the exact exchange-correlation functional  $E_{\text{XC}}[\rho]$  would be known. At present, for  $E_{\text{XC}}[\rho]$  only approximations are available which can be grouped according to their nature of including the electron density for describing this term. One of the simplest exchange–correlation functionals, developed for materials with a homogeneous electron density, is the LDA. Although working well for solid state calculations, for molecular systems with a rapidly varying electron density LDA type functionals have shown only little success [50]. Improvement could be reached by taking into account the first derivative of the electron density with respect to spatial coordinates, resulting in general gradient approximation (GGA) type functionals. There are many more groups of exchange–correlation functionals, such as meta-GGA, which also includes the second derivative of the electron density, or hybrid functionals where a part of the HF exchange is included [47]. Nevertheless, all of the present-day exchange–correlation functionals suffer from their approximate nature, which is problematic, e.g., for describing dispersion energies, or systems with strongly correlated electrons [50, 51].

### 3.3.1. Broken-symmetry DFT

The description of antiferromagnetically coupled spin centers (atoms or molecular fragments with unpaired electrons) usually requires a multi-determinant description. However, as mentioned before, multi-determinant electronic structure methods are computationally demanding, which is why one often bypasses this problem by using broken-symmetry DFT [52]. This approach is based on a single determinant description with a broken spin symmetry, where in the simplest case two spin centers are antiferromagnetically coupled with one spin-up electron on center 1 and one spin-down electron on center 2 (Figure 3.3). In a wave-function theory, such spin-localization poses a problem for antiferromagnetically coupled systems, because with a multi-determinant wavefunction, the spindensity would be zero everywhere.

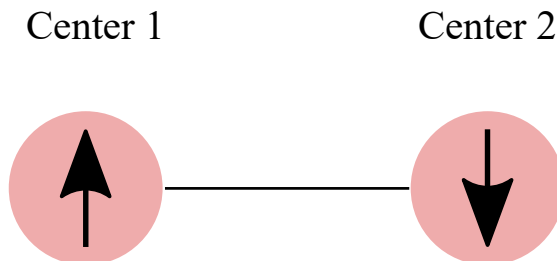


Figure 3.3.: Two antiferromagnetically coupled spincenters.

The broken-symmetry determinant can be understood as an equal admixture of the ferromagnetically and antiferromagnetically coupled state, which in our example (Figure 3.3) would be the triplet and singlet state [53]. This leads to what is called spin-contamination [54], i.e. the broken-symmetry determinant is not an eigenfunction of the  $\hat{S}^2$  operator. However, since in KS-DFT the single-determinant wave function describes a noninteracting reference system rather than the true many-electron ensemble, it is by no means clear whether this poses a problem or not (the matter has been discussed in the literature extensively [55–60]). In practice, broken-symmetry DFT is widely and successfully used in quantum chemistry for evaluating exchange coupling constants, hyperfine coupling constants and  $g$ -tensors [61–63].

## 3.4. Introduction to Green's functions

In this section, we will briefly introduce the concept of Green's functions (propagators) in quantum mechanics, because this technique is important for understanding

upcoming chapters of this thesis. Green's functions are commonly used in classical mechanics to solve linear differential equations. However, this powerful technique was successfully adopted and applied in quantum mechanics, for instance, in the field of molecular electronics regarding Landauer's formalism of coherent electron transport [64], or in quantum physics for describing systems of strongly correlated electrons [65].

For a time-independent Hamiltonian operator ( $\hat{H}$ ) the Green's function is generally defined as [66]:

$$(E - \hat{H} \pm i\eta)\hat{G}(E) = \hat{1} \quad (3.11)$$

$$\hat{G}(E) = (E - \hat{H} \pm i\eta)^{-1} \quad (3.12)$$

In the following, the operator hat of the Green's function will be dropped, as usual in the literature. If an effective one-particle problem is solved, as e.g. the Hartree-Fock equation, one obtains the eigenfunctions  $\psi_i$  and the corresponding eigenvalues  $\epsilon_i$ . They can be used to build the Green's function of this problem directly as,

$$G(E) = \sum_n \frac{|\psi_n\rangle\langle\psi_n|}{(E - \epsilon_n \pm i\eta)}. \quad (3.13)$$

Equation (3.13) is the so-called Lehmann representation of a Green's function [66], where  $i\eta$  is an infinitesimal small imaginary offset. For  $+i\eta$  the (retarded) Green's function  $G^r$  can be continued analytically on to the upper complex plane, whereas for  $-i\eta$  the (advanced) Green's function  $G^a$  can be continued analytically on to the lower complex plane. In passing, we have introduced the first important property of Green's functions, namely  $G^r$  and  $G^a$  are conjugate transposes of each other [66,67],

$$G^r(E) = [G^a(E)]^\dagger. \quad (3.14)$$

Both the advanced and the retarded Green's function have the same physical meaning, and one can stick either to one of them. In the following (and throughout the rest of this section) we assume the limit  $i\eta \rightarrow 0$  so that we can replace  $E \pm i\eta \rightarrow E$ .

Inspired by the textbook of Cuevas and Scheer [66], we consider in the following a simple tight binding model for a hydrogen molecule (Figure 3.4) for getting a feel for using Green's functions in practice. In this example, both hydrogen atoms represent a so-called site, which is coupled to another one via a hopping term  $t$ . For such a system, the Hamiltonian takes the following matrix form,

$$H = \begin{pmatrix} \epsilon_0 & t \\ t & \epsilon_0 \end{pmatrix}. \quad (3.15)$$

Here,  $\epsilon_0$  are the on-site energies. The eigenvalues of this tight binding model are  $\epsilon_+ = \epsilon - |t|$  and  $\epsilon_- = \epsilon + |t|$ , corresponding to a bonding and anti-bonding state  $\psi_+ = \frac{|1\rangle+|2\rangle}{\sqrt{2}}$  and  $\psi_- = \frac{|1\rangle-|2\rangle}{\sqrt{2}}$ .

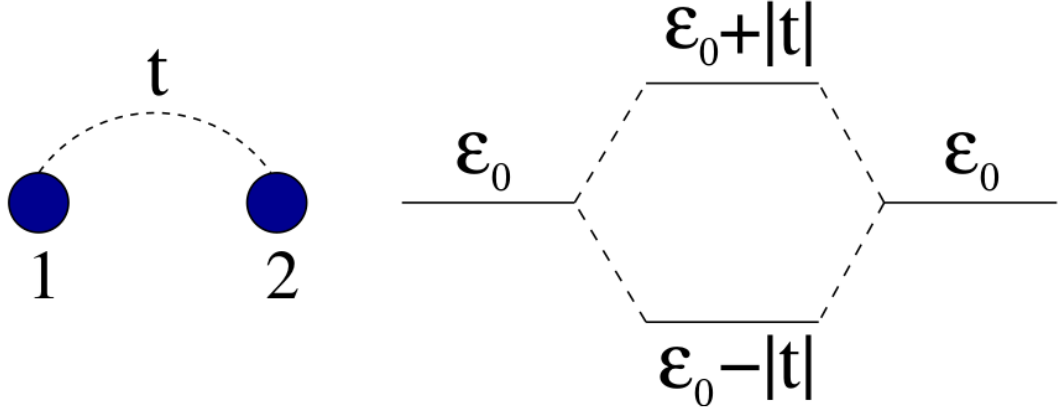


Figure 3.4.: A hydrogen molecule in a minimal basis (one orbital per atom), for which the coupling between both orbitals is described by a hopping term  $t$ . Figure taken from Reference [66].

There are different ways to obtain the matrix Green's function for this system. One can either directly build the Green's function by using the definition of Equation (3.15), or by using the eigenvalues to build the Green's function from the Lehmann representation (Equation (3.13)). Building the Green's function directly from the matrix form of the Hamiltonian (Equation (3.15)) yields

$$G^{-1}(E) = \begin{pmatrix} E - \epsilon_0 & -t \\ -t & E - \epsilon_0 \end{pmatrix}, \quad (3.16)$$

and after inversion,

$$G(E) = \frac{1}{(E - \epsilon_0)^2 - (-t)^2} \begin{pmatrix} E - \epsilon_0 & t \\ t & E - \epsilon_0 \end{pmatrix}. \quad (3.17)$$

Equation (3.17) is the full Green's function of the model system, however, often one is only interested in local properties (as it will be important later on in this thesis), and therefore the local Green's function of site 1 can be computed by taking the element  $g_{11}(E)$  of  $G(E)$ ,

$$g_{11}(E) = \frac{E - \epsilon_0}{(E - \epsilon_0)^2 - (t)^2}. \quad (3.18)$$

Here a small letter  $g$  was introduced for local Green's functions. Equation (3.18) can be rewritten as

$$g_{11}(E) = \frac{1/2}{E - (\epsilon_0 + t)} + \frac{1/2}{E - (\epsilon_0 - t)}, \quad (3.19)$$

where one can see that the local Green's function of site 1 has poles at the eigenvalues  $\epsilon_0 + |t|$  and  $\epsilon_0 - |t|$ .

One important property of Green's function is that the imaginary part (remember that a substitution of  $E \rightarrow E \pm i\eta$  was done) of it contains information about the local density of states<sup>5</sup> of a system as

$$\rho_{11}(E) = -\frac{1}{\pi} \text{Im} g_{11}(E), \quad (3.20)$$

where  $\rho_{11}(E)$  is the local density of states of site 1. By inversion of Equation (3.18), one can see how site 1 is affected by the presence of site 2 and the resulting coupling  $t$  between both sites,

$$g_{11}^{-1}(E) = \frac{(E - \epsilon_0)^2 - (-t)^2}{E - \epsilon_0} = E - \epsilon_0 - \frac{t^2}{E - \epsilon_0} = (g_{11}^0(E))^{-1} - \underbrace{t^2 g_{22}^0(E)}_{\Delta_{11}(E)}. \quad (3.21)$$

Here we have introduced the unperturbed Green's functions  $g_{11}^0(E)$  and  $g_{22}^0(E)$  (as it would appear if we set  $t = 0$ ). In this example  $g_{11}^0(E) = g_{22}^0(E) = \frac{1}{E - \epsilon_0}$ , because both atoms have the same on-site energy  $\epsilon_0$ .

It shall further be noted that the last term in Equation (3.21) arises due to the coupling, or hybridization of site 1 with site 2. This term is in the literature often called as energy dependent hybridization function ( $\Delta_{11}(E)$ ). The prefix "energy-dependent" will later be discussed in more detail (see Section 4), and we are now interested in obtaining the Green's function of site 1 by using the Lehmann representation. This is achieved by inserting the eigenvalues of our model system into Equation (3.13) and taking the element  $\langle 1|G(E)|1\rangle$ ,

$$g_{11}(E) = \frac{\langle 1|\psi_+\rangle\langle\psi_+|1\rangle}{E - \epsilon_+} + \frac{\langle 1|\psi_-\rangle\langle\psi_-|1\rangle}{E - \epsilon_-} = \frac{|\langle 1|\psi_+\rangle|^2}{E - \epsilon_+} + \frac{|\langle 1|\psi_-\rangle|^2}{E - \epsilon_-}. \quad (3.22)$$

Because  $\langle 1|\psi_+\rangle = \langle 1|\psi_-\rangle = \frac{1}{\sqrt{2}}$ , it follows that

$$g_{11}(E) = \frac{1/2}{E - \epsilon_+} + \frac{1/2}{E - \epsilon_-}, \quad (3.23)$$

---

<sup>5</sup>Note, that we have taken the local Green's function of site 1, and in general the imaginary part of a Green's function of the entire system contains the information about its total density of states.

which is the same as Equation (3.19).

In Equation (3.22), we have done a projection of the full Green’s function  $G(E)$  onto the local site 1. As we will show in the next section, this will be of further interest for solving the many-body problem of an impurity coupled to large number of states, which gives rise to an energy-dependent hybridization function as mentioned before.

### 3.5. How to define “electron correlation”?

Before proceeding with the next sections, it is worthwhile to spend some attention on different definitions and uses of the terms “strong”, “static” and “dynamical” correlation. For the term “strong correlation”, we follow here the definition given by Peter Fulde [41]. It states that a material is strongly correlated if the Coulomb repulsion on an orbital is large compared to the kinetic energy gained by overlapping with different orbitals. In a tight binding model this could be expressed as  $t < U$ , where  $t$  is a hopping parameter (similar to what we have already introduced in Section 3.4), and  $U$  is the Coulomb repulsion on an orbital. For  $t < U$ , the charge fluctuations on an atom are reduced, which in a chemistry sense can be understood as the electronic wave function consisting of only a small amount of ionic configurations [41, 68] (see Section A.1 what ionic configurations means at the example of  $H_2$ ).

This is so far a qualitative estimation of the correlation strength, and after this explanation a quantum chemist would expect that in the situation of strong correlation in a molecule, there exists molecular orbitals which character is mainly that of the atom-centered basis functions (which form the molecular orbital) with only little overlap between them. This comes true for instance, in the bond breaking scenario of a  $H_2$  molecule (Figure 3.5) where the highest occupied molecular orbital (HOMO) has  $1s$  character on both hydrogen atoms, with only little (or vanishing) overlap between them. For this, the true wave function has to be a linear combination of multiple Slater determinants as shown in Equation (3.8). This is essentially what chemists call static correlation. On the other hand, at equilibrium distance, the correlation in a hydrogen molecule is dominated by the so-called dynamical correlation. This is the correlation energy which arises due to the electrons avoiding each other<sup>6</sup>.

---

<sup>6</sup>It should be mentioned that at equilibrium distance the amount of correlation is small compared to the kinetic energy in a hydrogen molecule, which is why  $H_2$  does not belong to the class of strongly correlated materials.

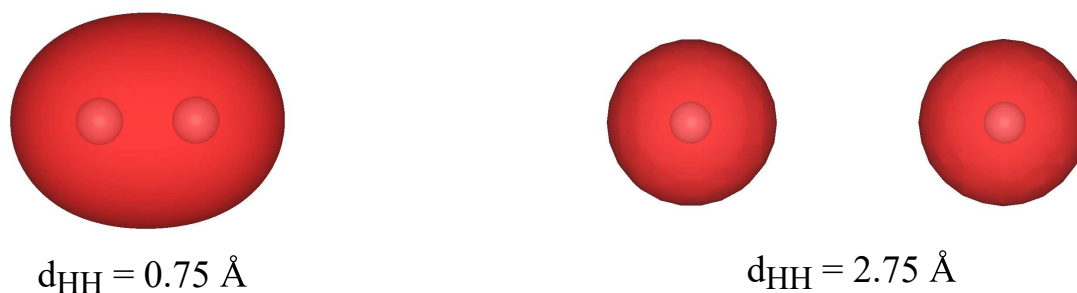


Figure 3.5.: HOMO of  $\text{H}_2$  at equilibrium distance  $d_{\text{HH}} = 0.75 \text{ \AA}$  (BP86/STO-3G), as well as at  $d_{\text{HH}} = 2.75 \text{ \AA}$ . ISO-value: 0.1.

For the  $\text{H}_2$  example, we introduced the definition of static and dynamical correlation in the chemistry sense. The former arises from mixing different electron configurations (Slater determinants) that are close in energy, or nearly degenerate with the HF Slater determinant, whereas the latter has its origin from electrons that are spatially close to each other, and there is no excited Slater determinant that mixes with the HF determinant [46, 47] (in the wavefunction shown in Equation (3.8)).

Now that we have introduced the chemistry definition of static and dynamical correlation, it shall be mentioned that Fulde’s definition of strong correlation does not distinguish between these two. A strongly correlated material can thus be one in which either the dynamical or static correlation (or both) is large compared with the kinetic energy of the electrons. Furthermore, this definition shall not be confused with the definition of the term correlation energy, which the physicists also define as the the difference between the Hartree-Fock energy and the true ground-state energy of a system (see Section 3.2), but is rather rarely used in the context of strongly correlated materials.

As if things were not complicated enough, in the physics community the terms dynamical and static correlation are used differently than introduced above. In physics, the term “dynamical” is used for frequency or energy-dependent quantities such as, e.g., when the self-energy or the hybridization function<sup>7</sup> are not constant in energy [37].

“Static” in this sense means the opposite situation, e.g., in Hartree-Fock theory the self-energy is a pure energy/frequency-independent term, due to the mean-field character of this theory [44, 69]. When referring to DFT +  $U$  (see Section 3.6.2) as

<sup>7</sup>It will later be discussed what these quantities are.

being non dynamical/static, we mean that the self-energy in this approach is still frequency-independent (although DFT does include what chemists call dynamical correlation, i.e., including the effect of electrons avoiding each other due to their Coulomb repulsion), because the added Coulomb potential is just a mean-field-like term [37].

Of course, these definitions must be treated with care, because DFT is in principle exact and can also account for what a chemist calls static correlation [70–75] (dynamical correlation in the physics sense, as introduced above), although in an unsystematic manner [76]. It is most likely that the physical interpretation of the term “dynamical” (from a chemist point of view), can rather be understood as electron correlation taken into account explicitly, which then yields an energy-dependent self-energy (a quantity which is only rarely used in quantum chemistry). In DFT the electron correlation is not described explicitly, which is probably the reason why it is called a static electronic structure method.

### 3.6. Beyond DFT — explicit treatment of electron correlation

Going beyond the usual KS-DFT approach is sometimes necessary to compensate the drawbacks of this method, which are caused by the approximate nature of present-day exchange–correlation functionals. In this part, two approaches to treat strong electron correlation shall be introduced, as they are used throughout this work.

Density functional theory has been applied successfully to a wide range of materials and molecules, but in systems where the electrons become more and more localized, and the Coulomb interaction plays a major role, LDA and GGA type functionals heavily underestimate the band gap, e.g. in nickel oxide (NiO). For this material, DFT predicts a semiconducting behavior with a band gap of 0.15–0.5 eV [77,78], although experiments reveal that NiO is an insulator [79] with band gap of 4.3 eV. Furthermore, DFT is not capable of describing the correlation effects leading to the Kondo effect, which would require a multi-determinant description in wave-function theory (static correlation in the chemistry sense, see Section 3.5). There are new developments, however, for extending DFT towards Kondo systems, e.g., Jacob and Kurth developed an approach to extract the many-body spectral function (this is the excitation spectrum of an interacting system) from a steady state DFT calculation [80], which yields promising results in recovering the Kondo peak using the ground-state density of DFT.

The NiO conundrum can be resolved by using the DFT+ $U$  approach (see Section 3.6.2), where a Coulomb potential is added to the Ni atoms. A different choice would be to use hybrid functionals for a better description of the NiO electronic structure [81–83], which would have the advantage of being free of system specific parameters as compared to DFT+ $U$ . However, using hybrid functionals in combination with periodic boundary conditions (PBC) is not practical, due to the high computational effort [84], which is why DFT+ $U$  has become well established for material scientists.

While DFT+ $U$  is capable to describe certain correlation effects, like the antiferromagnetic insulating state in NiO, other effects are beyond its capabilities. These include the paramagnetic metal to insulator (Mott) transition in NiO or the Kondo effect [85–87]. For this, dynamical electron correlation (in the physics sense, see Section 3.5) is needed to describe these many-body phenomenons correctly. In such cases, combinations of DFT and the Anderson impurity model (AIM) [88] or the Hubbard model [89, 90] have shown great success, which are often referred to as DFT++ [37], and will be described in Section 3.6.3 in more detail (focusing on the combination of DFT+AIM).

Before introducing DFT +  $U$  and DFT++, it is necessary to spent some attention on the Coulomb tensor and its approximations done in practice. This will be the focus of the following discussion.

### 3.6.1. The Coulomb interaction tensor

In the DFT++ framework, as well as in the DFT+ $U$  approach, one often treats the Coulomb interaction of the impurity shell in an approximate way, as it is also done in the scope of this work. To this end, the approximations used will be introduced here briefly. Since we will be concerned mostly with single atoms as the impurity, the discussion here is focused on the Coulomb tensor (often referred to as Coulomb matrix) for the sub-shell of a single atom. The full Coulomb tensor reads

$$\hat{H}_{ee} = \frac{1}{2} \sum_{ijkl} U_{ijkl} \hat{d}_i^\dagger \hat{d}_j^\dagger \hat{d}_l \hat{d}_k, \quad (3.24)$$

with  $\hat{d}_i^\dagger$  and  $\hat{d}_i$  being creation and annihilation operators acting on the impurity orbital  $i$ .  $U_{ijkl}$  are matrix elements which are given as, [91]

$$U_{ijkl} = \int \int d\mathbf{r} d\mathbf{r}' \phi_i(\mathbf{r}) \phi_j(\mathbf{r}') \frac{1}{|\mathbf{r} - \mathbf{r}'|} \phi_k(\mathbf{r}) \phi_l(\mathbf{r}') = \langle ij|V|kl \rangle. \quad (3.25)$$

Here,  $\phi_x$  ( $x = i, j, k, l$ ) being any atom-centered basis function.

The approximation of the Coulomb interaction can be a specific parametrization of the elements of the tensor based on few parameters (often  $U$  and  $J$ ), and/or by taking into account only a part of the full Coulomb interaction (see later for a discussion). Without such a truncation, it is computationally demanding to evaluate the Coulomb interaction within the AIM.

In what follows, we discuss a parametrization scheme for the Coulomb interaction commonly used in many-body physics which is the so-called Slater parametrization [92]. This is often used in practical applications, because one does not need to evaluate the integral appearing in Equation (3.25). For this parametrization, it is important to know that one assumes atomic orbitals of hydrogen type  $\phi$  that have the form

$$\phi(\mathbf{r}) = R_{nl}(r)Y_{lm}(\theta, \phi). \quad (3.26)$$

Here  $R_{nl}(r)$  is a radial function, and  $Y_{lm}(\theta, \phi)$  is a spherical harmonic function. The indices  $n$ ,  $l$ , and  $m$  are the principal, azimuthal and the magnetic quantum number. For the solution of the hydrogen atom see, e.g., the textbook of Reinhold [45].

It is useful to expand the quotient  $V = \frac{1}{|\mathbf{r}-\mathbf{r}'|}$  in spherical harmonics, which yields [45]

$$\frac{1}{|\mathbf{r}-\mathbf{r}'|} = \sum_{\lambda=0}^{\infty} \frac{4\pi}{2\lambda+1} \frac{r_{<}^{\lambda}}{r_{>}^{\lambda+1}} \sum_{m=-\lambda}^{+\lambda} Y_{\lambda m} Y_{m\lambda}, \quad (3.27)$$

with  $r_{<}$  and  $r_{>}$  being the smaller and greater of  $\mathbf{r}$  and  $\mathbf{r}'$ .

Inserting Equation (3.27) into Equation (3.25) leads to a differential equation that can be separated into an angular and a radial part. Furthermore, the infinite sum over  $\lambda$  can be truncated to a finite number, because the matrix elements of Equation (3.25) (after insertion of Eq. (3.27)) leads to an integral over three spherical harmonics, which is only different from zero if  $\lambda \leq 4$  (in the case of  $d$  orbitals where  $\lambda = 2 \cdot l = 2 \cdot 2 = 4$ ) [45].

In general, the integration of the radial part is not carried out and is left unspecified as the so-called Slater parameter (or Slater-Condon parameter) [45, 92]:

$$F^{\lambda} := F^{\lambda}(nl; nl) = \langle R_{nl}(i)R_{nl}(i) \frac{r_{<}^{\lambda}}{r_{>}^{\lambda+1}} R_{nl}(j)R_{nl}(j) \rangle. \quad (3.28)$$

The integration of the angular part leads to a single coefficient  $c^{\lambda}(ij; kl)$ , from which one can obtain the full Coulomb matrix elements as

$$U_{ijkl} = \sum_{\lambda=0}^{2l} c^{\lambda}(ij; kl) F^{\lambda}. \quad (3.29)$$

In practice, the Coulomb matrix is often parameterized by the two parameters  $U$  and  $J$ , for which the following relation holds (for  $3d$  systems) [91]

$$U = F^0 = \frac{1}{(2l+1)^2} \sum_{ij} U_{ijij}, \quad (3.30)$$

$$J = \frac{1}{14}(F^2 + F^4). \quad (3.31)$$

$U$  and  $J$  are called the average Coulomb and exchange parameter. It was found for the isolated  $3d$  ions, that the ratio  $\frac{F^4}{F^2}$  depends only little on the choice of the basis (Slater-type orbitals, Wannier functions) [93, 94], and is also similar in the crystal structure of these ions [94] (where one has no spherical symmetry), which is why in practice one parameterizes the Coulomb matrix in a spherical symmetry by only a few parameters. For  $3d$  systems one commonly chooses  $\frac{F^4}{F^2} = 0.625$  [91, 93].

As mentioned before, electronic structure calculations using the full Coulomb interaction are often computationally demanding, which is why several approximations have been proposed. One choice is to use the density–density terms only ( $i = k, l = j$ ), what in second quantization notation results in  $\hat{n}_{i\sigma} = \hat{d}_{i\sigma}^\dagger \hat{d}_{i\sigma}$  and  $\hat{n}_{j\sigma} = \hat{d}_{j\sigma}^\dagger \hat{d}_{j\sigma}$ , and discarding all other matrix elements. Thus, the Coulomb part reduces to [91]

$$\begin{aligned} \frac{1}{2} \sum_{\substack{ijkl \\ \sigma\sigma'}} U_{ijkl} \hat{d}_{i\sigma}^\dagger \hat{d}_{j\sigma'}^\dagger \hat{d}_{l\sigma'} \hat{d}_{k\sigma} &\approx \frac{1}{2} \sum_{\substack{ij \\ \sigma\sigma'}} U_{ij} \hat{n}_{i\sigma} \hat{n}_{j\sigma'} \\ &+ \frac{1}{2} \sum_{\substack{i \neq j \\ \sigma}} (U_{ij} - J_{ij}) \hat{n}_{i\sigma} \hat{n}_{j\sigma} = \hat{H}_{\text{dens}}. \end{aligned} \quad (3.32)$$

A different approximation, often found in practical applications, is the so-called Kanamori approximation, which reads [91]

$$\hat{H}_{\text{Kana}} = \hat{H}_{\text{dens}} + \frac{1}{2} \sum_{i \neq j, \sigma, \sigma'} J_{ij} (\hat{d}_{i\sigma}^\dagger \hat{d}_{j\sigma'}^\dagger \hat{d}_{i\sigma'} \hat{d}_{j\sigma} - \hat{d}_{i\sigma}^\dagger \hat{d}_{i\sigma'}^\dagger \hat{d}_{j\sigma} \hat{d}_{j\sigma'}). \quad (3.33)$$

The Kanamori approximation tends to maximize  $\hat{S}^2$ , whereas with the density–density approximation  $\hat{S}_z$  is maximized (see supporting information of Reference [95] for further details). For this reason, the later overestimates the magnetization on atoms, which has been found in several model calculations [96, 97].

Towards a full ab-initio treatment one faces the task to calculate the Coulomb tensor explicitly for the system under consideration, which means solving the integral appearing in Equation (3.25) (and using all elements of the Coulomb matrix).

This would have the advantage of taking into account the correct symmetry of the system, as well as evaluating the Coulomb matrix in the same basis as used for solving the Anderson impurity model.

Furthermore, this would lead to the inclusion of system-dependent screening effects of the bare Coulomb interaction (that of an isolated atom), which results from forming electron-hole pairs between the impurity and the electronic bath. This leads to a drastic reduction of the bare Coulomb interaction, which is roughly 15 eV to 27 eV for the 3d elements (see, e.g., Reference [98]), to only several electron volts [99].

Nowadays, the most widely used approaches to evaluate the Coulomb interaction from first-principles are constrained density functional theory (cDFT) [100–102] and the constrained random-phase approximation (cRPA) [103]. In the former, one constrains the occupation number on chosen orbital  $n_i$  of the impurity and calculates the total energy of the system. The idea is then to evaluate the energy as a function of the orbital occupation, from which one can estimate the effective Coulomb interaction on orbital  $i$  as [104, 105]

$$U_i = E(n_i + 1) + E(n_i - 1) - 2E(n_i). \quad (3.34)$$

Here,  $E(n_i)$  is the ground-state energy, and  $E(n_i \pm 1)$  are the corresponding energies with  $n_i \pm 1$  electrons on the chosen impurity orbital. Later, this approach was improved using a linear response formalism [106, 107]. The cDFT approach, however, does not yield the entire Coulomb tensor (Equation (3.25)), because one only calculates the effective Coulomb energy resulting from interactions between two electrons on one orbital.

An improvement over cDFT is to evaluate the integral in Equation (3.25) explicitly, by replacing  $\frac{1}{|\mathbf{r}-\mathbf{r}'|} = V_{\text{bare}}$  with the screened analogue  $V_{\text{screened}}$ . The latter can for instance be determined by using the simple Thomas-Fermi model [105, 108, 109], or as mentioned earlier, using the cRPA which yields the full tensor for the shells in question including screening and symmetry effects [103, 110, 111].

A different approach to calculate the average Coulomb and exchange interaction was proposed by Carter *et al.* [112]. Their approach is based on an unrestricted Hartree-Fock embedded cluster calculation using molecular orbitals to calculate  $U$  and  $J$ , with the advantage of being a true first-principles scheme. This approach yields promising results for  $\text{Cr}_2\text{O}_3$  using DFT+ $U$  in combination with the ab-initio calculated values  $U$  and  $J$ . The disadvantage here lies in a proper evaluation of the optimal cluster size used, with respect to the convergence of  $U$  and  $J$ .

### 3.6.2. DFT+U

In a DFT+ $U$  approach, one combines a density functional theory calculation with a simple Hubbard  $U$ -term. The total energy is then a sum of the DFT energy  $E_{\text{DFT}}$  (Equation (3.10)) and an electron interaction term  $E_{\text{ei}}$ , with accounting for the double-counting of electron correlation by subtracting a so-called double-counting (DC) term  $E_{\text{DC}}$ , which is required due to the fact that a part of the electron correlation is already captured within DFT [113],

$$E_{\text{DFT}+U} = E_{\text{DFT}} + E_{\text{ei}} - E_{\text{DC}}. \quad (3.35)$$

The term  $E_{\text{ei}}$  is given as [113, 114],

$$E_{\text{ei}} = \sum_{ijkl} \sum_{\sigma\sigma'} \langle ij|V|kl \rangle n_{ij}^{\sigma} n_{kl}^{\sigma'} + (\langle ij|V|kl \rangle - \langle ij|V|lk \rangle) n_{ij}^{\sigma} n_{kl}^{\sigma}. \quad (3.36)$$

Here,  $n_{ij}^{\sigma}$  is the density matrix for spin  $\sigma$ . The matrix elements appearing in Equation (3.36) are those discussed in Section 3.6.1. Note that in practice, in Equation (3.36) an additional sum runs over all atoms on which the  $U$  correction is applied. In this work, however, we limit the discussion to only one impurity atom, so that the sum can be neglected (note that the  $U$  correction can also be applied to molecular orbitals [115]).

The double-counting energy  $E_{\text{DC}}$  will also be important for Section 3.7.3, where we show how the total energy within a DFT++ approach can be calculated. In the literature, two commonly used approaches to account for the double-counting of electron correlation are used, which are called around-mean-field (AMF) [116] and fully localized limit (FLL) [114, 116, 117]. In AMF it is assumed that all orbitals are equally distributed among all correlated orbitals, and the DC term reads [113],

$$E_{\text{DC}}^{\text{AMF}} = U N_{\uparrow} N_{\downarrow} + \frac{1}{2} (N_{\uparrow}^2 + N_{\downarrow}^2) \frac{2l}{2l+1} (U - J). \quad (3.37)$$

$N_{\uparrow}$  and  $N_{\downarrow}$  are the total number of spin-up and spin-down electrons in the correlated sub-space and  $l$  is the azimuthal quantum number.  $U$  ( $F^0$ ) and  $J$  ( $\frac{1}{14}(F^2 + F^4)$ ) are the average Coulomb and exchange energies between the electrons in the correlated sub-space.

In this work we focus on the FLL approach, which estimates the double-counting as,

$$E_{\text{DC}}^{\text{FLL}} = \frac{1}{2} U N (N - 1) - \frac{1}{2} J N_{\uparrow} (N_{\uparrow} - 1) - \frac{1}{2} J N_{\downarrow} (N_{\downarrow} - 1), \quad (3.38)$$

$N$  is the total number of electrons in the correlated sub-space.

### 3.6.3. The Anderson impurity model as parameterized by DFT (DFT++)

For describing the electron correlation effects of magnetic impurities, the AIM has become well established in the physics community [118]. It takes into account the correlation on a defined set of orbitals (the correlated sub shell) of the impurity explicitly. This set of orbitals are mostly the  $d$  or  $f$  shells of transition metal atoms, but can also be molecular orbitals (MOs) of an adsorbate [119–121]. The “rest” of the system, the so-called electronic bath, is assumed to be effectively non-interacting. In this section we use small Greek letters for the electronic bath, small Latin (Roman) letters for the impurity orbitals, and capital Latin (Roman) letters for Kohn–Sham eigenvalues and orbitals.

The Anderson Hamiltonian in its general multi-orbital form is written as

$$\hat{H} = \sum_{\nu\sigma} \epsilon_{\nu} \hat{c}_{\nu,\sigma}^{\dagger} \hat{c}_{\nu,\sigma} + \sum_{\nu i\sigma} [V_{\nu i} \hat{c}_{\nu,\sigma}^{\dagger} \hat{d}_{i,\sigma} + V_{\nu i}^* \hat{d}_{i,\sigma}^{\dagger} \hat{c}_{\nu,\sigma}] + \sum_{i\sigma} \epsilon_i \hat{d}_{i\sigma}^{\dagger} \hat{d}_{i\sigma} + \frac{1}{2} \sum_{\substack{ijkl \\ \sigma\sigma'}} U_{ijkl} \hat{d}_{i\sigma}^{\dagger} \hat{d}_{j\sigma'}^{\dagger} \hat{d}_{l\sigma'} \hat{d}_{k\sigma}. \quad (3.39)$$

In Eq. (3.39),  $\epsilon_i$  is the energy of the local orbital  $i$  of the impurity (often defined as the  $3d$  orbitals), and  $\epsilon_{\nu}$  is effectively the kinetic energy of an electron in the bath orbital  $\nu$ .  $\hat{c}_{\nu\sigma}/\hat{c}_{\nu\sigma}^{\dagger}$  are creation and annihilation operators for electrons with spin  $\sigma$  acting on the  $\nu$ th orbital state, whereas  $\hat{d}_{i\sigma}/\hat{d}_{i\sigma}^{\dagger}$  are the corresponding operators acting on the local orbital  $i$ . The bath electrons are coupled to the impurity via the hybridization  $V_{\nu i}$ , and  $U_{ijkl}$  is the local Coulomb interaction as introduced by Slater [122] (see Section 3.6.1 for more details).

In this work, the AIM is solved within the CT-QMC method (see Section 3.7), parametrized by KS-DFT. In practice, this is done by calculating the so-called energy-dependent hybridization function,

$$\Delta_{ij}(\omega) = \sum_{\nu} \frac{V_{\nu i} V_{\nu j}^*}{\omega + i\eta - \epsilon_{\nu}}. \quad (3.40)$$

Here,  $\eta$  is an infinitesimal small offset, and  $\omega$  is the energy<sup>8</sup> on which the hybridization function depends on.

The starting point for solving the AIM is the non-interacting KS Green’s function, which in terms of the KS eigenvalues  $\epsilon_K$  reads (for  $N$  KS eigenfunctions)

$$G^{KS}(\omega) = \sum_K^N [\omega + i\eta + \mu - \epsilon_K]^{-1}. \quad (3.41)$$

<sup>8</sup>In the context of many-body physics, one often uses the symbol  $\omega$  (frequency) in units of the energy. The relation between a frequency and the energy is given by the Planck–Einstein relation [123, 124].

Here,  $\mu$  is the chemical potential. By projection of  $G^{KS}(\omega)$  onto a set of atom-centered basis functions on the impurity (which is usually called the correlated sub-space), one obtains the non-interacting local Green's function,

$$g_{ij}(\omega) = \sum_K^N \hat{P}_i G_K^{KS}(\omega) \hat{P}_j = [(\omega + i\eta)\delta_{ij} - \underbrace{(\epsilon_{ij} + \Delta_{ij}(\omega))}_{\tilde{\Delta}_{ij}(\omega)}]^{-1}. \quad (3.42)$$

In Equation (3.42),  $\epsilon_{ij}$  are the matrix elements of the KS operator in that local basis, which for  $i = j$  (after solving the secular equations) are the subsystem energies (in the literature often referred to as the static-crystal field energies), and  $\delta_{ij}$  is the Kronecker delta.  $\hat{P}_i$  is a projection operator defined as

$$\hat{P}_i = |\phi_i\rangle\langle\phi_i|, \quad (3.43)$$

with  $\phi_i$  a local basis function of the correlated sub shell (see Section 4.1 for more details).

The matrix elements  $\epsilon_{ij}$  can be obtained as,

$$\epsilon_{ij} = \sum_{KL} \hat{P}_i H_{KL} \hat{P}_j, \quad (3.44)$$

with  $H$  being the effective single-particle Kohn–Sham Hamiltonian matrix. Note that in some implementations Equation (3.44) is not directly evaluated, and the elements  $\epsilon_{ij}$  are observed by taking the limit  $\lim_{\omega \rightarrow \infty} \tilde{\Delta}_{ij}(\omega) = \epsilon_{ij}$ , because  $\lim_{\omega \rightarrow \infty} \Delta_{ij}(\omega) = 0$  (i.e. there are no bath orbitals to hybridize with at  $\omega \rightarrow \infty$ ).

Solving Equation (3.42) for  $\Delta_{ij}(\omega)$  yields

$$\Delta_{ij}(\omega) = -[g_{ij}^{-1}(\omega) + \epsilon_{ij} - (\omega + i\eta)\delta_{ij}]. \quad (3.45)$$

The energy-dependent hybridization function is of central importance, because it captures the effect of the impurity orbitals being broadened and shifted by the interaction with the bath states. This concept will be explained in more detail in Section 4.

Once the AIM has been solved, one obtains the interacting impurity Green's function  $g_{\text{int},ij}(\omega)$ , which is related to the non-interacting one by the Dyson equation,

$$g_{\text{int},ij}^{-1}(\omega) = g_{ij}^{-1}(\omega) + \Sigma_{ij}(\omega). \quad (3.46)$$

Here,  $\Sigma_{ij}(\omega)$  is the self-energy which describes the dressing of impurity electrons by low-energy excitations caused by electron correlation (which we already mentioned

in Section 3.1). Same as for  $\Delta_{ij}(\omega)$ , the real part of  $\Sigma_{ij}(\omega)$  acts as a shift of the energy levels, and the imaginary part broadens the energy levels [44].

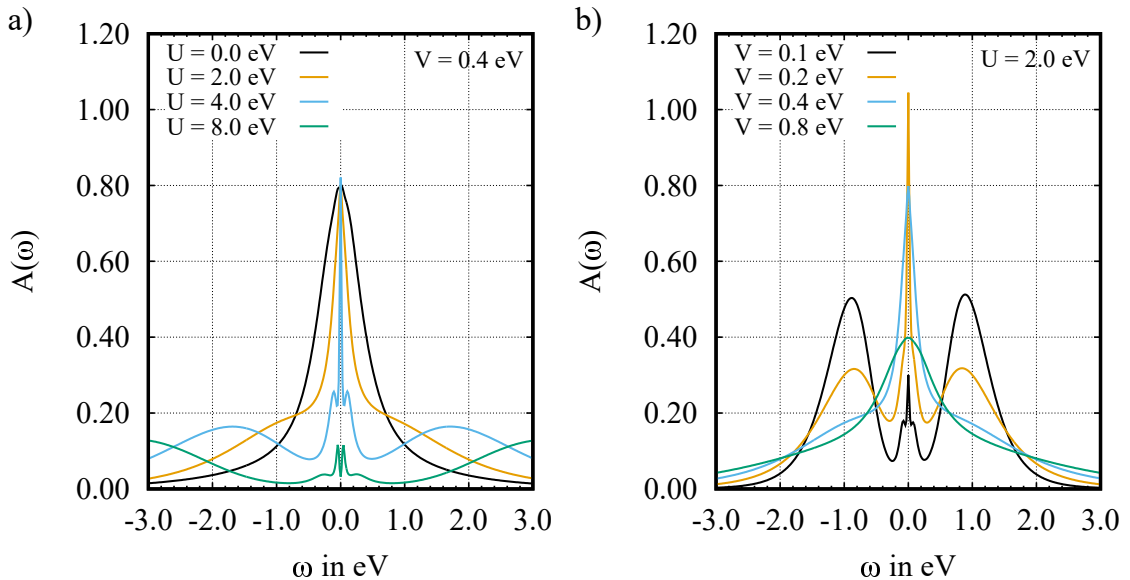


Figure 3.6.: Spectral function of the symmetric AIM for a single impurity with a constant hybridization (after Hewson’s Equation (5.42) [40]). a) The bandwidth  $D$  is 10.0 eV, the hybridization  $V = 0.4$  eV and  $\epsilon = -U/2$ . Results obtained from CT-QMC (see Section 3.7) at  $\beta = 100$  eV $^{-1}$  ( $T = 116$  K).

From the imaginary part of the impurity Green’s function, one obtains the spectral function  $A_{ij}(\omega)$  as

$$A_{ij}(\omega) = -\frac{1}{\pi} \text{Im}g_{\text{int},ij}(\omega). \quad (3.47)$$

The spectral function should not be confused with the DOS, although it is often called DOS<sup>9</sup> in the literature, because it is obtained from the imaginary part of the interacting impurity Green’s function (compare Equation (3.20)). Following Reference [125], the spectral function corresponds to transitions between many-body states, whereas the DOS refers to single-particle levels. So the features in a DOS do not include many-body effects while the spectral function does.

In the following, it shall be demonstrated how the spectral function for the simplest Anderson model, one impurity orbital with a constant hybridization function, be-

<sup>9</sup>Note that an interpretation in terms of a DOS is only possible if  $i = j$ .

haves by changing the hybridization strength<sup>10</sup>  $V$  and the Coulomb potential  $U$ , as obtained from a continuous-time quantum Monte Carlo calculation (this method will be explained in detail in Section 3.7).

For different interaction parameters  $U$  and a constant hybridization  $V = 0.4$  eV, the spectral functions are shown in Figure 3.6 a). By increasing the Coulomb parameter  $U$  (note that in the case of one impurity orbital  $J = 0.0$  eV), the broad peak at the Fermi energy ( $\omega = 0.0$  eV) in the non-interacting case ( $U = 0.0$  eV) narrows in favor of two broad peaks at  $-1/2U$  and  $+1/2U$ , which are the so-called lower and upper Hubbard bands. The sharp feature remaining at the Fermi energy is the Kondo resonance, that disappears if  $U \gg V$ . In Figure 3.6 b), the spectral function is shown for a constant Coulomb interaction and different hybridization strengths  $V$ . From here one can see that a too strong coupling ( $V = 0.8$  eV) leads to the “destruction” of the Kondo resonance.

What we have discussed above is the so-called symmetric Anderson impurity model, because the upper and lower Hubbard bands are symmetrically centered around the Fermi energy, which is the case if one sets the impurity level  $\epsilon$  to the value of  $-U/2$ . In the so-called asymmetric AIM, the spectral function will be modified according to different shifts of the impurity level, as beautifully demonstrated, for instance, in Reference [126]. Here, the lower and upper Hubbard bands are no longer symmetrically centered around the Fermi energy.

### 3.6.4. The energy window for the projection onto the impurity orbitals

In practical applications, one limits the sum over the states appearing in Equation (3.42) to a certain energy window. The reason for this lies in the nature of the projection of the KS orbitals onto a set of local orbitals (e.g. Wannier orbitals or any other atom-centered basis), as for instance extensively discussed in References [127] and [128]. In principle, the energy window has to be large enough so that all of the contribution of the local orbitals (e.g. the  $3d$  orbitals of the transition metal atoms) to the entire band structure of a system is taken into account. There are cases in which one can limit this energy window for the projection to only a small range of several eV, if one can identify almost isolated  $3d$  bands in the band structure of a system (as e.g. in  $\text{SrVO}_3$ ). In the case of molecules or atoms adsorbed on a metal surface, the  $3d$  orbitals will rather mix (hybridize) with many different bands of the substrate. In order to get all the contribution of the local ( $3d$ )

---

<sup>10</sup>The hybridization function has been calculated according to Hewson’s Equation (5.42) [40] with a bandwidth  $D = 10.0$  eV and impurity level  $\epsilon = -U/2$ .

orbitals to the entire band structure in this case, one has to include all occupied bands and unoccupied bands up to a certain energy above the Fermi level (in this work not higher than 10 eV above the Fermi level) in the projection.

In Reference [129], it is discussed that the energy window should not be chosen too large (which means not to include too many unoccupied bands, or virtual orbitals), in case to avoid mixing of states of similar character (which would lead to an artificially small spread of the projected localized orbitals). This in turn would require a larger Coulomb interaction [128]. Thus, for a full ab-initio treatment one would have to calculate the Coulomb matrix for the chosen basis (the projected orbitals) individually for each system, which is not always possible due to the limited availability of programs in which this is implemented.

A further argument for limiting the number of virtual orbitals in the projection might be that from a physical point of view, the inclusion of too many unoccupied states leads to very large values of the impurity (subsystem) energies (Equation(3.44)), which can then be far above the Fermi energy (we will discuss this later in more detail, see Section 4.2). This lowers the occupation number of the correlated sub-space to unphysical (or unchemical) values. Therefore, the energy window has to be chosen with care, which requires a chemical, or physical intuition for the system under consideration.

## 3.7. The Continuous-time quantum Monte Carlo (CT-QMC) method

The CT-QMC method has its roots in the works by Prokof'ev *et al.* (1996) [130], and by Beard and Wiese (1996) [131], for the calculation of lattice models. The discovery of this method being applicable to impurity models was the beginning for the development of different CT-QMC solvers. The two most important ones are the weak coupling formulation (CT-INT) [132, 133] and the hybridization expansion (CT-HYB) [134]. The latter formalism is used throughout this work, and will thus be explained in more detail in the following.

### 3.7.1. Introduction

The advantage of the quantum Monte Carlo method in general is that for impurity models at non-zero temperature, the size of the Hilbert space will not affect the simulation [135]. The reason for this is that the electronic bath, i.e., the surrounding or environment of the impurity, is assumed to be non-interacting, so that its

contribution to the full partition function is just a single determinant (see below). This allows for treating impurity models (such as the AIM) with more than one correlated orbital, without further truncation of the bath states. The partition function takes the form [135]

$$Z = \text{Tr}[e^{-\beta\hat{H}}] \quad (3.48)$$

with  $\hat{H}$  being the Hamiltonian of the impurity model and  $\beta = \frac{1}{k_b T}$  ( $k_b$  is the Boltzmann constant) the inverse temperature.

For strongly correlated materials, solving an impurity model actually means computing the (local) interacting Green's function, which is usually done on the imaginary time-axis ( $\tau = \frac{it}{\hbar}$ ). On this axis, the physical quantities are periodic over the interval  $\tau \in [0, \beta]$  [44], which is why the interacting impurity Green's function is calculated on this interval as [135]

$$g_{\text{int}}(\tau) = -\langle \hat{T}_\tau \hat{d}(\tau) \hat{d}^\dagger(0) \rangle = \frac{1}{Z} \text{Tr}[e^{-(\beta-\tau)\hat{H}} \hat{d} e^{-\tau\hat{H}} \hat{d}^\dagger]. \quad (3.49)$$

In Equation (3.49),  $\hat{T}_\tau$  is the time-ordering operator that orders the creation and annihilation operators chronologically (with the later times to the left of the earlier times).  $\hat{d}$  and  $\hat{d}^\dagger$  are annihilation and creation operators on the impurity site. Note that  $g_{\text{int}}$  is actually a matrix, but for the sake of simplicity we dropped the impurity orbital indices ( $i$  and  $j$ ) here and in the following.

Within CT-QMC, the partition function is evaluated as a sum of weights  $w_c$  of a (partition function) configuration  $c$  [135, 136],

$$Z = \sum_c w_c. \quad (3.50)$$

Later on, it will be shown what these weights are in detail. The configurations  $c$  are in the literature referred to as diagrams of order  $k$ , as will later be discussed in more detail. By satisfying the two conditions of ergodicity and balance, one can estimate the impurity Green function as [135],

$$g_{\text{int}}(\tau) = -\frac{\sum_c w_c g_{\text{int}}^c(\tau)}{\sum_c w_c} \quad (3.51)$$

with  $g_{\text{int}}^c(\tau)$  as the Green function of configuration  $c$ .

### 3.7.2. The hybridization expansion

In this part, the general idea of the hybridization expansion shall briefly be outlined. The Anderson Hamiltonian in the interaction representation is split into two

parts  $\hat{H}_A$  and  $\hat{H}_B(\tau)$  [134,136], for which one chooses  $\hat{H}_A$  to be time-independent. The partition function in this representation becomes

$$Z = \text{Tr} \hat{T}_\tau e^{-\beta \hat{H}_A} \exp \left[ - \int_0^\beta d\tau \hat{H}_B(\tau) \right]. \quad (3.52)$$

The part that depends on  $\hat{H}_A$  is exactly solvable and well understood, because it is independent of  $\tau$ , whereas the part that depends on  $\hat{H}_B$  is more difficult to solve, which is why it is usually treated perturbatively [137]. In the hybridization expansion  $\hat{H}_B$  takes the form

$$\hat{H}_B = \sum_{\nu i \sigma} [V_{\nu i} \hat{c}_{\nu, \sigma}^\dagger \hat{d}_{i, \sigma} + V_{\nu i}^* \hat{d}_{i, \sigma}^\dagger \hat{c}_{\nu, \sigma}] \quad (3.53)$$

$\hat{H}_A$  is then the remainder of the Anderson Hamiltonian,

$$\hat{H}_A = \underbrace{\sum_{\nu \sigma} \epsilon_\nu \hat{c}_{\nu, \sigma}^\dagger \hat{c}_{\nu, \sigma}}_{\hat{H}_{\text{bath}}} + \underbrace{\sum_{i \sigma} \epsilon_i \hat{d}_{i, \sigma}^\dagger \hat{d}_{i, \sigma} + \frac{1}{2} \sum_{\substack{ijkl \\ \sigma \sigma'}} U_{ijkl} \hat{d}_{i, \sigma}^\dagger \hat{d}_{j, \sigma'}^\dagger \hat{d}_{l, \sigma'} \hat{d}_{k, \sigma}}_{\hat{H}_{\text{loc}}}. \quad (3.54)$$

The idea is to substitute  $\hat{H}_A$  and  $\hat{H}_B$  into Equation (3.52), and to expand the partition function in powers of  $\hat{H}_B$ . One finds that the bath degrees of freedom can be integrated out, since the bath is non-interacting. A detailed review about this expansion is given in Reference [136]. One ends up with a partition function of the form

$$Z = Z_{\text{bath}} \sum_k \int \int \int d\tau_1 \dots d\tau'_k \sum_{i_1 \dots i_k} \sum_{i'_1 \dots i'_k} \times \text{Tr} [\hat{T}_\tau e^{-\beta \hat{H}_{\text{loc}}} \hat{d}_{i_k}(\tau_k) \hat{d}_{i'_k}^\dagger(\tau'_k) \dots \hat{d}_{i_1}(\tau_1) \hat{d}_{i'_1}^\dagger(\tau'_1)] \det \Delta, \quad (3.55)$$

where the first summation runs over the expansion order  $k$ , and  $Z_{\text{bath}}$  is defined as [136, 138]

$$Z_{\text{bath}} = \text{Tr} e^{-\beta \hat{H}_{\text{bath}}} = \prod_\sigma \prod_\nu (1 + e^{-\beta \epsilon_\nu}). \quad (3.56)$$

$\det \Delta$  appearing in Equation (3.55) is the determinant of the anti-periodic hybridization function  $\Delta(\tau)$  with the elements  $\Delta_{lm}(\tau)$  (here  $l$  and  $m$  are impurity indices),

$$\Delta_{lm}(\tau) = \sum_\nu \frac{V_\nu^{l*} V_\nu^m}{e^{\epsilon_\nu \beta} + 1} \times \begin{cases} -e^{-\epsilon_\nu(\tau - \beta)}, & 0 < \tau < \beta \\ e^{-\epsilon_\nu \tau}, & -\beta < \tau < 0 \end{cases} \quad (3.57)$$

As mentioned earlier, one aims for computing the local Green's function, which in this expansion reads [136]

$$\begin{aligned}
 g_{lm}(\tau_l, \tau_m) = & -Z_{\text{bath}} \sum_k \int \int \int d\tau_1 \dots d\tau'_k \sum_{i_1 \dots i_k} \sum_{i'_1 \dots i'_k} \\
 & \times \text{Tr}[\hat{T}_\tau e^{-\beta \hat{H}_{\text{loc}}} \hat{d}_l(\tau_l) \hat{d}_m^\dagger(\tau_m) \hat{d}_{i_k}(\tau_k) \hat{d}_{i'_k}^\dagger(\tau'_k) \dots \hat{d}_{i_1}(\tau_1) \hat{d}_{i'_1}^\dagger(\tau'_1)] \det \mathbf{\Delta}.
 \end{aligned} \tag{3.58}$$

By comparing with the partition function shown in Equation (3.55), one finds that  $g_{lm}(\tau_l, \tau_m)$  is simply the partition function with two additional operators (and a minus sign)  $\hat{d}_l(\tau_l) \hat{d}_m^\dagger(\tau_m)$ .

In Equation (3.50), the weights  $\omega_c$  have been introduced, which can now be sampled by quantum Monte Carlo as

$$\omega_c = \text{Tr}[\hat{T}_\tau e^{-\beta \hat{H}_{\text{loc}}} \hat{d}_{i_k}(\tau_k) \hat{d}_{i'_k}^\dagger(\tau'_k) \dots \hat{d}_{i_1}(\tau_1) \hat{d}_{i'_1}^\dagger(\tau'_1)]. \tag{3.59}$$

To evaluate the operator trace in Equation (3.59) there exists different ways (see Reference [136]). For the density-density approximation,  $\hat{H}_{\text{loc}}$  commutes with the number operator of each orbital, which is why the time evolution of the impurity can be represented by a collection of segments. Each segment is a time interval at which an electron of a certain flavor (spin and orbital) resides on the impurity (Figure 3.7). The weights  $w_{\text{loc}}$  then become,

$$\omega_c = s \exp\left(\mu \sum_l^N L_l - \sum_{k < l}^N U_{kl} O_{kl}\right). \tag{3.60}$$

In Equation (3.60),  $s$  is a sign factor due to permutation of the operators depicted in Fig. 3.7,  $L_l$  is the length of the segment of flavor  $l$  (bold lines in Fig. 3.7), and  $O_{kl}$  is the overlap between segments of flavor  $k$  and  $l$  (orange areas in Fig. 3.7), while  $U_{kl}$  is the Coulomb interaction between the two flavors, and  $\mu$  is the chemical potential. The steps in the DFT++ approach employed here are depicted in Figure 3.8 at the example of a single impurity orbital (note that the indices have been dropped for this reason). Generally, one has to calculate the hybridization function as obtained from DFT on the so-called Matsubara axis at the discrete frequencies [136, 139]

$$\omega_n = \frac{(2n+1) \cdot \pi}{\beta}. \tag{3.61}$$

Here,  $n$  is an integer starting from zero (0, 1, 2, ...), and  $\beta$  is the inverse temperature ( $\frac{1}{k_B T}$ ).

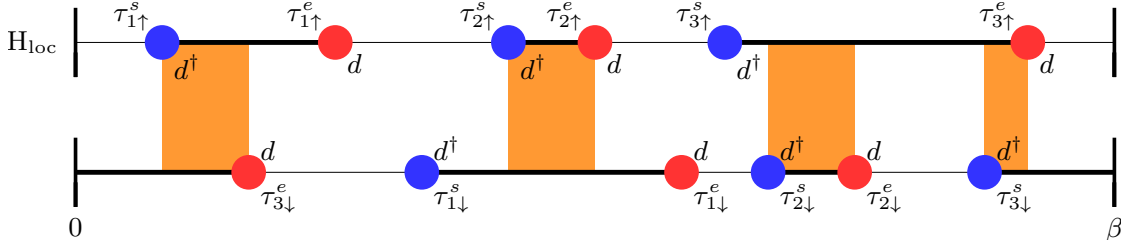


Figure 3.7.: Depiction of the segment picture in CT-HYB for a one-orbital Anderson model. The upper line corresponds to the spin-up and the lower line to the spin-down channel. The blue and red circles are a guide for the eye, to distinguish between creation (blue) and annihilation (red) operators. The bold line is for an occupied orbital and the length of the orange area contributes to the Coulomb energy via  $O_{kl}$  (second sum term in Equation (3.60)). Time increases from left to right. For further description, see text. The figure was taken from Ref. [136], where the hats of the operators were neglected.

As described before, the CT-QMC algorithm is defined on the imaginary time axis, for which one uses a Fourier transformation (FT) to obtain the hybridization function on this axis as input for solving the impurity model. Afterwards, the interacting impurity Green's function  $g_{\text{int}}(\tau)$  is Fourier-transformed onto the fermionic Matsubara axis to calculate the self-energy via the Dyson equation (Equation (3.46)).

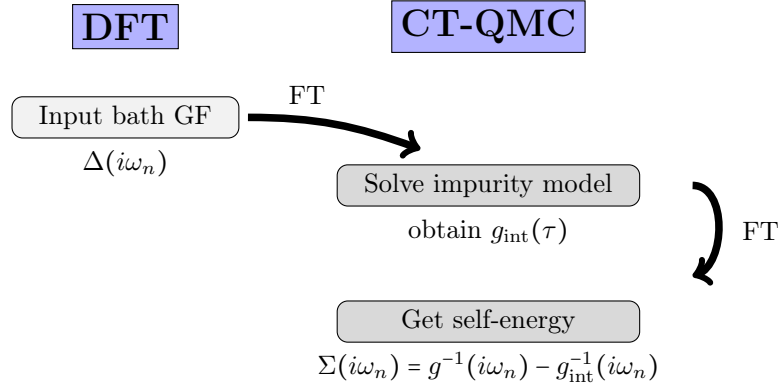


Figure 3.8.: Depiction of the DFT++ approach using CT-QMC in the case of a single impurity orbital (for which reason the indices have been dropped). For solving the impurity model, see Section 3.6.3. GF is a short form for Green's function, and FT means that Fourier transformation is necessary at this point.

### 3.7.3. Total energy within CT-QMC

The evaluation of the total energy within CT-QMC is, for instance, implemented in ABINIT [128, 140] in the framework of the DMFT [24, 119]. DMFT is used to treat periodically repeating impurities by solving the AIM iteratively until the self-energy is converged. In case of a single impurity (as in our cases) one obtains the total energy by solving the DMFT cycle only once.

The expression for the DFT++ energy reads [128]

$$E_{\text{DFT}++} = T_0^{\text{DFT}++} + E_{\text{XC}}[\rho(\mathbf{r})] - E_{\text{Ha}}[\rho(\mathbf{r})] + \int d\mathbf{r} V_{\text{ext}}(\mathbf{r})\rho(\mathbf{r}) + E_{\text{pot}} - E_{\text{DC}}. \quad (3.62)$$

In Equation (3.62),  $V_{\text{ext}}$  is the external potential,  $E_{\text{XC}}$  is the exchange–correlation functional, and  $E_{\text{Ha}}$  is the Hartree energy (the Coulomb interaction between the electrons),  $E_{\text{pot}}$  is the on-site interaction term (Coulomb interaction on the impurity), which is directly calculated from the impurity solver (i.e. CT-QMC),  $E_{\text{DC}}$  is the double-counting correction (see Section 3.6.2), and  $T_0^{\text{DFT}++}$  is the kinetic energy term that is an analogue to the DFT kinetic energy, but with a correction due to the solution of AIM (i.e. the occupation of the Kohn–Sham orbitals changes, and consequently the kinetic energy has to be corrected according to the new density obtained from DFT++) [128].

The on-site potential energy  $E_{\text{pot}}$ , as obtained from CT-QMC (with density–density type interaction) is evaluated as [136]

$$E_{\text{pot}} = \frac{1}{2} \sum_{ij\sigma\sigma'} U_{ij} \langle \hat{n}_{i\sigma} \hat{n}_{j\sigma'} \rangle + \frac{1}{2} \sum_{i \neq j\sigma} (U_{ij} - J_{ij}) \langle \hat{n}_{i\sigma} \hat{n}_{j\sigma} \rangle. \quad (3.63)$$

Here,  $\langle \hat{n}_{i\sigma} \hat{n}_{j\sigma'} \rangle$  is the so-called double-occupancy.

### 3.7.4. Magnetic properties of the impurity atom

In this part, it will briefly be discussed how the local magnetic properties of an impurity atom can be evaluated. It will be focused on quantities which are used throughout this work.

Within CT-QMC, we are able to evaluate the spin–spin correlation function  $\chi(\tau)$  on the imaginary time axis [141, 142]

$$\chi_i(\tau) = \langle \chi_i(\tau) \chi_i(0) \rangle = \langle \hat{S}_Z^i(\tau) \hat{S}_Z^i(0) \rangle. \quad (3.64)$$

In Equation (3.64),  $\hat{S}_Z^i(\tau)$  is the local spin on the impurity orbital  $i$  at imaginary time  $\tau$ . Evaluating  $\chi(\tau)$ , one can gain insight into the magnetic behavior of the system under consideration. The local spin at the initial time  $\tau = 0$  is equivalent to the magnetization before interaction with the surroundings takes place. Another special value, which is known as the long-time correlation value of  $\chi(\tau)$ , is  $\tau = \beta/2$ , from which one can estimate to which extent the impurity electrons are localized on one of the impurity orbitals, or delocalized/screened due to interaction with the substrate and the ligands [143]. The latter case is indicated by a rather rapid drop of  $\chi(\tau)$  as  $\tau \rightarrow \beta/2$ , whereas a finite value at  $\chi(\beta/2)$  suggest that there is spin density located on one of the impurity orbitals even in the presence of the bath.

From  $\chi_i(\tau)$ , it is possible to calculate the so-called physical susceptibility  $\chi_i^{\omega=0}$  via integration [142],

$$\chi_i^{\omega=0} = g^2 \int_0^\beta d\tau \chi_i(\tau). \quad (3.65)$$

Here,  $g$  is the spin gyromagnetic factor ( $-2.0$ ). Since the susceptibility is actually an energy-dependent quantity, the physical susceptibility is obtained at the frequency  $\omega = 0$ . Note that  $\chi_i^{\omega=0}$  can be studied as a function of  $T$ , because the integration interval appearing in Equation (3.65) varies with  $\beta = \frac{1}{k_b T}$ .

### 3.7.5. Fermi-liquid properties of the impurity atom

In Section 3.1, it has been introduced that the Kondo effect exhibits the same properties as known from Fermi-liquid theory, as shown by Nozières [43]. Although as mentioned before, we do not want to go too deep into the details of this theory, it is important to discuss some of the properties of a Fermi-liquid, as they will be used throughout this work for scrutinizing the existence of the Kondo effect.

On the real energy axis, the imaginary part of the self-energy as introduced in Equation (3.46) behaves in the Fermi-liquid regime as [40]

$$\text{Im}\Sigma(\omega) \propto \omega^2 \quad (3.66)$$

as  $\omega \rightarrow 0$ . Since CT-QMC works on the imaginary time axis, we obtain the self-energy (after Fourier transformation) on the Matsubara axis at the discrete energies  $\omega_n$ , which in the Fermi liquid regime shows the behavior [144]

$$\text{Im}\Sigma(\omega_n) \propto \omega_n \quad (3.67)$$

as  $\omega_n \rightarrow 0$ . Another tool for probing the Fermi-liquid properties is the so-called first Matsubara-frequency ( $\omega_0$ ) rule [145], which states that  $\text{Im}\Sigma(\omega_0)$  should go linearly to zero as  $T \rightarrow 0$  K.

The transition to the Fermi-liquid regime can also be studied by considering the physical susceptibility  $\chi_i^{\omega=0}(T)$ . As mentioned in Section 3.1, in the case of a well-defined and unscreened local moment,  $\chi_i^{\omega=0}(T)$  obeys the Curie law ( $\propto 1/T$ ). If the temperature is low enough, so that the local moment can be Kondo-screened by the conduction electrons,  $\chi_i^{\omega=0}(T)$  has to cross over to a Pauli behavior ( $\chi_i^{\omega=0}(T)$  is constant in  $T$ ) in the Fermi liquid regime. This has also consequences for the spin-spin correlation function  $\chi_i(\tau)$ , as this function yields the physical susceptibility via integration (see Equation (3.65)). It turns out that the special point  $\chi_i(\beta/2)$  behaves as  $T^2$  in the Fermi liquid regime<sup>11</sup> [143, 146].

### 3.7.6. From the imaginary to the real energy axis (Analytic continuation)

The CT-QMC method, although being numerically exact, suffers from being defined on the imaginary time axis. Fourier transformation onto the frequency domain leads to the discrete Matsubara frequencies. On this axis, quantities can only hardly be interpreted in physical terms, which requires an analytical continuation onto the real frequency axis. If the analytic form of these quantities would be known, this would in principle mean to just replace  $i\omega_n \rightarrow \omega + i$  ( $\eta$  is a small offset). In CT-QMC algorithms, however, the quantities are measured on specific points  $\tau$  and possess statistical noise (and so they do on the Matsubara axis).

Here we are interested in obtaining the spectral function  $A(\omega)$ , which has already been introduced in Section 3.6.3, and which is in general connected to the imaginary part of a Green's function. As mentioned before, the impurity Green's function in CT-QMC is usually measured in imaginary time, which can be Fourier-transformed to the frequency domain with the frequencies  $\omega_n = \frac{\pi}{\beta}(2n + 1)$  (we have dropped the orbital indices for the sake of simplicity here and in the following) [147],

$$g_{\text{int}}(i\omega_n) = \int_0^\beta d\tau g_{\text{int}}(\tau) e^{i\omega_n \tau}. \quad (3.68)$$

The inverse Fourier transform reads

$$g_{\text{int}}(\tau) = \frac{1}{\beta} \sum_n g_{\text{int}}(i\omega_n) e^{i\omega_n \tau}. \quad (3.69)$$

The Green's function on the Matsubara axis is connected to the spectral function by the relation [147]

$$g_{\text{int}}(i\omega_n) = \int_{-\infty}^{\infty} d\omega \frac{A(\omega)}{i\omega_n - \omega} \quad (3.70)$$

<sup>11</sup>Remember that  $\beta = 1/k_B T$ .

Inserting Equation(3.70) into Equation (3.69) yields [147]

$$g_{\text{int}}(\tau) = \int_{-\infty}^{\infty} d\omega \frac{e^{-\tau\omega}}{1 + e^{e-\beta\omega}} A(\omega). \quad (3.71)$$

Solving Equation (3.71) is ill-posed, because it requires the inversion of the integral kernel [147], in addition to the problem of the statistical noise. For this reasons, one has to estimate  $A(\omega)$  using Bayesian inference, by finding the most probable  $A(\omega)$  for a measured value  $\bar{g}_{\text{int}}(\tau)$ . However, this will not be part of this discussion (details can be found in Ref. [147]), but it shall be mentioned that this can be done by the so-called Maximum entropy method (often called “MaxEnt”), which says that the most probable  $A(\omega)$  can be assigned by maximizing the information entropy [147–149]

$$S = - \int d\omega A(\omega) \log \left( \frac{A(\omega)}{m(\omega)} \right). \quad (3.72)$$

Here,  $m(\omega)$  is the so-called default model [147]), which can be any distribution function such as a Gaussian distribution or some other model distribution. The maximum value of  $S$  ( $=0$ ) is when  $A(\omega) = m(\omega)$ , in all other cases  $S$  is negative [147]. The MaxEnt procedure used throughout this work makes use of the algorithm by Bryan [150], which was implemented and provided to us by Lewin Böhnke.

### 3.7.7. Comparison with other quantum Monte Carlo methods

Apart from the CT-HYB method there exist other quantum Monte Carlo implementations. Here, we will briefly introduce them, focusing on the advantages and disadvantages over CT-HYB.

Historically, CT-QMC was developed roughly 10 years after the so-called Hirsch–Fye Quantum Monte Carlo (HF-QMC) method. The latter is based on the work of Hirsch and Fye [151, 152], and is formulated to sample the impurity Green’s function on discretized imaginary times  $\Delta\tau$  (for more details see, e.g., Reference [153]). The HF-QMC is numerically only exact in the limit  $\Delta\tau \rightarrow 0$  [154], which is a clear disadvantage over the continuous-time quantum Monte Carlo methods. Furthermore, the time-discretization makes the HF-QMC method much more expensive as compared to CT-QMC [155], which limits it to rather large electronic temperatures.

It has already been introduced that there exists a second implementation of CT-QMC, in which  $\hat{H}_B$  of Equation (3.52) takes the form of the interaction part of

the Anderson Hamiltonian (last term of Equation (3.39)). This implementation is rather suited for Hubbard-like models [136]. Both the CT-INT and CT-HYB methods suffer from a so-called sign problem, which arises due to the anticommutation relation for fermionic operators. The exchange of two electrons can lead to negative weights in the CT-QMC sampling, which can not be interpreted in terms of a probability for a given configuration  $c$ . However, it turned out that this problem is rather relevant for lattice models (e.g., periodically repeated impurities), and only little important in case of a single impurity (it is nevertheless still present) within the density–density and Kanamori approximation [155,156]. Further improvement concerning the sign error can be reached by eliminating off-diagonal terms in the hybridization function by diagonalizing the correlated sub-space [157].

There are other version of QMC methods such as Continuous-Time Auxiliary-Field Algorithm (CT-AUX), which is a variant of CT-INT, and there are also attempts to implement CT-QMC on the real time axis (CT-HYB and CT-AUX). For further details about these implementations, the reader is referred to the excellent review by Gull *et al.* [136], and to References [158–160]

## 4. Towards a conceptual understanding of the Kondo effect in terms of chemical bonding

The Kondo effect is often regarded as an open-shell singlet state formed by the localized spin and the electrons of the conduction band of a substrate [41]. The Kondo effect can also be observed in nanoparticles, which are usually called “Kondo box”, due to the confinement of the “bath” states provided by the nanoparticle [161–163]. This can be considered as an impurity being coupled to “a particle in a box”, rather than to a continuum of states (band) as in a bulk system. The smallest Kondo systems are, surprisingly, molecular ones, as suggested by the theoretical results of Fulde and Dolg [164–166] about bis( $\pi$ -[8]annulene)cerium ( $\text{Ce}(\text{C}_8\text{H}_8)_2$ ), with experimental evidence provided by the work of Booth *et al.* [167].

For the simplest Anderson model, as discussed in Section 3.6.3, the Kondo resonance strongly depends on the Coulomb interaction  $U$  and the hybridization  $V$  of the impurity to the bath states. The latter is readily available from a DFT calculation, which makes it promising for us to study how a qualitative understanding of the Kondo effect can be gained by analyzing such DFT calculations.

Our aim is therefore to get insights from a chemistry perspective, by using the concept of chemical bonds for studying structure–property relations concerning the Kondo effect. In solid-state physics, such analysis is often realized by constructing a local Wannier basis from Bloch orbitals, but they are not unique and care must be taken by localizing them onto atoms or chemical bonds, as well as to their symmetry [129, 168–170]. For this reasons, it is promising to use quantum chemistry programs (commonly implemented in an atom-centered basis) for evaluating the hybridization function using chemical tools, which also allows for an interpretation in terms of molecular orbitals. For a chemical analysis, this would further have the advantage of working in real-space instead of the reciprocal-space often used in solid-state physics. The idea of a chemical analysis of Kondo systems is motivated

by the textbook of R. Hoffmann [22], who explained the bonding in solid-state systems in terms of chemical bonds. Merging this with state-of-the-art concepts from physics, it is believed to obtain new insights for understanding the control of the Kondo effect, either by mechanical or chemical manipulation.

From the technical point of view, quantum chemistry programs often allow the use of a wider range of exchange–correlation functionals, which can be particularly important in cases where the most commonly used LDA and GGA type functionals fail to describe the correct electronic structure of a system. Thus, the chemical concept introduced in this section allows for an evaluation of the results from state-of-the-art DFT++ calculations for Kondo systems, which are due to the large computational effort along with, e.g., hybrid functionals, often restricted to be parameterized by LDA or GGA type functionals.

To this end, we introduce a scheme for a local decomposition of hybridization functions, which combined with the concept of molecular orbitals could pave the way towards new insights into the chemical and mechanical control of the Kondo effect. This requires a prior description of an implementation for evaluating hybridization functions (Equation (3.45)) within an atom centered basis set. Because the concept of the hybridization as an energy-dependent function is only little known in chemistry, it will furthermore be explained here using some simple examples.

The first example will be an iron porphyrin (Fe(porph)), in which the Fe  $3d$  orbitals represent the correlated sub-space (the impurity orbitals), coupled to an electronic bath provided by the ligand. This choice was made to validate the correctness of the implementation described in Section 4.1, by comparing the Fe  $3d$  hybridization functions with the results obtained by Bhandary *et al.* [171]. Furthermore, first aspects of the hybridization function will be discussed at this example, and we will also compare the expected ligand field splitting of a square planar complex with the Fe subsystem  $d$  energies (the  $3d$  splitting) as obtained by projecting the KS Green’s function onto the Fe  $3d$  orbitals. For this, the effect of different energy windows applied in the projection scheme (see, e.g. Sec. 3.6.4) onto the Fe subsystem  $d$  energies will be analyzed.

Knowing that the implementation works well, the dissociation of a hydrogen molecule will be investigated with respect to the hybridization strength and the open-shell character at different bond distances. In this example, one of the H atoms is considered as an impurity atom coupled to an electronic bath which is provided by the second H atom. Here the connection between an open-shell singlet and the Kondo effect can be illustrated, because we encounter a similar situation as shown for the Kondo effect in the simplest Anderson impurity model (introduced at the end of Section 3.6.3). That is the formation or destruction of the Kondo

effect by varying the hybridization parameter  $V$ , which is similar to the transition of an closed-shell to open-shell singlet state in  $H_2$  by stretching it's bond.)

In the following part, it will be considered how the energy dependence of the hybridization function can be understood as a consequence of an orbital being coupled to a continuum of effective single-particle states (a so called band), rather than discrete molecular levels. For this purpose, the hybridization function of a helium atom coupled to a chain of hydrogen atoms will be compared for different chain lengths<sup>1</sup>. Last but not least, it will be discussed why in practice the AIM is parametrized by a spin-unpolarized DFT calculation, although dealing with spin-polarized adsorbates on metallic surfaces throughout this thesis.

After the concept for analyzing hybridization functions using tools from chemistry has been explained, and realistic Kondo systems have been characterized within DFT++, such an analysis will later be applied to a tetra carbonyl cobalt complex on Cu(001) (Section 9) to obtain insights into the chemical control of the Kondo effect.

## 4.1. Introducing a local decomposition of hybridization functions

In this part, the implementation for projecting MOs onto localized orbitals shall be described. This allows the evaluation of hybridization functions with quantum chemistry programs and the decomposition into different parts of the electronic bath. For this, the overlap matrix of the atom-centered basis, the KS Hamiltonian matrix, the KS eigenvalues, and the MO coefficients of a converged DFT calculation are required. The entire procedure of this implementation is depicted in Figure 4.1 and explained in the following.

In our case, the full Hilbert space  $F$  (with dimension  $n \times n$ ) is spanned by a set of non-orthogonal atom-centered basis functions  $\{|a\rangle\}$ <sup>2</sup>, which generally have a non-zero overlap between different basis functions ( $S_{ab} \neq 0$ ). This is in contrast to a plane-wave basis as used in the solid state programs, which form an orthogonal set of basis functions. For this reason, we transform our non-orthogonal basis  $\{|a\rangle\}$

---

<sup>1</sup>This system is without a doubt rather unphysical, but simple enough to understand how the energy dependence of  $\Delta_{ij}(\omega)$  arises as the consequence of an atomic orbital being coupled to a quasi-continuum of effective single-particle states.

<sup>2</sup>Note that the short-hand form  $\phi_a = |a\rangle$  has been used here.

into a Löwdin-orthogonalized basis  $\{|a'\rangle\}$ ,

$$|a'\rangle = \sum_b S_{a'b}^{-1/2} |b\rangle, \quad (4.1)$$

so that we have  $S_{a'b'} = \delta_{a'b'}$ .

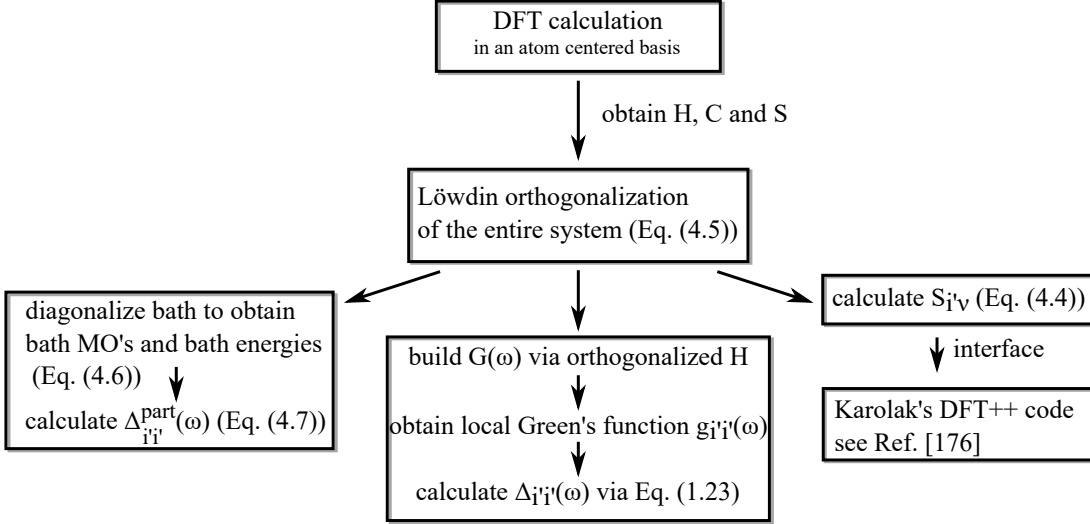


Figure 4.1.: Flow chart of the projection scheme implementation.

It should be mentioned that the Löwdin-orthogonalized basis is in general not atom-centered, which is why the projection performed later is not entirely locally defined. However, the Löwdin basis resembles the original atom-centered basis as good as possible [172], which is why it is applied successfully for population analysis of a broad range of system in quantum chemistry.

We now want to project the full Hilbert space onto the correlated sub-space  $C$  ( $C \in F$ ) spanned by  $\{|i'\rangle\}$ . The sub-space  $C$  represents in our case the impurity orbitals, which are usually in the context of strongly correlated materials the  $d$  or  $f$  orbitals of an atom (see Figure 4.2). Consequently, the remainder of  $F$  represents the electronic bath which spans the space  $B$ . In general, the sub-space  $C$  could also be extended to include other orbitals, such as  $s$  and  $p$  orbitals or MOs, and is not only restricted to a single atom (see for instance Reference [121]). Note that  $\{|i'\rangle\}$  is in our case an element of  $\{|a'\rangle\}$ , but not necessarily has to be<sup>3</sup>.

<sup>3</sup>In principle  $\{|i'\rangle\}$  could be any local basis functions centered on an impurity atom, which is not an element of the Hilbert space  $F$ .

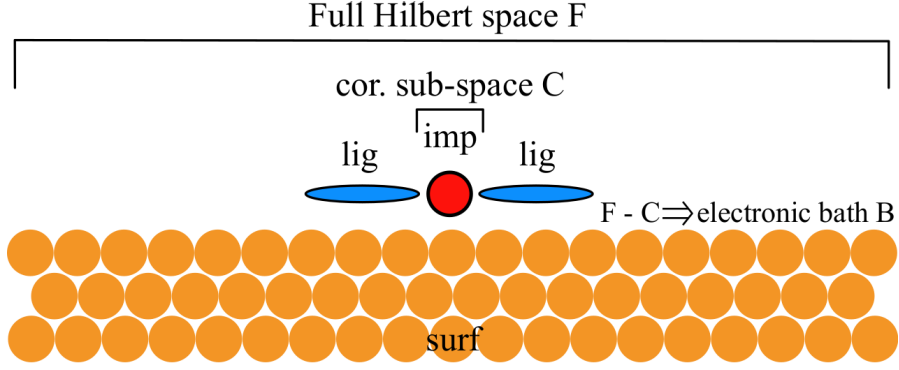


Figure 4.2.: Schematic illustration of a molecule on a surface (surf), with one impurity (imp) atom and two ligands (lig). The basis functions of the entire systems constitutes to the full Hilbert space  $F$ , whereas the correlated sub-space  $C$  contains selected basis functions of the impurity atom (in this work the  $3d$  orbitals of a transition metal atom). Note that  $C$  can in general be extended to more orbitals, including those on different kind of atoms, as e.g. in Reference [121]. The electronic bath is simply defined as the difference between the spaces  $F$  and  $C$ .

Due to the prior orthogonalization of the full Hilbert space  $F$  and since  $\{|i'\rangle\} \in \{|a'\rangle\}$ , the subspace  $C$  is orthogonal, too (i.e.  $S_{i'j'} = \delta_{i'j'}$ ). The projection operator  $\hat{P}$  is defined as

$$\hat{P} = \sum_{i' \in C} |i'\rangle \langle i'|. \quad (4.2)$$

Applying the projection onto the Green's function in the Lehmann representation as defined in Equation (3.13) yields (for the orthogonalized subspace  $C$ )

$$g_{i'i'}(\omega) = (\hat{P}G(\omega)\hat{P})_{i'i'} = \sum_K^N \frac{|i'\rangle \langle i'|\psi_K\rangle \langle \psi_K|i'\rangle \langle i'|}{\omega - \epsilon_K \pm i\eta}. \quad (4.3)$$

Here  $|\psi_K\rangle$  are the Kohn–Sham eigenfunctions with the corresponding eigenenergies  $\epsilon_K$ , and the sum runs over  $N$  eigenfunctions which are usually selected within a certain energy window (see discussion in Section 3.6.4).

From Equation (4.3) it can be deduced that the overlap elements  $S_{i'K} = \langle i'|K\rangle$  have to be evaluated, with  $|K\rangle = |\psi_K\rangle = \sum_a c_{Ka}|a\rangle$ , and  $c_{Ka}$  being the MO coefficients of a converged DFT calculation<sup>4</sup>. The elements  $S_{i'K}$  are in the following referred

<sup>4</sup>It is important to remember that the KS eigenfunctions  $|K\rangle = |\psi_K\rangle$  are a linear combination of the non-orthogonal basis  $\{|a\rangle\}$ .

to as projectors  $P_{i'K}$ , to align with common literature [173].  $P_{i'K}$  can be rewritten as

$$P_{i'K} = \sum_{a \in F} \langle i'|a \rangle c_{aK} = \sum_{a \in F} S_{i'a} c_{aK}, \quad (4.4)$$

with  $S_{i'a}$  being the overlap matrix elements of the non-orthogonalized basis function  $|a\rangle$  with the Löwdin orthogonalized basis function  $|i'\rangle$  of subspace  $C$ . The overlap elements  $S_{i'a}$  are equal to  $S_{ia}^{1/2}$ , which can be obtained by using that  $|i'\rangle = \sum_{b \in F} S^{-1/2}|b\rangle$  (Equation (4.1)). The hybridization function  $\Delta_{i'j'}(\omega)$  is then calculated via Equation (3.45).

Note that in general it is also possible to obtain the local Green's function  $g_{i'i'}(\omega)$ , by building the Green's function  $G(\omega)$  of the entire system in the matrix form as explained in Section 3.4. For this, the effective single-particle Hamiltonian matrix  $H$  is transformed into the Löwdin orthogonalized basis

$$H' = S^{-1/2} H S^{-1/2}, \quad (4.5)$$

and then used to evaluate the matrix Green's function (according to the definition in Equation (3.12)) by inversion of  $H'$ .  $g_{i'i'}(\omega)$  is then simply the element  $i'i'$  of  $G(\omega)$ .

For the projection of Bloch orbitals onto a set of localized orbitals we use the implementation within the projector augmented plane-wave (PAW) framework in solid-state codes (e.g. ABINIT [140, 173] or VASP [174, 175]) from which one obtains the projectors  $P_{i'K}$  (after orthogonalization of the correlated sub-space). When using VASP, we do the projection of the Kohn–Sham Green's function (Equation (3.42)) and the calculation of the hybridization function using an interface developed by Karolak *et al.* [176], whereas in ABINIT these routines are already existing in the standard implementation.

In terms of a chemical analysis of hybridization functions, the energies and molecular orbitals of the electronic bath are evaluated by diagonalizing only the subset  $B$  (black matrix elements) of the  $n \times n$  Hamiltonian matrix  $H'$  (for the sake of simplicity we assume here to have only one orbital in the correlated sub-space, which is why the block matrix of space  $B$  has a dimension of  $(n-1) \times (n-1)$ ),

$$H' = \begin{pmatrix} H'_{11} & H'_{12} & \cdots & \cdots & H'_{1n} \\ H'_{21} & H'_{22} & \cdots & \cdots & H'_{2n} \\ \vdots & \vdots & \ddots & \ddots & \vdots \\ \vdots & \vdots & \ddots & \ddots & H'_{n-1n} \\ H'_{n1} & H'_{n2} & \cdots & H'_{nn-1} & H'_{i'i'} \end{pmatrix},$$

as

$$\bar{H}_{\text{bath}} = T_{\text{bath}}^\dagger H' T_{\text{bath}}. \quad (4.6)$$

Here,  $T_{\text{bath}}$  is a diagonalization matrix of dimension  $n \times n$ , which contains the eigenvectors of the bath part (the entries of the sub-space  $C$  are zero), and  $\bar{H}_{\text{bath}}$  is the Hamiltonian matrix which is diagonal in the space  $B$  spanned by the basis functions of the electronic bath (green matrix elements):

$$\bar{H}_{\text{bath}} = \begin{pmatrix} \epsilon_1 & 0 & \cdots & \cdots & V_{1i'} \\ 0 & \epsilon_2 & \cdots & \cdots & V_{2i'} \\ \vdots & \vdots & \ddots & \ddots & \vdots \\ \vdots & \vdots & \ddots & \epsilon_\nu & V_{\nu i'} \\ V_{i'1} & V_{i'2} & \cdots & V_{i'\nu} & \epsilon_{i'} \end{pmatrix},$$

where  $\epsilon_\nu$  are the energies of the bath orbitals and  $V_{\nu i'}$  are the coupling elements between the bath and the impurity orbitals, which were already introduced in Equation (3.40).

In the following, we would like to introduce a scheme to decompose the hybridization function  $\Delta_{ij}(\omega)$  (for the sake of simplicity we write  $i = i'$  and  $j = j'$ ) into different parts, so that we can partition the contribution of different parts of the electronic bath to the full hybridization function. A possible choice would be the decomposition into a ligand (lig) and a surface (surf) part, as depicted in Figure 4.2. In the case of more than one ligand, it is also possible to analyze the contribution of each ligand individually, which is promising for studying the isolated effect of them onto the hybridization function of the correlated sub-space (the impurity orbitals).

For this reason, we weight the hybridization function by  $\sum_a c_{\nu a}^2$ , where the coefficients  $c_{\nu a}$  are those of the bath MOs  $|\nu\rangle$  appearing in the columns of the diagonalization matrix  $T_{\text{bath}}$ . This sum is 1 if the bath orbitals are normalized. and if the sum runs over all elements of space  $B$  (the electronic bath). Truncating the sum over  $a$  to basis functions of a specific part of the system yields,

$$\Delta_{ij}^{\text{part}}(\omega) = \sum_\nu \sum_{a \in \text{part}} \frac{c_{\nu a}^2 V_{\nu i} V_{\nu j}^*}{\omega + i\eta - \epsilon_\nu}, \quad (4.7)$$

where ‘‘part’’ can contain the basis functions of the ligands or the surface (or in principle any part of the electronic bath). Following our example of Figure 4.2, the full hybridization function can be recovered as,

$$\Delta_{ij}(\omega) = \Delta_{ij}^{\text{lig}}(\omega) + \Delta_{ij}^{\text{surf}}(\omega). \quad (4.8)$$

To fulfill Equation (4.8), the remaining basis functions of the impurity atom (or atoms) need to appear in the sum over  $a$ . For instance, if the correlated sub-space  $C$  consists only of the  $3d$  orbitals of one atom, polarization functions<sup>5</sup>, the  $1s$  shell, the  $2s$  shell, etc., have to be included in the sum, too.

Combined with state-of-the-art DFT++ calculations, the decomposition of the hybridization function is a promising tool as it might give new insight into understanding the chemical and mechanical control of the Kondo effect. In addition, such an analysis can be complemented by considering the bath MOs, as a tool for an analysis in terms of chemical bonding.

## 4.2. A porphyrin ligand as a discrete electronic bath: Comparison with ligand field theory

Iron porphyrin (Fe(porph)) and its derivatives are not only interesting in science due to its biological relevance, but also for its potential for spintronic applications [177–179]. It could be shown that the Fe spin state in Fe(porph) can be switched between  $S=2$  and  $S=1$  by mechanically stretching and squeezing it in a molecular junction-like setup [180]. This spin-crossover behavior motivates researchers to investigate and develop new materials based on such molecules. From a theoretical point of view, Bhandary *et al.* [171] have applied the DFT++ approach to explain that the spin-crossover behavior in Fe(porph) is a delicate interplay between Fe subsystem  $d$  energies (often referred to as the static crystal field splitting in the literature), the energy-dependent hybridization of the Fe  $3d$  orbitals with the porphyrin ligand, and by the local Coulomb interaction on the Fe  $3d$  shell.

Using DFT++, one parametrizes the Anderson impurity model by a spin-unpolarized DFT calculation, due to the closed-shell character of the porphyrin ligand (which represents here the so-called electronic bath). This might seem a little confusing, because the electronic structure of Fe(porph) exhibits an open-shell character. It will later be shown in more detail (Section 4.4.3) that the parametrization of the AIM using closed-shell DFT works well in principle. At this point, it shall be noted that the magnetic character of the Fe atom will be recovered by solving the AIM<sup>6</sup>.

---

<sup>5</sup>Depending on the basis set which is used one would also have to include the diffuse basis functions etc..

<sup>6</sup>Although this requires that the spin density of the molecule is entirely located on the Fe atom, in particular on the  $3d$  shell.

In the following, Fe(porph) was chosen to validate the implementation described in Section 4.1 using the results of Bhandary *et al.* [171] as a reference. Furthermore, first aspects of hybridization functions shall be explained at this system, in which the Fe 3d orbitals (the impurity) are coupled to a discrete electronic bath provided by porphyrine. To this end, the results will be compared to what one would expect from molecular orbital theory.

### 4.2.1. Computational methodology

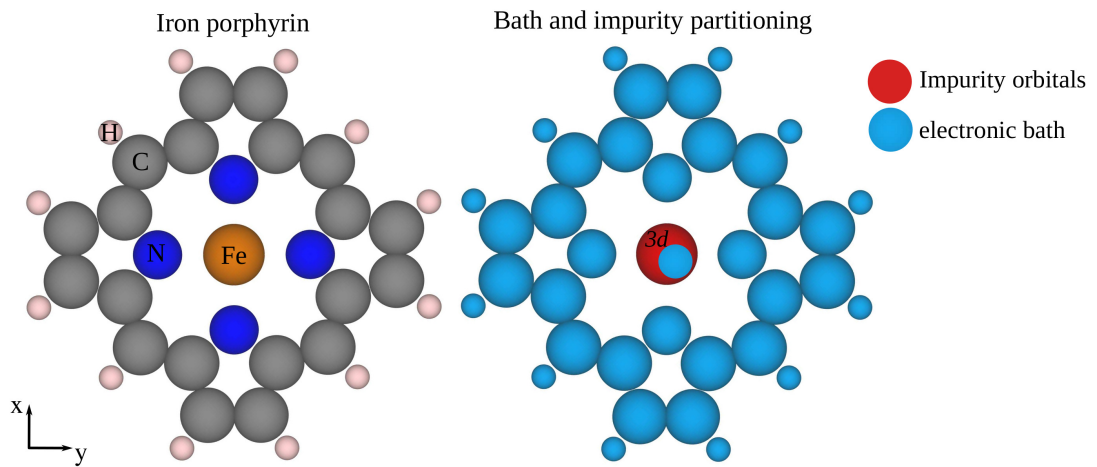


Figure 4.3.: Iron porphyrin (left) split into an electronic bath and the impurity orbitals. Note that the impurity orbitals comprise the Fe 3d shell only.

Fe(porph) was optimized with TURBOMOLE [181] using PBE/def2-TZVP [182–185], with convergence criteria for the SCF algorithm of  $1 \cdot 10^{-6}$  Hartree, and  $1 \cdot 10^{-4}$  Hartree/Bohr for the gradient. The hybridization function was obtained from a closed-shell single point calculation (PBE/def2-TZVP [182–185]), where again a convergence criterion of  $1 \cdot 10^{-6}$  Hartree for the SCF algorithm was used. According to Equation (4.4), we calculated the overlap of the impurity orbitals with the Kohn–Sham eigenfunctions (molecular orbitals), which were used as an input for Karolak’s DFT++ code [176] to extract the hybridization function for different energy windows. Note that the impurity consists of the Fe 3d orbitals only, and that the remaining Fe basis functions were included in the electronic bath (see Figure 4.3). To make our results comparable to the ones reported by Bhandary *et al.* [171], the hybridization function is based on a spin-unpolarized DFT calculation. This

is a common choice in the literature for the parametrization of the AIM for the case of a non-magnetic electronic bath, and will later be discussed in more detail (Section 4.4.3).

### 4.2.2. Fe subsystem $d$ energies and hybridization function as obtained from different projection windows

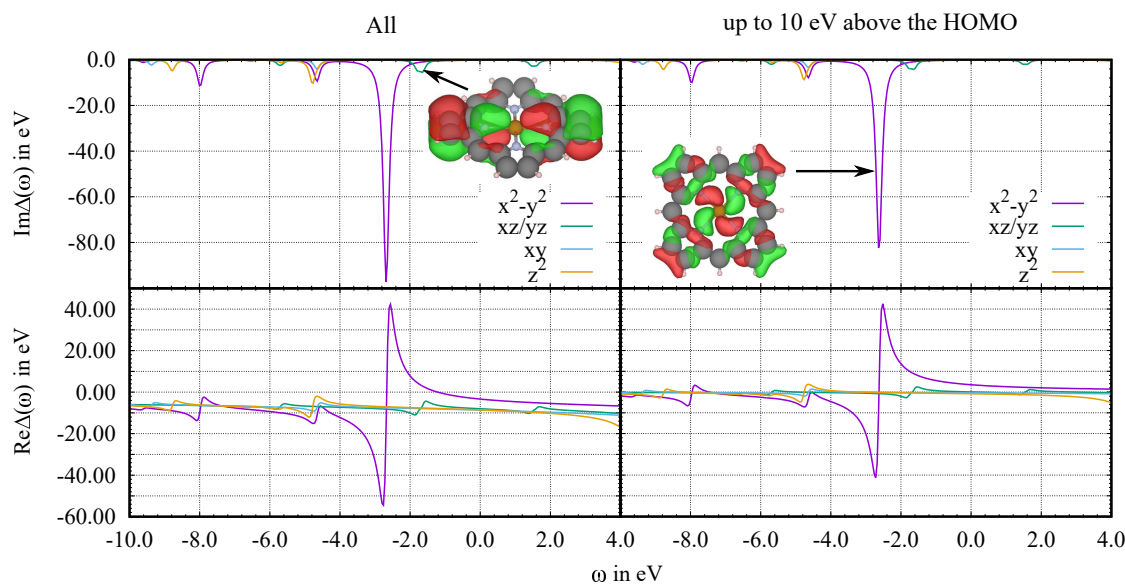


Figure 4.4.: Fe  $3d$  hybridization function of an iron porphyrin as obtained from PBE/def2-SVP. In the left panel, the projection was done with all single-particle orbitals of the system, whereas in the right panel we show the same results, but only took into account orbitals with an energy up to 10 eV above the energy of the HOMO. In this plot, a smearing (the imaginary off-set) of 0.1 eV was used. Note that the bath MOs shown in the plots have also Fe character, because the electronic bath consists of all basis functions on the ligand and the remaining Fe basis functions which are not the  $3d$  orbitals (however, the electronic bath includes the  $3d$  polarization functions). Isosurface value for bath MO plots: 0.02.

The Fe  $3d$  hybridization function of Fe(porph) is shown in Figure 4.4, for two different energy windows (see Sec. 3.6.4 for a brief discussion) used for the projection. In both cases, the top panel shows the imaginary part of the hybridization function, whereas the real part is shown in the bottom panel. The former describes

the effect of the Fe 3d orbitals being broadened due to the porphyrin backbone, whereas the latter is the energy-dependent shift of the 3d orbitals (therefor often referred to as the dynamical<sup>7</sup> crystal field) in the literature. In simple words, the hybridization function of the Fe 3d orbitals exhibit peaks at the effective single-particle energies of the electronic bath<sup>8</sup>. (in the following sections, this concept will become more clearly).

Qualitatively, the projections with both energy windows yield similar results for the real and imaginary parts of the hybridization function. Comparing with Ref. [171], one can see that our hybridization functions exhibit the same features as the (VASP) results of Bhandary *et al.* However, our peaks are shifted to lower energies compared with the results of Ref. [171], which might result from the different basis sets used in VASP and TURBOMOLE, as well as from small differences in the molecular structure.

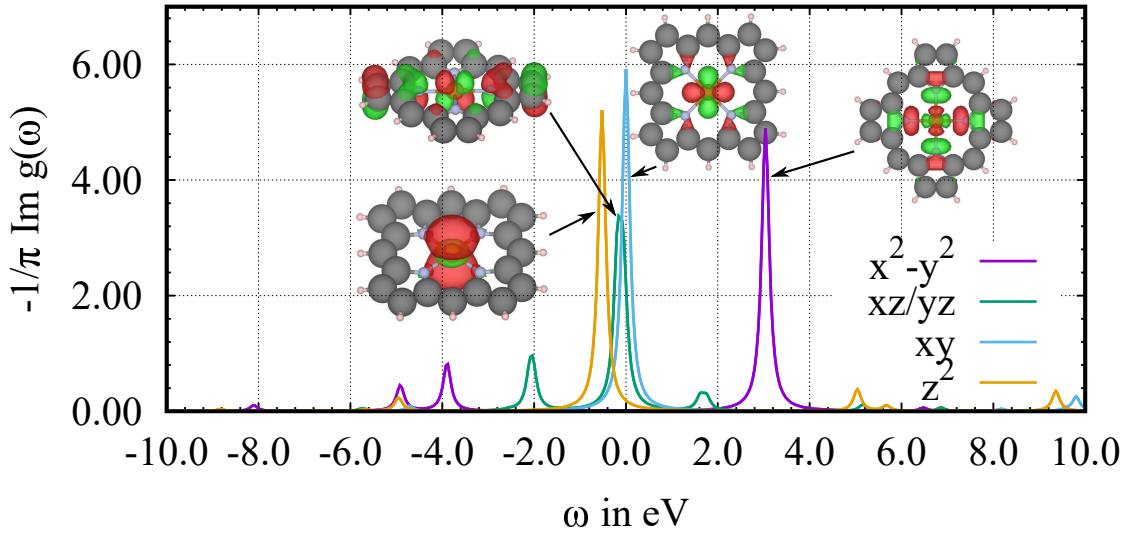


Figure 4.5.: Density of states projected onto the Fe 3d orbitals ( $-\frac{1}{\pi}\text{Im}g_i(\omega)$ ) of an iron porphyrin molecule. Results obtained from PBE/def2-TZVP, by taking into account all eigenstates of this system up to 10 eV above  $\epsilon_{\text{HOMO}}$  for the projection (see text for an explanation). The energies were shifted against the HOMO, so that  $\omega = 0.0 \text{ eV} = \epsilon_{\text{HOMO}}$ . Isosurface value for MO plots: 0.015.

At  $\omega = -2.7 \text{ eV}$ , one obtains a large peak in the imaginary part of the hybridization

<sup>7</sup>As already mentioned in Sec. 3.5, the term “dynamical” is often used for energy/frequency dependent quantities in physics.

<sup>8</sup>The effective single-particle energies of the electronic bath can be obtained by diagonalizing the bath part of the Kohn–Sham Hamiltonian, as discussed in Sec. 4.1.

function of the  $d_{x^2-y^2}$  orbital, which is caused by the formation of a  $\sigma$ -bond of this orbital with the ligand<sup>9</sup>. The resulting anti-bonding molecular orbital has strong Fe  $3d_{x^2-y^2}$  character and is shifted upwards in energy (see Figure 4.5) as compared to the remaining  $3d$  orbitals (at the same time the bonding linear combination is shifted downwards in energy), which is the reason for the large feature in the real part of the hybridization function (bottom panel of Figure 4.4). For the remaining Fe  $3d$  orbitals, the features in the real and imaginary parts of the hybridization function are rather small, which is presumably due to the much weaker  $\pi$ -type interaction. This is probably the reason why these orbitals are only little shifted against each other, as seen in the PDOS.

It is believed that the dynamical or energy-dependent shift (described by the real part of the hybridization function) of the  $3d$  orbitals can presumably be understood as the splitting between the bonding and anti-bonding orbitals formed by the hybridization of the Fe  $3d$  orbitals with the bath orbitals (or what in chemistry would be called ligand group orbitals (LGOs)), which is depicted in Figure 4.6. Note that this is not a molecular orbital diagram as usually drawn in chemistry, but this figure illustrates that  $d_{x^2-y^2}$  orbitals is shifted most significantly, which agrees with the observation of  $\text{Re}\Delta_{x^2-y^2}(\omega)$  exhibiting the largest feature among the Fe  $3d$  orbitals, whereas the remaining  $3d$  orbitals are only little affected (in agreement with the rather featureless real part of the hybridization function for these orbitals). Furthermore, this figure demonstrates that the imaginary part (and also the real part) exhibits peaks at the energies of the bath orbitals, which is why  $\text{Im}\Delta_i(\omega)$  it is often referred to as the bath density of states which can be “seen” by the impurity orbitals (in Section 4.4 another example will be introduced to enlarge upon the concept of the hybridization function), and that these energies are different than the KS eigenvalues of the entire system.

Before discussing the Fe subsystem  $d$  energies obtained from Equation (3.44), it shall be mentioned that for the square planar Fe(porph) complex one would expect a  $d^6$  electron configuration on the Fe(II) atom, which results in a triplet ground-state [186] (see Figure 4.7 for the qualitative  $3d$  splitting in this case). The orbital with the largest energy is expected to be the  $d_{x^2-y^2}$  orbital, because the porphyrin ligand is contacting the central atom directly on the  $x/y$ -axis.

In the following, it shall be analyzed how the energy window for the projection (Equation (3.42)) affects the Fe subsystem  $d$  energies. As mentioned in Section 3.6.4, a too large window (taking into account too many virtual orbitals) can lead to physically unreasonable results.

---

<sup>9</sup>The molecule lies in the  $xy$ -plane with opposing N atoms being aligned on the  $x$  and  $y$  axis, respectively.

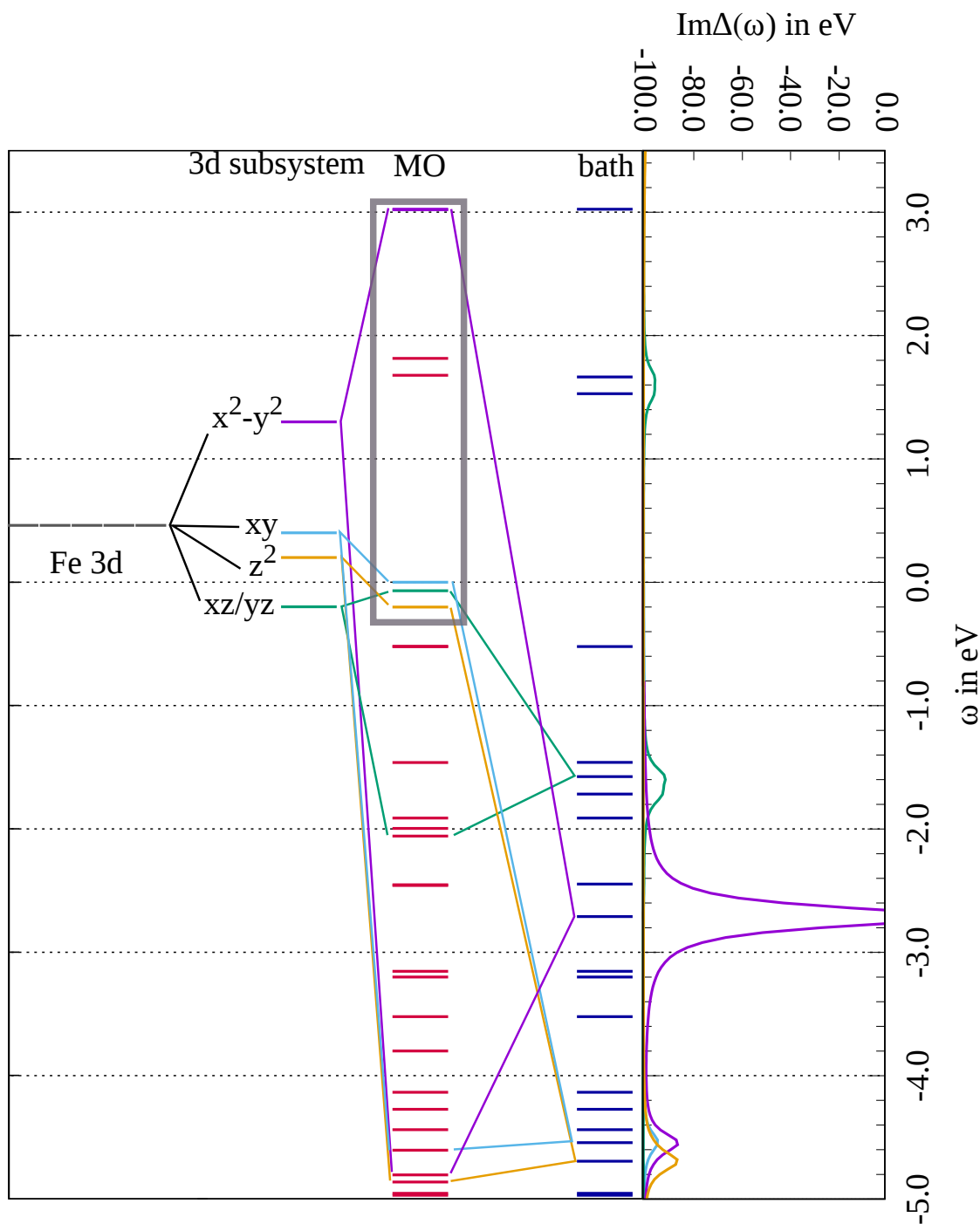


Figure 4.6.: A combined picture of the Fe 3d hybridization function with the energies of the electronic bath, the energies of the Fe  $d$  subsystem, the molecular orbital energies, and the Fe 3d energies of an isolated Fe atom. Results obtained from PBE/def2-TZVP. The energies of the Fe  $d$  subsystem were obtained by evaluating  $\lim_{\omega \rightarrow \infty} \tilde{\Delta}_i(\omega) = \epsilon_i$ , after projection of the KS Green's function onto the Fe 3d orbitals by taking into account all occupied and all virtual orbitals up to +10 eV above  $\epsilon_{\text{HOMO}}$  (sum over  $K$  appearing in Equation (3.42)).

In Table 4.1, the Fe subsystem  $d$  energies are shown (as evaluated by  $\lim_{\omega \rightarrow \infty} \tilde{\Delta}_i(\omega) = \epsilon_i$ ). Note that the energies are shifted against the Fermi energy (i.e. the energy of the HOMO  $\epsilon_{\text{HOMO}}$  was set to zero). By taking into account all Kohn–Sham orbitals (sum over  $K$  appearing in Equation (3.42)) one finds that the Fe subsystem  $d$  energies are all above the Fermi energy (which is here the energy of the HOMO). That these values are physically unreasonable is indicated by the total Fe  $3d$  occupation of 4.6, because for an  $\text{Fe}^{2+}$  ion in  $\text{Fe}(\text{Porph})$  a  $3d$  occupation of 6 electrons would be expected [187,188]. By truncating the sum over  $K$  appearing in Equation (3.42), the subsystem  $d$  energies are decreasing, and as a consequence the Fe  $3d$  occupation ( $n_d$ ) is close (virtual orbitals included: +10 eV above  $\epsilon_{\text{HOMO}}$ ), or equal to 6 (virtual orbitals included: +6 eV above  $\epsilon_{\text{HOMO}}$ ), and reflects the expected  $3d^6$  configuration for an iron(II) complex, as mentioned before.

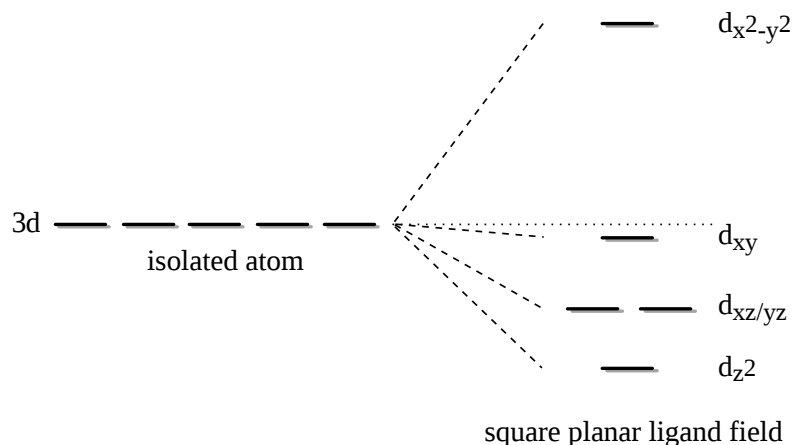


Figure 4.7.: Splitting of the  $3d$  orbitals in a square-planar ligand field [189,190].

Comparing the Fe subsystem  $d$  energies with the expected splitting from ligand field theory (Figure 4.7), one observes a qualitatively consistent picture, except for the positions of the  $d_{z^2}$  and  $d_{xz/yz}$  orbitals being exchanged for the Fe subsystem  $d$  energies, when all KS orbitals up to +10 eV above  $\epsilon_{\text{HOMO}}$  are taken into account for the Green’s function projection. Interestingly, considering all KS orbitals, as well as truncating the virtual orbitals included in the projection to those which energy is not larger than +6 eV above  $\epsilon_{\text{HOMO}}$ , the qualitative ordering of the Fe  $3d$  orbitals is consistent with the one shown in Figure 4.7. However, for the former the difference between  $\epsilon_{z^2}$  and  $\epsilon_{xy}$  is too large compared to what one observes by considering the KS molecular orbitals with mainly Fe  $3d$  character (of the full  $\text{Fe}(\text{Porph})$  system) as shown in Figure 4.6. This observation furthermore demonstrates that too many virtual orbitals accounted for in the KS Green’s function projection lead to physically unreasonable results.

Table 4.1.: Fe subsystem  $d$  energies ( $\epsilon_i$ ) with respect to the Fermi energy ( $\epsilon_{\text{HOMO}}$ ) of the Fe  $3d$  orbitals in Fe(porph) as obtained for truncating the number of virtual orbitals used in the projection (sum over  $K$  appearing in Equation (3.42)) (all occupied orbitals included). As described in Section 3.6.3,  $\epsilon_i$  was obtained by evaluating  $\lim_{\omega \rightarrow \infty} \tilde{\Delta}_i(\omega) = \epsilon_i$ .  $n_d$  is the total Fe  $3d$  occupation as obtained by integrating the PDOS. Energies in eV.

virtual orbitals included	all	+10 eV above $\epsilon_{\text{HOMO}}$	+6.0 eV above $\epsilon_{\text{HOMO}}$
$\epsilon_{x^2-y^2}$	9.2	1.4	1.3
$\epsilon_{xy}$	8.6	0.4	-0.1
$\epsilon_{xz/yz}$	7.8	-0.2	-0.3
$\epsilon_{z^2}$	7.7	0.2	-0.4
$n_d$	4.6	6.0	6.2

Altogether, it was shown that the projection scheme implemented within an atom-centered basis set (Section 4.1) can qualitatively reproduce the hybridization function of the  $3d$  orbitals in Fe(porph), and the  $3d$  orbital splitting of the impurity atom is in line with the chemical expectation from ligand field theory. Although small qualitative differences could be observed for the order of the  $d_{z^2}$  and  $d_{xz/yz}$  orbitals by using different energy windows, one can conclude that taking into account all occupied KS orbitals, as well as all virtual orbitals with energies of 6-10 eV above  $\epsilon_{\text{HOMO}}$  might be a reasonable choice for the projection of the KS Green's function onto the Fe  $3d$  orbitals in Fe(Porph), to use the hybridization function and the Fe subspace  $d$  energies as input for the AIM. On the other hand, if one is only interested in a qualitative analysis of the hybridization function (e.g. for studying adsorbate-surface interactions), the energy window for such a projection can be chosen arbitrarily with respect to the number of virtual orbitals, because we found that  $\Delta_i(\omega)$  depends only little on it.

### 4.3. $H_2$ dissociation — closed-shell to open-shell singlet transition

In Section 3.6.3, we already discussed that a too strong hybridization between the impurity and the electronic bath leads to the destruction of the Kondo resonance at the Fermi level. In this part, a similar situation shall be discussed, which is the bond stretching of a hydrogen molecule. If  $H_2$  is at its equilibrium distance,

the molecule is in a closed-shell situation which can be transferred into an open-shell system (a similar situation occurring in the Kondo effect) by pulling the H atoms apart from each other. By doing so, we follow the  $S^2$  expectation values at different H-H bond distances and at the same time, we consider the hybridization function of one of the H atoms.

### 4.3.1. Computational Methodology

H<sub>2</sub> was optimized using BP86/STO-3G [191–195] as implemented in the TURBO-MOLE program package [181], with convergence criteria for the SCF algorithm of  $1 \cdot 10^{-6}$  Hartree, and  $1 \cdot 10^{-4}$  Hartree/Bohr for the gradient. In Figure 4.8 a), the optimized hydrogen molecule at its equilibrium distance  $d_{\text{H}_2} = 0.75 \text{ \AA}$  is shown.

For mimicking the bond-breaking scenario, we performed single-point calculations of the hydrogen molecule after increasing the bond distance by  $x \text{ \AA}$  using a broken-symmetry approach (as described in Section 3.3.1).

### 4.3.2. Hybridization functions and $S^2$ expectation values at different H-H bond distances

The  $S^2$  expectation value can be used as an indicator for the detection of an open-shell character in molecules [196]. At the example of H<sub>2</sub>, this value is assumed to be zero due to the closed-shell situation mentioned above, and should get larger when the open-shell character increases at larger bond distances. It will become clear that similar to the destruction of the Kondo peak (corresponding to the destruction of an open-shell singlet state) caused by a too strong hybridization, there is a similar open-shell to closed-shell transition in the H<sub>2</sub> bond breaking scenario which is more familiar to the community of chemists.

At each distance under consideration, the  $S^2$  expectation values are shown in Figure 4.8 b). At equilibrium distance ( $x = 0.0 \text{ \AA}$ ), and for not too large changes in the bond distance, the Value of  $S^2$  is 0.0 which indicates that the hydrogen molecule is in a closed-shell situation. For  $x = 1.0 \text{ \AA}$ , the  $S^2$  value starts to differ from 0.0 due to localization of spin density on the hydrogen atoms. At  $x = 2.0 \text{ \AA}$ ,  $S^2$  takes roughly the value of 1.0, because the  $\alpha$  (spin-up) electron is well localized on one of the H atoms, whereas the  $\beta$  (spin-down) electron is located on the other H atom. Note that such a broken-symmetry Kohn–Sham wave function is not an eigenfunction of the  $\hat{S}^2$  operator, and  $S^2$  takes an intermediate value between the singlet ( $S^2 = 0.0$ ) and triplet values ( $S^2 = 2.0$ ).

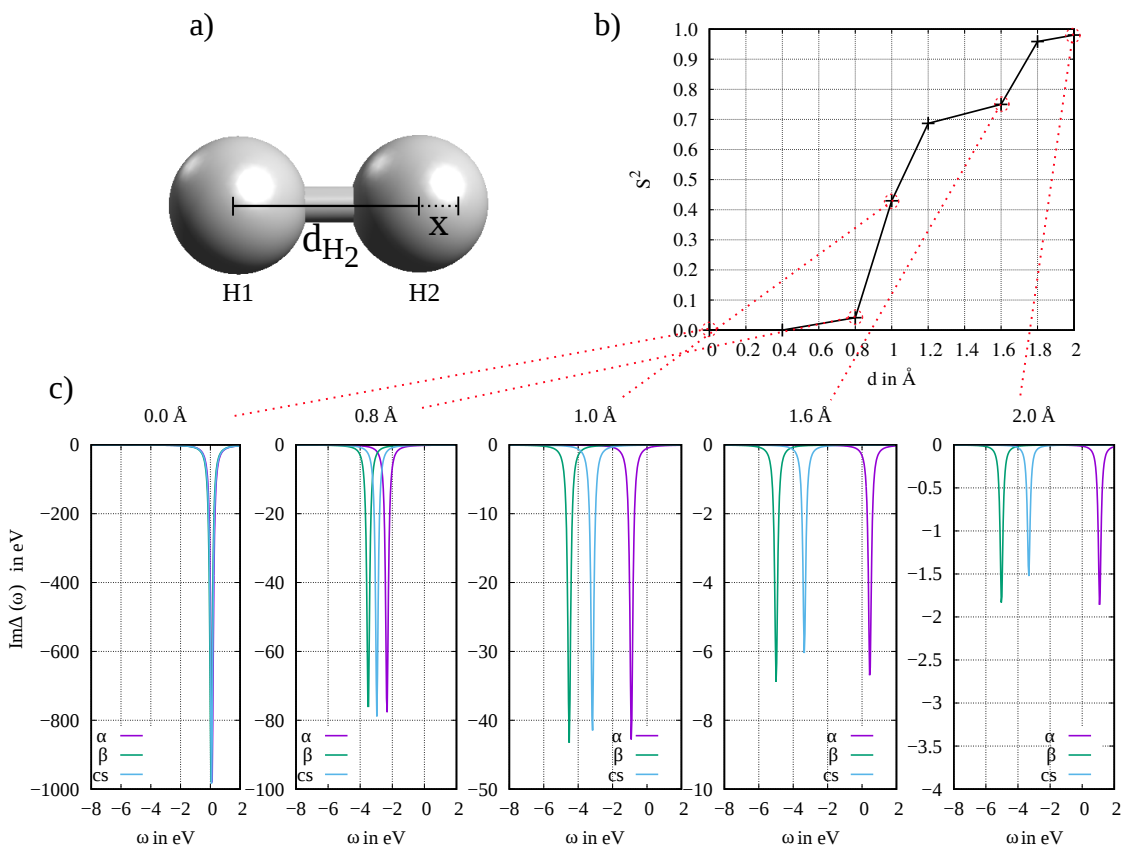


Figure 4.8.: a) Optimized (BP86/STO-3G)  $H_2$  molecule. b)  $S^2$  expectation values at different displacements of the H-H bond length, as obtained from unrestricted DFT. As indicated by  $S^2$ , unrestricted DFT can yield a closed-shell solution ( $S^2 = 0$ ), as well as a broken-symmetry solution ( $S^2 > 0$ ). c) Imaginary part of the hybridization function of the 1s orbital (H1), for  $\alpha$  (spin-up) and  $\beta$  (spin-down) electrons (unrestricted DFT), and as obtained from closed-shell (cs) DFT. Note that the energy was not shifted against the energy of the HOMO.

The imaginary part of the hybridization function of the 1s orbital in H1 is shown in Figure 4.8 c). At  $x = 0.0$  Å, the  $H_2$  molecule is in a closed-shell situation ( $S^2 = 0.0$ ), for which one obtains that the hybridization of the H1 1s  $\alpha$  orbital is the same as the hybridization of the H1 1s  $\beta$  orbital, due to the fact that the  $\alpha$  and  $\beta$  wave functions are equal in the  $S^2 = 0$  case. As expected, both ( $\alpha$  and  $\beta$ ) hybridizations also agree with the H1 1s hybridization as obtained from a closed-shell (cs) calculation. This is different if the bond length of  $H_2$  is increased and the Kohn–Sham wave function takes more and more the character of the broken-symmetry solution (i.e. the  $\alpha$  and  $\beta$  orbitals are not equal anymore). In these

cases, the  $\alpha$ ,  $\beta$ , and the closed-shell hybridization functions have peaks at the corresponding bath energies.

By further inspection of Figure 4.8 c) from the right to the left, one observes that the peak of the hybridization (for  $\alpha$ ,  $\beta$  and cs) increases as the bond distance is decreased, which is noticeable at the growing scale of the  $y$ -axis from the right to the left. As the hybridization strength increases, the  $S^2$  value decreases as mentioned before. This is similar (but not equal) to the simplest Anderson model (as discussed in Section 3.6.3), where a too strong hybridization parameter  $V$  leads to the destruction of the Kondo effect, being in agreement with the “destruction” of an open-shell singlet state at  $H_2$  bond distances close to the equilibrium distance (reflected in  $\langle S^2 \rangle \rightarrow 0$ ).

Having in mind that a Kondo effect is often considered as an open-shell singlet state [41], it was indeed possible to demonstrate that there are simple parallels between the  $H_2$  bond-breaking scenario and the Kondo effect in the simplest AIM. An open-shell singlet state in  $H_2$  is suppressed close to its equilibrium distance, because both H  $1s$  orbitals are strongly hybridized with each other, similarly to the destruction of a Kondo effect at a too strong hybridization parameter  $V$  (see Section 3.6.3). In the further course of this thesis, it will be shown that this observation will be beneficial for the interpretation of more complex systems.

## 4.4. From discrete energies to a continuous bath

While in physics one often deals with solid-state systems, in chemistry one is typically rather interested in the properties of single molecules or supramolecular systems. Molecular spintronics is at the interface of both disciplines, and topics such as molecules on surfaces benefit from comparing (and ideally bringing together) the viewpoints and concepts from both communities. To this end, we are focusing on simple model systems for understanding how adsorbates couple to a band rather than to discrete molecular orbitals (the latter was already discussed in the preceding sections).

It should be recalled that a band is formed if the number of atoms is infinitely large, caused by the vanishing gap between the MO energies as depicted in Figure 4.9 a). Imagine one would add an additional atom to this system, as e.g. an adsorbate as depicted in Figure 4.9 b)<sup>10</sup>.

---

<sup>10</sup>The choice of this example has been made, because throughout this work we will focus on molecules on surfaces.

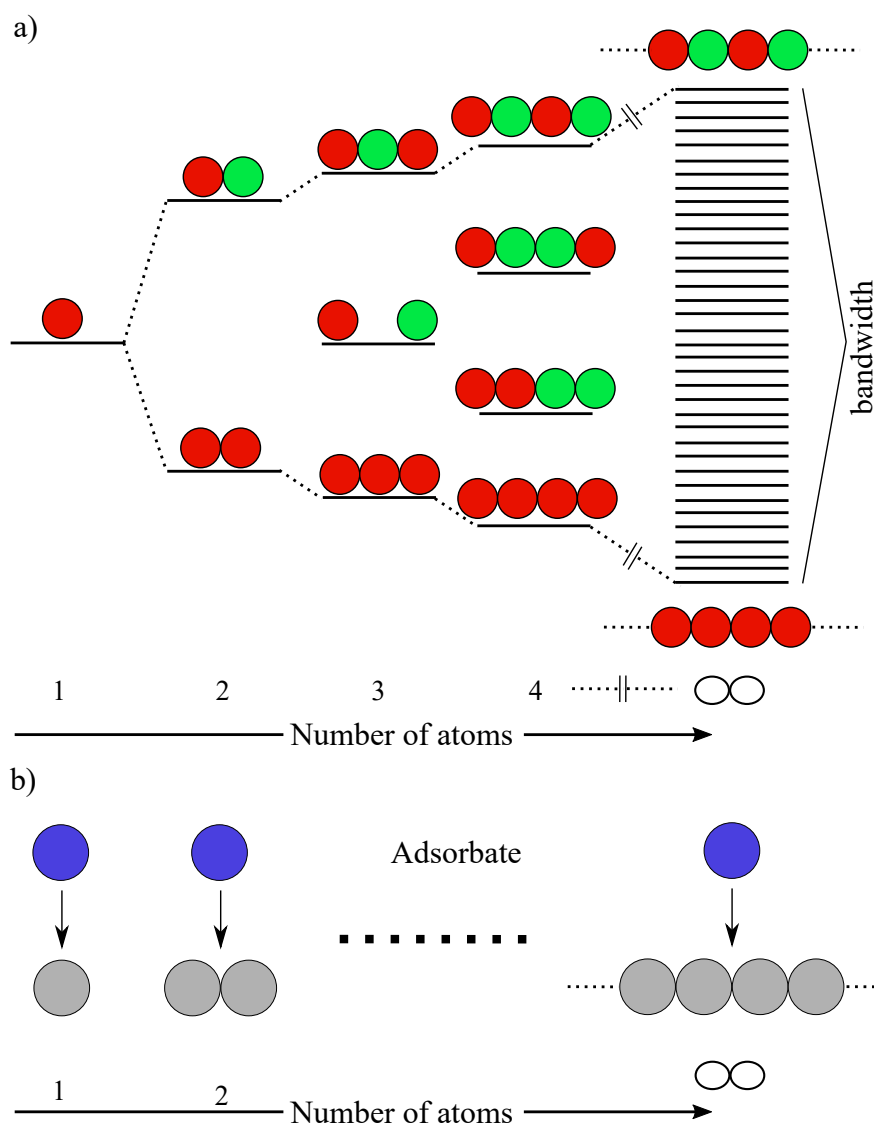


Figure 4.9.: a) Schematic representation of the band structure evolution from a single atom to a chain of an infinite number of atoms. The red and green circles represent the phases of  $s$ -atomic orbitals. b) Adsorbate–ligand system for different numbers of ligand atoms (eventually forming a chain).

Each of the molecular orbitals formed by the chain of atoms (Figure 4.9 a)) can then be considered as a LGO, from which one could immediately build a molecular orbital diagram of the adsorbate–ligand system. The resulting MOs are due to hybridization of the adsorbate’s orbitals with the LGOs.

In physics, the concept of molecular orbitals is indeed known, but one is typically rather interested in the effect of the ligands (or in this context the chain of atoms) on the atomic or molecular orbitals of the adsorbate. As mentioned in Section 3.6.3, these effects are captured in the so-called hybridization function, which is a complex, energy-dependent function. The energy dependence is a consequence of the emerging band structure if the “ligand” is not a molecule or an atom with discrete single particle energies, but an infinitely large solid with a continuum of these energies.

In the following, the concept of the hybridization function will be merged with the chemist’s view of a molecular orbital diagram. It will quickly become clear that the picture of a MO diagram becomes unmanageable for a too large hydrogen chain, whereas the hybridization function is a convenient tool to deal with such systems.

#### 4.4.1. Computational methodology

*Helium coupled to a hydrogen chain:*

To follow the transformation of discrete orbitals into a band, a hydrogen chain length is increased step-by-step. The hydrogen atoms are spaced by  $a = 0.75 \text{ \AA}$ , and the helium was placed  $0.80 \text{ \AA}$  ( $d_{\text{ad}}$ ) above the hydrogen chain in a bridged position as depicted in Figure 4.10. For each chain length, a single-point calculation (PBE/STO-3G [182, 183, 197]) was done using TURBOMOLE [181], with a convergence criterion of  $1 \cdot 10^{-6}$  Hartree for the SCF algorithm. The hybridization functions were then calculated from the impurity Green’s function (see Equations (3.42) and (3.45)), using the projectors as calculated within an atom-centered basis set (Equation (4.4)).

*Spin-up and spin-down hybridization of a spin-polarized adsorbate on a metallic surface:*

The Cu monolayer was modeled as a  $n \times n$  grid of Cu atoms (each spaced by  $2.57 \text{ \AA}$ ), as shown in Figure 4.14. The Co atom was placed in the center of the Cu monolayer, with an adsorption distance of  $1.52 \text{ \AA}$ . For each grid size a single point calculation was done using TURBOMOLE [181] (PBE/def2-SVP [182–185]), with a convergence criterion of  $1 \cdot 10^{-6}$  Hartree for the SCF algorithm. The hybridization functions were then calculated from the impurity Green’s function (see Equations (3.42) and (3.45)), using the projectors as calculated within an atom-centered basis set (Equation (4.4)).

### 4.4.2. Helium coupled to a hydrogen chain

The test system of choice is a helium atom “adsorbed” on a chain of hydrogen atoms, which acts as a toy model to mimic how an adsorbate interacts with a conduction band of a metal. In this example, it is unimportant whether the adsorbate is a closed-shell (as in this case) or open-shell system, as it shall just demonstrate how the energy dependence of hybridization functions can be understood as a consequence of the band structure evolution from a single atom to a chain of an semi-infinite number of atoms.

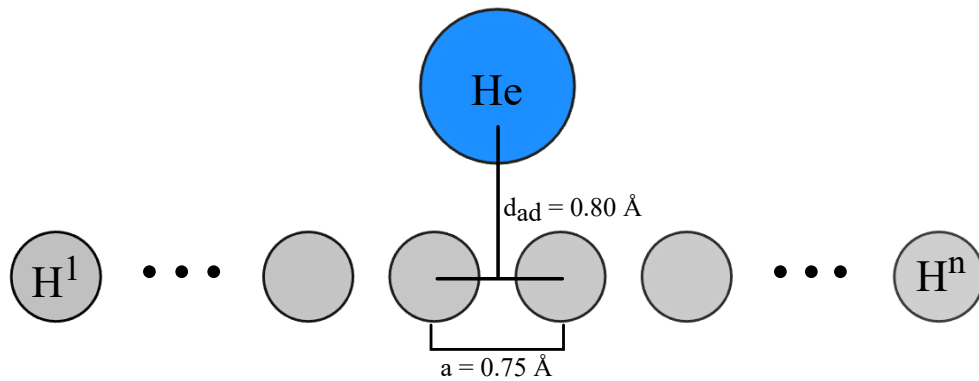


Figure 4.10.: A helium atom adsorbed on a hydrogen chain of  $n$  atoms. The hydrogen atoms are spaced by  $a = 0.75 \text{ \AA}$ , and the helium atom has an adsorption distance of  $d_{\text{ad}} = 0.80 \text{ \AA}$ .

In the simplest case, the helium atom (formally) adsorbs on a single hydrogen molecule  $\text{H}_2$  ( $n = 2$ ), that provides two LGOs for the He–substrate interaction (see Figure 4.11 a)). Due to symmetry, the He  $1s$  orbital can only interact with LGO1 of  $\text{H}_2$ . This gives rise to a bonding molecular orbital ( $-17.7 \text{ eV}$ ) with mainly He  $1s$  character. In the PDOS ( $-\frac{1}{\pi}\text{Im}g_{1s}(\omega)$ ) of the He  $1s$  orbital (Figure 4.12 a),) one can perceive this as a large peak at the energy of the bonding molecular orbital ( $-17.7 \text{ eV}$ ). Further, one observes a second smaller peak slightly below  $\omega = 0.0 \text{ eV}$ , which corresponds to the He  $1s$  contribution to the anti-bonding molecular orbital at  $-0.6 \text{ eV}$ , and as mentioned earlier, due to symmetry reasons we do not observe a peak at the MO with the highest energy ( $\omega = 3.4 \text{ eV}$ ), because there is no coupling of the He  $1s$  orbital with LGO2.

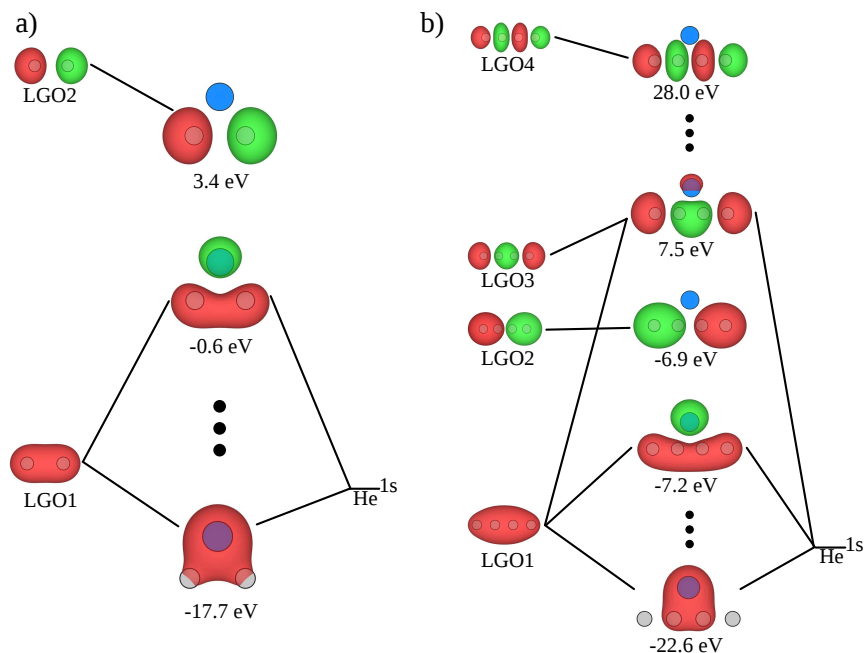


Figure 4.11.: Schematic representation of a molecular orbital diagram for a He atom “adsorbed” on a hydrogen chain with  $n = 2$  (left) or 4 (right) H atoms. Results obtained from PBE/STO-3G. The LGO orbitals are the molecular orbitals as obtained for the hydrogen chains without the adsorbate. Note that the energies of LGO2 (left) and LGO4 (right) are larger than the corresponding molecular orbitals in the adsorbate–substrate system. Isosurface value: 0.15

The hybridization function of the He  $1s$  orbital (for  $n = 2$ ) is shown in Figure 4.12 b). The peak occurring in the imaginary part of the hybridization function is shifted towards lower energy as compared to the peak at  $-0.6$  eV in the PDOS. This can be understood by considering the physical meaning of the hybridization function: It can be seen as the bath density of states (the bath is here the hydrogen chain) weighted by the hybridization  $V_{i\nu}$ , or hopping, elements  $t$  (see, e.g., the last term of Equation (3.21)), thus we expect the peaks occurring in  $\Delta(\omega)$  to be at the energies of the subsystem MOs of the electronic bath spanned by the hydrogen chain<sup>11</sup>, and not at the KS eigenvalues of the entire system (at which the peaks in the PDOS can be observed). In simple words, the imaginary part of  $\Delta(\omega)$  is the bath density of states which is “seen” by the impurity (here the He  $1s$  orbital). The reason that there is only one peak (Figure 4.12 b)) is a consequence of the He  $1s$

<sup>11</sup>These are obtained by solving the secular equation for the hydrogen block in the Kohn–Sham Hamiltonian.

orbital hybridizing with only one LGO, which can be understood by considering the molecular orbital scheme sketched in Figure 4.11 a).

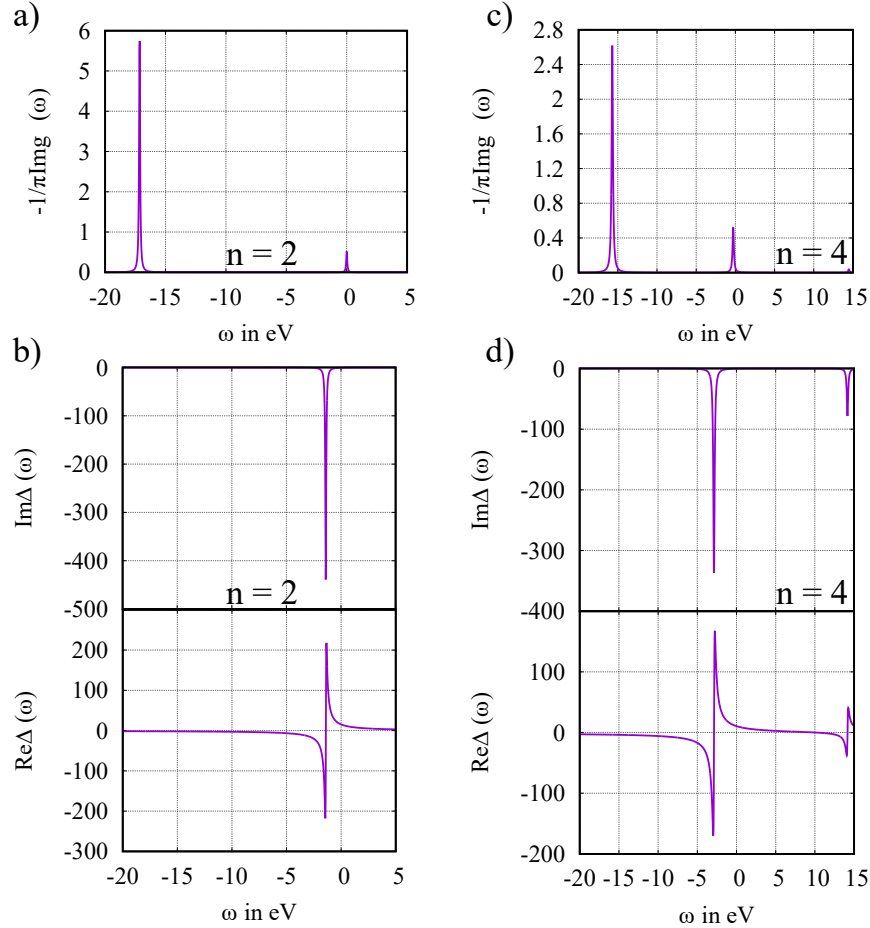


Figure 4.12.: a) and c): Projected density of states of the He 1s orbital for the cases  $n = 2$  (a)) and  $n = 4$  (c)). b) and d): Imaginary and real part of the He 1s hybridization function as obtained from STO-3g/PBE for  $n = 2$  and  $n = 4$ .

By increasing the H-chain length to  $n = 4$ , one obtains four LGOs, two of which can hybridize with the He 1s orbital, as depicted in Figure 4.11 b). In Figure 4.12 c) one can see that a third peak in den PDOS emerges in contrast to the example with  $n = 2$ , which is caused by the He 1s orbital contributing to three molecular orbitals. The imaginary part of the hybridization function (Figure 4.12 d)) of the He 1s orbital has two peaks, which are due to the hybridization with LGO1 and LGO3.

Assuming the number  $n$  of the hydrogen atoms would further increase, one could imagine that at the same time, the number of peaks in the hybridization function increases, too. A molecular orbital diagram for this scenario would become hard to interpret, and rather the concept of the energy-dependent hybridization function proves to be of value, as discussed in the following.

In Figure 4.13, the He 1s hybridization function is shown for  $n = 8, 32$  and by applying PBC with 32 H atoms in the unit cell (and a  $k$  grid of  $12 \times 1 \times 1$ <sup>12</sup>). The formation of a hydrogen 1s-band (PBC(PAW)) leads to a physically reasonable energy dependence in the hybridization function of the He 1s atom, because the number of peaks in the hybridization function increases, and at the same time the distance between them decreases (which leads to a smoother function)<sup>13</sup>. From a chemistry point of view, this “smoothing” can be understood as being caused by the hybridization of the He 1s orbital with a large number of LGOs, as introduced at the beginning of Section 4.4. However, in this example the KS eigenvalues are still too discretized, likely due to a too small number of  $k$  points considered in the DFT calculation, which is why for PBC(PAW) the hybridization does not show an infinite number of peaks, as one would expect by applying periodic boundary conditions.

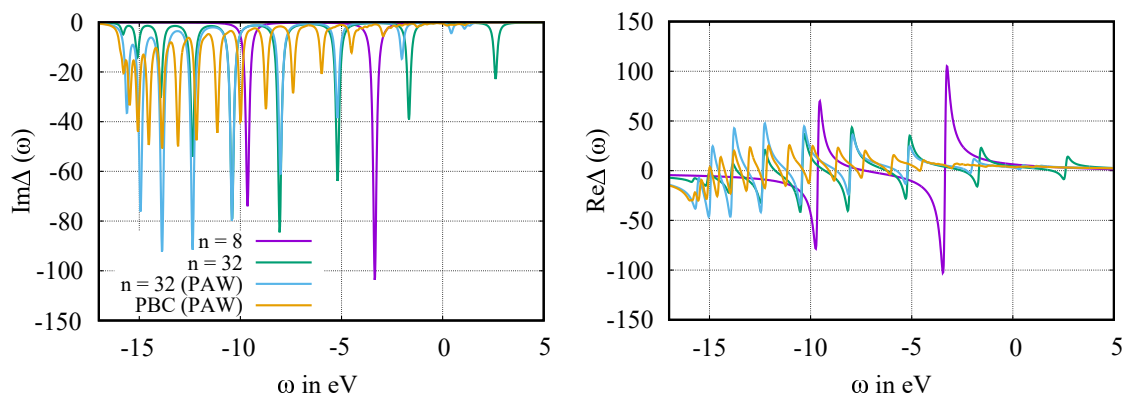


Figure 4.13.: Real and imaginary part of  $\Delta(\omega)$  of a He 1s orbital coupled to a chain of hydrogen atoms. The hydrogen chain is modeled by  $n = 8$  and 32 atoms. In the PAW cases, the projectors as obtained from VASP have been used, whereas in the other cases we used TURBOMOLE (PBE/STO-3G) as described in Section 4.1.

<sup>12</sup>Here we used the PAW method as implemented in VASP [174, 175] using the PBE exchange–correlation functional [182, 183].

<sup>13</sup>To obtain an ever smoother hybridization function as shown in this example, a larger number of hydrogen atoms would be required.

To conclude, it has been shown at a very simply model system how the energy-dependence of the hybridization function emerges when the number of states of the bath is increased to form a band. It is evident that for a more realistic substrate, a full MO diagram will become too complex as the only tool for interpreting adsorbate–surface systems. This illustrates that the concept of the hybridization function used in this work is a benefit for analyzing the bond properties of an adsorbate to its substrate, which can in combination with a molecular orbital picture bring new insights in such systems. This is of particular interest in the context of the present thesis, learning more about the chemical and mechanical control the Kondo effect.

#### 4.4.3. Spin-up and spin-down hybridization of a spin-polarized adsorbate on a metallic surface

As common in the literature, the AIM is parametrized by a spin-unpolarized DFT calculation, as long as the substrate/surface is a non-magnetic system. This might appear physically unreasonable for adsorbates with open-shell character, for which one would typically rather use unrestricted DFT. The reason for using the spin-unpolarized version lies in the nature of the (in our cases) non-magnetic substrate, which is why the hybridization of the correlated orbitals (of the adsorbate) have to be similar to the spin-up and spin-down electrons of the substrate. The magnetization on the impurity is then recovered by solving the AIM.

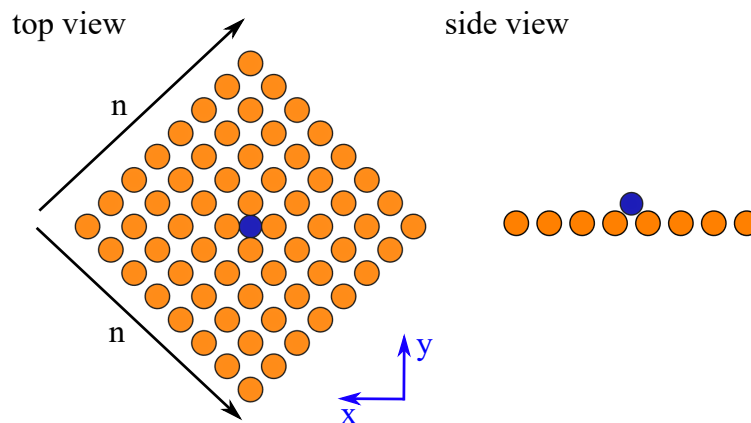


Figure 4.14.: Schematic representation of a single Co atom on a Cu(001) monolayer with  $n \times n$  dimensions.

In order to show that a spin-unpolarized DFT calculation yields physically meaningful results for spin-polarized adsorbates on non-magnetic substrates, we calcu-

late the Co 3d hybridization function for  $\alpha$  (spin-up) and  $\beta$  (spin-down) electrons in the case of a Co atom adsorbed on differently sized Cu monolayers (Figure 4.14). It will be shown that with an increasing size of the Cu monolayer, the  $\alpha$  and  $\beta$  hybridizations function of the Co 3d shell become more and more equal.

The Cu grid of  $2 \times 2$ , which is the smallest under consideration, shows the strongest deviation between the  $\alpha$  and  $\beta$  hybridizations (Figure 4.15). This difference gets significantly smaller if the Cu grid size is increased, and already at a grid size of  $8 \times 8$ , there is a good agreement between the  $\alpha$  and  $\beta$  hybridization functions of the Co 3d shell. This comes from the fact that with a sufficient number of Cu atoms for mimicking a surface, the electronic structure of this is more and more “realistically” described by DFT, which leads to the non-magnetic character as mentioned before.

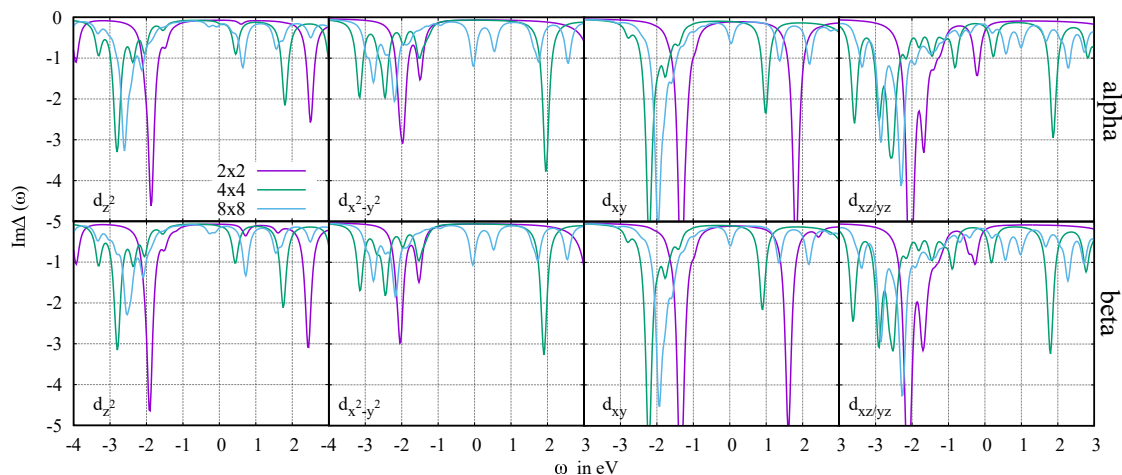


Figure 4.15.: Imaginary part of the hybridization function of Co on a Cu monolayer with different numbers of Cu atoms ( $n \times n$ ). Results are obtained from PBE/def2-SVP, and projection onto the Co 3d shell. The Fermi level (HOMO) was set to  $\omega = 0$  eV.

In summary, it could be shown that the  $\alpha$  and  $\beta$  hybridization functions of a spin-polarized adsorbate on a non-magnetic substrate become identical in the case of a proper description of the substrate, and demonstrates that one can use a non-magnetic DFT calculation for the parametrization of the AIM. In the following part of this thesis, the AIM will be applied to Co/Cu(001), whereas the Cu(001) surface will be described by applying periodic boundary conditions.

# 5. A Cobalt atom on Cu(001) - The interplay between strong correlation and adsorption distances

---

Published: Marc Philipp Bahlke, Michael Karolak  
and Carmen Herrmann  
Phys. Rev. B **2018**, 97, 035119.

---

## 5.1. Introduction

To study how the Kondo effect can be controlled chemically, it is worthwhile to get insight into the structure–property relation of a known Kondo system, for instance with respect to certain property changes as a function of the adsorption distance. In an experimental setup this might be realized by the displacement of a STM tip [198, 199], or through changing the chemical environment (e.g. ligand substitution and modification). For studying this, the focus will be on a single Co atom on Cu(001), which is a structural simple system, i.e. that there are no ligands to take care of which might complicate things, as we will see later throughout this work.

Co/Cu(001) has been the topic of many experimental [200–203] and theoretical [111, 199] investigations, regarding the Kondo effect. Experimentally, it was found that the Kondo temperature of Co/Cu(001) is  $T_K = 88 \pm 4$  K [200–203], as extracted from a Fano-fit of the zero-bias ( $dI/dV$ ) resonance in a STS experiment. Theoretically, this system was already described using the AIM by Jacob

(one crossing approximation) [111] and Baruselli *et al.* (numerical renormalization group) [199], and identified as a  $S = 1$  system with the Co  $3d_{z^2}$  and  $3d_{x^2-y^2}$  orbitals having one unpaired electron. Both works conclude, that only the local moment of the  $3d_{z^2}$  orbital is screened due to a Kondo effect, which is therefore called “underscreened Kondo effect”.

In this part, the focus is not on the Kondo effect in particular, but the DFT++ approach will be used to investigate the potential energy surface (PES) scan along the adsorption coordinate of Co/Cu(001). It will be shown that adding electron correlation in the scope of the AIM, but also by using DFT+ $U$  the minimum adsorption distance is shifted towards larger values, and that such a shift can have significant consequences for the electronic structure of Co. In particular, this is an important observation for studying Kondo systems, as the choice of the electronic structure method for structural relaxation will, e.g., affect the Kondo temperatures. Nevertheless, it will be discussed that a proper choice of the exchange–correlation functional is sufficient for this task, and one does not necessarily need apply the more expensive DFT++ method. Further, we use the results of the simplest Kondo model to approximate the Kondo temperatures based on our DFT parameters at different points of the PES, to study how the Kondo temperature is affected by these distances. For more details see Reference [204]. Note that some of the results were also part of my master’s thesis [205].

## 5.2. Computational methodology

We modeled the Cu(001) surface by a  $4 \times 4$  super cell with five Cu layers. The lattice parameter was set to a value of  $3.615 \text{ \AA}$  [206]. As determined in Reference [200], the adsorption position of Co on Cu(001) is the four-fold hollow position, which is therefore used in this study. Single-point calculations were performed at Co–surface distances ( $d_{\text{Co-surface}}$  between  $1.3 \text{ \AA}$  and  $1.7 \text{ \AA}$  in increments of  $0.10 \text{ \AA}$ , with a finer spacing of  $0.02 \text{ \AA}$  around the energetic minimum. All calculations (DFT, DFT+ $U$  and DFT++) were done with the ABINIT 7.10.4 program package [140] using a PAW basis set [207,208]. For the exchange–correlation functional, the GGA of Perdew *et al.* [183] and the local density approximation (LDA) for the exchange–correlation functional of Perdew and Zunger [209,210] were applied. In addition, the effect of including spin-polarization (DFT<sub>SP</sub>) is investigated, by comparing the results against spin-unpolarized calculations. The latter were used to parameterize the AIM, as already mentioned in Section 4.4.3. For all calculations we used a  $k$ -grid of  $4 \times 4 \times 1$  centered around the  $\Gamma$ -point.

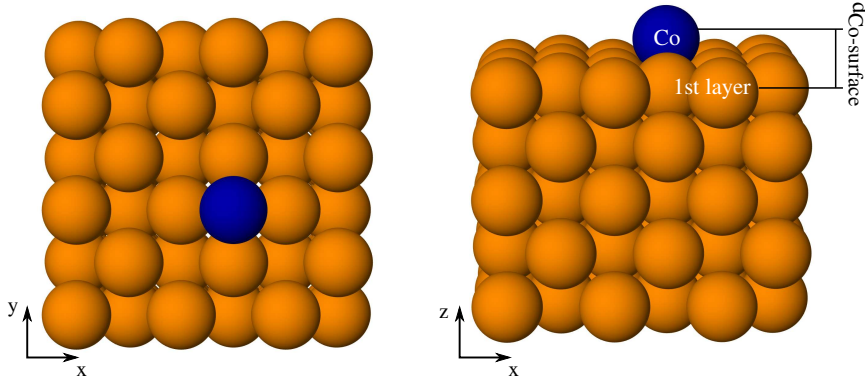


Figure 5.1.: Unit cell used for calculating the PES for Co/Cu(001) adsorption.  $d_{\text{Co-surface}}$  is the difference between the  $z$ -coordinate of the Cu atoms in the first layer (they were aligned so that all Cu atoms in the first layer have a  $z$ -coordinate of 0.00) and the  $z$ -coordinate of the Co atom.

We solved the AIM within the CT-QMC method as explained in Section 3.7. For all DFT++ single-point calculations we used an inverse temperature of  $\beta = 100 \text{ eV}^{-1}$ . The Coulomb interaction tensor was approximated by using density-density type interaction only, with the Slater parameters  $U = F^0 = 3.0 \text{ eV}$ ,  $3.8 \text{ eV}$ ,  $4.0 \text{ eV}$ ,  $4.2 \text{ eV}$  and  $5.0 \text{ eV}$ , and  $J = \frac{1}{14}(F^2 + F^4) = 0.9 \text{ eV}$  with  $\frac{F^4}{F^2} = 0.625$ . To account for the double-counting problem, the fully localized limit was used. In the following we are going to discuss the effect of strong electron correlation on the potential energy surface along the Co/Cu(001) adsorption coordinate  $d_{\text{Co-surface}}$  comparing DFT with DFT++ and DFT+ $U$  results. The former are split in spin-unpolarized and spin-polarized calculations. We consider the spin-polarized calculations as our DFT reference, and for a physically correct description of the non-magnetic behavior of the copper surface, we use the spin-unpolarized solution as a starting point for the DFT++ calculations where the magnetic moment of the Co  $3d$  shell is described correctly by the AIM, as is common in the literature [111].

After we have discussed the potential energy surfaces, we will consider the electronic structure in more detail. We provide extensive data at selected values for  $d_{\text{Co-surface}}$  to show the sensitivity of the electronic properties as described by the AIM to the adsorption distance. This allows us to judge the importance of accurate adsorption distances for strongly correlated systems. As mentioned in the introduction, it was found that Co on Cu(001) exhibits a Kondo effect with a Kondo temperature of  $88 \pm 4 \text{ K}$  [200–202]. In this work, we will not focus on this temperature in detail, because the largest inverse temperature  $\beta = 100 \text{ eV}^{-1}$  employed here corresponds to  $\sim 116 \text{ K}$  which is too high to observe a Kondo effect in

our calculations<sup>1</sup>. We will use our DFT results for a qualitative assessment of the Kondo physics, as will be discussed in Section 5.4.

### 5.3. Potential energy surface scan along the adsorption coordinate

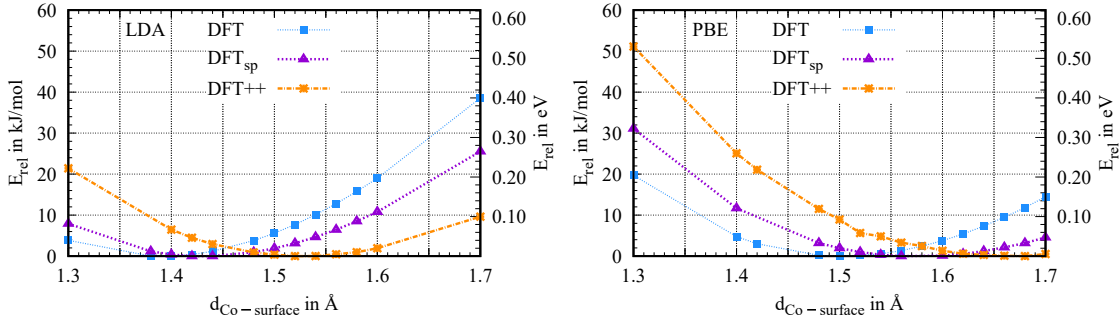


Figure 5.2.: Relative energies obtained from spin-unpolarized DFT (DFT), spin-polarized DFT (DFT<sub>sp</sub>) and DFT++ for different adsorption distances of Co on Cu(001). The DFT++ calculations were performed at  $\beta = 100 \text{ eV}^{-1}$ . The DFT++ results for  $U = 3.8 \text{ eV}$ ,  $4.0 \text{ eV}$  and  $4.2 \text{ eV}$  are nearly on top of each other (see Section A.2), which is why we limit this plot to the results of  $U = 4.0 \text{ eV}$ . The exchange parameter for all values of  $U$  is  $J = 0.9 \text{ eV}$ . For the definition of  $d_{\text{Co-surface}}$  see Fig. 5.1.

The PES of a cobalt atom on a Cu(001) surface is studied with DFT (spin-polarized and spin-unpolarized) and DFT++, with the presently most used approximate exchange correlation functionals in solid state physics, namely LDA (LDA++) and PBE (PBE++). Furthermore, we provide the adsorption distance as obtained from structural relaxation with DFT+ $U$  (and keeping the Cu(001) surface fixed). The DFT++ calculations are completely parametrized by the underlying DFT calculation, except for the Coulomb matrix (last term in Eq. (3.39)) and the double-counting energy  $E_{\text{DC}}$ , which are often in practice unknown (note that the FLL is just an estimation to the real DC value). Although, it should be mentioned that efforts to compute the Coulomb matrix [111], as well as the double-counting [211]

<sup>1</sup>At lower temperatures (e.g.  $\beta = 200 \text{ eV}^{-1}$  ( $\sim 58 \text{ K}$ )) one would need a sufficiently large  $k$ -point grid for a proper integration of the Greens function resulting in a large computational effort, which will in detail be discussed in Section 6.

from first-principles exist. The variation of the latter can be used to control the occupation<sup>2</sup> on the correlated atom (the Co atom in our case) manually (as, e.g. in Ref. [212]), but here we need a unique way to define the double-counting at each adsorption distance, which is achieved by applying the FLL double-counting correction (Eq. (3.38)). Of course, the same argumentation holds for choosing  $U$ . As mentioned before, in this study we address this issue by comparing three different fixed values for  $U$  ( $U = 3.8, 4.0$  and  $4.2$  eV) and one fixed value for  $J$  (0.9 eV) at each data point, allowing for the investigation of the PES with increasing  $U$  (for the parametrization details see Sec. 3.6.1). In addition, we checked for  $U = 3.0$  eV and  $U = 5.0$  eV if the adsorption distance (LDA++ only) changes for these values, by computing only a few points around the LDA++ ( $U = 4.0$  eV) minimum of  $1.52$  Å (see Section A.2), suggesting that slightly varying  $U$  around 4.0 eV has no large impact on the adsorption distance.

The total energies as a function of the adsorption distance for DFT and DFT++ ( $\beta = 100$  eV<sup>-1</sup>  $\sim$  116 K) are shown in Fig. 5.2 for the two functionals discussed here. They were plotted relative to the lowest energy obtained for a given method (all minimum-energy adsorption distances are provided in Tab. 5.1).

Table 5.1.: Adsorption distances in Å at which the energy minima were obtained within the different methods employed here. The values for  $U$  are provided in the table and the value for  $J$  is 0.9 eV.

	LDA	PBE
DFT	1.40	1.50
DFT <sub>sp</sub>	1.44	1.56
DFT++ (3.0 eV)	1.52	-
DFT++ (3.8 eV)	1.52	1.68
DFT++ (4.0 eV)	1.52	1.68
DFT++ (4.2 eV)	1.54	1.68
DFT++ (5.0 eV)	1.54	-
DFT+ $U$ (4.0 eV)	1.53	1.69

It was found (Tab. 5.1) that the minima are shifted to higher adsorption distances in the series DFT < DFT<sub>sp</sub> < DFT++/DFT+ $U$ . Remember that the “DFT” results are without spin polarization, thus the effect of including it (DFT<sub>sp</sub>) is a small shift towards higher adsorption distances by about 0.04 Å to 0.06 Å. The effect of

---

<sup>2</sup>Unless the exact exchange correlation functional is known, the exact occupation is unknown too.

adding dynamical electron correlation (in the physics sense) by applying DFT++ continues shifting the PES towards larger adsorption distances: the shift from LDA<sub>sp</sub> (LSDA) to LDA++ is about 0.08 Å to 0.10 Å, and 0.12 Å for PBE<sub>sp</sub> to PBE++. For DFT+*U* we have not calculated the PES for the surface adsorption, but rather optimized Co on Cu(001) with all Cu atoms kept frozen, which is why we provide the minima in Tab. 5.1. The shift of the adsorption minimum from LDA<sub>sp</sub> to LDA+*U* (1.44 Å → 1.53 Å) is in agreement with LDA++, as it is for PBE<sub>sp</sub> to PBE+*U* (1.56 Å → 1.69 Å) compared to PBE++.

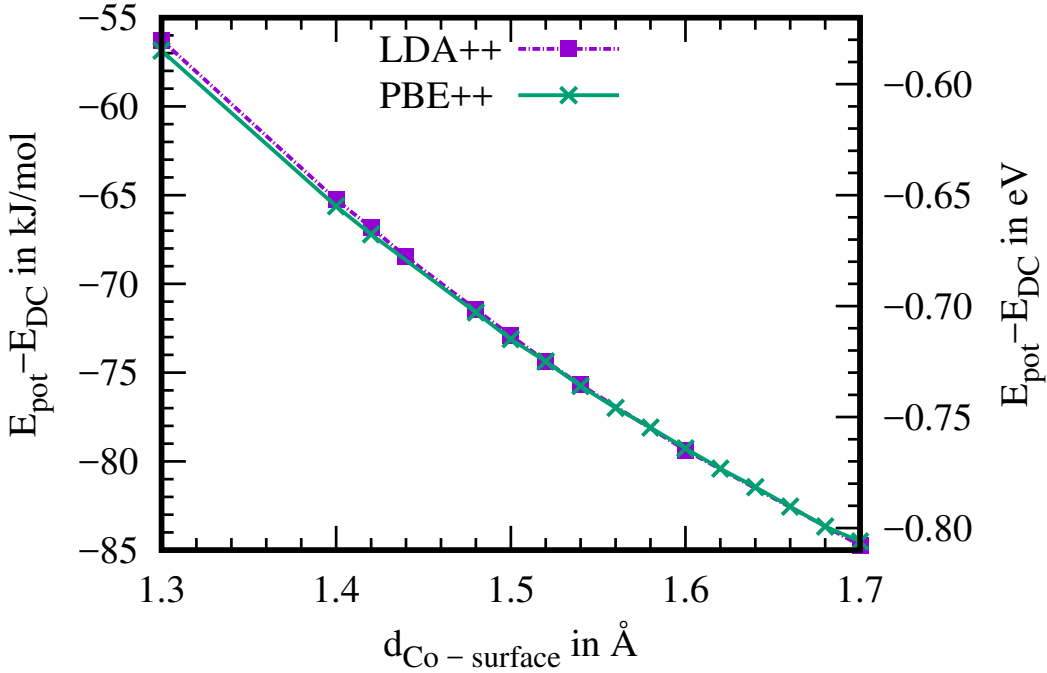


Figure 5.3.:  $E_{\text{pot}} - E_{\text{DC}}$  as obtained from LDA++ and PBE++ at  $\beta = 100 \text{ eV}^{-1}$  with  $U = 4.0 \text{ eV}$  and  $J = 0.9 \text{ eV}$ .

Generally, LDA (LDA<sub>sp</sub>) predicts a smaller adsorption distance than PBE (PBE<sub>sp</sub>) which is not unexpected, because LDA is known for its overbinding character [213–215]. Accordingly, it is not surprising that we found the LDA<sub>sp</sub> minimum 0.12 Å below the minimum of PBE<sub>sp</sub>. To account for dynamical electron correlation within the DFT++ framework, however, does not solve this issue. Instead, it shifts the PESs of LDA and PBE towards higher adsorption distances, and further increases the difference between the minima for the two functionals (see Tab. 5.1). Further, the much cheaper DFT+*U* method provides a similar answer as DFT++

concerning the minimum adsorption distance of Co/Cu(001).

To explain the shifts introduced by DFT++ in contrast to DFT, we will proceed by separating the correlation energy ( $E_{\text{pot}} - E_{\text{DC}}$ ) introduced by CT-QMC from the total DFT++ energy ( $E_{\text{DFT++}}$ , see Equation (3.62)). The remaining terms should account for the isolated effect of the electron density being modified by adding explicit correlation.  $E_{\text{pot}} - E_{\text{DC}}$  as a function of the adsorption distance is shown in Fig. 5.3. It is negative and its absolute value increases with adsorption distance.

The physical interpretation of the increasing  $|E_{\text{pot}} - E_{\text{DC}}|$  with increasing distance is that the electrons on the Co  $3d$  shell get more correlated at larger adsorption distances, similar to  $\text{H}_2$  being more statically correlated (in the chemistry sense) when stretched, as indicated by the open-shell character at an increased bond distance discussed in Section 4.3. In contrast to the interaction term  $E_{\text{pot}} - E_{\text{DC}}$ , the remaining terms of Eq. (3.62) (shown in yellow in Fig. 5.4) have a minimum close to the corresponding DFT<sub>SP</sub> minimum, and from that the energy only slightly increases with increasing adsorption distance so that the decreasing  $E_{\text{pot}} - E_{\text{DC}}$  term “dominates” and shifts the minimum towards a larger distance.

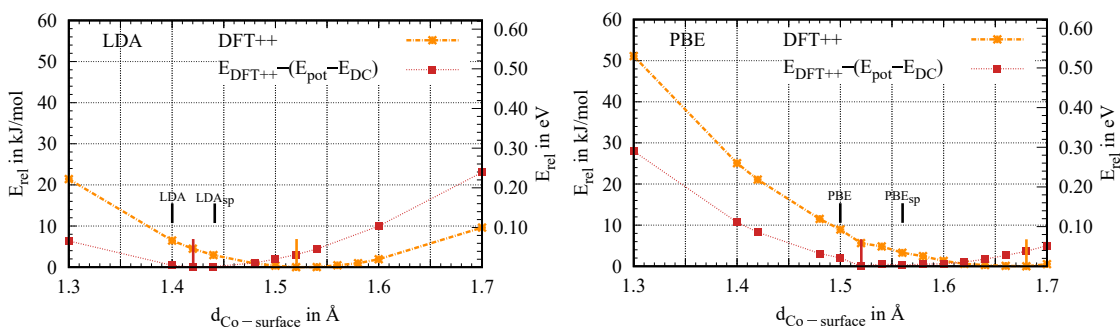


Figure 5.4.: Relative energy obtained from DFT++ for different adsorption distances of Co on Cu(001) and for  $E_{\text{DFT++}} - (E_{\text{pot}} - E_{\text{DC}})$ . Results obtained at  $\beta = 100 \text{ eV}^{-1}$  with  $U = 4.0 \text{ eV}$  and  $J = 0.9 \text{ eV}$ . Bars in black marking the adsorption distances for DFT/DFT<sub>SP</sub>, and colored bars marking the DFT++ ( $U = 4.0 \text{ eV}$ ) respectively the  $E_{\text{DFT++}} - (E_{\text{pot}} - E_{\text{DC}})$  adsorption distance.

## 5.4. Electronic structure of Co/Cu(001)

In the previous section, we could show that there is a non-negligible shift of the PES minimum by taking into account the dynamical effects within the DFT++

framework, as well as by adding a Coulomb potential in the framework of DFT+ $U$ . Here we would like to gain insight into how different adsorption distances affect the electronic structure of an adsorbate.

Besides the parametrization of the Coulomb matrix (discussed in Sec. 3.6.1), it is important for this discussion to have a look at the hybridization functions and impurity levels (the crystal-field splitting<sup>3</sup>) at different adsorption distances, because these parameters as obtained from DFT are those entering the AIM. However, to keep this discussion concise, we will focus on the most relevant orbitals, namely the ones which are singly occupied, and thus the most promising for rationalizing the experimentally observed Kondo effect.

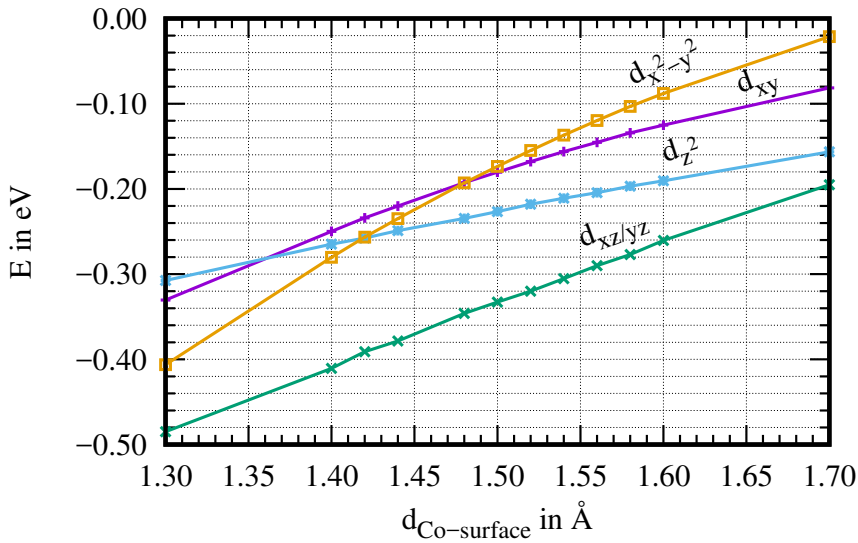


Figure 5.5.: Static crystal-field splitting (i.e.  $3d$ -orbital energies of Co) of the Co  $3d$  shell as obtained from LDA (spin-unpolarized), as a function of the adsorption distance. The Fermi level is set to zero.

By inspection of Tab. 5.2, one can identify the  $d_{xy}$  and the  $d_{z^2}$  orbital to be the orbitals of interest which is in agreement with Refs. [216] and [111]<sup>4</sup>. The energy level of each Co  $3d$  orbital as observed from spin-unpolarized LDA with respect to the Fermi level (0 eV) is shown in Fig. 5.5, where the energetic difference between

<sup>3</sup>The impurity levels are actually the diagonal elements obtained from solving the secular equations for the Co  $3d$  subspace of the KS Hamiltonian. In the context of the AIM this is often referred to as the static crystal field splitting.

<sup>4</sup>Note the different orientation of the  $x$ - and  $y$ - axis.

Table 5.2.: Occupation of the Co 3*d* shell as obtained from LDA++ at  $\beta = 100 \text{ eV}^{-1}$  and  $U = 4.0 \text{ eV}$  ( $J = 0.9 \text{ eV}$ ) via integration of the interacting impurity Green’s function  $G_{\text{IMP}}$ , at selected values for the adsorption distance. All values were obtained by setting the double-counting as calculated from the fully localized limit. Values in parentheses are obtained from integration of the non-interacting Green’s function (Eq. (3.42)). We also show the expectation value of the spin, as well as the weight  $w$  of the most probable local many-body configuration, which is  $d^8$ ,  $S=1$  with half-filled  $d_{xy}$  and  $d_{z^2}$ . See Section A.2.5 for the full state histogram.

$d_{\text{Co-surf.}}$	$d_{xy}$	$d_{xz/yz}$	$d_{z^2}$	$d_{x^2-y^2}$	total	$\langle S_z \rangle$	$w$
1.3 Å	1.08 (1.45)	1.86 (1.57)	1.07 (1.56)	1.86 (1.72)	7.73 (7.87)	0.95	0.54
1.5 Å	1.04 (1.47)	1.88 (1.56)	1.05 (1.57)	1.88 (1.71)	7.73 (7.87)	0.99	0.61
1.7 Å	1.02 (1.47)	1.89 (1.55)	1.03 (1.58)	1.90 (1.70)	7.73 (7.85)	1.01	0.65

the Co 3*d* levels can be seen as the crystal field splitting. The results of PBE are qualitatively and almost quantitatively in agreement with LDA (see Section A.2.4). One can notice that with increasing adsorption distance the crystal-field splitting changes qualitatively and quantitatively, e.g., for adsorption distances between 1.35 Å and 1.50 Å, the energetic ordering of  $d_{xy}$ ,  $d_{x^2-y^2}$  and  $d_{z^2}$  changes multiple times. Regardless of the adsorption distance, the  $d_{xy}$  and the  $d_{z^2}$  orbitals are singly occupied (Tab. 5.2), although above 1.48 Å the  $d_{x^2-y^2}$  orbital is highest in energy. We emphasize here that this observation is not a violation of the Aufbau principle, which is fulfilled for the Kohn–Sham Bloch wavefunction. Instead, the Co 3*d* orbitals whose occupations are reported here result from projection onto local orbitals, as mentioned in Sec. 3.6.3. This and the parametrization of the Coulomb matrix yields the atomic part of the Anderson Hamiltonian (last two terms of Eq. (3.39)), which in the hybridization expansion of CT-QMC is solved first. We can follow the change of the atomic ground state from  $d^8$ ,  $S=1$  with half-filled  $d_{xy}$  and  $d_{z^2}$  at smaller distances to  $d^8$ ,  $S=1$  with half-filled  $d_{x^2-y^2}$  and  $d_{z^2}$  at larger distances (as intuitively expected by inspection of Fig. 5.5). In the course of the QMC calculation the dynamical hybridization  $\Delta(\omega)$  (for its real part, see Fig. A.5 of Section A.2.2) is evaluated in a formal perturbation theory to all orders, and precisely this dynamics ensures that for the complete Hamiltonian the local configuration with the largest contribution to the ground state is  $d^8$ ,  $S=1$  with half-filled  $d_{xy}$  and  $d_{z^2}$  at all distances. In Tab. 5.2 we show the contribution of said atomic state to the many-body ground state as well as the expectation value of  $\hat{S}_z$ . Both are consistent with the system becoming more decoupled from the surface and thus more atomic as the distance is increased (see Fig. A.8 of Section A.2 for

a more detailed evaluation of the different charge and spin contributions).

In the following, we consider the imaginary part of the hybridization function as obtained from LDA ( $\text{Im}\Delta$  obtained from PBE is provided in Fig. A.4 of Section A.2, and is in agreement with LDA), which can be regarded as the dynamical broadening of the impurity levels, due to the hybridization with the Cu(001) surface. We focus on the half-filled orbitals (Fig. 5.6) and find that they retain their qualitative features when changing the adsorption distance, but as one would expect, the hybridization increases systematically as the adsorption distance is lowered. Fig. 5.6 shows that this effect is a little bit more pronounced for the  $d_{xy}$  orbital than for the  $d_{z^2}$  orbital. Thus, we would expect that the Kondo effect in the  $d_{xy}$  orbital is somewhat more sensitive towards changes in the adsorption distance than it is in the  $d_{z^2}$  orbital. We can check this behavior of  $T_K$  with the simplest Kondo-model (one-band with a constant hybridization  $\Gamma$ ) [40], as already introduced in Equation (3.2), by setting  $\Gamma = -\text{Im}\Delta(0.0 \text{ eV})$ .

Table 5.3.: Estimated Kondo temperature as obtained from a one-band model with a constant hybridization.  $\text{Im}\Delta(0)$  is the value of the imaginary part of the hybridization function at  $\omega = 0 \text{ eV}$  (Fermi level).  $\epsilon_{xy/z^2}$  are the energies of the Co  $d_{xy/z^2}$  orbitals relative to the Fermi level. Values taken here are obtained from LDA, and for  $U$  we have chosen  $4.0 \text{ eV}$ . For the estimation of the Kondo temperature  $T_K$  see Equation (3.2). Experimental value for  $T_K = 88 \pm 4 \text{ K}$  [200–202].

$d_{\text{Co-surf.}}$	$-\text{Im}\Delta_{xy}(0)$	$-\text{Im}\Delta_{z^2}(0)$	$\epsilon_{xy}$	$\epsilon_{z^2}$	$T_{K,xy}$	$T_{K,z^2}$
1.30 Å	0.258	0.202	-0.330	-0.308	147.7	62.68
1.40 Å	0.212	0.181	-0.250	-0.265	165.7	67.33
1.50 Å	0.172	0.160	-0.180	-0.227	208.4	69.32
1.60 Å	0.139	0.140	-0.125	-0.190	280.2	75.82
1.70 Å	0.112	0.122	-0.081	-0.156	419.3	85.36

In Tab. 5.3, we have summarized the estimated Kondo temperatures for both the  $d_{xy}$  and the  $d_{z^2}$  orbital at different adsorption distances, obtained with the Co  $3d$ -orbital energies ( $\epsilon$ ) and hybridization strength ( $\text{Im}\Delta(0)$ ) from spin-unpolarized LDA. Obviously, this estimation predicts too large Kondo temperatures for the  $d_{xy}$  orbital. Although the hybridization at the Fermi level ( $\omega = 0 \text{ eV}$ ) is strongly decreasing for larger adsorption distances, the Kondo temperature is increasing to unrealistic values (about  $419.3 \text{ K}$  at  $1.70 \text{ Å}$ ). The increasing Kondo temperature with increasing distance is a result of the impurity level being shifted towards the

Fermi energy, thus overcompensating the decreasing hybridization. For the  $d_{z^2}$  orbital, the Kondo temperature behaves qualitatively similar as for the  $d_{xy}$  orbital. However, the obtained values for  $T_K$  are in much better agreement with the experiment, and, as assumed earlier, are less dependent on the adsorption distance compared to the  $d_{xy}$  orbital. An estimation of the Kondo temperatures from spin-unpolarized PBE yields a qualitatively similar picture as from LDA (see Section A.2).

From our simple estimates of the Kondo temperatures, one observes the serendipitous nature of such simplistic assumptions for multi-orbital Kondo systems. In the present case, we would conclude that the  $d_{xy}$  orbital would be dominant over  $d_{z^2}$  in an underscreened or two-stage Kondo situation. However, a low temperature investigation [111] using a perturbative solver suggests that it is in fact the other way around, the  $d_{z^2}$  Kondo temperature being larger which is caused by more pronounced charge fluctuations. From this observation one could conclude, that the  $d_{z^2}$  orbital is weaker correlated compared to the  $d_{xy}$  orbital, if one remembers that larger charge fluctuations are similar to the wave function becoming more ionic character, as briefly introduced in Section 3.5. We would like to mention here that these investigation differs from ours in the way that it includes the effect of a tip, as well as a different description of the Cu(001) surface. The latter is in Ref. [111] modeled by a cluster approach embedded in a tight binding Bethe-lattice, whereas we applied periodic boundary conditions.

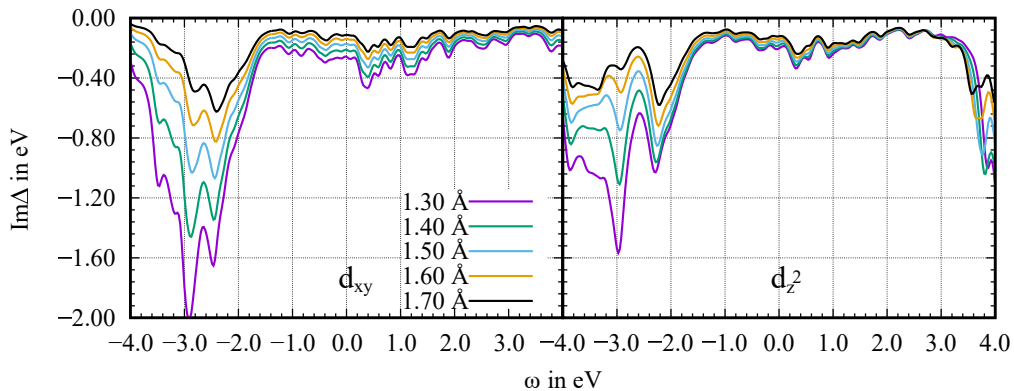


Figure 5.6.: Imaginary part of the hybridization function for the Co  $3d_{xy}$  and the Co  $3d_{z^2}$  orbital as obtained from LDA, for selected values of  $d_{\text{Co-surface}}$ . Results for PBE are given in Section A.2.

To complete our comparative study, we provide the self-energies on the Matsubara axis<sup>5</sup> as obtained from DFT++ in Figure 5.7. This quantity is necessary for the

<sup>5</sup> $\omega_n = \frac{(2n+1)\pi}{\beta}$ , with  $n = 0, 1, 2, \dots$

interpretation of the electron correlation effects within the AIM. We limit the discussion to the half-filled orbitals only. From Fig. 5.7 a) and b), one can see by comparing the LDA++ with the PBE++ results, that both electronic structure methods agree well with each other at all selected adsorption distances. This can be understood as follow: the parametrization for the AIM is completely done by DFT, as introduced in Sec. 3.6.3, which yields the energy-dependent hybridization function (Eq. (3.40)), describing the coupling of the Co 3d shell to a non-interacting “bath” of electrons (the Cu(001) surface).

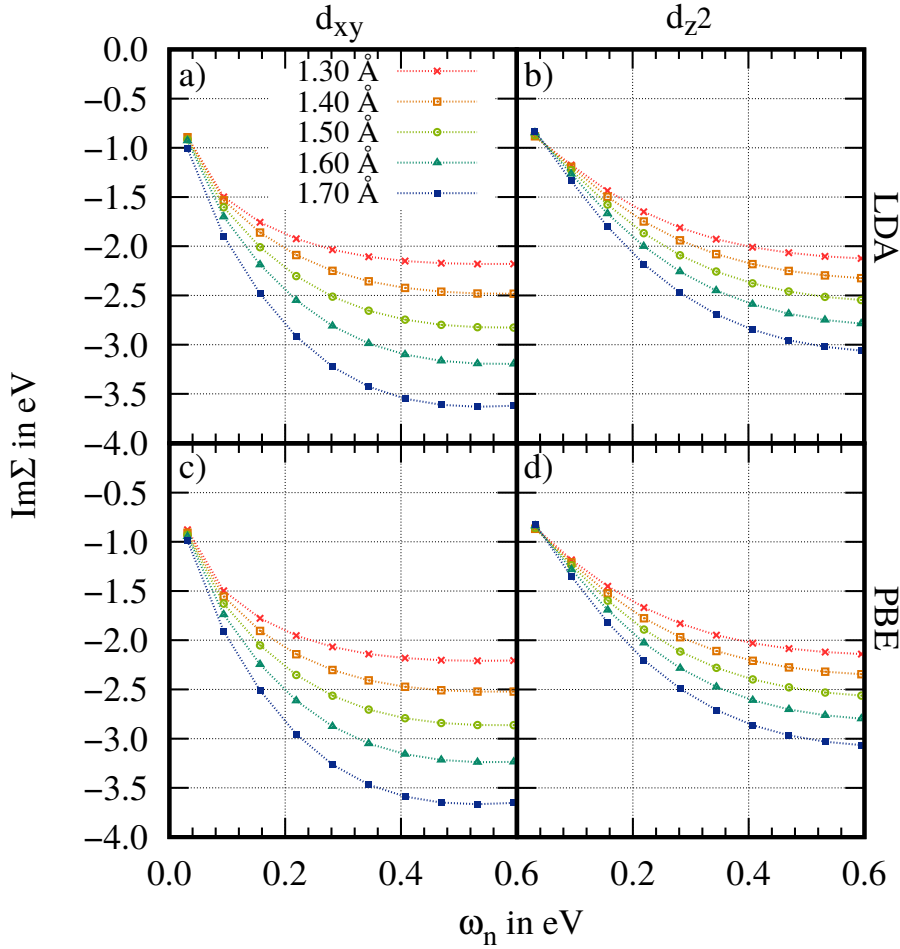


Figure 5.7.: Self energies (last term of Eq. (3.46)) obtained from DFT++ at  $\beta = 100 \text{ eV}^{-1}$  with  $U = 4.0 \text{ eV}$  and  $J = 0.9 \text{ eV}$ . a)  $\text{Im}\Sigma$  for the Co  $3d_{xy}$  orbital as obtained from LDA++ and PBE++. b)  $\text{Im}\Sigma$  for the Co  $3d_{z^2}$  orbital as obtained from LDA++ and PBE++.

Consequently, the agreement between both functionals is due to the similar de-

scription of the coupling of the Co  $3d$  shell to the Cu(001) surface at a given adsorption distance (compare Fig. 5.6 and Fig. A.4 of Section A.2).

By further inspection of Fig. 5.7, one can see that we are not in the Fermi liquid regime (for  $\beta = 100 \text{ eV}^{-1}$ ), because  $\text{Im}\Sigma(\omega_n)$  does not behave linearly as  $\omega_n \rightarrow 0$ . It is nonetheless worthwhile to consider  $\text{Im}\Sigma(\omega_n)$  at as a function of the adsorption distance, because the results of the AIM are potentially affected by the distance, due to changes in the hybridization function. Indeed, for both orbitals  $\text{Im}\Sigma$  drops to larger absolute values as the distance is increased, which means that the electrons are “more” correlated at larger adsorption distances, and is thus in agreement with the increasing term  $|E_{\text{pot}} - E_{\text{DC}}|$  (Fig. 5.3) discussed before. In contrast, the electron correlation in the almost fully occupied orbitals (Co  $3d_{xz/yz}$  and  $3d_{x^2-y^2}$ ) are only little affected by the adsorption distances, as can be seen from  $\text{Im}\Sigma(\omega_n)$  shown in Fig. A.6 of Section A.2 (note the reduced abscissa). Consequently, the double occupancies showing the strongest variation as a function of the distance are  $\langle \hat{n}_{xy\sigma} \hat{n}_{xy\bar{\sigma}} \rangle$ ,  $\langle \hat{n}_{z^2\sigma} \hat{n}_{z^2\bar{\sigma}} \rangle$  and  $\langle \hat{n}_{xy\sigma} \hat{n}_{z^2\bar{\sigma}} \rangle$ . While all other terms change only by at most  $\pm 5\%$  from  $1.3 \text{ \AA}$  to  $1.68 \text{ \AA}$ , these terms decrease by 57-68%. This leads to the conclusion that the shifts of the minima discussed in Sec. 5.3 mainly originates from both the Co  $d_{xy}$  and the Co  $3d_{z^2}$  orbital. The self-energies further reveal that the  $d_{xy}$  orbital is more correlated than the  $3d_{z^2}$  orbital, because the absolute values of  $\text{Im}\Sigma_{xy}(\omega_n)$  are larger compared to  $|\text{Im}\Sigma_{z^2}(\omega_n)|$ . This is in agreement with the results reported in Reference [111], which we mentioned earlier in this section.

## 5.5. Conclusion

In summary, we could show that for Co/Cu(001) adsorption distances increases when applying the AIM on top of spin-unpolarized DFT by about  $0.14\text{-}0.23 \text{ \AA}$ , and  $0.08\text{-}0.12 \text{ \AA}$  when comparing with spin-polarized DFT. The shifts can be explained by a larger amount of correlation (thus reducing the total energy) at larger distances as suggested by our data. However, this effect is already captured by  $\text{DFT}+U$ , which is much cheaper than  $\text{DFT}++$ . On the other hand, given that the difference in adsorption distance between DFT and  $\text{DFT}++/\text{DFT}+U$  are of the same order as the DFT error bar<sup>6</sup>, this implies that the effect of strong correlation on these distances could also be adequately described by a suitable chosen approximate exchange–correlation functional within DFT.

<sup>6</sup>Although Kohn–Sham density functional theory is formally correct, the exact exchange–correlation functional is still unknown, for which reason one has to rely on present-day approximate exchange–correlation functionals. The approximate nature of these functionals causes an error compared to experimental values (e.g. for lattice parameters and adsorption distances), as comprehensively shown in Ref. [217–219]

Further, for the self-energies as obtained from DFT++, it is less important whether the AIM is parametrized by LDA or PBE in the case of Co/Cu(001). However,  $\text{Im}\Sigma$  delicately depends on the adsorption distance of Co on Cu(001) for the Co  $d_{xy}$  and  $d_{z^2}$  orbitals, implying that the increasing correlation effects (with increasing distance) in these orbitals are mainly responsible for the observed shifts. That the electron correlation increases as a function of the distance is in particular interesting, because the results (such as transition temperatures to the Kondo regime) might strongly be affected by structural optimizations using different electronic structure methods (as it will also be shown in the later course of this work).

Concerning the correlation strength in both singly occupied orbitals, our results are in agreement with Reference [111], suggesting that the  $d_{xy}$  orbital is slightly more correlated than the  $d_{z^2}$  orbital. From this one would conclude that the latter should have a larger Kondo temperature, but to clarify this further DFT++ calculations at lower electronic temperatures than shown here are required.

To this end, in the next section we will focus on only one adsorption distance of Co/Cu(001), and will investigate the electronic structure within the AIM in more detail, which includes lower electronic temperatures, as well as comparing the effect of different Coulomb interaction schemes (which were introduced in Section 3.6.1) onto the Fermi liquid properties of Co/Cu(001).

# 6. Kondo screening in Co on Cu(001) with full Coulomb interaction

---

To be submitted: Marc Philipp Bahlke, Alexander Kowalski,  
Michael Karolak, Angelo Valli,  
Carmen Herrmann and Giorgio Sangiovanni

---

## 6.1. Introduction

A single cobalt atom on metal surfaces such as Au, Ag, or Cu is paradigmatic for the Kondo effect [202, 220, 221]. From the experimental site it is only hardly to detect, due to the manifestation of this effect at low temperatures. In the theory, one is rather challenged to find an appropriate balance between the applied approximations and the accuracy of the observed results. Concerning the Kondo effect, the truncation of the number of correlated orbitals, or bath states, as well as approximating the description of the Coulomb interaction might have a deep impact on the physics of the system under consideration. In addition to this, it is inevitable that from a DFT point of view a proper choice of the exchange–correlation functional has to be taken, in order to get molecular structures and adsorption distances as accurate as possible, as discussed for example in Section 5.

As already mentioned in Section 5, the currently accepted scenario with state-of-the-art calculations is, that in principle the Co  $3d_{z^2}$  and  $3d_{xy}$ <sup>1</sup> orbitals are Kondo

---

<sup>1</sup>Depending on the orientation of the unit cell, one sometimes finds the  $3d_{x^2-y^2}$  orbital instead of the  $3d_{xy}$  orbital.

active, due to its occupation closest to one electron. Clearly, the description of the Coulomb interaction (see Section 3.6.1) within the AIM plays an important role in the Kondo physics, besides the hybridization of the Co  $3d$  orbitals with the Cu(001) surface. Treating the full Coulomb tensor within a five-band model (all five  $3d$  orbitals are included in the calculations) is, however, a computationally expensive task [136] for which reason in most studies found in the literature approximations to the Coulomb tensor are used. Since we use DFT++ as a reference concerning the Kondo effect, we have to check whether the results obtained by applying such approximations are physically meaningful or not. As shown later, this will become an important aspect at lower electronic temperatures.

Because the exact value of the double-counting energy (which shifts the total occupation on the impurity shell) is unknown, one would also have to study this effect on the observed DFT++ results. The total occupation on the Co  $3d$  shell plays, without a doubt, a major role in such many-body situations. In this study, we fix the occupation  $n_d$  of the Co  $3d$  shell such that we have a well-defined  $S=1$  state, which leads to an occupation of  $n_d = 8.0$ . This occupation was confirmed by correlated wave-function-based calculations where a Co/Cu $_n$  cluster is embedded in a periodic embedding potential [216].

In this section, we apply the numerically correct CT-QMC approach to solve the AIM including all five Co  $3d$  orbitals, and compare the Fermi liquid properties within different Coulomb interaction schemes. It will also be discussed the importance of a proper description of the Cu surface concerning the  $k$  point sampling of the Brillouin zone, as this is important for the parametrization of the AIM. Within this discussion we show the limitations of the density–density approximation for Co/Cu(001) at low  $T$ , and that by error compensation by an inappropriate description of the surface one gets supposedly correct results, but these are due to wrong reasons.

## 6.2. Computational methodology

The DFT calculations have been performed with the Vienna ab-initio simulation program (VASP) [174,175], using the PAW basis set as provided within this program package. We modeled the Cu(001) surface as a  $4\times 4$  slab consisting of 5 Cu layers using the experimentally observed lattice constant of  $3.615 \text{ \AA}$  [206]. The Co adatom was placed in the fourfold-hollow position at an adsorption distance of  $1.52 \text{ \AA}$  with respect to the first Cu(001) layer, which we identified in Section 5 to be the energetically favored distance by using a combination of LDA and the AIM.

We used a  $k$ -grid centered around the  $\Gamma$ -point of size  $100 \times 100 \times 1$  in order to achieve a sufficiently accurate description of the Cu(001) substrate, which will be necessary for the parametrization of the AIM especially at low temperatures (this will be discussed later in more detail). After projecting the KS Green's function onto the correlated sub-space (Co  $3d$  shell), we obtained the hybridization function (Figure 6.1) on the real energy axis by using Equation (3.45), which acts as the starting point for solving the AIM within CT-QMC.

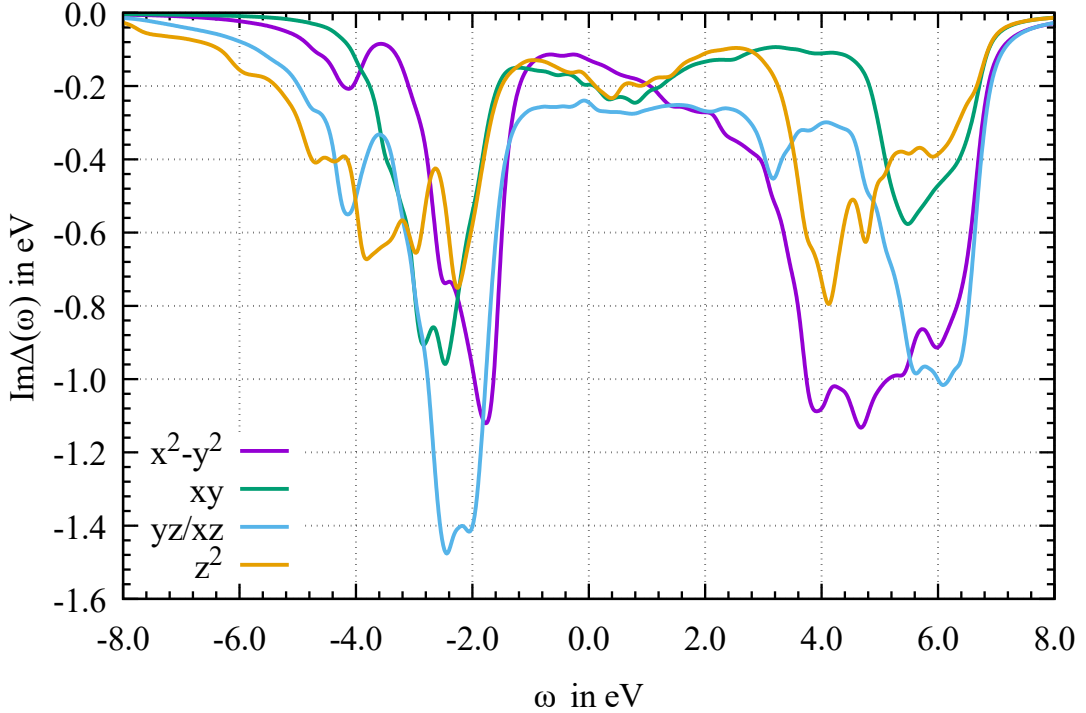


Figure 6.1.: Imaginary part of the hybridization function for the Co  $3d$  orbitals of Co/Cu(001). The results were obtained from LDA using a  $k$ -grid of  $100 \times 100 \times 1$ .

The AIM is solved by using the numerically exact (CT-QMC) method as implemented in `w2DYNAMICS` [222, 223]. The Coulomb matrix was parameterized using Slater integrals (see Sec. 3.6.1), with  $U = 4.0$  eV and  $J = 0.9$  eV. The lowest accessible temperature for Co/Cu(001) in the scope of the full Coulomb interaction reached here is  $\beta = 250$  eV $^{-1}$  ( $T = 46.6$  K)<sup>2</sup>. To our knowledge, this was applied for the first time to a single Co adatom on Cu(001) using full periodic boundary

<sup>2</sup>I thank Alexander Kowalski for doing the CT-QMC calculations with the full Coulomb interaction and the Kanamori approximation.

conditions and solving the AIM for a five-band model (all Co 3d orbitals are in the correlated sub-space)) using the full Coulomb interaction. We compare the results against using different parametrization schemes which have been introduced in Section 3.6.1.

### 6.3. Fermi liquid properties of Co on Cu(001)

We start by investigating the magnetic properties of Co/Cu(001) as a function of the temperature for the three Coulomb interaction schemes under consideration here. For this reason, we measure the spin–spin correlation function  $\chi_i(\tau)$  as described in Section 3.7.4, and obtained the spin susceptibility  $\chi_i^{\omega=0}$  via integration of  $\chi_i(\tau)$  (see Equation (3.65)).

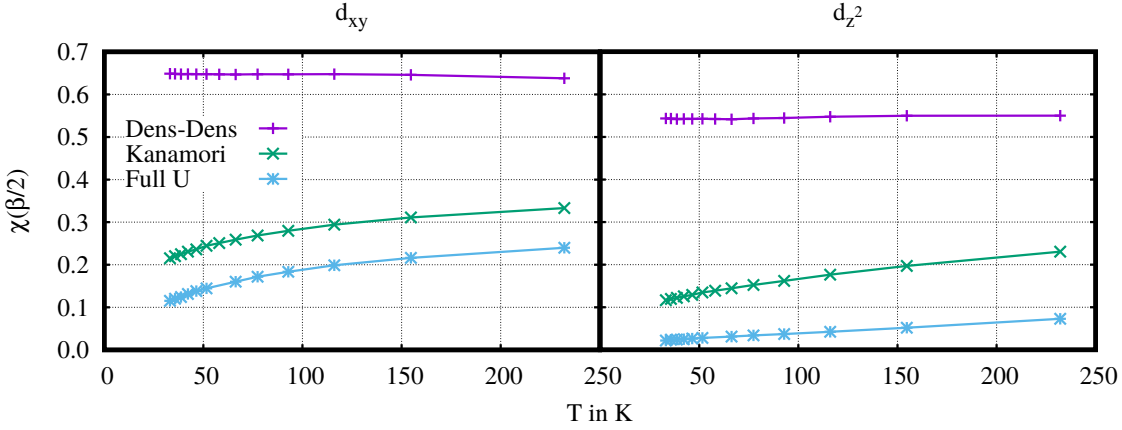


Figure 6.2.: Local spin–spin response  $\chi(\tau)$  at  $\tau = \beta/2$  as a function of the temperature for the Co  $3d_{xy}$ - and  $3d_{z^2}$  orbital. The results are shown for density–density and Kanamori approximation, as well as using full Coulomb interaction.

In Figure 6.2, we show  $\chi(\beta/2)$  as a function of  $T$  for both Kondo-relevant orbitals in Co/Cu(001), which are the Co  $3d_{z^2}$  and  $3d_{xy}$  orbitals as already discussed in Ref. [111, 199] (note the different orientation of the  $xy$ - plane in this thesis). One can see whether the local moment is screened at low temperatures by a vanishing value of  $\chi(\beta/2)$ . For the full Coulomb interaction, the value of  $\chi(\beta/2)$  for both orbitals decreases as the temperature is lowered, with the Co  $3d_{z^2}$  orbital having smaller absolute values as compared to the Co  $3d_{xy}$  orbital. The results of  $\chi(\beta/2)$  as obtained from the Kanamori interaction, agree qualitatively with the behavior discussed for the full Coulomb interaction, although the values are larger in

this case. It is evident that within the density–density approximation,  $\chi(\beta/2)$  for both orbitals ( $3d_{z^2}$  and  $3d_{xy}$ ) behaves qualitatively and quantitatively different compared to what we have observed for the Kanamori approximation and the full Coulomb interaction. Here,  $\chi(\beta/2)$  is rather constant in  $T$  for both orbitals, which is reminiscent of a frozen moment regime (i.e. we have an unscreened local moment) [143].

For further analysis of the Kondo properties, it is worth checking for a behavior according to the the Fermi liquid regime, as manifested in a  $T^2$  behavior of  $\chi(\beta/2)$ . With the temperatures reached here, we cannot make the transition to this regime visible, neither with the results obtained from the full Coulomb interaction, nor from the results of the Kanamori approximation.

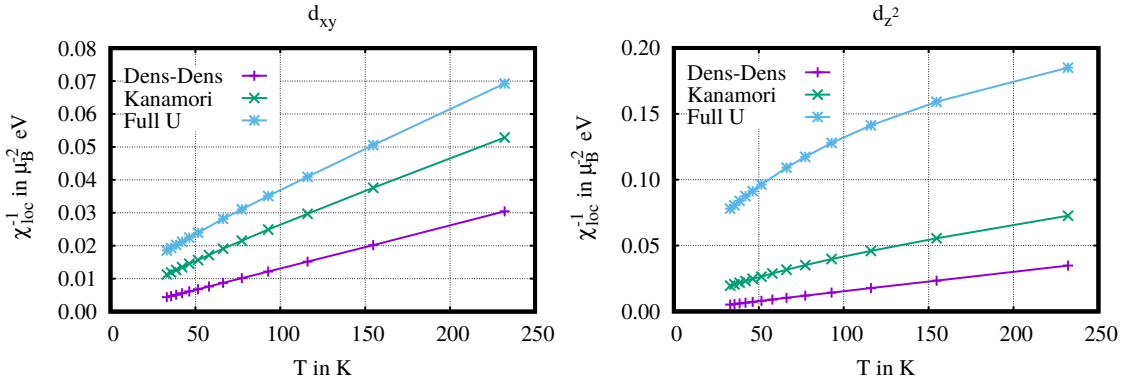


Figure 6.3.: Inverse spin susceptibility  $\frac{1}{\chi^{\omega=0}(T)}$  of the Co  $3d_{xy}$  and  $3d_{z^2}$  orbital as obtained from LDA+AIM using different interaction schemes.

The non-Fermi liquid behavior is so far in agreement with the inverse susceptibilities (Figure 6.3) for the Co  $3d_{z^2}$  and  $3d_{xy}$  orbital, and are discussed in the following. As pointed out earlier, within the density–density approximation, the Co  $3d_{z^2}$ - and  $3d_{xy}$  orbitals are presumably in a frozen moment regime, which is visible here in the linear behavior of  $\frac{1}{\chi^{\omega=0}(T)}$  indicating agreement with the Curie law ( $1/T$  behavior of  $\chi^{\omega=0}(T)$ ). For the Co  $3d_{xy}$  orbital we observe a slight deviation from this linear dependence of  $\frac{1}{\chi^{\omega=0}(T)}$  on  $T$  for both the results as obtained from the full Coulomb interaction as well as for the Kanamori approximation. For the Co  $3d_{z^2}$  orbital,  $\frac{1}{\chi^{\omega=0}(T)}$  most clearly deviates from a linear dependence on  $T$  using the full Coulomb interaction, probably due to the largest screening of the local moment in this orbital (as shown in Figure 6.2).

The Fermi liquid behavior can also be studied by considering the imaginary part of the self-energy at the first Matsubara frequency as a function of  $T$ . For a Fermi

liquid, it is expected that  $\text{Im}\Sigma(\omega_0)$  shows a linear dependence on the  $T$  at low enough temperatures [145]. In general, our data (Figure 6.4) confirm what we have found for  $\chi(\beta/2)$  and  $\frac{1}{\chi^{\omega=0}(T)}$ , but point out more clearly the difference between the orbitals studied here. For the Co  $3d_{xy}$  orbital,  $\text{Im}\Sigma(\omega_0)$  agrees qualitatively among the different interaction schemes, but the absolute values decrease from the density–density to the Kanamori approximation, and decrease further by using full Coulomb interaction. For the Co  $3d_{z^2}$  orbital, one can clearly notice that the density–density approximation predicts a different physical picture for this orbital than for the Kanamori approximation and the full Coulomb interaction. In case of the density–density approximation,  $3d_{z^2}$  behaves rather insulating as indicated by the negative slope at lower temperatures (for  $T \rightarrow 0$  K). The results obtained from the Kanamori approximation suggest that  $\text{Im}\Sigma(\omega_0)$  could go linearly to zero as  $T \rightarrow 0$  K at lower temperatures as shown here, and this is even more pronounced if one uses the full Coulomb interaction. However, a clear transition to the Fermi liquid regime is still not visible.

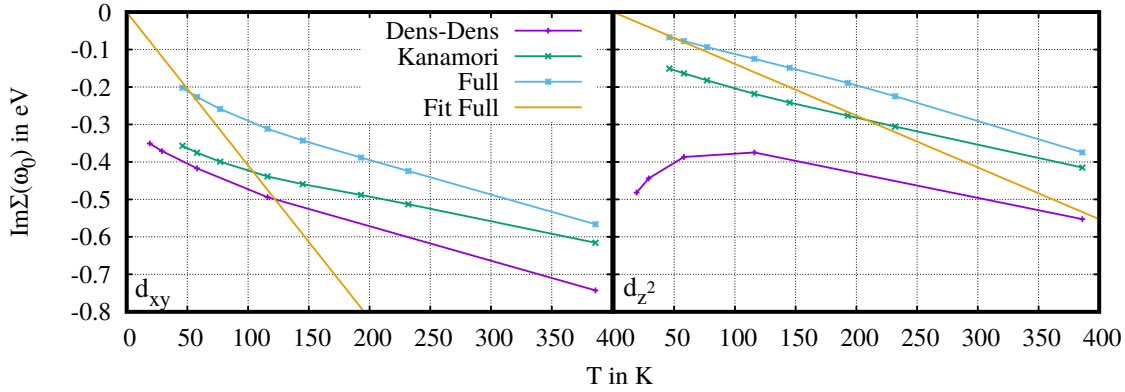


Figure 6.4.: First Matsubara frequency rule for Co/Cu(001) at  $d_{\text{Co-surf.}} = 1.52 \text{ \AA}$  as obtained from LDA++, within different parametrization schemes for the local Coulomb interaction.

## 6.4. Role of the coulomb interaction scheme onto the Fermi liquid properties of Co on Cu(001)

So far, we have shown that the choice of the interaction scheme can alter the physical picture of Co/Cu(001) completely. To get a more physical insight into the roles of the three different interaction schemes, we consider the doubly-occupancies for same- ( $\langle n_{i\sigma}n_{j\sigma} \rangle$ ) and opposite spin ( $\langle n_{i\sigma}n_{j\bar{\sigma}} \rangle$ ) direction (Figure 6.5). The upper part of Figure 6.5 shows the same-spin double occupancy  $\langle n_{i\sigma}n_{j\sigma} \rangle$  as obtained from

#### 6.4. Role of the coulomb interaction scheme onto the Fermi liquid properties of Co on Cu(001)

the three interaction schemes under study here. The diagonal elements are equal to the electron density per spin on each individual Co 3d orbital (the off-diagonal terms are the so-called Hund's double occupancies), and one observes that within the density–density approximation, the Co 3d<sub>xy</sub> orbital and the Co 3d<sub>z<sup>2</sup></sub> orbital are close to half-filling (0.5 electrons per spin), whereas the remaining Co 3d orbitals are almost full.

For the Kanamori approximation, the occupation of the 3d<sub>z<sup>2</sup></sub> and 3d<sub>xy</sub> orbitals is slightly increased as compared to the results of the density–density approximation. However, this might be coming from the fact that the total 3d electron density in this case is slightly larger ( $n = 4.04$  per spin) as it is in the density–density case ( $n = 4.01$  per spin). Comparing the differences of the occupation between both orbitals ( $\delta n = n_{z^2} - n_{xy}$ ), one finds that within the Kanamori interaction  $\delta n$  is larger as compared to the density–density approximation, which indicates that the charge fluctuations in the 3d<sub>z<sup>2</sup></sub> orbital are larger than in the 3d<sub>xy</sub> orbital.

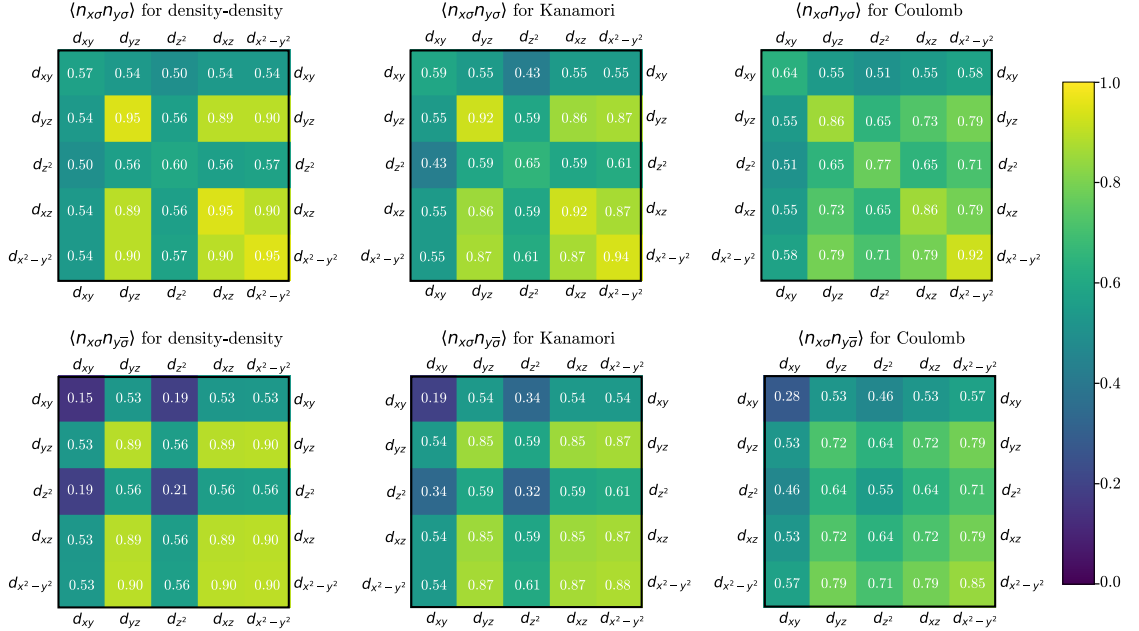


Figure 6.5.: Same ( $\langle n_{x\sigma}n_{y\sigma} \rangle$ ) and opposite ( $\langle n_{x\sigma}n_{y\bar{\sigma}} \rangle$ ) spin double occupancy as obtained from LDA++ at  $\beta = 175 \text{ eV}^{-1}$ . Results are shown for the density–density approximation, the Kanamori approximation, and the full Coulomb tensor (Coulomb).

For the full Coulomb interaction, the electron density is distributed more homogeneously among the Co 3d sub-space, and the filling of the 3d<sub>xy</sub> and 3d<sub>z<sup>2</sup></sub> orbitals increases at the expense of the remaining Co 3d orbitals (the charge fluctuations

are increased for both orbitals). Furthermore, the difference of the fillings between both orbitals  $\delta n$  is larger as compared with the Kanamori (and density–density) case, which suggests that the charge fluctuations in the  $3d_{z^2}$  orbital is more and more favored if the local Coulomb interaction is described more precisely. In numbers, for the full Coulomb interaction one obtains that the Co  $3d_{z^2}$  orbital of Co/Cu(001) carries 0.13 electron density (per spin) more than the  $3d_{xy}$  orbital, whereas in the Kanamori case the difference is only 0.06. Furthermore, based on the larger value for the electron density on the Co  $3d_{z^2}$  orbital (for all interaction schemes under study here), one could assume that the Co  $3d_{z^2}$  orbital is less correlated as compared to the  $3d_{xy}$  orbital, and this is most prominent for the “true” interaction (full Coulomb).

This observation is confirmed by the opposite spin double-occupancy  $\langle n_{i\sigma} n_{j\bar{\sigma}} \rangle$  shown in the bottom part of Figure 6.5. Considering the diagonal elements (same-orbital opposite-spin double occupancy, Fig 6.5) for all interaction schemes, one can notice that they are larger for the Co  $3d_{z^2}$  orbital than for the  $3d_{xy}$  orbital, which supports the observation of the less correlated character of the  $3d_{z^2}$  orbital.

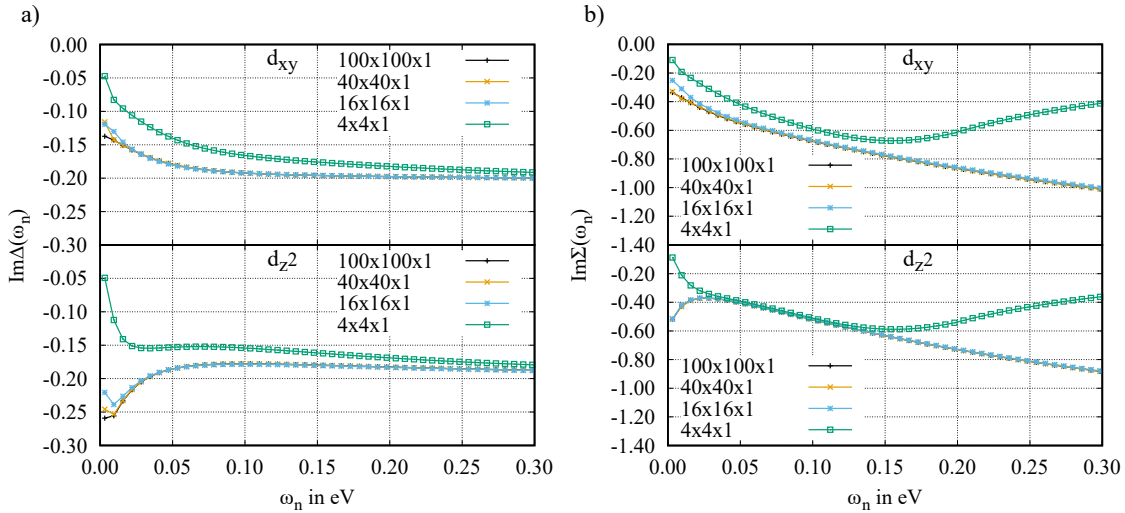


Figure 6.6.: a) Imaginary part of the hybridization function on the Matsubara axis at  $\beta = 1000 \text{ eV}^{-1}$  as obtained from different  $k$ -grids. b) Imaginary part of the self energy on the Matsubara axis at  $\beta = 1000 \text{ eV}^{-1}$  as obtained from different  $k$ -grids (density–density interaction).

As mentioned before, the diagonal values  $\langle n_{i\sigma} n_{i\sigma} \rangle$  (same orbital same spin double occupancy) equal the electron density per spin on each Co  $3d$  orbital. From this one can calculate the corresponding uncorrelated double occupancies  $\langle n_{i\sigma} \rangle \langle n_{j\bar{\sigma}} \rangle$ , which by comparing them with  $\langle n_{x\sigma} n_{x\bar{\sigma}} \rangle$  gives us an estimator of how correlated the Co

$3d$  orbitals are (the larger the difference between these two values, the larger the correlated character). For instance, with full Coulomb interaction, one finds for the non-interacting double occupancy of the  $3d_{xy}$  orbital ( $\langle n_{x\sigma} \rangle \langle n_{x\bar{\sigma}} \rangle$ ) a value of 0.41, and for the  $3d_{z^2}$  orbital a value of 0.59. The non-interacting double-occupancy of the  $3d_{z^2}$  orbital is clearly closer to its correlated double occupancy ( $\langle n_{x\sigma} n_{x\bar{\sigma}} \rangle$ ), in contrast to the  $3d_{xy}$  orbital, resulting from the less correlated character of the  $3d_{z^2}$  orbital. For the density–density- and Kanamori approximations, one observes a similar qualitative behavior, but the differences between  $\langle n_{x\sigma} \rangle \langle n_{x\bar{\sigma}} \rangle$  and  $\langle n_{x\sigma} n_{x\bar{\sigma}} \rangle$  increase, and are largest for the density–density-type interaction. This implies that the density–density type interaction overestimates the correlation strength in the Co  $3d_{xy}/3d_{z^2}$  orbitals as compared to the other interaction schemes under consideration here.

## 6.5. *k*-grid dependence of the hybridization function and consequences for the Fermi liquid properties

Throughout our study, we paid a lot of attention to the density–density approximation, and found that the physical picture of Co/Cu(001) delicately depends on the size of the chosen *k*-grid. Figure 6.6 shows the hybridization function  $\text{Im}\Delta(\omega_n)$  of the Co  $3d_{z^2}$  and  $3d_{xy}$  orbitals on the Matsubara axis ( $\beta = 1000 \text{ eV}^{-1}$ ) for different *k*-grid sizes, as well as the corresponding LDA+AIM self-energies ( $\text{Im}\Sigma(\omega_n)$ ) as obtained using the density–density approximation. One can see that using a *k*-grid of  $4 \times 4 \times 1$  leads to a rather bad convergence of  $\text{Im}\Delta(\omega_n)$  in the low frequency part. In fact, for the  $3d_{z^2}$  it shows a different qualitative behavior for  $\omega_n < 0.05 \text{ eV}$  as compared to larger *k*-grid sizes. The correct qualitative trend of  $\text{Im}\Delta(\omega_n)$  for the Co  $3d_{z^2}$  is observed for a *k*-grid size of  $16 \times 16 \times 1$ , although at the first Matsubara frequency ( $\omega_0$ )  $\text{Im}\Delta(\omega_n)$  still changes little when we increase the *k*-grid from  $40 \times 40 \times 1$  to  $100 \times 100 \times 1$ . For the  $3d_{xy}$  orbital a *k*-grid size of  $4 \times 4 \times 1$  yields at least the correct qualitative behavior compared to our most accurate calculation ( $100 \times 100 \times 1$ ).

In panel b) of Fig. 6.6 one can see the consequences for the self-energy by using a too small *k*-grid ( $4 \times 4 \times 1$ ). For the  $3d_{z^2}$  orbital one would conclude, that  $\text{Im}\Sigma(\omega_n)$  behaves as a Fermi liquid by using a *k*-grid of  $4 \times 4 \times 1$ . For the same grid, the self-energy of the  $3d_{xy}$  orbital seems to exhibit a non-zero intercept with the ordinate, which would then be in agreement with an underscreened Kondo effect as discussed in the literature [111, 199]. However, within the density–density approximation

$\text{Im}\Sigma(\omega_n)$  behaves completely different at low frequencies for the Co  $3d_{z^2}$  orbital of Co/Cu(001) by using larger  $k$ -grid sizes. As discussed in Sec. 6.3, the self-energy shows an insulating behavior for this orbital, which can only be corrected by going beyond the density–density approximation.

The first Matsubara frequency as a function of  $T$  is shown in Fig. 6.7, for the smallest  $k$ -grid ( $4\times 4\times 1$ ) under study here (density–density approximation only), and confirms the observation that using this  $k$ -grid the Co  $3d_{z^2}$  orbital behaves as a Fermi liquid below  $T = 25.0$  K. This clearly shows the need of an appropriate description of the metallic substrate in order to get a correct physical picture of the system under consideration.

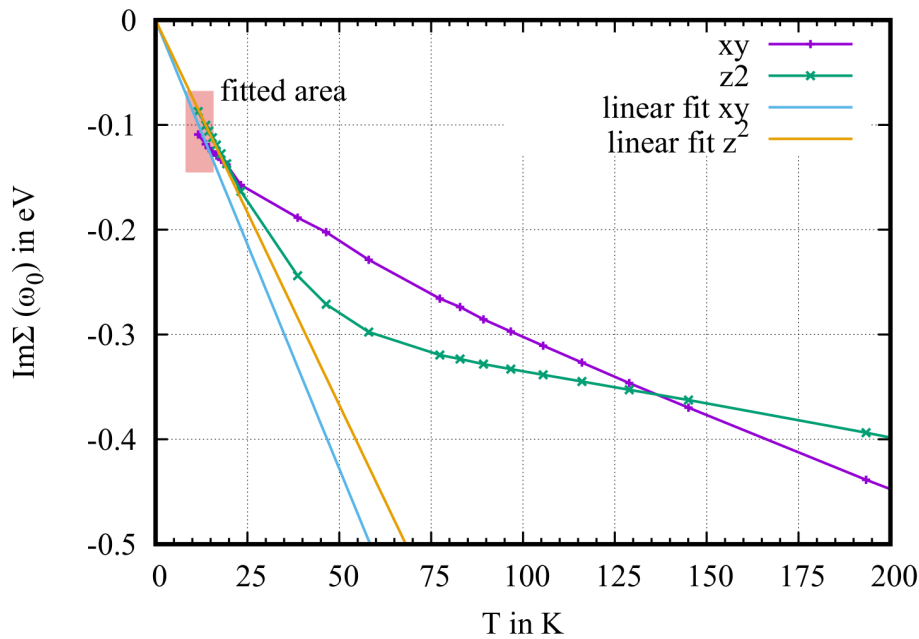


Figure 6.7.: First Matsubara frequency rule for Co/Cu(001) as obtained from LDA+AIM, within the density–density approximation of the local Coulomb interaction. The parametrization of the Anderson impurity model was done with a  $k$ -grid of  $4\times 4\times 1$  centered around the  $\Gamma$  point.

## 6.6. Conclusion

The correlation of a localized electron with its surrounding conduction band electron in an adsorbate–surface situation, can lead to the rather complex Kondo effect

below a certain temperature. From a theoretical point of view, solving the Anderson impurity model can be considered as state-of-the-art for concerning this effect, in which one reduces the space for taking into account electron correlation effects explicitly onto a few local orbitals.

By studying the Kondo effect in Co/Cu(001), the AIM was solved within the numerically exact CT-QMC method. We compared the effect of different approximations to the Coulomb interaction on the Fermi liquid properties of the Co 3*d* electrons. Furthermore, we highlighted the importance of the *k*-grid on the observed results, especially by going to low electronic temperatures.

For the atomistic structure of Co/Cu(001) used in this study, we were not able to reach the transition to the Fermi liquid regime (with a *k*-grid of 100×100×1), required in the spirit of a Kondo effect, with all interaction schemes under consideration. It could rather be shown that the physical properties of Co/Cu(001) delicately depends on approximation made to the Coulomb interaction. Within the density–density approximation, the strength of the correlation on the *d*<sub>z<sup>2</sup></sub> and *d*<sub>xy</sub> orbitals are overestimated, which probably leads to what is called a frozen-moment regime (i.e. the local moments on both orbitals are unscreened by the conduction band electrons). This observation could have its origin in the inherent property of this approximation to overestimate magnetization (as discussed in Section 3.6.1). Using the Kanamori approximation, one obtains at least a qualitative similar physical picture compared to taking into account all Coulomb matrix elements, although quantitatively there are still large differences. These differences originate from the electron density being more homogeneously distributed among the Co 3*d* shell by using the full Coulomb interaction, as in contrast to what one observes from the Kanamori-, or density–density approximation. Similar importance for taking into accounts all Coulomb matrix elements was found for Co in Cu(111), reported in Ref. [224].

Furthermore, we have shown that there is a delicate dependence of the Fermi liquid properties in Co/Cu(001), concerning the description of the surface with respect to the *k*-grid size, which is important for the construction of the wave function in the Brillouin zone. Although, a grid of 4×4×1 (within our unit cell) is sufficient for the electronic structure on the level of DFT, for instance for comparing energies among different methods (as shown in Section 5), it fails for low temperature ( $T < 116$  K) DFT++ calculations.

For studying the chemical and mechanical control of the Kondo effect, it was shown that approximations to the Coulomb interaction, as well as the *k*-grid used in the underlying DFT calculation can have significant effects onto the electronic structure of Co/Cu(001). Especially concerning the density–density approximation

one may ask whether this scheme is reliable for such a study. In the following sections of this thesis it will be shown that using only the density–density terms of the Coulomb tensor can indeed yield physical meaningful results for carbonyl cobalt complexes on Cu(001) (Section 8), but fails for a single cobalt atom on Ag(001) (Section 7) similarly to Co/Cu(001).

# 7. Co on Ag(001) at low $T$ : A general problem with approximate Coulomb interaction for Co on metal surfaces?

## 7.1. Introduction

It has been shown in Section 6 that approximating the Coulomb interaction can lead to a suppression of the Fermi-liquid properties in Co/Cu(001), and thus the formation of a Kondo resonance. With this in mind, it is worthwhile to investigate whether this is a more general problem of a single Co atom on metal surfaces or not.

In a STS study [201], it was found that Co on Ag(001) shows a zero bias anomaly due to a Kondo effect, with a Kondo temperature of  $T_K = 41$  K (determined by a Fano fit). This observation could be confirmed later by photoemission experiments, which yields the excitation spectra of Co/Ag(001) [225] (and other  $3d$  metals on Ag(001)). These were directly compared to the spectral functions as obtained from HF-QMC calculations.

The theoretically obtained spectra [225] were, however, calculated at a rather large electronic temperature ( $T = 580$  K) by using only the density–density terms of the Coulomb tensor. From what we have learned earlier, it is an open question whether the feature in the spectral function can be interpreted in terms of a Kondo effect or not. For this reason, we apply low temperature DFT++ calculation (with a sufficiently large  $k$ -grid for the underlying DFT calculation), to check whether one observes a similar deviation between an experimentally observed Kondo effect and the absence of it by using the density–density approximation (for details about this approximation, see 3.6.1).

It will be shown that similarly to Co/Cu(001) the self-energy ( $T = 29.0$  K) suggests that none of the Co  $3d$  orbitals agree within a Fermi-liquid picture for Co  $3d$  fillings

between 7.86 and 7.97 (in Reference [225] a filling of 7.8 and 7.9 was used). This observation points towards a general problem of the density–density approximation for the description of Co on metal surfaces, which is particularly important for future studies about the Kondo properties in these systems.

## 7.2. Computational methodology

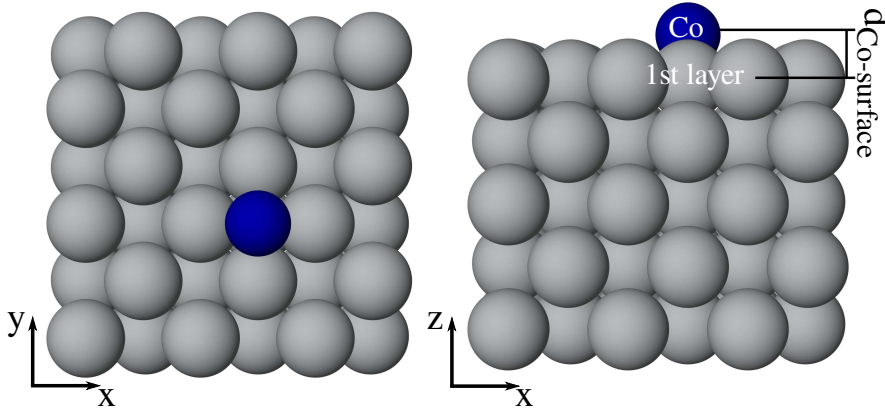


Figure 7.1.: Optimized Co on Ag(001) using PBE.  $d_{\text{Co-surface}}$  is the difference between the  $z$  coordinate of the Cu atoms in the first layer (they were aligned such that all Cu atoms in the first layer have a  $z$  coordinate of 0.00) and the  $z$  coordinate of the Co atom.

The Ag(001) surface was modeled by a  $4 \times 4$  supercell with 5 Ag layers (Figure 7.1). The Co atom was placed in the fourfold hollow position, as reported in Reference [225]. We optimized the adsorption distance of the cobalt atom by keeping all Ag(001) layers fixed using the VASP [174,175] package. All calculations were performed with the PBE exchange–correlation functional as implemented in the PAW formalism, with a  $k$ -grid size of  $4 \times 4 \times 1$  centered around the  $\Gamma$  point. The convergence criteria on the electronic wave function was set to  $2.7 \cdot 10^{-5}$  eV, and the structural relaxation was stopped after all forces were below  $0.01$  eV/Å. We found that Co on Ag(001) adsorbs at  $d_{\text{Co-surface}} = 1.58$  Å above the Ag(001) surface.

For the parametrization of the AIM, we performed a single-point calculation on the optimized Co/Ag(001) using a  $k$ -grid size of  $19 \times 19 \times 1$ . The AIM was solved within the CT-HYB method as explained in Section 3.7, using an average Coulomb interaction value of  $U = 5.0$  eV and  $1.0$  eV for the average exchange interaction  $J$  (values taken from Reference [225]). The Coulomb interaction was approximated by density–density type interactions, as discussed in Section 3.6.1.

Table 7.1.: Occupation of the Co 3d shell in Co/Ag(001) as obtained from PBE++ at  $\beta = 100 \text{ eV}^{-1}$  and  $U = 5.0 \text{ eV}$  ( $J = 1.0 \text{ eV}$ ) via integration of the local interacting impurity Green's function  $g_{\text{int}}$ .

	$d_{xy}$	$d_{xz/yz}$	$d_{z^2}$	$d_{x^2-y^2}$	total
FLL	1.01	1.95	1.01	1.94	7.86
FLL - 2.0 eV	1.04	1.97	1.03	1.96	7.97

### 7.3. Excitation spectra of Co on Ag(001) and Fermi-liquid properties

In Table 7.1, we present the Co 3d occupations as obtained from PBE++ at  $\beta = 100 \text{ eV}^{-1}$  ( $T = 116 \text{ K}$ ). Within the fully localized limit, we obtain a total Co 3d occupation of  $n_d = 7.86$ , which is in good agreement with the value of 7.8 ( $\beta = 20 \text{ eV}^{-1}$ ) reported in Reference [225]. In addition, we shifted the FLL value by -2.0 eV, which leads to  $n_d = 7.97$ . In Figure 7.2, we show the orbitally resolved spectral functions after analytical continuation of the CT-HYB results onto the real energy axis. A feature at the Fermi energy ( $\omega = 0.0 \text{ eV}$ ) in the spectral function can only be observed for the  $d_{xy}$  orbital by shifting the DC value by -2.0 eV ( $n_d = 7.97$ ) from the FLL value (Figure 7.2 b)). This is already visible at  $T = 580 \text{ K}$  ( $\beta = 20 \text{ eV}^{-1}$ ), and does not further grow by lowering the temperature to  $T = 29 \text{ K}$  ( $\beta = 400 \text{ eV}^{-1}$ ), as would have been expected in the Kondo regime [40].

By considering  $\text{Im}\Sigma(\omega_n)$  at our lowest accessible electronic temperature ( $\beta = 400 \text{ eV}^{-1} = 29 \text{ K}$ ), one can see that using the FLL, both singly occupied orbitals ( $d_{xy}/d_{z^2}$ ) clearly disagree with a linear dependence of  $\text{Im}\Sigma$  on  $\omega_n$  as  $\omega_n \rightarrow 0$ , as would be required for a Fermi-liquid (see Section 3.7.5). By shifting the DC value by -2.0 eV from the FLL value, the absolute value of  $\text{Im}\Sigma(\omega_n)$  for all orbitals is significantly reduced compared with the results obtained within the FLL. For both the  $d_{xy}$  and  $d_{z^2}$  orbital at  $n_d = 7.97$  (FLL - 2 eV) the transition to the Fermi-liquid regime could not be reached within the lowest temperature under consideration here, which is in agreement with the lack of a Kondo resonance at the Fermi energy.

Furthermore, our data suggest that there is a delicate dependence of the self energy on the total occupation on the Co 3d shell. This might be of importance for further studies, because in practice the exact value for the double counting (which shifts the total occupation on the correlated sub space) is unknown, and in this study we limited the values of  $n_d$  to 7.86 and 7.97.

<sup>1</sup>We obtained  $n_d = 7.77$  at  $\beta = 20 \text{ eV}^{-1}$ .

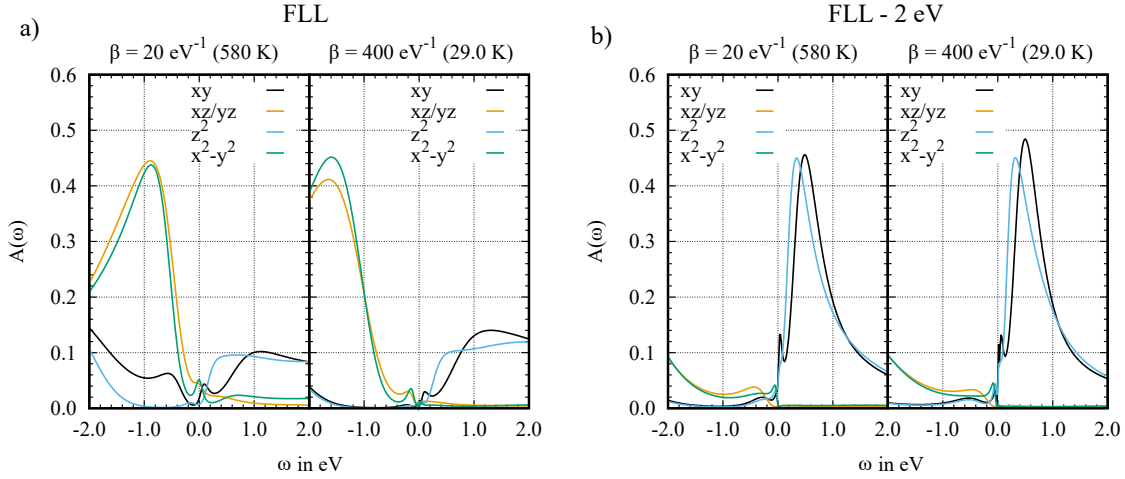


Figure 7.2.: Orbitaly resolved spectral function of the Co 3d orbitals in Co on Ag(001), as obtained from PBE++ at different electronic temperatures and for different values for the double counting correction. a) Results as obtained using the fully localized limit, and b) results as obtained by shifting the double counting by -2.0 eV apart from the FLL value.

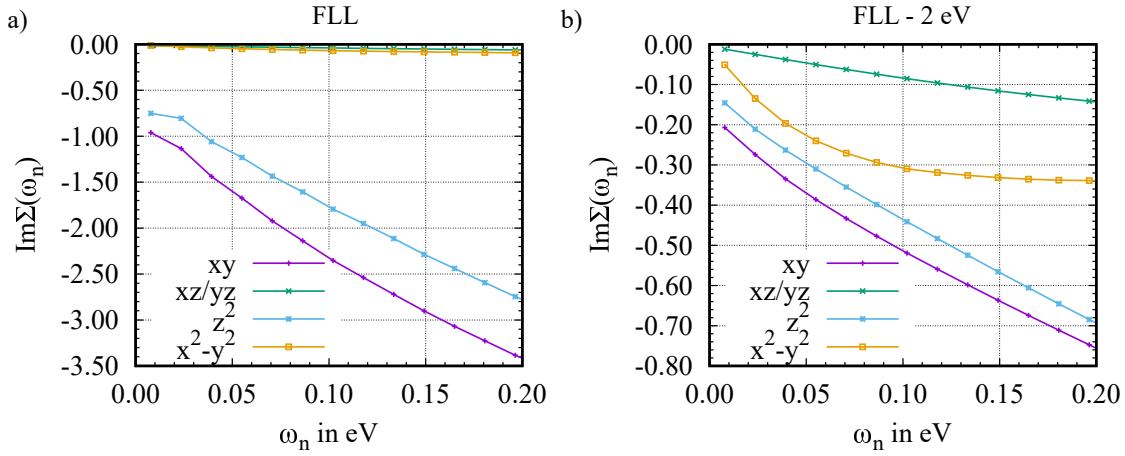


Figure 7.3.: Imaginary part of the self-energy of Co on Ag(001) of all Co 3d orbitals, as obtained from PBE++ at  $\beta = 400 \text{ eV}^{-1}$  and for different values for the double counting correction.

The observation of the lacking Kondo resonance could be of the same origin as in the case of Co on Cu(001), which was already discussed in Section 6. Here, we observe again an almost integer occupation on the  $d_{xy/z^2}$  orbitals within the

density–density approximation, probably due to an overestimation of the correlation strength on these two orbitals, similar to Co/Cu(001) within the same approximation to the Coulomb interaction.

## 7.4. Conclusion

Although the density-density approximation to the Coulomb tensor has been successfully applied to a wide range of systems in the literature [125, 226–228], our results suggest that it fails in describing the Kondo properties at the example of Co/Ag(001). In this system, the self-energy ( $\text{Im}\Sigma(\omega_n)$ ) depends delicately on the value of the double counting (and thus on the total occupation  $n_d$  on the Co  $3d$  shell), which is challenging because the exact DC value is unknown, and small changes have a strong impact on the results. Comparing this with Co/Cu(001) (Section 6), one could assume that the reason for the lacking Kondo resonance is of the same origin, that is the density-density approximation to the Coulomb tensor leading to an overestimation of the electron correlation strength on the Co  $d_{xy}/d_{z^2}$  orbitals.

In order to identify the origin of the lacking Kondo resonance in Co/Ag(001) within this study, more work is required on comparing results obtained by using the density–density approximation with using all matrix elements of the Coulomb tensor (in a similar way as in Section 6). Furthermore, it would be of importance to treat other transition metal atoms on Ag(001) within low-temperature CT-QMC calculations (and a simultaneous comparison of different interaction schemes), to see whether they are similarly affected by approximating the Coulomb part in the AIM, as in the cases of Co on Ag(001) and Cu(001).

# 8. $\text{Co}(\text{CO})_n/\text{Cu}(001)$ : Towards understanding chemical control of the Kondo effect

---

Published: Marc Philipp Bahlke, Peter Wahl, Lars Diekhöner and Carmen Herrmann,  
*J. Appl. Phys.* **2019**, 125, 142910.

---

## 8.1. Introduction

In this part, we would like to focus on the effect molecular ligands on the Kondo effect. Wahl *et al.* [1] have shown that the coupling of the local moment on a Co atom to the conduction band electrons of a Cu(001) substrate can be enhanced by attaching CO ligands to the Co atom (forming  $\text{Co}(\text{CO})_n$  complexes), by extracting the Kondo temperature from STS experiments. The number of CO ligands might not only affect the hybridization of the Co atom, but will also change the splitting of the  $3d$  shell, as a consequence of the different symmetries of the complexes. For  $n = 2$ , a four-fold symmetry was found in the scanning tunneling microscopy (STM), which is due to a thermally induced rotation of the intrinsically two-fold symmetric adsorbate on Cu(001), which happens on a faster time scale than what the STM can resolve.  $\text{Co}(\text{CO})_3/\text{Cu}(001)$  is observed to have no rotational ( $C_{3v}$ ) symmetry, whereas the complex with four ligands exhibits  $C_{4v}$  symmetry (which could result both from an intrinsically  $C_{4v}$ -symmetric structure or from a rotating  $C_{2v}$ -symmetric one with two opposing ligands being closer to the surface than the other two). The Kondo temperatures  $T_K$ , as extracted from a Fano fit of the STS spectra, increase with the number of CO ligands:  $165 \pm 21$  K ( $n =$

2),  $170 \pm 16$  K ( $n = 3$ ) and  $283 \pm 36$  K ( $n = 4$ ) [1]. We want to gain insight into this behavior as a step towards establishing structure–property relationships for the Kondo effect, by solving the Anderson impurity model parametrized by Kohn–Sham density functional theory (DFT++). In doing so, we will point out how shortcomings in present-day first-principles electronic-structure methods when predicting the atomistic structures of adsorbates on surfaces can strongly affect predicted Kondo properties. This is particularly relevant for systems with CO ligands, since interaction of CO with metal surfaces poses a challenge to electronic structure methods (“CO-puzzle”) [229].

## 8.2. Computational methodology

In DFT, a proper choice of the exchange–correlation functional is crucial for the optimization of molecular structures on surfaces, because it needs to describe the electronic structure of the surface, as well as of the adsorbate correctly, to predict accurate adsorption distances, angles, adsorption sites and symmetries. For the description of molecular adsorbates, it usually requires a large number of atoms in the unit cell, which is why one often chooses local density approximation (LDA) and general gradient approximation (GGA) type exchange–correlation functionals, as they are a good compromise between accuracy and computational effort in practice. These classes of exchange–correlation functionals are problematic for the description of the CO ligands, due to an underestimated gap between the highest occupied and the lowest unoccupied molecular orbital (HOMO and LUMO). This contributes to the well-known problem of DFT in predicting the correct adsorption sites of CO molecules on different metal substrates, which is known as the “CO-puzzle” [229] in the literature [115,230]. In the following, we give a brief overview of attempts to overcome this puzzling challenge by using DFT.

The work of Alaei *et al.* [231] shows that using BLYP (a GGA functional) can at least solve the problem of predicting the correct adsorption sites for CO on some metal substrates, such as Rh(111), Pt(111) and Cu(111), but without solving the problem of the underestimated HOMO-LUMO gap of a CO molecule. On the other hand, the work of Favot *et al.* [232] shows that PBE (a GGA functional) is able to predict the correct adsorption site of CO on a Cu(001) surface. A more systematic improvement can be reached by taking into account non-local correlation effects [233], as in the scope of the van der Waals-density functional (vdW-DF with revPBE) developed by Dion *et al.* [234], although its generalizations to spin-polarized systems [235,236] are not broadly available in electronic structure codes

(for a great overview of recent progress in the “CO-puzzle”, see Ref. [237]). Therefore, we focus on spin-polarized PBE and BLYP here for structure optimizations, including their DFT+ $U$  variants as we have found this to mimic the effect of strong correlation on adsorption distances [204]. Furthermore, we applied Grimme’s dispersion correction (DFT-D3) in all cases [238, 239]. In addition, a brief summary of the atomistic structures of the carbonyl cobalt complexes as obtained from non-local exchange–correlation functionals is given in the appendix (Section A.3.2).

All Kohn–Sham DFT calculations were performed with the Vienna Ab initio Simulation Package (VASP) using the projector augmented-wave method [174, 175], for which we set the kinetic energy cutoff for the plane wave single-particle basis to 400 eV. For the carbonyl cobalt complexes under study here, we modeled the Cu(001) surface by a super cell size of  $4\times 4$  Cu atoms with five Cu layers in total. It was found that structural relaxation using a  $k$ -grid of  $4\times 4\times 1$  yields no improvement over a grid size of  $2\times 2\times 1$ , for which reasons we chose the latter for all optimization protocols applied here. The convergence criteria for the self-consistent field algorithm was set to  $2.7\cdot 10^{-5}$  eV, and  $0.027$  eV/Å for the force acting on each atom. In addition to the adsorbates, we allowed the two topmost Cu layers to be relaxed, and also the cell shape (i.e. the lattice parameter). The relaxed lattice parameter is 3.48–3.49 Å for all systems under investigation, consistently for all optimization protocols. In addition, we optimized the systems (adsorbate and the two topmost Cu layers) with a fixed lattice parameter of 3.615 Å [206], which is denoted by the index “fix”. For DFT+ $U$ , we used an on-site Coulomb potential of  $U = 4.0$  eV and  $J = 0.9$  eV applied on the Co  $3d$  orbitals.

The electronic structure of the optimized carbonyl cobalt complexes on Cu(001) was then analyzed with a combination of density functional theory and the Anderson impurity model, using the numerically exact CT-HYB method [136, 138], as implemented in IQIST [139]. For this purpose, we calculated the electronic structure with spin-unpolarized DFT (as usual in the literature and discussed in Section 4.4.3) using the PBE exchange–correlation functional and a  $k$ -grid of  $17\times 17\times 1$  centered around the  $\Gamma$ -point (it was found that this grid size is sufficient up to inverse temperatures  $\beta = 150$  eV $^{-1}$ ).

The Coulomb term of Equation (3.39) is described within the density–density approximation, parameterized by the Slater integrals [92, 122]  $F^0$ ,  $F^2$ , and  $F^4$  for which we used the average Coulomb interaction parameter  $U$  ( $F^0 = 4.0$  eV) and the exchange-interaction parameter  $J = 0.9$  eV ( $J = \frac{1}{14}(F^2 + F^4) = 0.9$  eV with  $\frac{F^4}{F^2} = 0.625$ ). For taking into account the double-counting of the electron correlation already captured in the framework of DFT, we applied the fully localized limit [114, 116, 117] as introduced in Section 3.6.2.

### 8.3. Atomistic structure of $\text{Co}(\text{CO})_n$ on $\text{Cu}(001)$

From the experimental site of view, it is difficult to obtain detailed information about bond lengths, bond angles, and adsorption distances of the carbonyl complexes. At the same time, as discussed above, metal surfaces with molecular adsorbates in general and with adsorbed CO in particular are challenging for present-day first-principles methods.

To address this problem, we have optimized all carbonyl cobalt complexes with PBE-D3 and BLYP-D3, with and without  $U$  correction, as well as the non-local correlation functionals (which were only applied to the tetra carbonyl species) vdW-DF [234] and vdW-DF2 [240]. In some cases we also compared the results of keeping the lattice parameters fixed (for this we use the index “fix”) with the results as obtained by relaxing the cell shape together with the atomic positions of the carbonyl complexes (and the surface atoms of the first two layers, see Section 8.2 for further details). In the following, we briefly summarize the most important observations about the structures of the carbonyl cobalt complexes on  $\text{Cu}(001)$ , while detailed information about the structural parameters can be found in Section A.3.1.

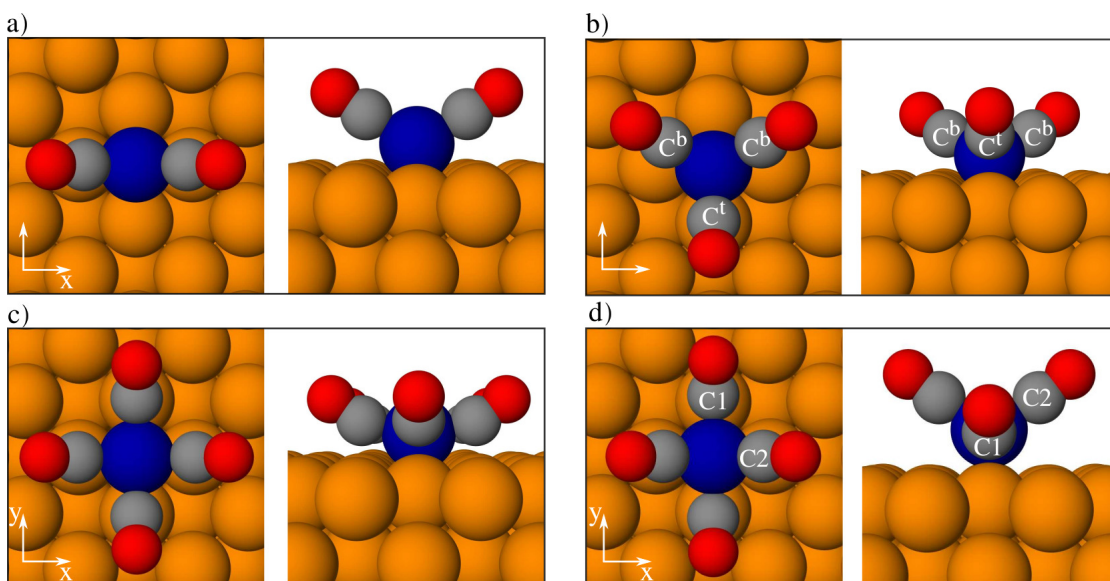


Figure 8.1.: a)  $\text{Co}(\text{CO})_2$ , b)  $\text{Co}(\text{CO})_3$ , c)  $\text{Co}(\text{CO})_4$  on  $\text{Cu}(100)$  ( $C_{4v}$ ) and d)  $\text{Co}(\text{CO})_4$  on  $\text{Cu}(100)$  ( $C_{2v}$ ) as obtained from BLYP-D3+ $U$ . We labeled the carbon atoms for  $\text{Co}(\text{CO})_3$  and  $\text{Co}(\text{CO})_4$  on  $\text{Cu}(100)$  ( $C_{2v}$ , according to the two symmetrically different CO ligands).

### 8.3.1. $\text{Co}(\text{CO})_2/\text{Cu}(001)$

For  $\text{Co}(\text{CO})_2/\text{Cu}(001)$ , one consistently obtains  $C_{2v}$  symmetry for all exchange–correlation functionals mentioned above, which is in agreement with Ref. [1]. It can also be confirmed that the rotational barrier of  $\text{Co}(\text{CO})_2/\text{Cu}(001)$  is rather low ( $6.4 \text{ kJ/mol} = 66 \text{ meV}$  as obtained from  $\text{PBE}_{\text{fix}}\text{-D3}$ ), which would support the observation of Wahl *et al.* [1] that this molecule is rotating faster than the STM time resolution on  $\text{Cu}(001)$  in the experimentally accessible temperature range.

Given that present-day approximate DFT has problems to describe the Kondo screening of the magnetic moment, we would expect to obtain a non-zero magnetic moment from spin-polarized DFT optimizations for systems showing a Kondo effect. However, we do not find such a magnetic moment on the adsorbate when using  $\text{PBE-D3}$  and  $\text{BLYP-D3}$ , both for the optimizations including and excluding the cell shape. When we apply a Hubbard  $U$  correction on the Co atom for  $\text{BLYP-D3}$ , we do obtain a magnetic moment of  $1.0 \mu_{\text{B}}$  on the Co atom of  $\text{Co}(\text{CO})_2/\text{Cu}(001)$  when we include the cell shape relaxation in the optimization protocol. As shown in Table 8.1, this has consequences for the adsorption distance as indicated by the increased Co–surface distance  $d_{\text{Co-surf.}}$  compared with the  $\text{BLYP-D3}$  optimized structure. A similar increase of the adsorption distance can be observed as a result of cell shape relaxation, as suggested by comparing the values for  $\text{BLYP-D3}_{\text{fix}}$  ( $1.39 \text{ \AA}$ ) and  $\text{BLYP-D3}$  ( $1.60 \text{ \AA}$ ). This might come from the slightly reduced lattice parameter (see Section 8.2) in cases with cell shape optimization, which effectively decreases the size of the four-fold hollow position and thus increases the adsorbate–surface distance. We will later show that there is a delicate dependence on the Kondo properties obtained from  $\text{DFT++}$  on the adsorption distance.

### 8.3.2. $\text{Co}(\text{CO})_3/\text{Cu}(001)$

The DFT-predicted symmetry of  $\text{Co}(\text{CO})_3/\text{Cu}(001)$  in this study differs from the one reported in Ref. [1] for all exchange–correlation functionals under study. Here, we obtain a rather  $C_{3v}$ -like<sup>1</sup> symmetry of the molecule (see Fig. 8.1), whereas in Ref. [1], the experimental structure suggests no such rotational symmetry. Of course one may argue whether the STM results (Fig. 1 in Ref. [1]) clearly exclude  $C_{3v}$  symmetry. However, since our optimized structures do not appear consistent with these data, and since we could not find Kondo features in the  $\text{DFT++}$  data

---

<sup>1</sup>It is actually not a perfect  $C_{3v}$  symmetry, because the two CO ligands in a bridged position (with respect to the  $\text{Cu}(001)$  surface) have slightly different structural parameters, compared to the one in top position.

(see below for further discussion) for any of these structures, we assume that the range of DFT variants employed here is not capable of describing the tricarbonyl structure reliably, and will not focus on it any further within the scope of this work (see Section A.3 for more details).

Table 8.1.: Adsorption distances of the carbonyl cobalt complexes on  $\text{Cu}(001)$  in Å as obtained from different optimizations. The index “fix” is used in cases where the experimental lattice constant was used. In all cases Grimme’s dispersion correction (DFT-D3) was applied.

	PBE <sub>fix</sub>	PBE	BLYP <sub>fix</sub>	BLYP	BLYP+U
Co (isolated)	1.46	-	-	-	1.78
Co(CO) <sub>2</sub>	1.33	1.54	1.39	1.60	1.74
Co(CO) <sub>3</sub>	1.58	-	1.66	1.75	1.76
Co(CO) <sub>4</sub> ( $C_{2v}$ )	1.90	-	-	2.07	2.26
Co(CO) <sub>4</sub> ( $C_{4v}$ )	1.69	-	-	1.89	1.85

### 8.3.3. $\text{Co}(\text{CO})_4/\text{Cu}(001)$

In the case of  $\text{Co}(\text{CO})_4/\text{Cu}(001)$ , it is challenging to obtain a four-fold ( $C_{4v}$ )-symmetric structure as suggested by the STM experiments of Wahl *et al.* [1], because in all attempts to optimize the structure the two-fold ( $C_{2v}$ ) symmetry was found to be lower in energy by about 30.2 kJ/mol (PBE<sub>fix</sub>-D3) to 42.1 kJ/mol (BLYP-D3+U). The non-local correlation functionals vdw-DF [234] and vW-DF2 [240] (with a fixed lattice constant) predicts the  $C_{2v}$  symmetry to be 70.4-73.3 kJ/mol lower in energy as compared to the  $C_{4v}$  symmetry. The rotational barrier of the molecule (as obtained for the PBE<sub>fix</sub>-D3 structure) in  $C_{2v}$  symmetry is 20 kJ/mol (0.21 eV), which suggests that a hypothetical rotation of this molecule in the STM experiments by Wahl *et al.* (taken at  $T = 6$  K) is not responsible for the observed  $C_{4v}$  symmetry. In addition to that, we can exclude a flipping mechanism of the CO ligands to mimic a  $C_{4v}$  symmetry in the STM experiments, due to an energy barrier larger than 80 kJ/mol (see Section A.3.3).

In the experiment, the preparation of the carbonyl complexes was done by first depositing cobalt on  $\text{Cu}(001)$ , and then saturating the surface with CO molecules. DFT (BLYP+U) suggests a rather short adsorption distance (Table 8.1) of an isolated Co on  $\text{Cu}(001)$  (1.78 Å), which is closer to the tetracarbonyl in  $C_{4v}$  symmetry (1.85 Å) than to the one in  $C_{2v}$  symmetry (2.26 Å). It is conceivable that

the formation of the  $C_{4v}$ -symmetric system is kinetically favored, due to the adsorption distance being closer to that of an isolated Co on Cu(001). Although the sample was annealed to  $T = 200\text{-}300$  K, the formation of the probably more stable  $C_{2v}$  structure (as suggested by DFT) may be inhibited.

In the DFT and DFT+ $U$  calculations, we again do not obtain a local magnetic moment on  $\text{Co}(\text{CO})_4/\text{Cu}(001)$  in both symmetries. For the  $C_{4v}$  symmetry (BLYP-D3+ $U$ ), it was also tested to obtain a magnetic moment by increasing the adsorption distance by about  $0.4 \text{ \AA}$ , which should favor the formation of a local moment similarly to a stretched  $\text{H}_2$  (see discussion in Section 4.3). However, no magnetic moment could be observed in this case. These observations could make an interpretation in terms of a Kondo effect difficult, but as we will see later, it is indeed possible to identify features in the DFT++ electronic structure for  $\text{Co}(\text{CO})_4/\text{Cu}(001)$  in  $C_{4v}$  symmetry which are in agreement with the experimentally observed Kondo effect. For the corresponding  $C_{2v}$  symmetry, no Kondo properties could be found, suggesting that only the  $C_{4v}$  symmetry is consistent with the experimental observations.

## 8.4. Kondo properties of $\text{Co}(\text{CO})_n/\text{Cu}(001)$

In the following, we will focus on the structures optimized with BLYP-D3+ $U$  (with optimization of the cell shape), since these show a non-zero local moment on the Co atom for the dicarbonyl complex. For  $\text{Co}(\text{CO})_4$  on Cu(001), we limit the discussion to the  $C_{4v}$  structure, because it fits to the experimentally observed symmetry (see Figure 1 of Ref. [1]), and allows for an interpretation in terms of a Kondo effect (see below). For these structures, we parametrize the AIM with closed-shell PBE, in order to correctly describe the non-magnetic character of the Cu(001) surface (and thus the coupling of the Co  $3d$  orbitals with a non-magnetic metal).

As the Kondo effect manifests itself as a sharp feature in the spectral function at the Fermi energy, we aim at identifying the relevant Co  $3d$  orbitals that might contribute to the experimentally observed zero-bias anomaly from the spectral functions of the individual orbitals [1]. Nozières [43] showed that a Kondo effect can be described within the Fermi liquid theory. We will use this to identify the transition point to the Fermi liquid regime, as an approximated value for the Kondo temperature  $T_K$ . Therefore, we will analyze the temperature dependence of the spin-spin correlation function  $\chi(\tau)$  at the special value  $\tau = \beta/2$ , which should behave as  $T^2$  in the Fermi liquid regime. Furthermore, we investigate the so-called first Matsubara-frequency rule [145], which states that  $\text{Im}\Sigma(\omega_0)$  should go linearly

to zero as  $T \rightarrow 0$  K, as another tool for probing the Fermi liquid properties of the di- and tetracarbonyl systems.

### 8.4.1. Spectral properties of $\text{Co}(\text{CO})_n/\text{Cu}(001)$

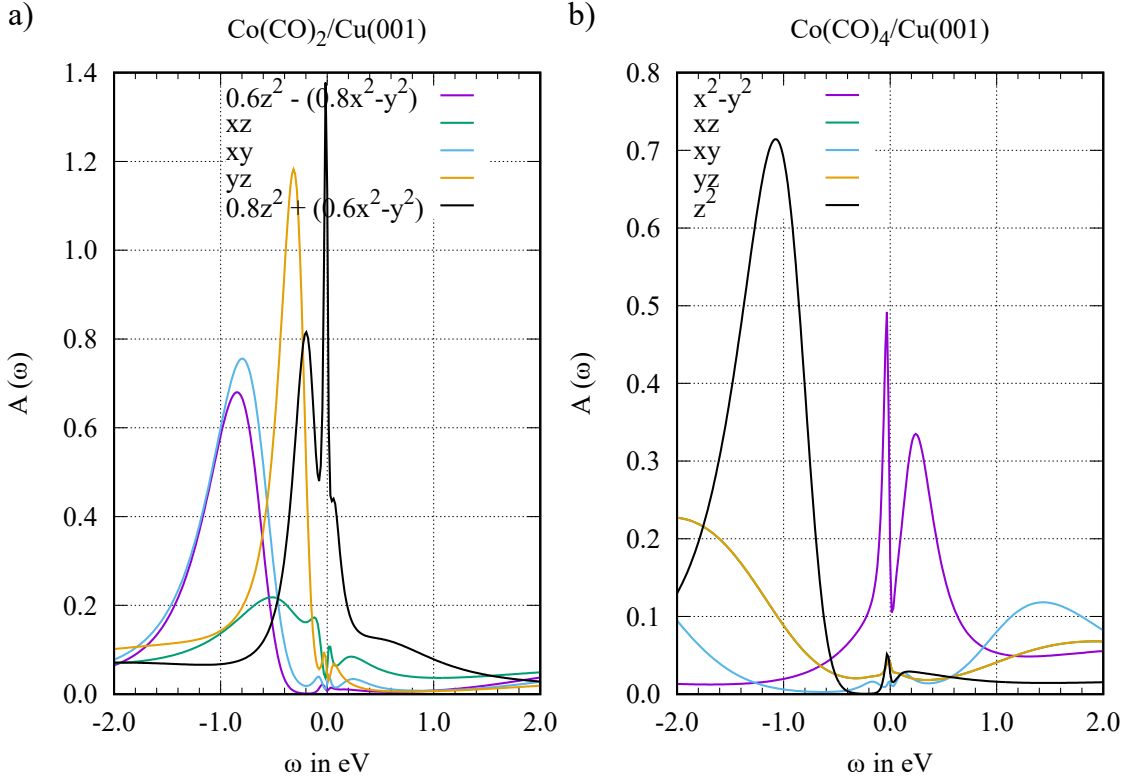


Figure 8.2.: Spectral functions as obtained from PBE++ for a)  $\text{Co}(\text{CO})_2$  and b)  $\text{Co}(\text{CO})_4$  on  $\text{Cu}(100)$  at  $\beta = 100 \text{ eV}^{-1}$  ( $T = 116 \text{ K}$ ). Here the fully localized limit was used for estimating the DC, and we chose  $U = 4.0 \text{ eV}$  and  $J = 0.9 \text{ eV}$ . In case of the notations  $0.6z^2 - 0.8(x^2 - y^2)$  and  $0.8z^2 + 0.6(x^2 - y^2)$ , the Co  $d_{z^2}$  and  $d_{x^2-y^2}$  orbitals are mixed after diagonalization of the Co  $3d$  sub-space.

In Figure 8.2, all Co  $3d$  spectral functions of  $\text{Co}(\text{CO})_2$  and  $\text{Co}(\text{CO})_4$  on  $\text{Cu}(100)$  are shown at  $T = 116 \text{ K}$ . Note that due to diagonalization of the Co  $3d$  subspace, some of the Co  $3d$  orbitals are mixed.  $\text{Co}(\text{CO})_2/\text{Cu}(001)$  (Figure 8.2 a)) shows a sharp feature at the Fermi energy ( $\omega = 0 \text{ eV}$ ) for the Co  $3d_{0.8z^2+0.6(x^2-y^2)}$  orbital, whereas the remaining Co  $3d$  orbitals only have broader features below the Fermi energy (in the energy range shown here). The sharp feature of this orbital thus

makes it a promising candidate for causing the experimentally observed Kondo effect, which will be further investigated in terms of its Fermi liquid properties later on. This is an interesting contrast to the bare Co atom on Cu(001), where (at least at relatively large temperature) it is likely the  $d_{z^2}$  orbital which is causing the Kondo properties<sup>2</sup>.

In the case of  $\text{Co}(\text{CO})_4/\text{Cu}(001)$  in  $C_{4v}$  symmetry, we would like to re-emphasize that DFT (using GGA-type functionals) predicts a magnetic moment of  $0.0 \mu_B$  on the Co atom. Nonetheless, the spectral function of  $\text{Co}(\text{CO})_4/\text{Cu}(001)$  obtained from DFT++ (Figure 8.2 b)) shows a sharp feature at the Fermi energy for the Co  $3d_{z^2}$  orbital. Based on this observation, there is reason to believe that DFT++ predicts a finite local moment on the Co atom of  $\text{Co}(\text{CO})_4/\text{Cu}(001)$  in this orbital, which is probably screened due to a Kondo effect and thus leading to the sharp feature in the spectral function, as we will confirm later. Due to the  $C_{4v}$  symmetry,  $\text{Co}(\text{CO})_4/\text{Cu}(001)$  would be a promising candidate for a so-called orbital Kondo effect (similar as reported for cobalt-benzene sandwich molecules [176]), because it has two degenerate orbitals ( $d_{xz/yz}$ ). However, the lack of a resonance at the Fermi energy for these orbitals suggests that this is not the case.

To conclude, for  $\text{Co}(\text{CO})_2/\text{Cu}(001)$  and  $\text{Co}(\text{CO})_4/\text{Cu}(001)$  ( $C_{4v}$ ), we could identify a sharp, Kondo-like feature at the Fermi energy, which gives us the opportunity to investigate the increasing Kondo temperature with an increasing number of CO ligands, for answering the question of how the Kondo effect can be chemically controlled.

### 8.4.2. Fermi liquid properties of $\text{Co}(\text{CO})_n/\text{Cu}(001)$

We study the Fermi liquid properties to probe the existence of a Kondo effect as suggested by the spectral functions for  $\text{Co}(\text{CO})_2$  and for  $\text{Co}(\text{CO})_4$  in  $C_{4v}$  symmetry.

#### 8.4.2.1. Spin–spin correlation function at high temperatures: Is there a magnetic moment to be screened?

First, we consider the spin–spin correlation functions of the carbonyl cobalt complexes in Figure 8.3. Here,  $\chi(\tau)$  is shown at  $T = 1160$  K, because we expect that at this temperature, no Kondo screening takes place, and a finite local moment

---

<sup>2</sup>It has been argued that a second orbital may be contributing to the Kondo properties of Co/Cu(001) at temperatures too low to be reached with the methodology employed here [111, 199]

should be observed. For  $\text{Co}(\text{CO})_2/\text{Cu}(001)$ ,  $\chi(\tau)$  of the  $3d_{0.8z^2+0.6(x^2-y^2)}$  and  $3d_{yz}$  orbitals drops to a non-zero value as  $\tau \rightarrow \beta/2$ , suggesting a persisting spin-density in these orbitals. Most of the magnetic moment observed for  $\text{Co}(\text{CO})_2/\text{Cu}(001)$  is located in the Co  $3d_{0.8z^2+0.6(x^2-y^2)}$  orbital, as suggested by the larger value at  $\chi(\beta/2)$ . This observation suggests that the feature at  $\omega = 0.0$  eV in the spectral function of the Co  $3d_{0.8z^2+0.6(x^2-y^2)}$  orbital is indeed a signature of a Kondo effect.

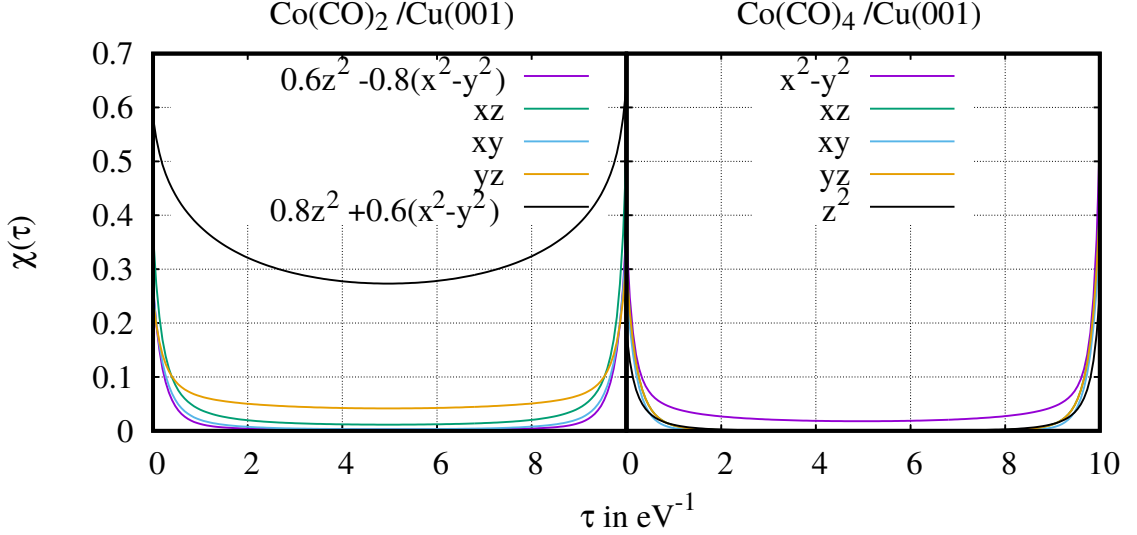


Figure 8.3.: Spin-spin correlation function  $\chi(\tau)$  as obtained from PBE++ at  $\beta = 10 \text{ eV}^{-1}$  ( $T = 1160 \text{ K}$ ) of all carbonyl cobalt complexes on  $\text{Cu}(001)$  under consideration here. The PBE++ calculation was done with  $U = 4.0 \text{ eV}$ ,  $J = 0.9 \text{ eV}$ , and using the fully localized limit for estimation the double-counting correction.

For  $\text{Co}(\text{CO})_4/\text{Cu}(001)$  ( $C_{4v}$ ), only the Co  $3d_{x^2-y^2}$  orbital shows a finite value of  $\chi(\beta/2)$  at  $T = 1160 \text{ K}$  (Figure 8.3), which is the same orbital contributing spectral weight at  $\omega = 0.0 \text{ eV}$  in form of a sharp feature. Thus, this orbital is a promising candidate for causing the observed Kondo effect in  $\text{Co}(\text{CO})_4/\text{Cu}(001)$ . For the  $C_{2v}$  symmetry, we observe that  $\chi(\beta/2)$  drops to zero for all Co  $3d$  orbitals, similar as for  $\text{Co}(\text{CO})_3/\text{Cu}(001)$  (see Section A.3.5).

To summarize, we were able to identify promising candidates for Kondo-relevant orbitals for  $\text{Co}(\text{CO})_2/\text{Cu}(001)$  ( $3d_{0.8z^2+0.6(x^2-y^2)}$ ) and  $\text{Co}(\text{CO})_4/\text{Cu}(001)$  in  $C_{4v}$  symmetry ( $3d_{x^2-y^2}$ ) from the spectral and spin-spin correlation functions.

8.4.2.2. Temperature dependence of  $\chi(\beta/2)$

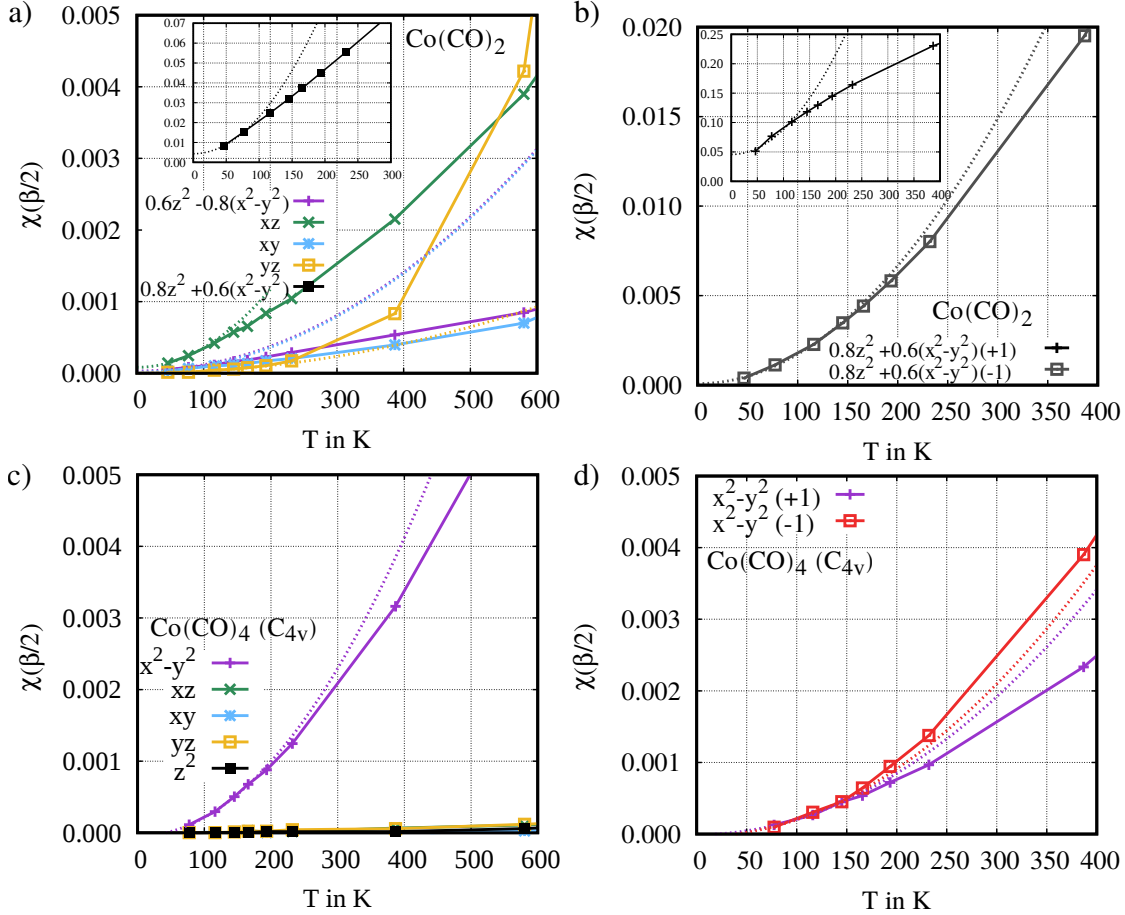


Figure 8.4.: a)  $\chi(\beta/2)$  as a function of  $T$  for all Co 3d orbitals of  $\text{Co}(\text{CO})_2/\text{Cu}(001)$  by using the fully localized limit for the double-counting correction. b)  $\chi(\beta/2)$  as a function of  $T$  for the Co  $3d_{0.8z^2+0.6(x^2-y^2)}$  orbital of  $\text{Co}(\text{CO})_2/\text{Cu}(001)$  Here the value of the double-counting was shifted by  $\pm 1.0$  eV with respect to the FLL value  $E_{\text{DC}}^{\text{FLL}}$ . c)  $\chi(\beta/2)$  as a function of  $T$  for all Co 3d orbitals of  $\text{Co}(\text{CO})_4/\text{Cu}(001)$  ( $C_{4v}$ ) by using the fully localized limit for the double-counting correction. b)  $\chi(\beta/2)$  as a function of  $T$  for the Co  $3d_{x^2-y^2}$  orbital of  $\text{Co}(\text{CO})_4/\text{Cu}(001)$  ( $C_{4v}$ ) Here the value of the double-counting was shifted by  $\pm 1.0$  eV with respect to the FLL value. The fits are quadratic fits of the first two data points. Note that the fits are meant as a guide for the eye to check whether the Fermi-liquid behavior is fulfilled or not.

As mentioned in Section 3.7.5, the Fermi liquid behavior is manifested as a  $T^2$  dependence of  $\chi(\beta/2)$ . In Figure 8.4 a), we study this behavior for all Co 3d orbitals of  $\text{Co}(\text{CO})_2/\text{Cu}(001)$  as obtained within the fully localized limit. In all cases  $\chi(\beta/2)$  drops as  $T$  is lowered, presumably approaching zero as  $T \rightarrow 0$  K. For the Kondo-relevant orbital  $3d_{0.8z^2+0.6(x^2-y^2)}$ , one does not observe  $T^2$  dependence (and thus no Fermi liquid behavior), due to the non-zero intercept with the ordinate. A better agreement within a Fermi liquid behavior can be observed by shifting the DC value by  $-1.0$  eV from the original FLL value  $E_{\text{DC}}^{\text{FLL}}$  (Figure 8.4 b)), which increases the occupation of the  $3d_{0.8z^2+0.6(x^2-y^2)}$  orbital from 1.31 (FLL) to 1.49 electrons (see Figure 8.5).

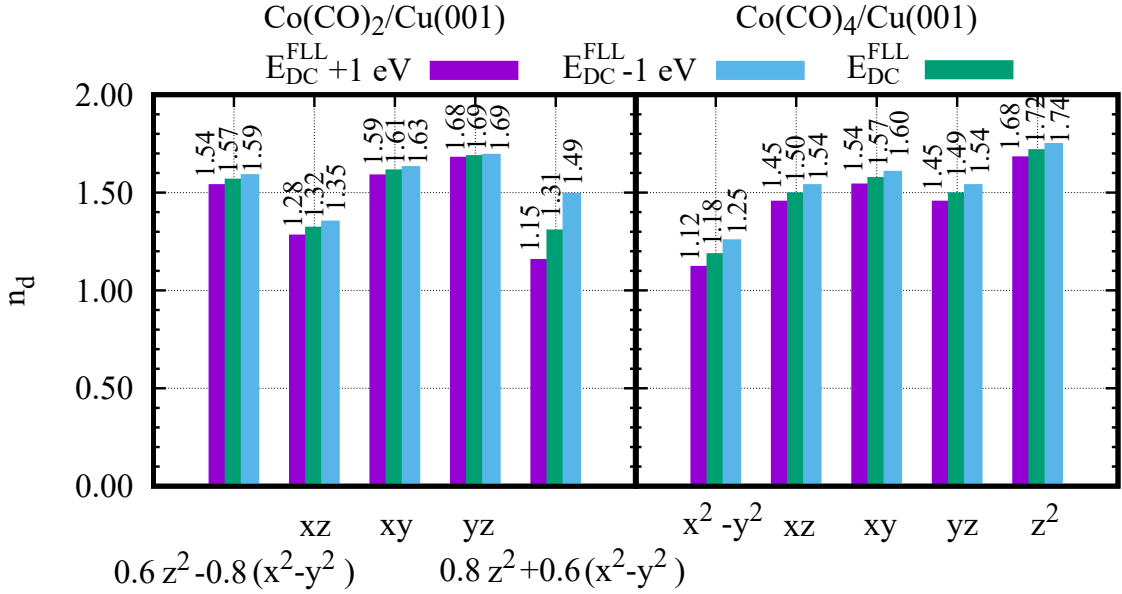


Figure 8.5.: Co 3d fillings of  $\text{Co}(\text{CO})_2$  and  $\text{Co}(\text{CO})_4$  on  $\text{Cu}(001)$  as obtained from PBE++ at  $\beta = 100 \text{ eV}^{-1}$  for different values of the double-counting correction.  $E_{\text{DC}}^{\text{FLL}}$  is the value as obtained from Equation (3.38). Total Co 3d occupations:  $n_d(E_{\text{DC}}^{\text{FLL}} + 1 \text{ eV}) = 7.24$ ,  $n_d(E_{\text{DC}}^{\text{FLL}}) = 7.47$ ,  $n_d(E_{\text{DC}}^{\text{FLL}} - 1 \text{ eV}) = 7.67$ .

Here one observes that the  $3d_{0.8z^2+0.6(x^2-y^2)}$  orbital of  $\text{Co}(\text{CO})_2/\text{Cu}(001)$  behaves quadratically in  $T$  below  $T = 150$  K. Shifting the DC value by  $+1.0$  eV from the original FLL value, the filling in the  $3d_{0.8z^2+0.6(x^2-y^2)}$  orbital reduces to 1.15 electrons, and the values of  $\chi(\beta/2)$  are significantly increased as compared to the results obtained within the FLL. The sensitivity of  $\chi(\beta/2)$  to the shift of the DC value comes from the fact that the occupation on the  $3d_{0.8z^2+0.6(x^2-y^2)}$  orbital of  $\text{Co}(\text{CO})_2/\text{Cu}(001)$  changes from 1.15 ( $E_{\text{DC}}^{\text{FLL}} + 1 \text{ eV}$ ) to 1.49 ( $E_{\text{DC}}^{\text{FLL}} - 1 \text{ eV}$ ), as

shown in Figure 8.5. This indicates that the charge fluctuations in this orbital are strongly increased when  $E_{\text{DC}}^{\text{FLL}}$  is shifted by  $-1$  eV. This leads to the observed transition to the Fermi liquid regime at roughly  $T = 150$  K, whereas for the other fillings under consideration here, it is not possible to see this transition for the temperature range considered.

In Figure 8.4 c), we depict  $\chi(\beta/2)$  as a function of  $T$  for  $\text{Co}(\text{CO})_4/\text{Cu}(001)$  ( $C_{4v}$ ) as obtained within the fully localized limit.  $\chi(\beta/2)$  of the Kondo-relevant orbital ( $3d_{x^2-y^2}$ ) behaves as  $T^2$  at temperatures below  $T = 165$  K, pointing to a transition to the Fermi liquid regime at this temperature. Shifting the DC by  $\pm 1$  eV with respect to the FLL value alters the temperature at which the transition to the Fermi liquid regime is observed only little (see Figure 8.4 d)). As one can see from Figure 8.5, this might be due to the fact that the filling on the  $3d_{x^2-y^2}$  orbital (1.12 ( $E_{\text{DC}}^{\text{FLL}} + 1$  eV)) to 1.25 ( $E_{\text{DC}}^{\text{FLL}} - 1$  eV)) electrons) is not affected as strongly as in the case of the  $3d_{0.8z^2+0.6(x^2-y^2)}$  orbital in  $\text{Co}(\text{CO})_2/\text{Cu}(001)$ .

#### 8.4.2.3. First Matsubara frequency rule

We find that a similar behavior of  $\text{Co}(\text{CO})_2/\text{Cu}(001)$  concerning the Fermi liquid properties can be found by considering the so-called first Matsubara-frequency rule depicted in Figure 8.6 a) and b). The only agreement with Fermi liquid behavior can be observed if  $E_{\text{DC}}^{\text{FLL}}$  is shifted by  $-1.0$  eV, as indicated by the linear behavior of  $\text{Im}\Sigma(\omega_0)$  as  $T \rightarrow 0$  K for temperatures below  $T = 150$  K. Thus, both  $\chi(\beta/2)$  and  $\text{Im}\Sigma(\omega_0)$  as a function of  $T$  lead us to conclude that the  $3d_{0.8z^2+0.6(x^2-y^2)}$  orbital behaves as a Fermi liquid, but the transition temperature strongly depends on the Co  $3d$  filling. Nevertheless, this gives further support to our initial conclusion that the sharp feature observed in the spectral function (Figure 8.2 a)) is a signature of a Kondo effect.

For  $\text{Co}(\text{CO})_4/\text{Cu}(001)$ , the first Matsubara-frequency rule (Figure 8.6 c) and d)) is also fulfilled for the  $3d_{x^2-y^2}$  orbital at all DC values under consideration here, and affirms furthermore the transition to the Fermi liquid regime roughly below  $T = 165$  K. This gives reason to believe that the observed feature at  $\omega = 0.0$  eV in the spectral function is a true Kondo signature.

#### 8.4.2.4. Discussion

To summarize, we could show that the Kondo-relevant orbitals of  $\text{Co}(\text{CO})_2/\text{Cu}(001)$  and  $\text{Co}(\text{CO})_4/\text{Cu}(001)$  ( $C_{4v}$ ) display the Fermi liquid properties expected for a

Kondo system. However, for  $\text{Co}(\text{CO})_2/\text{Cu}(001)$ , the transition temperature, or Kondo temperature, depends delicately on the choice of the double-counting value.

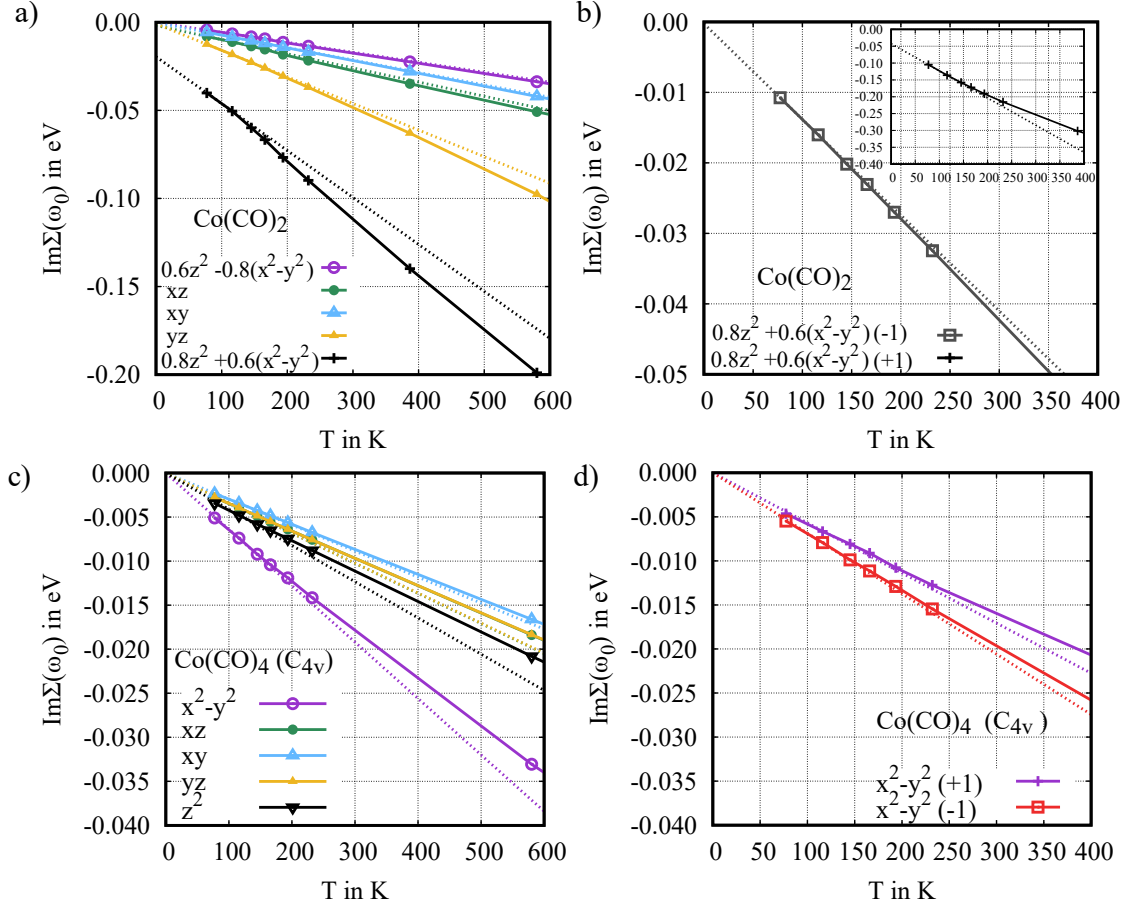


Figure 8.6.: a)  $\text{Im}\Sigma(\omega_0)$  as a function of  $T$  for all Co  $3d$  orbitals of  $\text{Co}(\text{CO})_2/\text{Cu}(001)$  as obtained by using the fully localized limit. b)  $\text{Im}\Sigma(\omega_0)$  as a function of  $T$  for the Co  $3d_{0.8z^2+0.6(x^2-y^2)}$  orbital of  $\text{Co}(\text{CO})_2/\text{Cu}(001)$ . Here the value of the double-counting was shifted by  $\pm 1.0$  eV with respect to the FLLvalue. c)  $\text{Im}\Sigma(\omega_0)$  as a function of  $T$  for all Co  $3d$  orbitals of  $\text{Co}(\text{CO})_4/\text{Cu}(001)$  ( $C_{4v}$ ) as obtained by using the fully localized limit. d)  $\text{Im}\Sigma(\omega_0)$  as a function of  $T$  for the Co  $3d_{x^2-y^2}$  orbital of  $\text{Co}(\text{CO})_4/\text{Cu}(001)$  ( $C_{4v}$ ). The fits in a)-d) are linear fits as a guide for the eye to check whether the Fermi-liquid behavior is fulfilled or not.

Within this work, it is only possible to see a transition to the Fermi liquid regime (at  $T = 150$  K) if the filling on the Co  $3d_{0.8z^2+0.6(x^2-y^2)}$  orbital is increased by

shifting the DC value by  $-1$  eV from the FLL value. By comparing the uncorrelated  $\langle n_\sigma \rangle \langle n_{\bar{\sigma}} \rangle$  and correlated double occupancies  $\langle n_\sigma n_{\bar{\sigma}} \rangle$  of the  $3d_{0.8z^2+0.6(x^2-y^2)}$  orbital, one finds that the difference between these quantities is larger by using the fully localized limit (0.074) compared to shifting it by  $-1$  eV (0.037). This suggests that in the FLL case the Kondo relevant orbital is more correlated, leading to the increased transition temperature to the Fermi liquid regime (similarly to what was found for  $\text{Co}/\text{Cu}(001)$  in Section 6).

In the case of  $\text{Co}(\text{CO})_4/\text{Cu}(001)$  ( $C_{4v}$ ), the transition to the Fermi-liquid regime is more robust against changes of the double-counting value, as confirmed unambiguously by  $\chi(\beta/2)$  and  $\text{Im}\Sigma(\omega_0)$  as a function of  $T$ . We find that for all DC values the transition to the Fermi-liquid regime of  $\text{Co}(\text{CO})_4/\text{Cu}(001)$  is at roughly  $T = 165$  K.

Concerning the question of how the Kondo effect is controlled by the number of CO ligands, one is now faced with the problem that the exact double-counting correction for both systems is unknown, and that the Kondo temperature of  $\text{Co}(\text{CO})_2/\text{Cu}(001)$  is only detectable (within the electronic temperatures reached here) if the value of the DC correction is shifted towards smaller values. However, comparing the Fermi liquid behavior of both systems as obtained from the fully localized limit  $\text{Co}(\text{CO})_4/\text{Cu}(001)$  has indeed a larger Kondo temperature than  $\text{Co}(\text{CO})_2/\text{Cu}(001)$  in qualitative agreement with the experimental data, since in the latter case the transition to the Fermi liquid regime occurs at temperatures lower than the ones considered here. Later, we will give an estimation of  $T_K$  based on the hybridization function of the  $\text{Co } 3d_{0.8z^2+0.6(x^2-y^2)}$  orbital in  $\text{Co}(\text{CO})_2/\text{Cu}(001)$ , which confirms this assumption.

### 8.4.3. Adsorbate-structure dependence of the local moment in $\text{Co}(\text{CO})_2$ on $\text{Cu}(001)$

In the context of the preceding section, one could ask how strongly the results for  $\text{Co}(\text{CO})_2/\text{Cu}(100)$  would change for a different molecular structure (see Section 8.3 for more details about how strongly structural parameters can vary depending on the computational parameters), as this might allow for a deeper insight into structure–property relations for the Kondo effect.

To investigate the dependence of the magnetization on the adsorption distance, we show the spin–spin correlation function at  $T = 1160$  K of the  $\text{Co } 3d_{0.8z^2+0.6(x^2-y^2)}$  orbital for selected structures (Figure 8.7). For the BLYP-D3 and PBE<sub>fix</sub>-D3-optimized structures,  $\chi(\tau)$  drops faster than for the BLYP-D3+ $U$ -optimized structure. This points to a stronger screening of the local moment if the adsorption

distance is decreased, suggesting a more weakly correlated nature at smaller distances, which agrees with what was reported for  $\text{Co}/\text{Cu}(001)$  [204]. At the same time the adsorption distance is increased, the bonding angle  $\phi_{\text{C-Co-C}}$  increases, too, from what one could suppose that the stronger screening depends on this angle. For the structures reported here, we can exclude that the spin-spin correlation function of the Co  $3d_{0.8z^2+0.6(x^2-y^2)}$  orbital is significantly affected by  $\phi_{\text{C-Co-C}}$  (see Section 8.4.3.1).

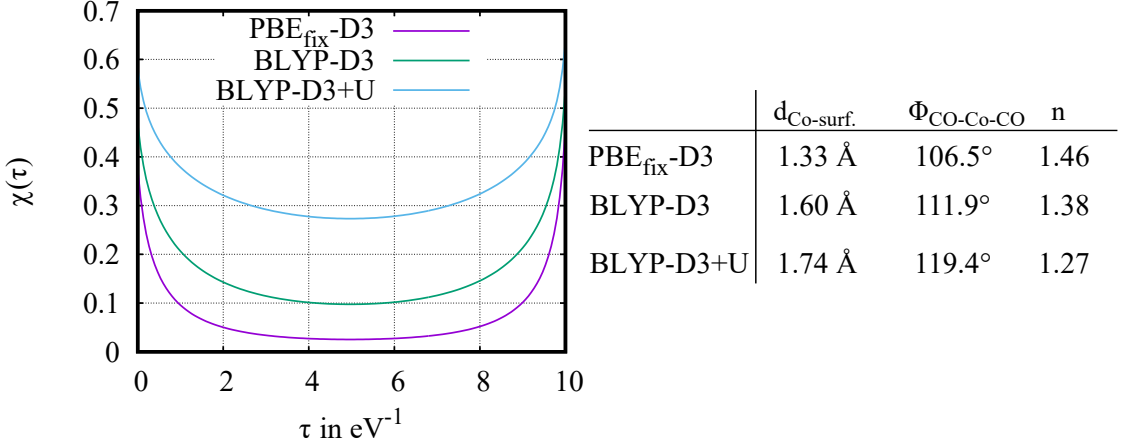


Figure 8.7.: a) Spin-Spin correlation  $\chi(\tau)$  as obtained from PBE++ at  $\beta = 10 \text{ eV}^{-1}$  ( $U = 4.0 \text{ eV}$  and  $J = 0.9 \text{ eV}$ ) of the Kondo-relevant orbital  $3d_{0.8z^2+0.6(x^2-y^2)}$  in  $\text{Co}(\text{CO})_2/\text{Cu}(001)$  for different optimized structures. b) Co-surface distance  $d_{\text{Co-surf.}}$ , C-Co-C bonding angle  $\phi_{\text{C-Co-C}}$  and  $3d_{0.8z^2+0.6(x^2-y^2)}$  filling  $n$  (PBE++) for  $\text{Co}(\text{CO})_2/\text{Cu}(001)$  as obtained from different structures.

The occupation of the Co  $3d_{0.8z^2+0.6(x^2-y^2)}$  orbital shows a delicate dependence on the structure, similar to its dependence on the DC value as shown for the BLYP-D3+ $U$  optimized structure. For this reason, it can be assumed that the transition to the Fermi-liquid regime is similarly affected by changes in the adsorption distance and the C-Co-C bonding angle, and therefore is very sensitive to the computational parameters with which the molecular adsorbates have been optimized. The structures under study here are likely a particularly challenging case because of their large structural flexibility (as opposed to more rigid phthalocyanines) and because of the challenges associated with describing CO binding to metal surfaces (“CO-puzzle”), as discussed in Section 8.3. These results also suggest that the Kondo effect in  $\text{Co}(\text{CO})_2/\text{Cu}(001)$  might be controllable via external stimuli affecting the adsorption distance (in particular, interactions between

STM tips and adsorbates), similarly to what has been reported for cobalt-benzene sandwich molecules bridged between two electrodes [241].

### 8.4.3.1. $\text{Co}(\text{CO})_2/\text{Cu}(001)$ : C-Co-C angle analysis

In this part, we take a brief look at the dependence of the high-temperature spin–spin correlation function and the hybridization function on the C-Co-C bonding angle  $\phi_{\text{C-Co-C}}$ . For this purpose,  $\text{Co}(\text{CO})_2$  molecules with different bonding angles were obtained by using the linear synchronous transit method [242] to interpolate structures between the optimized  $\text{Co}(\text{CO})_2/\text{Cu}(001)$  (BLYP-D3) and an artificially generated  $\text{Co}(\text{CO})_2$  by removing the two CO ligands from  $\text{Co}(\text{CO})_4/\text{Cu}(001)$  in  $C_{2v}$  symmetry (BLYP-D3), that are further away from the surface (marked as “C2” in Figure 8.1). In all cases, the obtained structures have an adsorption distance of 2.07 Å, which is the one as obtained from the BLYP-D3 optimized  $\text{Co}(\text{CO})_4/\text{Cu}(001)$  in  $C_{2v}$  symmetry.

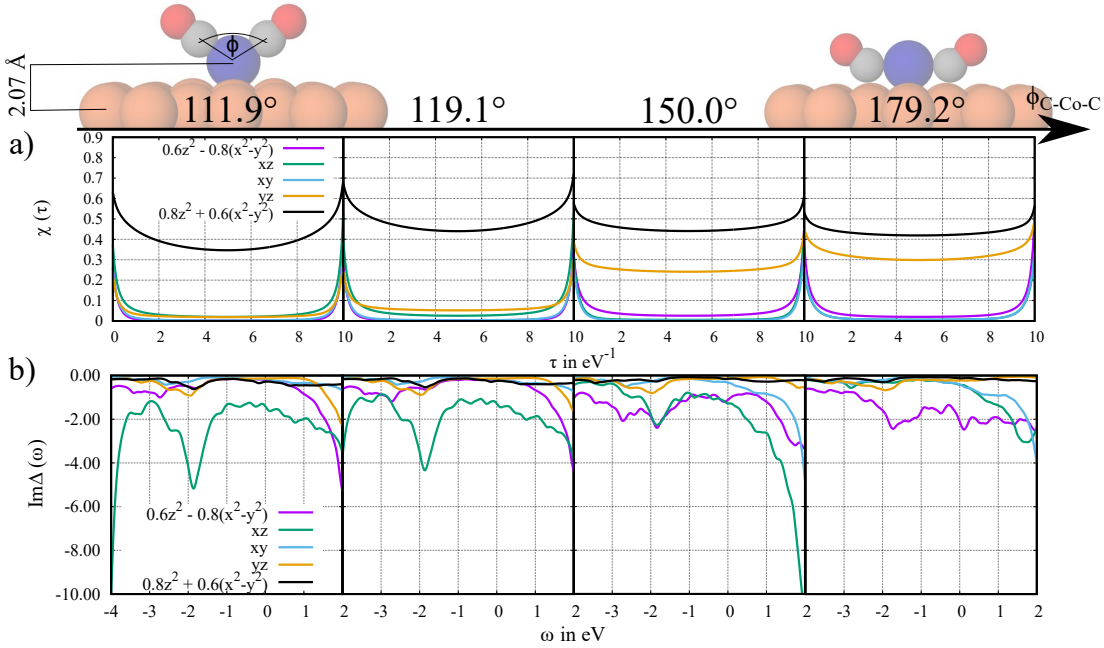


Figure 8.8.: a) Spin–spin correlation function at  $T = 1160$  K, as obtained from PBE++ for a dicarbonyl complex on Cu(001) with different C-Co-C bonding angles  $\phi_{\text{C-Co-C}}$ . b) Co 3d hybridization function as obtained from PBE for a dicarbonyl complex on Cu(001) with different C-Co-C bonding angles  $\phi_{\text{C-Co-C}}$ . For all calculations a Co-surface distance of 2.07 Å was used.

## 8.5. DFT-based analysis of the Kondo effect: What can we learn without solving the AIM?

---

The spin–spin correlation function at  $T = 1160$  K of the  $3d_{0.8z^2+0.6(x^2-y^2)}$  orbital depends only little on  $\phi_{\text{C-Co-C}}$ , as shown in Figure 8.8 a). If  $\phi_{\text{C-Co-C}}$  is increased to larger values than  $119^\circ$ , the  $d_{yz}$  orbital shows a localized magnetic moment, probably caused the increasing energy of this orbital at larger  $\phi_{\text{C-Co-C}}$ . However, such large bonding angles were not obtained for  $\text{Co}(\text{CO})_2/\text{Cu}(001)$  within the optimization protocols applied here.

The reason for the almost unaffected  $3d_{0.8z^2+0.6(x^2-y^2)}$ -spin–spin correlation function, could be that around the Fermi energy the hybridization function of this orbital (Figure 8.8 b)) is not sensitive to changes of the bonding angle. Whereas, the hybridization of the  $3d_{0.6z^2-0.8(x^2-y^2)}$  orbital in the vicinity of the Fermi energy increase as the bonding angle increases, which could probably be due to a stronger coupling of the CO ligands with the surface, and at the same time, due to a more appropriate coupling to this orbital (which exhibits more  $3d_{x^2-y^2}$  character as compared to the  $3d_{0.8z^2+0.6(x^2-y^2)}$  orbital).

## 8.5. DFT-based analysis of the Kondo effect: What can we learn without solving the AIM?

To gain further insight into the Kondo properties as obtained from solving the Anderson impurity model, it can be helpful to consider the spin-unpolarized PBE electronic structures, as they were used to parametrize the AIM (based on the BLYP-D3+ $U$  optimized structures).

In Figure 8.9, we show the projected density of states ( $-\frac{1}{\pi}\text{Im}g_i(\omega)$ ) of the Co  $3d$  orbitals, as well as the C  $2p$  local density of states (LDOS), which is the sum of the projected density of states of the C  $2p$  orbitals. They should exhibit peaks at the  $\sigma_2/\sigma_2^*$  and  $\pi/\pi^*$  orbitals of the CO ligands (a schematic representation of the molecular orbital diagram of an isolated CO molecule is provided in Section A.3.7). From this, one can learn which of the Co  $3d$  orbitals are interacting with the CO ligands, indicated by features in the Co  $3d$  PDOS at the same position as the C  $2p$  LDOS. This information might be useful to learn more about chemical control of the Kondo effect by increasing the number of CO ligands, as this will affect the coupling of the Co  $3d$  orbitals with the rest of the system.

For  $\text{Co}(\text{CO})_2/\text{Cu}(001)$ , the  $3d_{0.8z^2+0.6x^2-y^2}$  orbital shows only small features at the C  $2p$  LDOS, as a consequence of this orbital interacting only little with the CO ligands (as, e.g., compared to the  $3d_{xz}$  orbital). In contrast, the  $3d_{x^2-y^2}$  orbital in  $\text{Co}(\text{CO})_4$  ( $C_{4v}$ ) interacts with the CO ligands, as indicated by the features in the

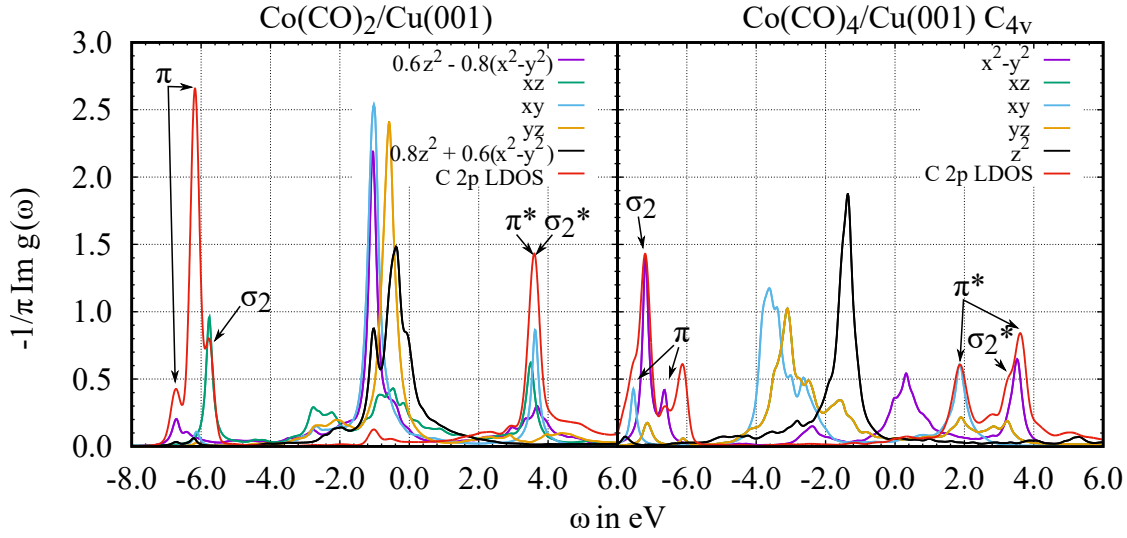


Figure 8.9.: Projected density of states of the Co  $3d$  orbitals ( $-\frac{1}{\pi}\text{Im } g_i(\omega)$ ), and local density of states of the  $2p$  orbitals (sum over all  $2p$  orbitals) of one of the C atoms. Results obtained from PBE (based on the BLYP-D3+ $U$  optimized structures).

PDOS at the position of the  $\sigma_2/\sigma_2^*$  orbitals of CO. This coupling might increase the Kondo temperature, as discussed below in more detail.

Considering the value of the energy-dependent hybridization function (Figure 8.10) at the Fermi energy ( $\omega = 0.0$  eV), one gets a more complete picture of how strong the Co  $3d$  orbitals are coupled with the rest of the system. This value is known from the simplest Kondo model (one-band with a constant hybridization) [40] to be directly connected to the Kondo temperature (see Equation (3.2)).

Focusing on the Kondo relevant orbitals of  $\text{Co}(\text{CO})_2/\text{Cu}(001)$  ( $3d_{0.8z^2+0.6x^2-y^2}$ ) and  $\text{Co}(\text{CO})_4/\text{Cu}(001)$  ( $3d_{x^2-y^2}$ ), the energy-dependent hybridization function is in both cases rather featureless in the range of  $\omega = -1.0$  eV to  $\omega = +1.0$  eV. As shown in Table 8.2, the value at  $\omega = 0.0$  eV for the  $3d_{x^2-y^2}$  orbital of  $\text{Co}(\text{CO})_4/\text{Cu}(001)$  is about four times larger than for the  $3d_{0.8z^2+0.6x^2-y^2}$  orbital in  $\text{Co}(\text{CO})_2/\text{Cu}(001)$ . This supports our assumption that the interaction of the  $3d_{x^2-y^2}$  orbital of  $\text{Co}(\text{CO})_4$  ( $C_{4v}$ ) with the CO  $\sigma_2/\sigma_2^*$  orbitals increases the coupling at the Fermi energy, which in turns results in a larger Kondo temperature ( $T_K \approx 165$  K) as discussed in Sec. 3.1. Assuming that the Kondo temperature for  $\text{Co}(\text{CO})_2/\text{Cu}(001)$  is lowered by the same factor as the hybridization at the Fermi energy of the  $3d_{0.8z^2+0.6x^2-y^2}$  orbital, one would expect it to be around  $T_K \approx 41$  K. The lowest electronic temperature under consideration in the DFT++ calculations discussed in Sec. 3.1 was  $T = 46.4$  K, which could explain why within the fully localized limit, we were not able

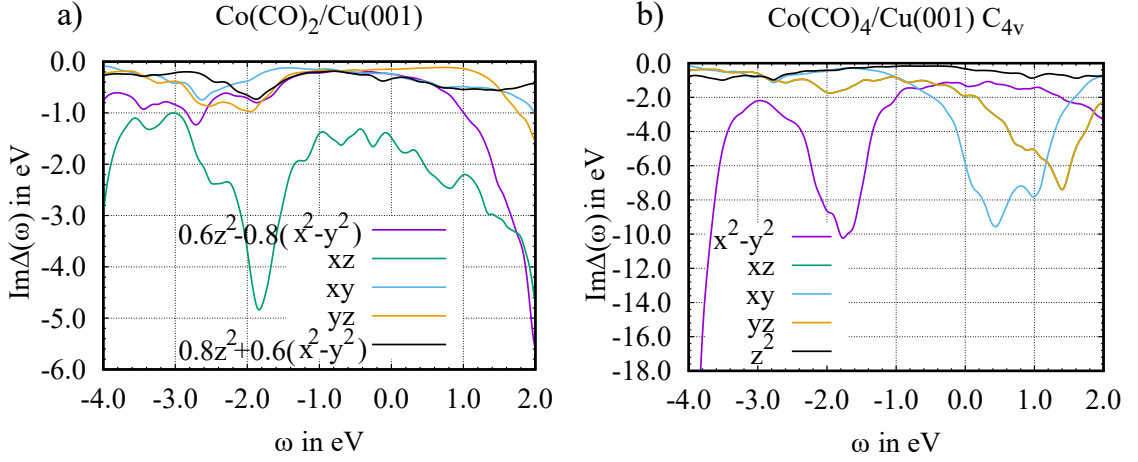


Figure 8.10.: Imaginary part of the hybridization function of a)  $\text{Co}(\text{CO})_2$  and b)  $\text{Co}(\text{CO})_4$  ( $C_{4v}$ ) on Cu(100) as obtained from PBE (based on the BLYP-D3+ $U$  optimized structures).

to reach the transition to the Fermi liquid regime. According to Sec. 8.4.3, the decreased adsorption distance of  $\text{Co}(\text{CO})_2/\text{Cu}(001)$  in, e.g., the BLYP-D3-optimized structure, shows a hybridization of the Kondo-relevant orbital at  $\omega = 0.0$  eV of 0.52 eV. Compared with  $\text{Im}\Delta(0 \text{ eV}) = 0.33$  eV obtained for the BLYP-D3+ $U$  structure, the Kondo temperature would therefore probably shift towards larger values for this structure.

Table 8.2.: Hybridization in eV at the Fermi energy  $-\text{Im}\Delta(0 \text{ eV})$  as obtained from spin-unpolarized PBE (based on the BLYP-D3+ $U$  optimized structures) for different carbonyl cobalt complexes on Cu(001). For  $\text{Co}(\text{CO})_2$ , the orbitals are labeled according to their largest contribution after diagonalizing the Co 3d sub-space.

	$d_{x^2-y^2}$	$d_{xz}$	$d_{xy}$	$d_{yz}$	$d_{z^2}$
$\text{Co}(\text{CO})_2$	0.24	1.48	0.24	0.1	0.33
$\text{Co}(\text{CO})_4$ ( $C_{4v}$ )	1.31	1.91	5.87	1.91	0.33

### 8.5.1. The effect of the CO–surface interaction on the Co 3d hybridization function

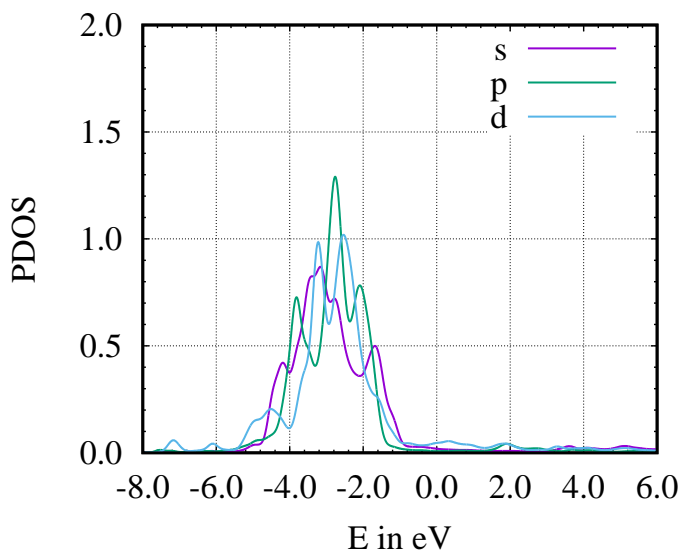


Figure 8.11.: Density of states of the 4s, 4p and 3d orbitals of one of the Cu surface atoms. Results obtained from PBE.

It would be interesting to study the contribution to the hybridization function of the Co 3d orbitals coming from the CO ligands directly, or indirectly as caused by the ligands being coupled to the Cu(001) surface. We try to make a step towards answering this question at the example of  $\text{Co}(\text{CO})_4/\text{Cu}(001)$  in  $C_{4v}$  symmetry. For this purpose, we compare the hybridization functions in Figure 8.12 of all Co 3d orbitals as obtained from an isolated Co on Cu(001), for an isolated  $\text{Co}(\text{CO})_4$  molecule (no surface) and for  $\text{Co}(\text{CO})_4$  on Cu(001). For the isolated molecule, we start from the optimized system and removed all Cu atoms, in order to see the contribution to the hybridization function of the CO ligands only. While this analysis neglects effects of, e.g., the surface on the CO ligands, which may in turn affect the way these ligands contribute to the hybridization of the Co orbitals, we do expect an elucidating qualitative picture of the relative importance of ligands and surface.

Note that the plots in Figure 8.12 are differently scaled on the  $y$ -axis. The hybridization functions of all Co 3d orbitals for an isolated Co atom on Cu(001) are rather small and featureless. In all cases, however, there is a small bump at

roughly  $E = -1.8$  eV to  $E = -2.5$  eV, which comes from the increased DOS of the Cu surface at this energy (as shown in Figure 8.11).

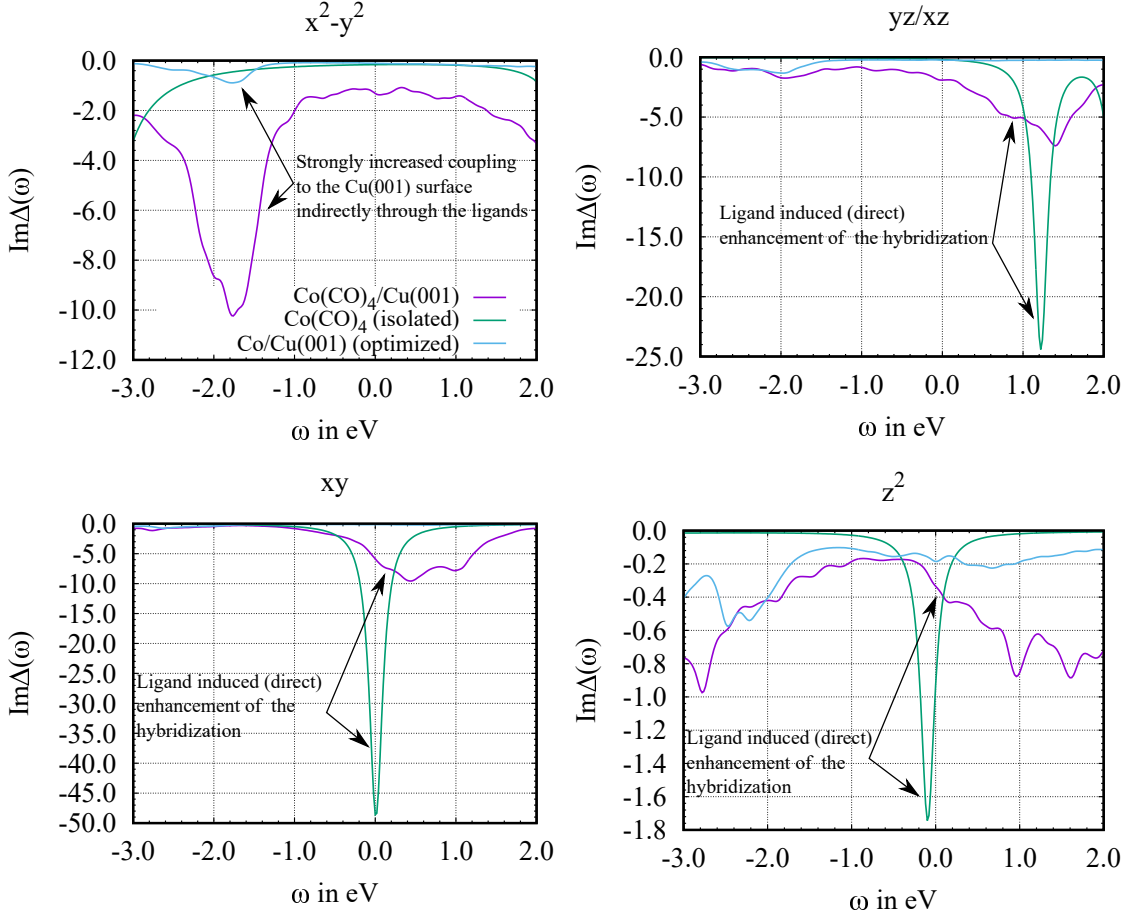


Figure 8.12.: Co 3d hybridization functions as obtained from an isolated (optimized) Co on Cu(001), from an isolated  $\text{Co}(\text{CO})_4$  molecule as obtained by removing the surface atoms from the optimized  $\text{Co}(\text{CO})_4/\text{Cu}(001)$  and from  $\text{Co}(\text{CO})_4$  on Cu(001). Hybridization functions as obtained from PBE, based on BLYP-D3+ $U$  optimized structures.

Considering the Co 3d hybridization functions (Figure 8.12) of the isolated molecule should give an impression of the contribution of the ligands to the hybridization of the Co 3d orbitals in the full system. For the isolated molecule, the hybridization functions of all 3d orbitals (except the  $d_{x^2-y^2}$  orbital) exhibit a sharp feature close to the Fermi energy, which is the reason for the hybridization function of these orbitals being increased in the vicinity of  $E = 0.0$  eV for the full system

$(\text{Co}(\text{CO})_4/\text{Cu}(001))^3$  compared to an isolated Co atom on Cu(001). We believe that this enhancement is directly induced by the hybridization with the ligands. For the  $d_{x^2-y^2}$  orbital the hybridization at  $E = -1.8$  eV is significantly increased compared to Co/Cu(001), although for the isolated molecule we do not observe a peak in  $\Delta(\omega)$  at this energy. Thus, we conclude that the increased hybridization is indirectly caused by the CO ligands, as they not only couple strongly to the Co  $d_{x^2-y^2}$  orbital (as pointed out in Section 8.5), but also to the Cu(001) surface.

## 8.6. Conclusion

Chemical and mechanical control of the Kondo effect in molecular adsorbates is an intriguing subject, which promises insight into strong electron correlation. We have studied such control exploring experimentally characterized cobalt carbonyl complexes on Cu(001) from a theoretical point of view, employing both DFT++ approaches for a full description of correlation, and DFT-derived properties for a conceptual understanding of structure–property trends. We find that it is indeed possible to optimize structures with DFT (employing BLYP-D3+U) whose Fermi liquid properties are compatible with the experimentally observed trend of larger Kondo temperatures with increasing number of ligands for the di- and tetracarbonyl complex (constraining the latter to  $C_{4v}$  symmetry). We can trace back this behavior to an increased hybridization at the Fermi energy, which correlates with a stronger interaction of the Kondo-relevant  $3d$  orbital with the CO ligands for the tetracarbonyl. This Kondo-relevant orbital is the  $d_{x^2-y^2}$  in both cases, with a strong admixture of  $d_{z^2}$  for the dicarbonyl system. It would be interesting to compare these data with newly developed approaches, in which a general projection scheme allows for extending the correlated impurity from the cobalt  $3d$  orbitals to molecular orbitals which include part of the CO ligands [121].

Our data also point to the challenges such systems pose for present-day first-principles electronic structure methods: The structural flexibility of cobalt carbonyl complexes, along with the known difficulty of describing direct carbonyl–metal binding by present-day DFT, implies that predictive modeling of their Kondo properties is virtually impossible. In particular, no atomistic structure could be obtained for the tricarbonyl which is compatible with the experimentally observed Kondo effect (and with the lack of threefold symmetry suggested by STM data). Furthermore, all DFT protocols employed here suggest that for the tetracarbonyl, a  $C_{2v}$ -symmetric structure is by at least 30 kJ/mol more stable than

---

<sup>3</sup>Although, for the  $d_{z^2}$  orbital this effect is only small, as can be seen by the low intensity of the peak of  $\Delta(\omega)$  in case of the isolated molecule, in contrast to the  $d_{xy}$  and  $d_{xz/yz}$  orbitals.

a  $C_{4v}$ -symmetric one, yet only for the latter can we obtain Fermi liquid properties consistent with the experimentally observed Kondo effect. This suggests that the fourfold-symmetric structure observed in the STM results from the intrinsic symmetry of the molecule rather than from a rotational process. This is an example of employing spectroscopic data rather than solely total energies for identifying molecular structure compatible with the experiment, as also done, for example, in theoretical extended X-ray absorption fine structure (EXAFS) studies [243]. For systems with less pronounced structural flexibility, such as metal phthalocyanines, it is likely that available first-principles methods are more reliable at present. On the upside, the strong dependence of Kondo properties on structural parameters suggested by our data could imply that these Kondo properties can be controlled mechanically, in particular by interactions with an STM tip.

In the following section, the focus will be on more detailed analysis of the hybridization function using the chemical concept introduced in Section 4, at the example of  $\text{Co}(\text{CO})_4$  ( $C_{4v}$ ). In addition, it will be shown how the Co  $3d$  hybridization functions are affected by applying a hybrid functional, which increases the HOMO-LUMO gap of the CO ligands.

## 9. $\text{Co}(\text{CO})_4$ on $\text{Cu}(001)$ : What can we learn from chemical concepts on the Kondo effect?

It is common in quantum chemistry to truncate a surface for studying the properties of adsorbates [244–250], or for simulating the electron transport properties through molecules in a molecular-junction setup [251–255]. This is called a cluster approach in this thesis. The reason for doing this is not only the lower computational effort compared to a PBC approach, but also the use of atom-centered basis functions instead of a plane-wave basis can be a valuable alternative to get chemical insight into these systems (in physics, such insights are often obtained by using Wannier orbitals as already mentioned in Section 4.1). For instance, we have shown (Section 4.1) that using an atom-centered basis set makes it possible to divide the hybridization function of a correlated sub-shell into different contributions from individual ligands or the surface (Equation (4.7)). Using such local decomposition of hybridization functions can be beneficial for new insights into structure–property relations for Kondo systems in combination with PBC-based DFT++ calculations.

Often, quantum chemistry programs allows for using a wide range of tools for local analysis (population analysis, bond orbital analysis [256], etc.), one can check the consistency of results for a broader variety of approximated exchange–correlation functionals, in contrast to the often rather limited availability of these functionals in solid state programs (or the often high cost of employing hybrid functionals within a PBC approach).

To this end, we use the projection scheme described in Section 4.1 for the calculation of the hybridization function of  $\text{Co}(\text{CO})_4/\text{Cu}(001)$  within a truncated cluster approach. It will be discussed whether such a rather chemical approach can qualitatively be compared with a DFT calculation using PBC (Section 8.5) focusing on the hybridization function only. We will continue the discussion of what one can learn from DFT about the Kondo effect (which we have started to discuss in Section 8.5).

## 9.1. Methodology

The  $\text{Co}(\text{CO})_4/\text{Cu}(001)$  ( $C_{4v}$ ) cluster was built from the PBC-optimized BLYP-D3+ $U$  structures as explained in detail in Section 8. For modeling the Cu(001) surface, a pyramid-like cluster with a surface of  $6 \times 6$  Cu atoms and 6 layers which results in 91 Cu atoms in total (see Figure 9.1), was excised from the PBC-optimized  $\text{Co}(\text{CO})_4/\text{Cu}(001)$  structure. The odd number of Cu atoms was chosen to enforce an overall closed-shell situation consistent with the DFT parametrization of the AIM as discussed in Section 8. Based on this, DFT single-point calculations were performed with the TURBOMOLE [181] program package (PBE/def2-SVP [182–185] and PBE0/def2-SVP [182–185, 257]). The convergence criterion for the energy in the SCF algorithm was set to  $1 \cdot 10^{-6}$  Hartree, and the hybridization functions were calculated as described in Section 4.1, without truncating the number of Kohn–Sham orbitals used for the projection. Furthermore, the Co  $3d$  sub-space was not diagonalized, because after the Löwdin orthogonalization of the entire system, and the subsequent projection of the Kohn–Sham states onto the Co  $3d$  orbitals, the local (Co  $3d$ ) Hamiltonian is already diagonal.

For CO HOMO-LUMO gaps, an isolated carbon monoxide was optimized with PBE/def2-SVP [182–185], with convergence criteria for the SCF algorithm of  $1 \cdot 10^{-6}$  Hartree, and  $1 \cdot 10^{-4}$  Hartree/Bohr for the gradient. Based on this structure, single point calculations were done with TPSS/def2-SVP [184, 185, 258], PBE0/def2-SVP (25% exact exchange) [182–185, 257] and PBEh-3c/def2-SVP (42% exact exchange) [184, 185, 259].

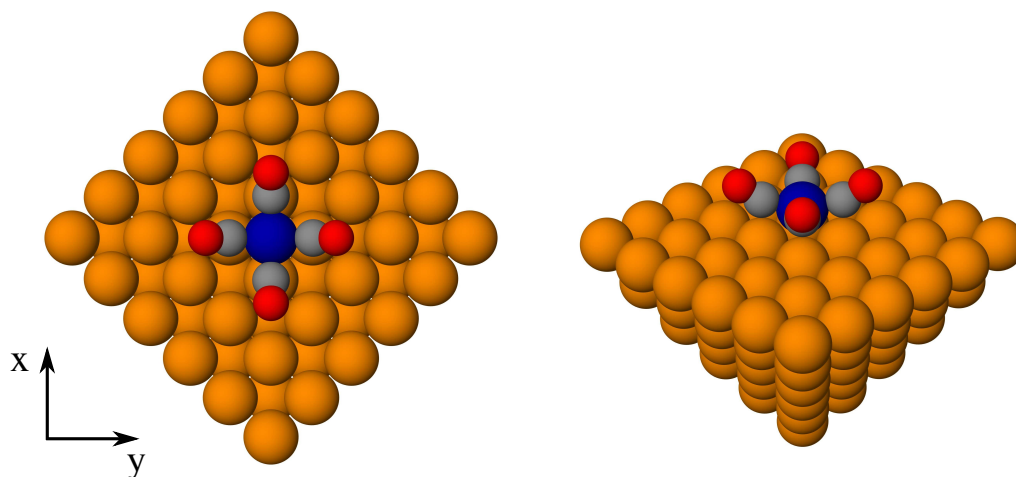


Figure 9.1.:  $\text{Co}(\text{CO})_4$  on a  $\text{Cu}_{91}(001)$ . The structure is based on the BLYP-D3+ $U$  PBC-optimization, see Section 8 for details.

## 9.2. Can a truncated cluster approach reproduce the hybridization function of an approach using periodic boundary conditions ?

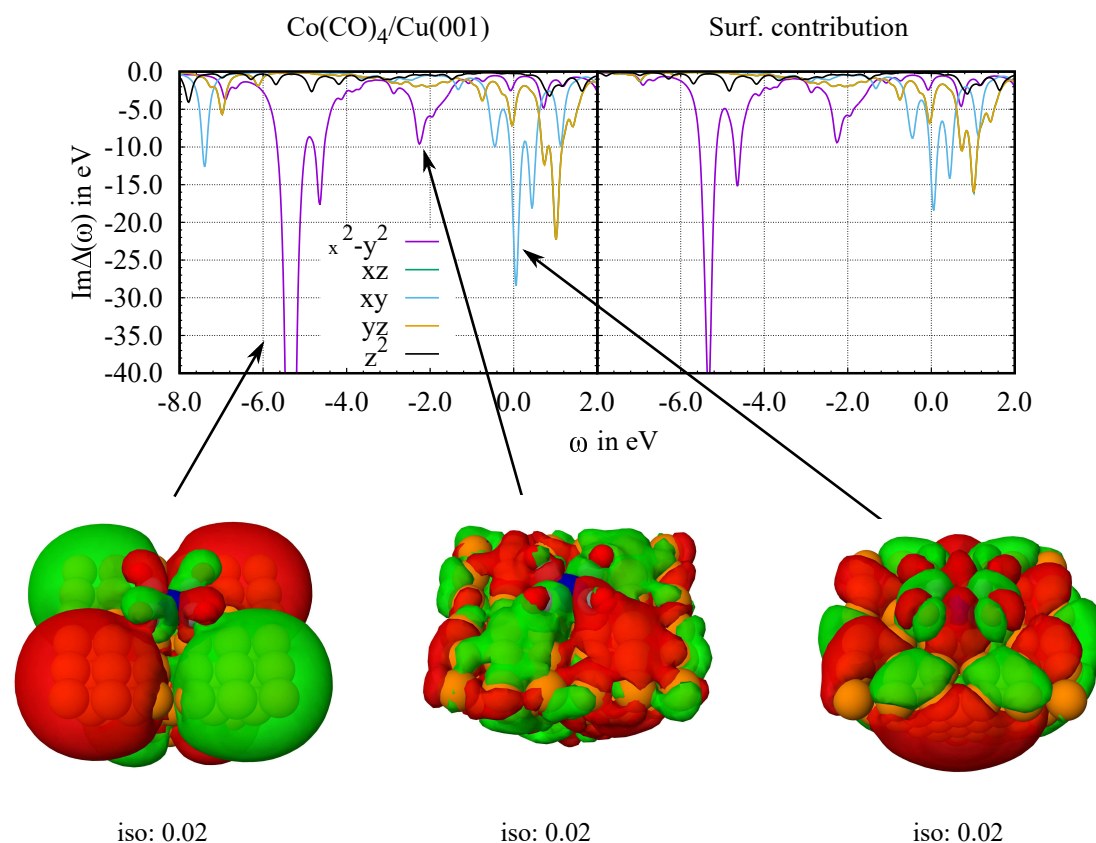


Figure 9.2.: Imaginary part of the Co  $3d$  hybridization function of  $\text{Co}(\text{CO})_4$  in  $C_{4v}$  symmetry, as well as the surface contribution as calculated with Equation (4.7). Additionally, some of the bath orbitals are shown. The Fermi level was set to  $\omega = 0.0$  eV. Results obtained from def2-SVP/PBE.

The hybridization function of the Co  $3d$  orbitals of  $\text{Co}(\text{CO})_4/\text{Cu}(001)$  is shown in Figure 9.2. Focusing on the range of  $\omega = -2.5$  eV to  $-1.5$  eV, the hybridization of the  $d_{x^2-y^2}$  orbital is strongly increased compared with the remaining Co  $3d$  orbitals. This feature is in agreement with the hybridization function as obtained from PBC (see Figure 8.10 b)).

9.2. Can a truncated cluster approach reproduce the hybridization function of an approach using periodic boundary conditions ?

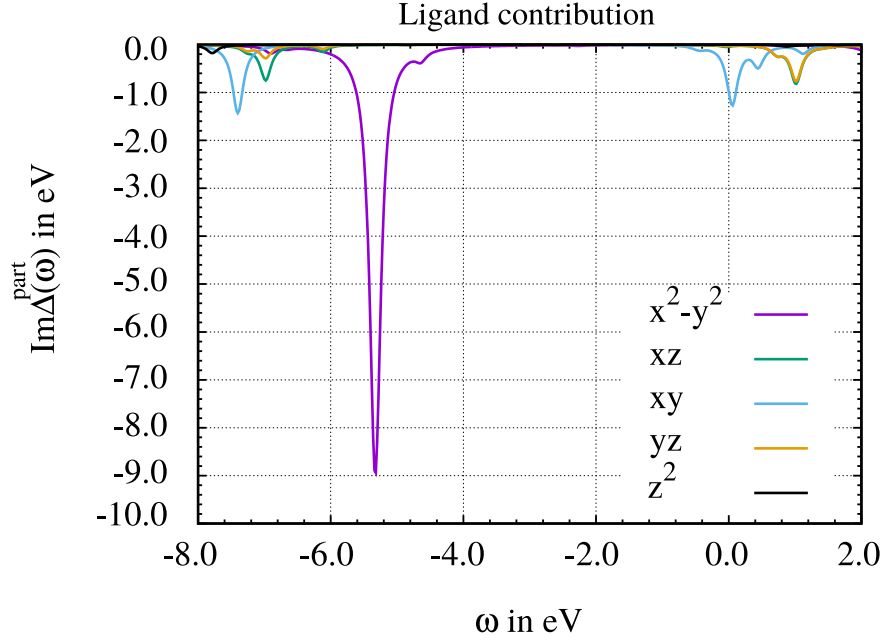


Figure 9.3.: Ligand (CO) contribution to  $\text{Im}\Delta_i(\omega)$  of the Co 3d orbitals in  $\text{Co}(\text{CO})_4/\text{Cu}(001)$ . Results obtained from PBE, using Equation (4.7).

At the Fermi energy ( $\omega = 0.0$  eV), the hybridization strength takes the following order (beginning from the largest value):  $\text{Im}\Delta_{xy}(0.0 \text{ eV}) > \text{Im}\Delta_{xz/yz}(0.0 \text{ eV}) > \text{Im}\Delta_{x^2-y^2}(0.0 \text{ eV}) > \text{Im}\Delta_{z^2}(0.0 \text{ eV})$ , which qualitatively reproduces the results of the PBC approach. Quantitatively, the hybridization of the  $d_{xy}$  orbital (cluster approach) seems to be overestimated compared with the PBC-results, which is caused by the discretization of the energies in a cluster approach. Presumably, this could be improved by using a larger Cu cluster, which would effectively “smear” the hybridization function. Nevertheless, the overall qualitative agreement between both approaches motivates us to use such an approach for analyzing the hybridization function in more detail.

In Section 8.5.1, it was discussed which parts of the hybridization functions are directly or indirectly increased through the CO ligands, by comparing the hybridization functions with those of an isolated Co on Cu(001). It should be recalled that for the Kondo-relevant orbital ( $d_{x^2-y^2}$ ),  $\text{Im}\Delta(\omega)$  was increased in the range of  $\omega = -3.0$  to  $2.0$  eV, with a significant enhancement of the hybridization at  $\omega = -2.0$  eV as compared to Co/Cu(001). We suggested that this is indirectly caused due to CO–surface interactions, indicating the general importance of such interactions with respect to the Kondo properties of an adsorbate. In the following, we apply

our tool to decompose the hybridization function (introduced in Section 4.1), for obtaining a more quantitative picture of how the CO ligands affect the hybridization of the Co  $d_{x^2-y^2}$  orbital, as a step towards understanding the chemical control of the Kondo effect.

In the right panel of Figure 9.2, the hybridization function is shown for the contributions coming from the surface, which we obtained after using Equation (4.7). The feature of the  $d_{x^2-y^2}$  orbital in the area of  $\omega = -2.5$  eV and  $-1.5$  eV comes purely from the Cu(001) surface, as can be seen by comparing the left and the right panel of Figure 9.2, or by considering the corresponding bath orbital (see also the ligand contribution to  $\text{Im}\Delta(\omega)$  in Figure 9.3). This is in agreement with the assumption made in Section 8.5.1, that in the vicinity of the Fermi energy the hybridization is purely of surface-character and is only indirectly enhanced by the ligands (compare with the strong hybridization of the C 2p orbitals with the surface at  $\omega = -2.0$  eV, as depicted in Figure 9.4), suggesting that the ligand–surface interaction might play an important role in the modification of the Kondo properties.

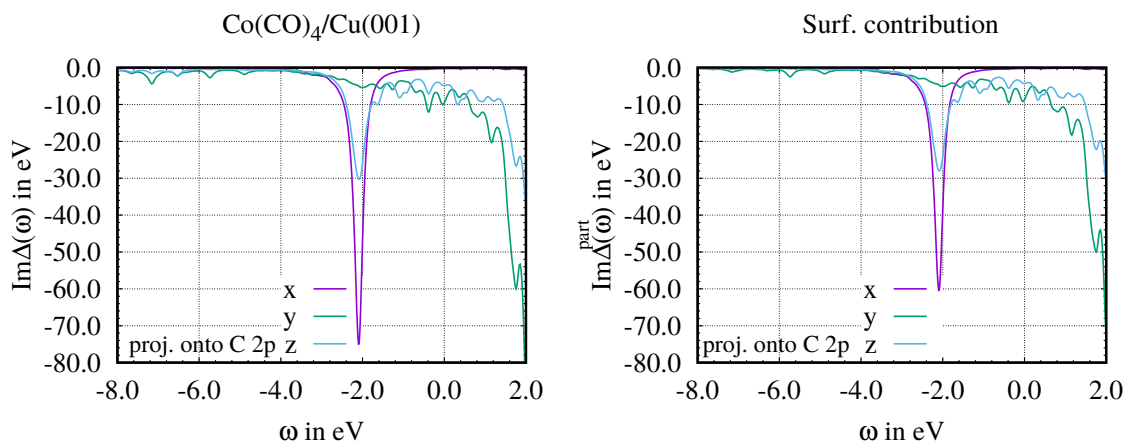


Figure 9.4.: Imaginary part of the C 2p hybridization function of  $\text{Co}(\text{CO})_4$  in  $C_{4v}$  symmetry, as well as the surface contribution as calculated with Equation (4.7). Results obtained from def2-SVP/PBE.

Most important for the Kondo physics is, however, the hybridization at the Fermi energy ( $\omega = 0.0$  eV). For the Kondo-relevant orbital  $d_{x^2-y^2}$ , which we identified in Section 8, we found that the hybridization at the Fermi level is increased as compared to an isolated Co atom on Cu(001). The surface contribution to the hybridization function shows that  $\text{Im}\Delta_{x^2-y^2}(0.0$  eV) is entirely dominated by the Cu surface. In other words, there is no bath orbital with CO character that couples with the Co  $3d_{x^2-y^2}$  at the Fermi energy. This leads to the conclusion that the CO ligands indirectly enhances the  $d_{x^2-y^2}$  hybridization at the Fermi energy, due

### 9.3. The effect of the exchange–correlation functional onto the hybridization function in $\text{Co}(\text{CO})_4$ ( $C_{4v}$ ) on $\text{Cu}(001)$

---

to CO-surface interactions, which is probably the explanation for the increasing Kondo temperatures in  $\text{Co}(\text{CO})_n$  complexes on  $\text{Cu}(001)$  when the number of CO ligands is increased.

In contrast to this, the  $d_{xy}$  orbital hybridizes strongest at the Fermi energy of all Co  $3d$  orbitals in the tetracarbonyl. Within our approach, we can identify that this comes from a bath orbital with  $\pi^*$ -character on the CO ligands (see Figure 9.2), which is located at the Fermi energy. On the other hand, the bath orbital with CO  $\sigma$ -character (at  $\omega = -5.4$  eV) which could hybridize with the  $d_{x^2-y^2}$  orbital, is at an energetic positions far away from the Fermi energy (the bath orbital with  $\sigma^*$ -character lies above  $\omega > 2.0$  eV which is beyond the energy range shown in Figure 9.2). This observation is in particular interesting for designing Kondo systems, as we have shown at the example of the simplest Anderson impurity model (Section 3.6.3) that a too strong hybridization can lead to the destruction of the Kondo resonance.

### 9.3. The effect of the exchange–correlation functional onto the hybridization function in $\text{Co}(\text{CO})_4$ ( $C_{4v}$ ) on $\text{Cu}(001)$

In Section 8, it was discussed that in general GGA-type functionals tend to underestimate the HOMO–LUMO gap in carbon monoxide, which can, e.g., be corrected by using hybrid functionals. For instance, we found a gap of 6.95 eV using PBE/def2-SVP /GGA) and a gap of 9.95 eV by applying the hybrid functional PBE0/def2-SVP (Figure 9.5). With the meta-GGA-type functional TPSS one finds a gap of 7.33 eV, whereas the recently proposed hybrid functional PBEh-3c yields the largest gap under consideration here (11.98 eV). Obviously, such significant differences in the HOMO-LUMO gap will result in drastic changes Co  $3d$  hybridization function. To demonstrate this, it will be discussed in this section what the effect of applying a hybrid functional (such as PBE0) can have on the Co  $3d$  hybridization functions, at the example of  $\text{Co}(\text{CO})_4$  ( $C_{4v}$ ) on  $\text{Cu}(001)$ .

In Figure 9.6,  $\text{Im}\Delta(\omega)$  of the Co  $3d$  orbitals in  $\text{Co}(\text{CO})_4/\text{Cu}(001)$  is shown as obtained from PBE (GGA-type functional) and PBE0 (hybrid functional with 25% exact exchange), as well as the contribution to  $\text{Im}\Delta(\omega)$  from the  $\text{Cu}(001)$  surface.

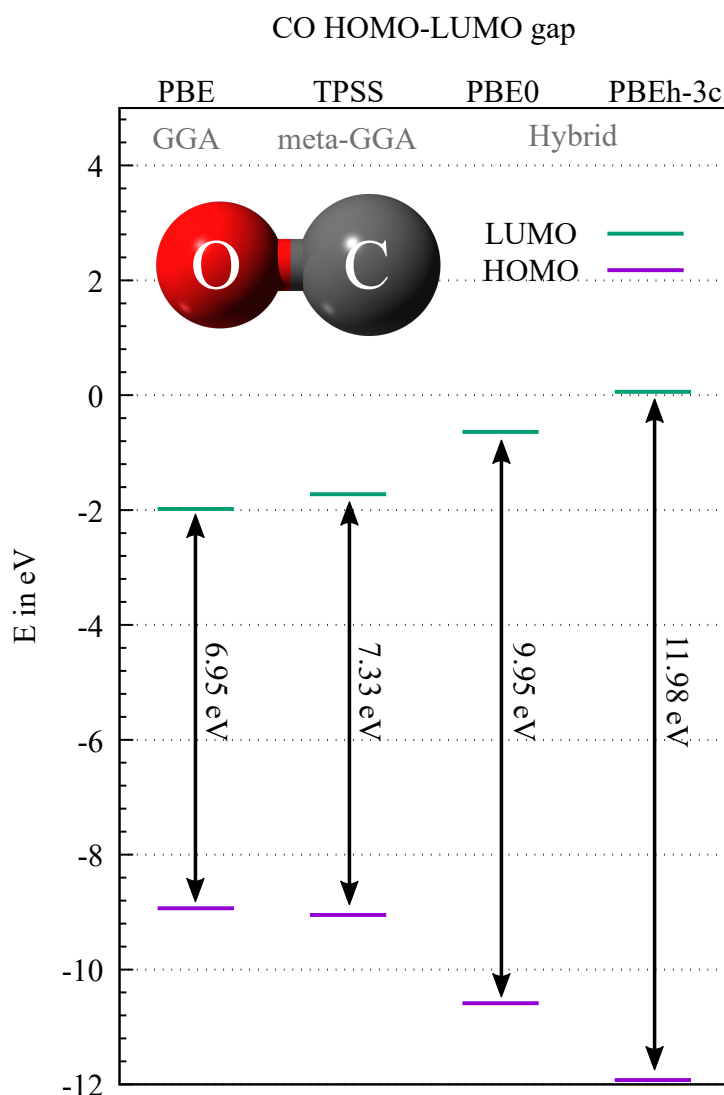


Figure 9.5.: HOMO-LUMO gap of a an isolated CO molecule as obtained from PBE/def2-SVP [182–185], TPSS/def2-SVP [184,185,258], PBE0/def2-SVP [182–185, 257] (25% exact exchange) and PBEh-3c/def2-SVP (42% exact exchange) [184,185,259]. All gaps were calculated on the basis of the PBE/def2-SVP optimized CO molecule.

The strong hybridization of the  $d_{x^2-y^2}$  orbital caused by the interaction with the CO  $\sigma$  orbital (marked as 1 in Fig. 9.6) as obtained from PBE is shifted towards lower energies (marked as 1' in Fig. 9.6) when using PBE0. At the same time, the hybridization of the  $d_{xy}$  orbital with the CO  $\pi^*$  orbital as obtained from PBE is shifted towards higher energies if PBE0 is applied ( $2 \rightarrow 2'$ ). This is exactly what is

9.3. The effect of the exchange–correlation functional onto the hybridization function in  $\text{Co}(\text{CO})_4$  ( $C_{4v}$ ) on  $\text{Cu}(001)$

expected from using a hybrid functional, which increases the HOMO-LUMO gap of CO. More interestingly, using PBE0 one obtains that the  $d_{x^2-y^2}$  orbital hybridizes most strongly at the Fermi energy ( $\omega = 0.0$  eV), whereas the hybridization of the  $d_{xy}$  orbital is significantly lowered compared to the PBE-results. The later is caused due to the  $\pi^*$  type orbitals of CO being shifted towards higher energies.

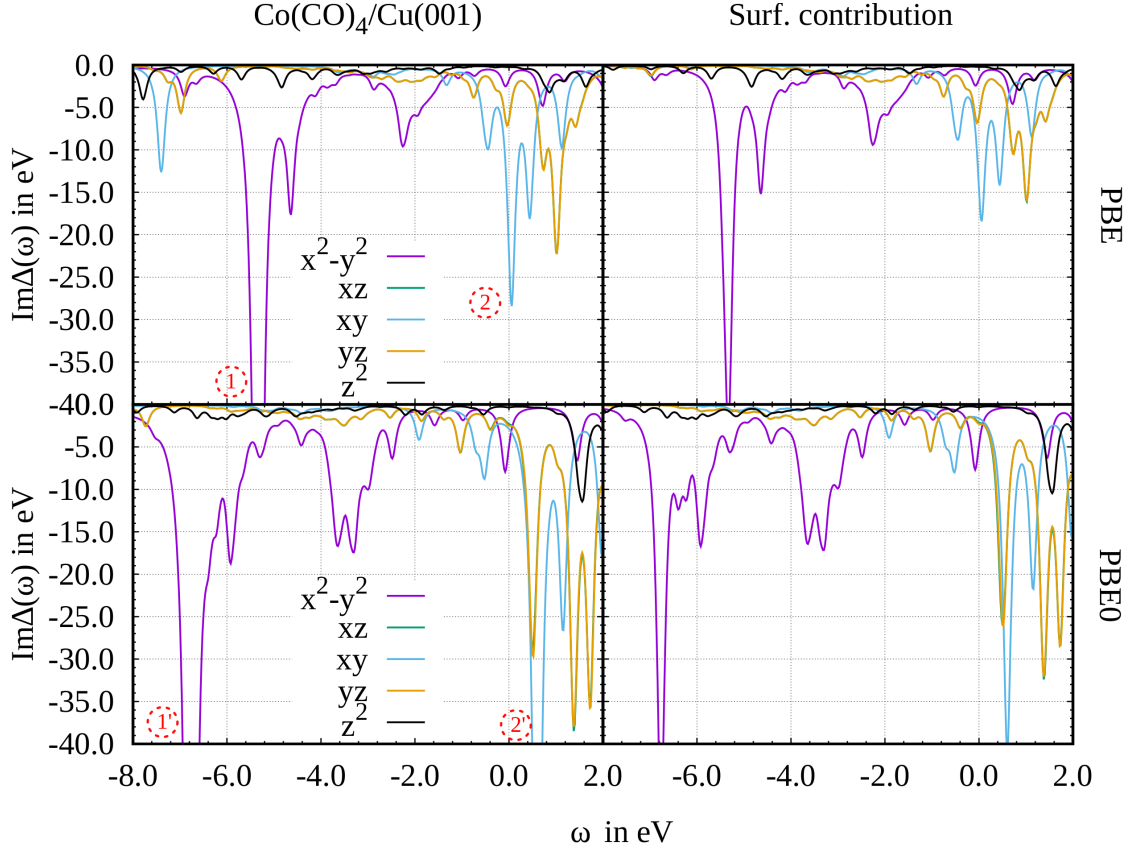


Figure 9.6.: Imaginary part of the Co 3d hybridization function of  $\text{Co}(\text{CO})_4$  in  $C_{4v}$  symmetry, as well as the surface contribution as calculated with Equation (4.7). Results obtained from def2-SVP/PBE and def2-SVP/PBE0.

It is assumed that the strong hybridization of the  $d_{x^2-y^2}$  orbital predicted by PBE0 would suppress the formation of a Kondo resonance at the Fermi energy, as shown in Section 3.6.3 at the simplest Kondo model. However, from the literature it is known that hybrid functionals might lead to serious troubles in the description of the electronic structure of metals [84, 260], which is why the results obtained here

(PBE0) should be interpreted with care, and a combination of different functionals (e.g. PBE applied to Cu and Co, and PBE0 applied to CO, as for instance possible within the frozen density embedding) could be a step towards solving this issue [261–265], or the use of local hybrid functionals with position-dependent exact-exchange admixture could be a promising route for future applications [266, 267]. Further studies should also include testing more recently proposed approximate exchange–correlation functionals, such as SCAN [268], M06-L [269] or vdW-DF [234].

## 9.4. Conclusion

Cluster approaches are a useful chemical tool for treating substrate–adsorbate systems, as it allows for using a rich zoo of exchange–correlation functionals (as, e.g., implemented in TURBOMOLE), and allowing for interpretations in terms of molecular orbitals. In this section we have shown that the resulting hybridization functions from a truncated cluster approach can at least recover qualitatively the features as observed from a PBC calculation. Furthermore, it has been shown that the molecular orbitals of the electronic bath can be used to identify the bath–impurity interaction in the hybridization function. It is likely that this can be extended to other system for understanding the adsorbate–surface interaction in more general, that can cause a switchable, or tunable Kondo effect [36, 125] .

The application of hybrid functionals (here PBE0) demonstrate that the features in the hybridization function of the Co  $3d$  orbitals is shifted towards lower, or higher energies (depending on the CO orbitals they are interacting with), due to an increased HOMO-LUMO gap in CO. This also results in a different picture of  $\text{Im}\Delta(0.0 \text{ eV})$  among the Co  $3d$  orbitals, as compared to what we have observed with PBE. However, due to the problem of GGA type functionals in describing the electronic structure of carbon monoxide and the fact that hybrid functionals should taken with care for the description of metals, it is proposed for future applications to use a combination of both type of exchange–correlation functionals, applied to different parts of the system or to test more recently proposed approximate exchange–correlation functionals.

## 10. Conclusion and perspective

The Kondo effect is an intriguing phenomenon caused by the correlation of a localized magnetic moment with a surrounding electronic bath. In spintronics, this effect can act as a probe for detecting electron tunneling pathways in a molecular junction setup or can be used for detecting spin localization on molecules on surfaces in the STS [28, 29]. Recently, the interest in manipulating the Kondo effect has grown, as this is equivalent to having control over the spin on molecules adsorbed on a substrate, which might give rise to new applications in spintronics or information processing technologies [270–272]. Such manipulation can for instance be mechanically induced or be realized by chemical modification of an adsorbate.

From a theoretical point of view, describing the Kondo effect of a system is a challenging task, because it delicately depends on the atomistic structure, as well as on input parameters required in state-of-the-art electronic structure calculations.

This work aimed for understanding the chemical and mechanical control of the Kondo effect. To this end, it was scrutinized how the results of the established electronic structure methods DFT and DFT++ depends on parameters such as  $U$ ,  $J$ ,  $k$ -space, the value of DC correction, and the choice of the exchange–correlation functional. In addition, for achieving new insights into the control of the Kondo effect, a conceptual analysis was proposed providing a link with tools and the language commonly used in chemistry.

### 10.1. Summary

As a first system, a single Co atom on Cu(001) was chosen due to its simple atomistic structure, and for being well characterized in experiments concerning its Kondo properties. We investigated the potential energy surface along the Co adsorption coordinate with different electronic structure methods, which mimics the simplest situation of an adsorbate being mechanically manipulated (e.g. by an STM tip), and provides an ideal playground for comparing the effect of different parameters on the adsorption distance and the electronic structure of Co/Cu(001).

Subsequently, we focused on carbonyl cobalt complexes on Cu(001), because it was found by Wahl *et al.* [1] in the STS that the Kondo temperature of these systems increases with the number of CO ligands attached to Co, which provides an optimal basis for analyzing chemical control of the Kondo effect. In all cases we used the AIM (DFT++) to obtain insight into the Kondo properties of the above-mentioned systems. This includes the introduction of a local decomposition scheme in line with chemical concepts such as partial charges or spins [273, 274], which allows studying the isolated effect of different parts of the electronic bath to the impurity hybridization function. Hereby, it was shown at the example of  $\text{Co}(\text{CO})_4/\text{Cu}(001)$  that using a truncated cluster approach for mimicking a metal surface yields results which are compatible with those obtained by applying PBC. This observation could pave the way towards understanding the Kondo effect using chemical tools, and to learn more about its dependence on external stimuli, as well as the effect to it by chemical modification.

We found that the adsorption minimum of a cobalt atom on Cu(001) using DFT++ or DFT+ $U$  is shifted towards larger adsorption distances as compared to spin-polarized DFT. The shift is, however, of the same order as changing the exchange-correlation functional and is barely affected by changing  $U$ . This suggests that a proper choice of this functional can produce accurate results, and adsorption distances obtained from DFT are not too far away from the more expensive DFT++ approach. To examine how the Kondo temperature  $T_K$  would be affected by different adsorption distances (e.g. as be caused by mechanical manipulation), we estimated  $T_K$  using the solution of the AIM for the simple Kondo model (one impurity orbital with a constant hybridization) [40]. For this, the impurity levels and hybridization strengths as obtained from DFT were used as input. It was found that  $T_K$  would be more affected in the  $d_{xy}$  orbital than in the  $d_{z^2}$  orbital (only these two are relevant for a Kondo effect in Co/Cu(001)) by manipulating the adsorption distance, because both the impurity level and the hybridization function of the  $d_{xy}$  orbital depend more strongly on changes in the adsorption distance. However, from the literature it is known that the  $d_{z^2}$  orbital exhibits a larger  $T_K$  compared to the  $d_{xy}$  orbital, which is not the case for our estimated results. This demonstrates that a simple approximations based on DFT input can lead to the wrong qualitative picture of multi-orbital Kondo systems, and thus requires the solution of the AIM for taking into account the complex correlation effects between the impurity electrons.

To this end, we tried to identify the transition to the Kondo regime focusing on only one adsorption distance as a starting point for a more quantitative analysis about the Kondo physics in Co/Cu(001). For such an analysis we performed DFT++ calculations at electronic temperatures down to  $T = 10$  K, which not

only requires a sufficiently dense  $k$ -grid (here we used  $100 \times 100 \times 1$ ), but also a proper description of the Coulomb part within the AIM. It was found that using only density–density terms of the Coulomb matrix (which was also employed for the PES scan) the physical properties of Co/Cu(001) at temperatures below  $T = 116$  K are qualitatively in disagreement by comparing it with the results with a full description of the Coulomb matrix. In fact, the spin–spin correlation function, as well as the local spin susceptibility suggest that the Co  $3d_{z^2}$  orbital is in a frozen moment regime when using the density–density approximation, which disagrees with the experimentally characterized Kondo effect and theoretical investigations [111, 199–201]. Using all matrix elements of the Coulomb tensor our results suggest that the local moment in  $3d_{z^2}$  orbital is screened by the conduction band electrons (as indicated by an increasing value of  $\chi(\beta/2)$  as  $T$  is lowered). For the electronic temperature applied here, however, the transition to the Fermi-liquid regime could not be observed, which would require further studies at electronic temperatures below 46.6 K.

Furthermore, we showed that using a too small  $k$ -grid ( $4 \times 4 \times 1$ ) for low temperature DFT++ calculations, one would reach the Kondo regime below  $T = 25$  K within the density–density approximation, which is probably caused by error compensation. This demonstrates the need for a numerically accurate description of the substrate, and suggests that there may be a general problem with the density–density approximation for describing Kondo systems in certain cases.

For answering this question, we changed the substrate of an adsorbed cobalt atom from Cu(001) to Ag(001), which is experimentally characterized as a Kondo system, too. Here we found a similar disagreement between experimental observations and the results obtained from low temperature ( $T = 29$  K) DFT++ in combination with the density–density approximation. On the other hand, from the literature it is known that the density–density approximation has been successfully applied to a wide range of systems [125, 226–228]. In addition, we could show for  $\text{Co}(\text{CO})_n$  ( $n = 2, 3, 4$ ) complexes on Cu(001) that a correct qualitative picture concerning the Kondo effect can be found (with a sufficiently large  $k$ -grid), which is in agreement with experimental results reported by Wahl *et al.* [1]. This suggests that using the density–density approximation might be problematic in the special case of single atoms on metal surfaces, for which the more expensive Kanamori approximation or a full description of the Coulomb matrix is required [136]. However, this could be of the expense of low temperature calculations in cases where all five  $d$  orbitals must be included. In order to draw a clear conclusion, more comparative studies including different transition metal atoms on metal surfaces would be required.

Knowing that DFT++ within the density–density approximation gives a physical picture for  $\text{Co}(\text{CO})_n/\text{Cu}(001)$  (for  $n = 2, 4$ ) which is compatible with experimental

results, it was used to study the chemical and mechanical control of the Kondo effect in these systems. First of all, suitable structures have to be found using DFT, for which one is faced with a problem which is likely related to the well known “CO-puzzle”. For example, for  $n = 3$ , no agreement between the theoretically observed symmetry and the one in the STM could be found, and for  $n = 4$ , DFT predicts a  $C_{2v}$  symmetric structure to be lowest in energy, although in the STM a  $C_{4v}$  symmetric one was observed. Nevertheless, we were able to obtain structures for the complexes with two and four ligands which are compatible with the ones reported in Reference [1], whereby the  $C_{4v}$  (for  $n = 4$ ) symmetry is at least 31 kJ/mol higher in energy than the  $C_{2v}$  symmetry.

Studying the control of the Kondo effect, it was found that in line with experimental observations [1], the Kondo regime manifests itself at larger temperatures for the case of  $n = 4$  compared to  $n = 2$ . The reason for this is an increased hybridization at the Fermi energy of the Kondo-relevant orbital if the number of ligands is increased. Using our chemical tool for analyzing the hybridization function of  $\text{Co}(\text{CO})_4/\text{Cu}(001)$ , it was found that the ligands contribute only indirectly to the hybridization at the Fermi energy, which suggest that the strong CO–surface interaction is probably responsible for the increased Kondo temperature. To support this assumption, more work would be necessary using our conceptional scheme, e.g. applying it to  $\text{Co}(\text{CO})_2/\text{Cu}(001)$ . This would give interesting insight into the control of the Kondo effect, by manipulating the ligand–surface interaction of a molecular complex on a surface, as for instance also shown for manganese phthalocyanine (MnPc) on  $\text{Ag}(001)$  [125] (although there the stronger ligand–surface interaction leads to a reduction of  $T_K$ ), and  $\text{CoPc}/\text{Au}(111)$  [32].

Further studies showed that for  $n = 2$ , there is a delicate dependence of the Kondo properties on the DC value, which was not the case for  $n = 4$ . This value controls the occupation on the Co  $3d$  shell, and a similar effect might be caused in experiments by mechanical stress. To this end, we evaluated the effect of different CO-Co-CO bonding angles and adsorption distances on the Kondo properties in  $\text{Co}(\text{CO})_2/\text{Cu}(001)$ . For structures reasonable within DFT, our results suggest that there is indeed a sensitive dependence of the Kondo temperature on the adsorption distance in  $\text{Co}(\text{CO})_2/\text{Cu}(001)$ , which might also be realizable in experiments by external stimuli. This observation is similar to  $\text{Co}/\text{Cu}(001)$ , as in both cases the Kondo effect would be shifted to smaller temperatures if the adsorption distance is increased. However, for  $\text{Co}(\text{CO})_2/\text{Cu}(001)$ , more studies would be needed to estimate a quantitative value of the  $T_K$  from DFT++, e.g. by identifying the transition temperature to the Fermi-liquid regime.

## 10.2. Outlook

Future work may build on the insights obtained in this thesis towards a deeper understanding of how magnetic molecules couple with surfaces, and to find new practical applications by designing Kondo systems that can be modulated by external stimuli:

- The projection scheme implementation (described in Section 4.1) is a useful tool for a chemical analysis of adsorbate–surface systems. It would require to be extended by a projection onto molecular orbitals similar to what is reported in References [121] and [275], which would yield MO hybridization functions with potentially more information about adsorbate–surface systems. This would yield an AIM which includes also ligand orbitals, or fragments of organic molecules on which the electron correlation effects would explicitly be accounted for, and is not only restricted to sub-shells of single atoms. Furthermore, the effect of the cluster size used for such a projection should be investigated in more detail with respect to a convergence of the results, as a step towards answering the question of “how local” the Kondo effect is in different systems.
- It was shown that the Kondo temperature of the carbonyl cobalt complexes on Cu(001) increases due to a stronger hybridization of the Kondo-relevant orbital with the number of CO ligands attached to cobalt. The increased hybridization at the Fermi energy was identified as being indirectly induced through ligand–surface interactions. To clarify this in more detail, other ligands with a less pronounced interaction to the surface should be investigated to form cobalt complexes on Cu(001). This would be a big step towards understanding the control of the Kondo effect via ligand substitution.
- For  $\text{Co}(\text{CO})_3/\text{Cu}(001)$ , we did not observe a Kondo resonance in our DFT++ calculations even though being observed in the experiment [1], and further work is required to address this problem. One strategy would be based on using all Coulomb matrix elements for solving the AIM, to see whether the Kondo effect is similarly suppressed by the density–density approximation as in the cases of Co on Cu(001) and Ag(001). The absence of a Kondo effect at electronic temperatures below the experimentally one would then further strengthen the assumption that the atomistic structure of  $\text{Co}(\text{CO})_3/\text{Cu}(001)$  is not reasonable, and new structural optimization protocols should be tested.
- In the literature, the density–density approximation has proven to be a good compromise between computational effort and accuracy, as well as being

widely applied due to its minor sign error in CT-QMC at low electronic temperatures [157, 212, 226, 276]. However, for an isolated Co atom on Cu(001) and Ag(001), we could show that no Kondo effect can be observed within DFT++ when using the density–density approximation, even though it was found in Ref. [225] using HF-QMC. The authors reported that in the series of the  $3d$  metals on Ag(001) the charge fluctuations of Co/Ag(001) are reduced compared to Fe and Ni (note that the authors used the density–density approximation to solve the AIM). It would be worthwhile to study whether this observation still holds by using the full Coulomb interaction to solve the AIM within the numerically exact CT-QMC method, similarly to what we have found for Co/Cu(001). Such information is important for future application of the AIM to magnetic adsorbates, concerning a proper description of the underlying physical picture which leads to a Kondo effect. In this context, future work may build on these observations to find clear rules for cases in which the density–density approximation is reasonable.

Altogether, from both the experimental and theoretical side, more test systems are required to learn more about the chemical and mechanical manipulation of the Kondo effect. Future experimental works may build on the investigation of molecular complexes with more structural flexibility as compared to the widely studied phthalocyanine and porphyrine systems. This would also include the ability to tune the Kondo properties via exchanging the ligands attached to a transition metal atom. Based on these studies, the door would be open for future theoretical investigations concerning the control of the Kondo effect, as well as for developing new methodologies for its analysis.

# A. Additional data

## A.1. The H<sub>2</sub> bond breaking scenario

Hartree–Fock theory (in its restricted form, referred to as RHF) is known to incorrectly describe the energy of H<sub>2</sub> in the bond breaking scenario, as shown in Figure A.1. Here, we do not want to discuss all the methods shown in this Figure in all details, because we are rather interested in a brief introduction about the reasons of the RHF theory for failing in the bond breaking scenario of H<sub>2</sub>.

The results obtained from the full configuration interaction (FCI) method are the exact solution to the electronic Schrödinger equation (within the basis set applied). Around the equilibrium distance of 0.71 Å, restricted Hartree–Fock (RHF) and unrestricted Hartree–Fock (UHF) exhibit the same qualitative picture compared to FCI. At larger bond distances, RHF begins to deviate from the FCI behavior, whereas the UHF results are still in good agreement with the exact solution. Note that Figure A.1 shows relative energies, i.e. for all three methods the energy at the equilibrium distance was set to zero. This is why the UHF energy suggests to be smaller than the FCI energy at larger distances, but this is indeed not the case if one would consider the absolute values.

In the following, it shall briefly be discussed where the deviating behavior at larger distances of the RHF method originates from. In a minimal basis, one has a basis function  $\phi$  (representing the 1s orbital) on each of the hydrogen atoms, which form a bonding  $\psi_+$  and anti-bonding  $\psi_-$  molecular orbital,

$$\psi_+ = \phi_A + \phi_B = A + B, \tag{A.1}$$

$$\psi_- = \phi_A - \phi_B = A - B. \tag{A.2}$$

In the HF wavefunction, the bonding orbital will be occupied by two electrons, for which the Slater determinant takes the form [47]

$$\Phi_{\text{HF}} = \begin{vmatrix} \psi_+(1) & \bar{\psi}_+(2) \\ \bar{\psi}_+(1) & \psi_+(2) \end{vmatrix}, \quad (\text{A.3})$$

where we have neglected the normalization factor, and the bar above the MO are for a spin-down ( $\beta$ ) electron, whereas no bar represents a spin-up ( $\alpha$ ) electron.

Rewriting Equation A.3 yields,

$$\Phi_{\text{HF}} = \psi_+\psi_+\alpha\beta - \bar{\psi}_+\bar{\psi}_+\beta\alpha = \psi_+\psi_+(\alpha\beta - \beta\alpha), \quad (\text{A.4})$$

for which the electrons are implicitly in the same order as the labels (i.e.  $\psi_+\psi_+\alpha\beta = \psi_+(1)\psi_+(2)\alpha(1)\beta(2)$ , and so on).

Because  $\hat{H}$  is independent on the spin of the electrons, one can express  $\Phi_{\text{HF}}$  in terms of the basis functions as [47],

$$\Phi_{\text{HF}} = (A + B)(A + B) = \underbrace{AA + BB}_{\text{ionic}} + \underbrace{AB + BA}_{\text{covalent}}. \quad (\text{A.5})$$

From Equation (A.5) one can see that the HF wave function is a 1 to 1 mixture of ionic and covalent contributions. In a RHF calculation this is independent of the  $\text{H}_2$  bond distance, which is clearly unphysical if both hydrogen atoms are far away from each other, where the amount of ionic configurations should be zero [47].

By using UHF, one introduces  $\alpha$  and  $\beta$  molecular orbitals, which in the case of  $\text{H}_2$  takes the form (for the bonding MO)

$$\psi_+ = (\phi_A + c\phi_B)\alpha, \quad (\text{A.6})$$

$$\bar{\psi}_+ = (c\phi_A + \phi_B)\beta. \quad (\text{A.7})$$

Here,  $c$  is a coefficient which can be varied to yield the energy minimum. More importantly, the coefficient  $c$  gives the UHF the flexibility to localize an electron on one of the hydrogen atoms (then  $c$  goes towards zero), which qualitatively reproduces the FCI behavior at larger bond distances (for further details see Reference [47]). At equilibrium distance  $c = 1$ , which corresponds to the RHF solution.

The decreasing amount of ionic configurations in the wave function, is related to what physicist call “decreasing charge fluctuations on an atomic site” [68], and corresponds to materials that are strongly correlated in the physical sense.

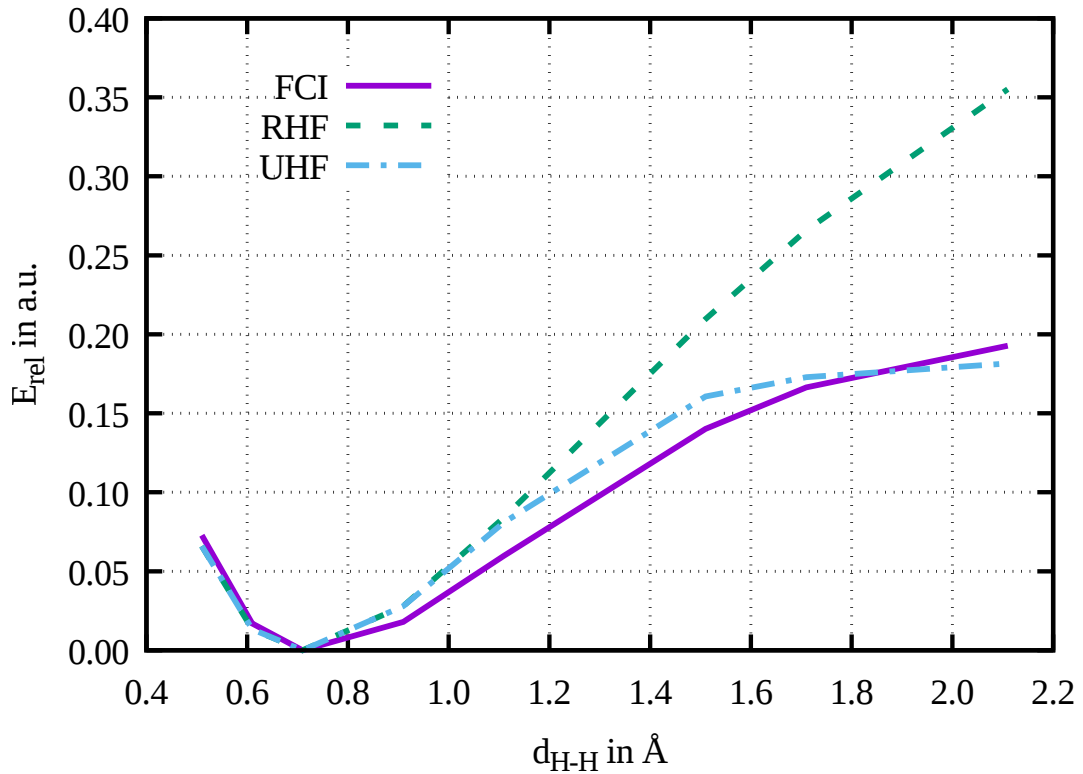


Figure A.1.:  $\text{H}_2$  dissociation energies as obtained in a minimal basis (STO-3G) from RHF, UHF, and FCI. For this calculations the GAUSSIAN program package was used [277].

## A.2. Cobalt on Cu(001)

### A.2.1. Potential energy surface

Fig. A.2 shows the PES as calculated with LDA++ and PBE++ with  $U = 3.8$  eV, 4.0 eV and 4.2 eV. For PBE++ there is no shift of the adsorption distance of Co on Cu(100), whereas for LDA++ the minimum shifts from 1.52 Å to 1.54 Å by increasing  $U$  from 4.0 eV to 4.2 eV. The adsorption distance of LDA++ does not further increase upon increasing  $U$  from 4.2 eV to 5.0 eV (see Fig. A.3, but note that the abscissa is reduced compared to Fig. A.2).

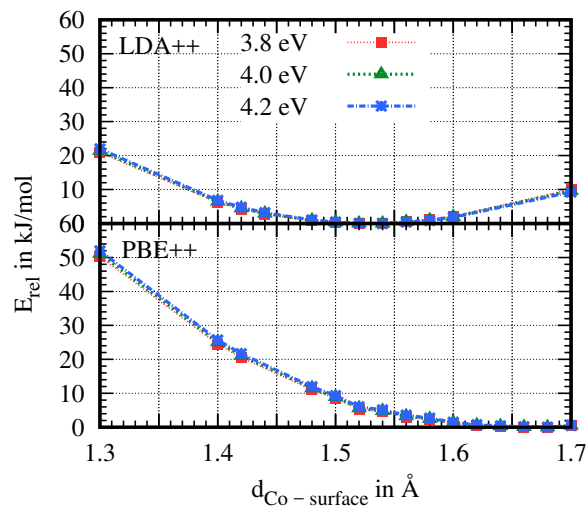


Figure A.2.: Relative energies as obtained from DFT++ for different adsorption distances of Co on Cu(100). The DFT++ calculations were performed at  $\beta = 100 \text{ eV}^{-1}$ . The DFT++ results for  $U = 3.8 \text{ eV}$ ,  $4.0 \text{ eV}$  and  $4.2 \text{ eV}$  are nearly on top of each other. The exchange parameter for all values of  $U$  is  $J = 0.9 \text{ eV}$ .

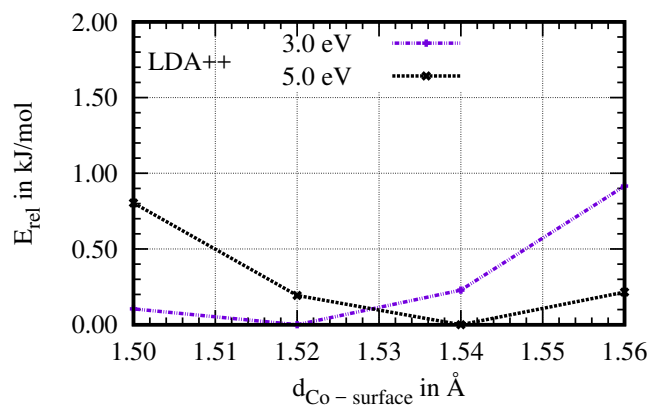


Figure A.3.: Relative energies as obtained from LDA++ for different adsorption distances of Co on Cu(100). The LDA++ calculations were performed at  $\beta = 100 \text{ eV}^{-1}$  for  $U = 3.0 \text{ eV}$  and  $5.0 \text{ eV}$ , both with  $J = 0.9 \text{ eV}$ .

### A.2.2. Hybridization functions

In Fig. A.4, the hybridization function of Co on Cu(100) as obtained from PBE is shown for selected values of  $d_{\text{Co-surface}}$ . By comparison with Fig. 5.6 of Section 5.4, one can notice that both functionals (LDA and PBE) yield a similar hybridization function at all adsorption distances shown here.

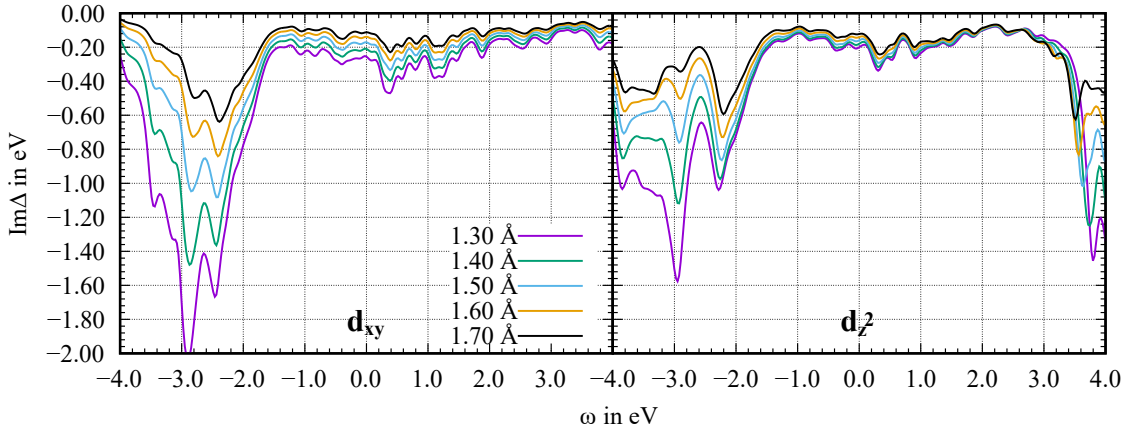


Figure A.4.: Imaginary part of the hybridization function for the Co  $3d_{xy}$  and the Co  $3d_{z^2}$  orbital as obtained from PBE, for selected values of  $d_{\text{Co-surface}}$ .

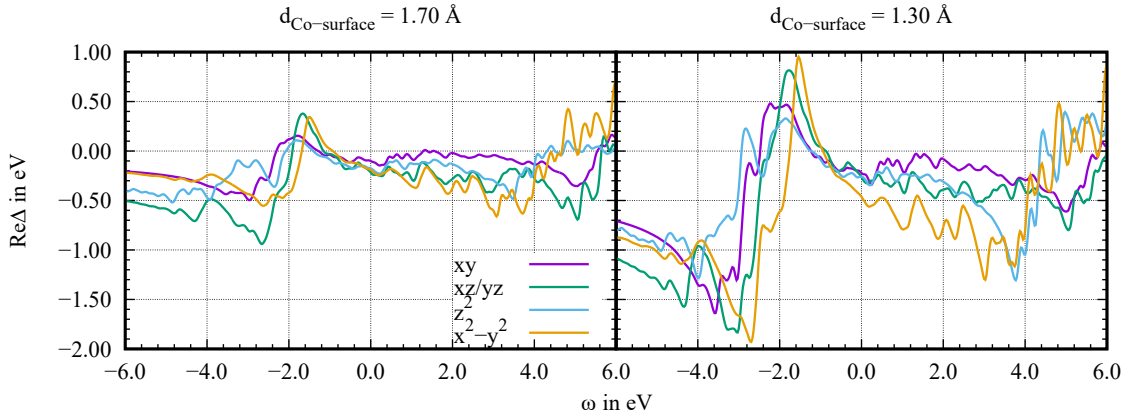


Figure A.5.: Real part of the hybridization function of all Co  $3d$  orbitals at  $d_{\text{Co-surface}} = 1.70 \text{ \AA}$  and  $1.30 \text{ \AA}$ . Results are obtained from LDA.

Fig. A.5 shows the real part of the hybridization function of Co on Cu(100) at  $1.30 \text{ \AA}$  and  $1.70 \text{ \AA}$  as obtained from LDA. The real part of the hybridization function can be seen as the energy/frequency dependent shift of the impurity level. By comparing  $\text{Re}\Delta(\omega)$  for both distances, one can see that the shift of the

impurity levels as a function of the energy is larger if Co is closer to the Cu(100) surface.

### A.2.3. Self-energies

In Fig. A.6 we provide  $\text{Im}\Sigma$  as obtained from DFT++ ( $U = 4.0$  eV and  $J = 0.9$  eV at  $\beta = 100^{-1}$  eV) at selected values for the adsorption distances for the Co  $3d_{xz/yz}$  and the  $3d_{x^2-y^2}$  orbital. Note that in contrast to Fig. 5.7 of Section 5.4 the abscissa in Fig.A.6 is reduced.

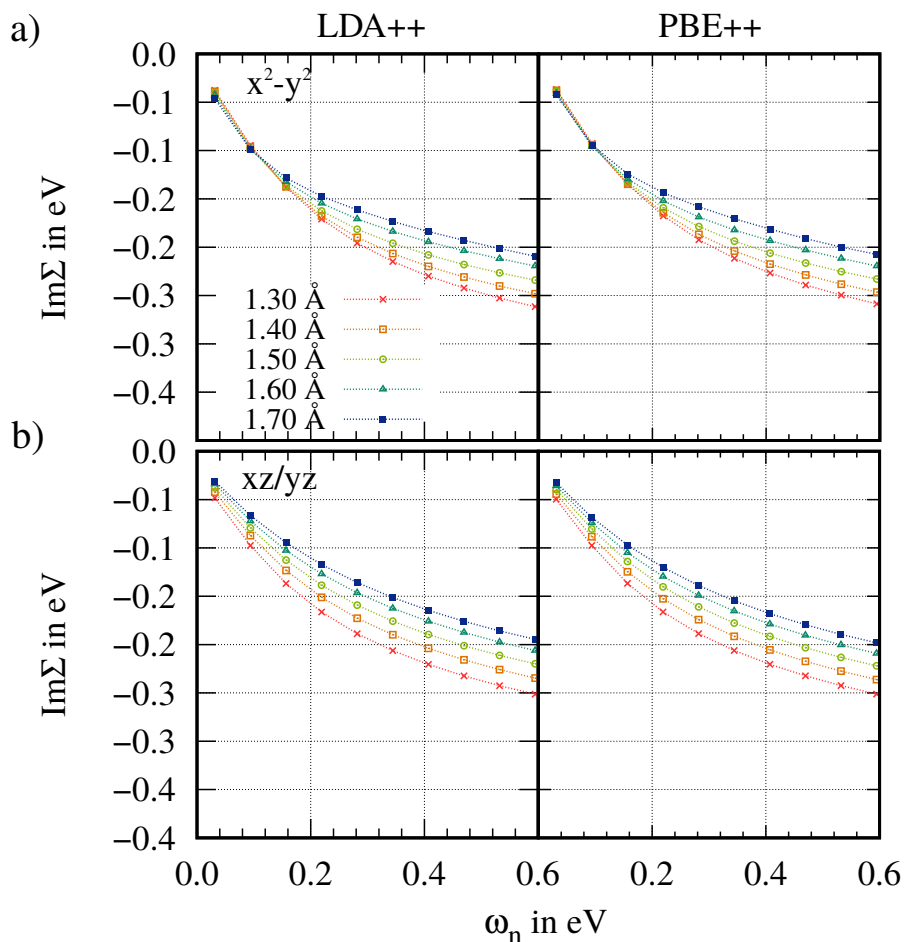


Figure A.6.: Self energies obtained from DFT++ at  $\beta = 100$  eV $^{-1}$  with  $U = 4.0$  eV and  $J = 0.9$  eV. a)  $\text{Im}\Sigma$  for the Co  $3d_{x^2-y^2}$  orbital as obtained from LDA++ and PBE++. b)  $\text{Im}\Sigma$  for the Co  $3d_{xz/yz}$  orbital as obtained from LDA++ and PBE++.

## A.2.4. PBE results

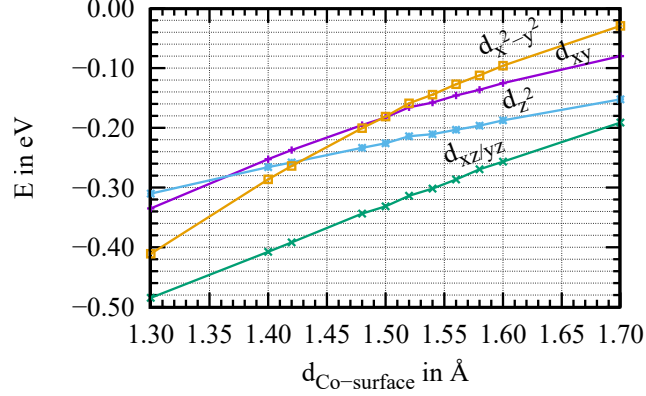


Figure A.7.: Static crystal-field splitting (i.e.  $3d$ -orbital energies of Co) of the Co  $3d$  shell as obtained from PBE (spin-unpolarized), as a function of the adsorption distance. The Fermi level is set to 0.0 eV.

Table A.1.: Estimated Kondo temperature as obtained from a one-band model with a constant hybridization.  $\text{Im}\Delta(0)$  is the value of the imaginary part of the hybridization function at  $\omega = 0$  eV (Fermi level).  $\epsilon_{xy/z^2}$  are the energies of the Co  $d_{xy/z^2}$  orbitals related to the Fermi level. Values taken here are obtained from PBE, and for  $U$  we have chosen 4.0 eV. For the estimation of the Kondo temperature  $T_K$  see Equation (3.2). Experimental value for  $T_K = 88 \pm 4$  K [200–202].

$d_{\text{Co-surf.}}$	$-\text{Im}\Delta_{xy}(0)$	$-\text{Im}\Delta_{z^2}(0)$	$\epsilon_{xy}$	$\epsilon_{z^2}$	$T_{K,xy}$	$T_{K,z^2}$
1.30 Å	0.255	0.200	-0.335	-0.310	133.4	58.55
1.40 Å	0.210	0.180	-0.253	-0.266	153.4	63.95
1.50 Å	0.171	0.159	-0.183	-0.226	195.0	69.52
1.60 Å	0.139	0.140	-0.125	-0.187	276.2	79.54
1.70 Å	0.112	0.122	-0.080	-0.152	428.0	94.00

In Fig. A.7 the Co  $3d$  crystal-field splitting as a function of the adsorption distance is shown, as obtained from PBE. Comparison with Fig. 5.5 of Section 5.4 shows that both functionals predict a similar crystal-field splitting at all adsorption distances under study here.

In Tab. A.1 we provide the estimated Kondo temperatures as obtained from Equation (3.2). For  $\epsilon_{xy/z^2}$  and  $\text{Im}\Delta_{xy,z^2}$  we used the values as obtained from spin-unpolarized PBE.

## A.2.5. Configuration- and spin state probabilities

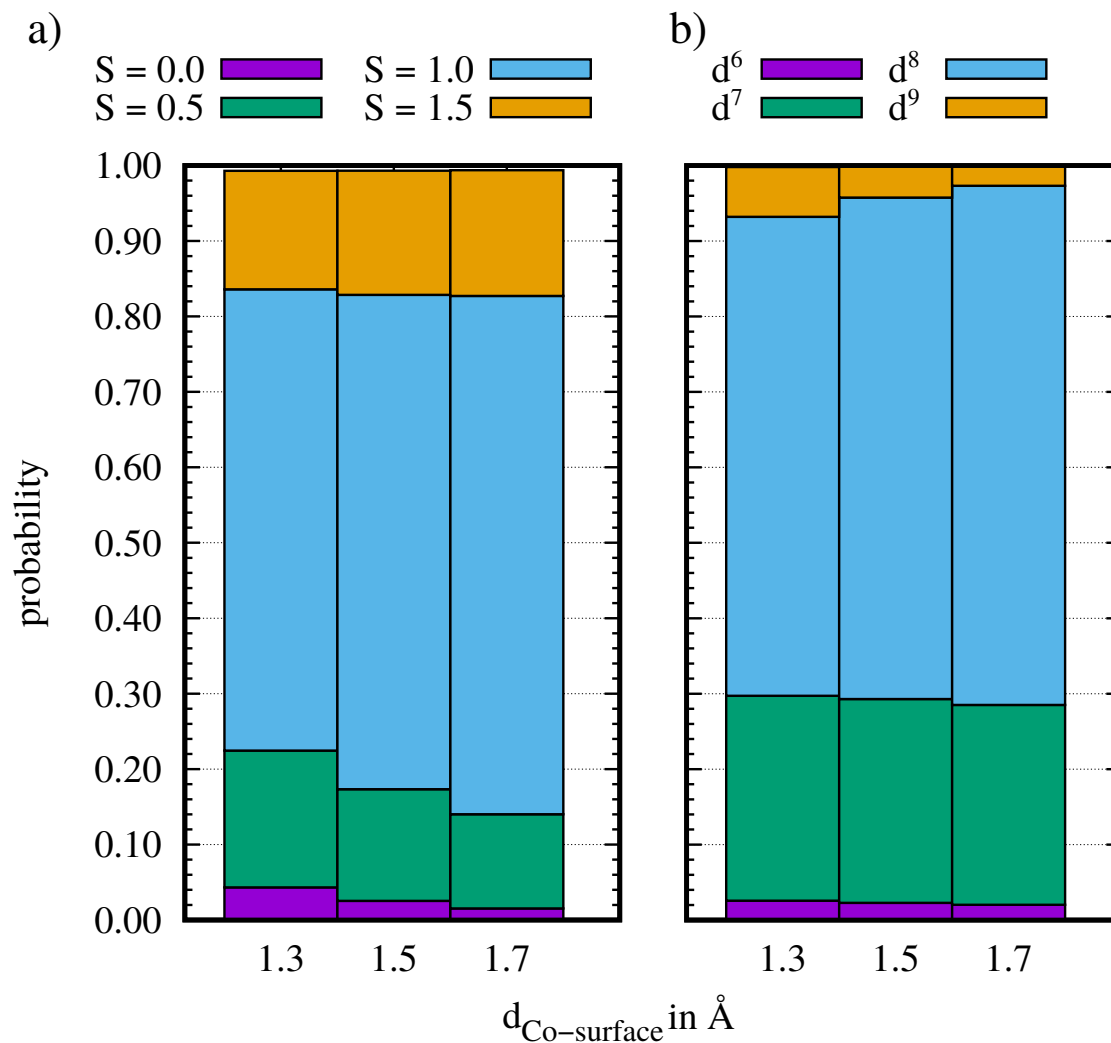


Figure A.8.: a) Most probable spin states ( $S$ ) and b) atomic configuration as obtained from LDA++ for Co/Cu(001) for selected values of  $d_{\text{Co-surface}}$ . The LDA++ (FLL) calculations were performed at  $\beta = 100 \text{ eV}^{-1}$ ,  $U = 4.0 \text{ eV}$  and  $J = 0.9 \text{ eV}$ .

From Fig. A.8 one can see that at all adsorption distances under study here the Co atom is predominantly in a  $d^8$ ,  $S=1$  configuration. The character of these configuration slightly increases for larger adsorption distances.

## A.2.6. Specification of the unit cell

Table A.2.:  $xyz$ -coordinates of all atoms contained in the unit cell with  $d_{\text{Co-surface}} = 1.30 \text{ \AA}$ . Values are given in  $\text{\AA}$ .

Atom	$x$ -coord.	$y$ -coord.	$z$ -coord.	Atom	$x$ -coord.	$y$ -coord.	$z$ -coord.
Cu	1.807445	9.037225	-7.229780	Cu	3.614890	5.422335	-1.807445
Cu	0.000000	7.229780	-7.229780	Cu	5.422335	5.422335	0.000000
Cu	0.000000	9.037225	-5.422335	Cu	3.614890	3.614890	0.000000
Cu	1.807445	9.037225	-3.614890	Cu	5.422335	3.614890	-1.807445
Cu	0.000000	7.229780	-3.614890	Cu	9.037225	5.422335	-7.229780
Cu	1.807445	7.229780	-5.422335	Cu	7.229780	3.614890	-7.229780
Cu	0.000000	9.037225	-1.807445	Cu	7.229780	5.422335	-5.422335
Cu	1.807445	9.037225	0.000000	Cu	9.037225	5.422335	-3.614890
Cu	0.000000	7.229780	0.000000	Cu	7.229780	3.614890	-3.614890
Cu	1.807445	7.229780	-1.807445	Cu	9.037225	3.614890	-5.422335
Cu	5.422335	9.037225	-7.229780	Cu	7.229780	5.422335	-1.807445
Cu	3.614890	7.229780	-7.229780	Cu	9.037225	5.422335	0.000000
Cu	3.614890	9.037225	-5.422335	Cu	7.229780	3.614890	0.000000
Cu	5.422335	9.037225	-3.614890	Cu	9.037225	3.614890	-1.807445
Cu	3.614890	7.229780	-3.614890	Cu	1.807445	1.807445	-7.229780
Cu	5.422335	7.229780	-5.422335	Cu	0.000000	0.000000	-7.229780
Cu	3.614890	9.037225	-1.807445	Cu	0.000000	1.807445	-5.422335
Cu	5.422335	9.037225	0.000000	Cu	1.807445	1.807445	-3.614890
Cu	3.614890	7.229780	0.000000	Cu	0.000000	0.000000	-3.614890
Cu	5.422335	7.229780	-1.807445	Cu	1.807445	-0.000000	-5.422335
Cu	9.037225	9.037225	-7.229780	Cu	0.000000	1.807445	-1.807445
Cu	7.229780	7.229780	-7.229780	Cu	1.807445	1.807445	0.000000
Cu	7.229780	9.037225	-5.422335	Cu	0.000000	0.000000	0.000000
Cu	9.037225	9.037225	-3.614890	Cu	1.807445	-0.000000	-1.807445
Cu	7.229780	7.229780	-3.614890	Cu	5.422335	1.807445	-7.229780
Cu	9.037225	7.229780	-5.422335	Cu	3.614890	-0.000000	-7.229780
Cu	7.229780	9.037225	-1.807445	Cu	3.614890	1.807445	-5.422335
Cu	9.037225	9.037225	0.000000	Cu	5.422335	1.807445	-3.614890
Cu	7.229780	7.229780	0.000000	Cu	3.614890	-0.000000	-3.614890
Cu	9.037225	7.229780	-1.807445	Cu	5.422335	-0.000000	-5.422335
Cu	1.807445	5.422335	-7.229780	Cu	3.614890	1.807445	-1.807445
Cu	0.000000	3.614890	-7.229780	Cu	5.422335	1.807445	0.000000
Cu	0.000000	5.422335	-5.422335	Cu	3.614890	-0.000000	0.000000
Cu	1.807445	5.422335	-3.614890	Cu	5.422335	-0.000000	-1.807445
Cu	0.000000	3.614890	-3.614890	Cu	9.037225	1.807445	-7.229780
Cu	1.807445	3.614890	-5.422335	Cu	7.229780	-0.000000	-7.229780
Cu	0.000000	5.422335	-1.807445	Cu	7.229780	1.807445	-5.422335
Cu	1.807445	5.422335	0.000000	Cu	9.037225	1.807445	-3.614890
Cu	0.000000	3.614890	0.000000	Cu	7.229780	-0.000000	-3.614890
Cu	1.807445	3.614890	-1.807445	Cu	9.037225	-0.000000	-5.422335
Cu	5.422335	5.422335	-7.229780	Cu	7.229780	1.807445	-1.807445
Cu	3.614890	3.614890	-7.229780	Cu	9.037225	1.807445	0.000000
Cu	3.614890	5.422335	-5.422335	Cu	7.229780	-0.000000	0.000000
Cu	5.422335	5.422335	-3.614890	Cu	9.037225	-0.000000	-1.807445
Cu	3.614890	3.614890	-3.614890	Co	5.422335	3.614890	1.30
Cu	5.422335	3.614890	-5.422335				

In Tab. A.2 we provide the coordinates of all atoms in the unit cell used in our calculations. Note that the Cu atoms were kept frozen, and only the Co  $z$ -coordinate was varied between 1.30 Å and 1.70 Å.

### A.3. $\text{Co}(\text{CO})_n/\text{Cu}(001)$

#### A.3.1. Information about the $\text{Co}(\text{CO})_n/\text{Cu}(001)$ atomistic structures

In Table A.3 we provide a collection of structural parameters of  $\text{Co}(\text{CO})_2/\text{Cu}(001)$  after optimizing the atomistic structure with different DFT protocols. In all cases the adsorbate shows  $C_{2v}$  symmetry, and we observed no magnetization on the adsorbate, except for BLYP-D3+ $U$  with a magnetization of 1.0  $\mu_B$ . Spin polarized DFT here leads to an increased adsorption distance (2.66 Å), which is roughly 0.2 Å to 0.3 Å larger than for the remaining (spin-unpolarized) optimized  $\text{Co}(\text{CO})_2/\text{Cu}(001)$  structures.

Table A.3.: Structural parameters for  $\text{Co}(\text{CO})_2/\text{Cu}(001)$  as obtained from different electronic structure methods and optimization schemes. For BLYP-D3+ $U$  we used  $U = 4.0$  eV and  $J = 0.9$  eV. In all cases Grimme’s dispersion correction was used (DFT-D3).

	PBE <sub>fix</sub>	PBE	BLYP <sub>fix</sub>	BLYP	BLYP+ $U$
$d_{\text{C-Co}}$	1.74	1.74	1.76	1.79	1.80
$d_{\text{C-surf.}}$	2.37	2.48	2.44	2.43	2.66
$d_{\text{Co-surf.}}$	1.33	1.54	1.39	1.60	1.74
$\phi_{\text{C-Co-C}}$	106.5	110.7	107.7	111.9	119.4

In Table A.4 we provide a collection of structural parameters of  $\text{Co}(\text{CO})_3/\text{Cu}(001)$  after optimizing the atomistic structure with different DFT protocols. Each of the optimizations leads to a magnetization of 0.0  $\mu_B$  (e.g. closed-shell character of the adsorbate).

Table A.4.: Structural parameters for  $\text{Co}(\text{CO})_3/\text{Cu}(001)$  as obtained from different electronic structure methods and optimization schemes. For BLYP-D3+ $U$  we used  $U = 4.0$  eV and  $J = 0.9$  eV. In all cases Grimme’s dispersion correction was used (DFT-D3).

	PBE <sub>fix</sub>	BLYP	BLYP+ $U$
$d_{\text{C}^{\text{t}}-\text{Co}}$	1.77	1.79	1.78
$d_{\text{C}^{\text{b}}-\text{Co}}$	1.76	1.78	1.76
$d_{\text{C}^{\text{t}}-\text{surf.}}$	2.27	2.43	2.43
$d_{\text{C}^{\text{b}}-\text{surf.}}$	2.30	2.45	2.48
$d_{\text{Co}-\text{surf.}}$	1.58	1.75	1.76

In Tables A.5 and A.6 we provide a collection of structural parameters after optimizing the atomistic structure with different DFT protocols for  $\text{Co}(\text{CO})_4/\text{Cu}(001)$  in  $C_{4v}$  and  $C_{2v}$  symmetry. For the truncated cluster optimization (PBE (cluster)) we used PBE-D3/def2-TZVP [183–185, 238, 239] as implemented in TURBOMOLE [181]. The resulting structure of  $\text{Co}(\text{CO})_4$  within this optimization protocol, shows a  $C_{2v}$  symmetry on Cu(001), as shown in Fig. A.9 (a  $C_{4v}$  symmetry could not be obtained).

Table A.5.: Structural parameters for  $\text{Co}(\text{CO})_4/\text{Cu}(001)$  in  $C_{4v}$  symmetry as obtained from different electronic structure methods and optimization schemes. For BLYP-D3+ $U$  we used  $U = 4.0$  eV and  $J = 0.9$  eV. Compared to the  $C_{2v}$  symmetry, the  $C_{4v}$  symmetry is 0.44 eV (PBE<sub>fix</sub>-D3), 0.31 eV (BLYP-D3), and 0.31 eV (BLYP-D3+ $U$ ) higher in energy. In all cases Grimme’s dispersion correction was used (DFT-D3).

	PBE <sub>fix</sub>	BLYP	BLYP+ $U$
$d_{\text{C}-\text{Co}}$	1.84	1.85	1.84
$d_{\text{C}-\text{surf.}}$	2.15	2.29	2.25
$d_{\text{Co}-\text{surf.}}$	1.69	1.89	1.85
$\phi_{\text{C}-\text{Co}-\text{C}}$	150.8	154.7	154.6

The atomistic structure of  $\text{Co}(\text{CO})_4/\text{Cu}(001)$  in  $C_{2v}$  symmetry as obtained from the cluster optimization is in good agreement with the PBE<sub>fix</sub> results. Furthermore, within a cluster approach (PBE) one finds no spin density on the adsorbate, which agrees with what we have reported in the main article.

Table A.6.: Structural parameters for  $\text{Co}(\text{CO})_4/\text{Cu}(001)$  in  $C_{2v}$  symmetry as obtained from different electronic structure methods and optimization schemes. The index “fix” means that the cell shape was kept fixed. For BLYP-D3+ $U$  we used  $U = 4.0$  eV and  $J = 0.9$  eV. PBE (cluster) was calculated with TURBOMOLE. In all cases Grimme’s dispersion correction was used (DFT-D3). Distances in Å and angles in °.

	PBE (cluster)	PBE <sub>fix</sub>	BLYP	BLYP+ $U$
$d_{\text{C1-Co}}$	1.91	1.90	1.91	1.88
$d_{\text{C2-Co}}$	1.80	1.78	1.80	1.78
$d_{\text{C1-surf.}}$	2.00	1.98	2.44	2.16
$d_{\text{C2-surf.}}$	2.74	2.82	2.98	3.22
$d_{\text{Co-surf.}}$	1.96	1.90	2.07	2.26
$\phi_{\text{C1-Co-C1}}$	173	174.8	197.2	173.8
$\phi_{\text{C2-Co-C2}}$	122	118.3	119.1	115.3

### A.3.2. Non-local correlation functional for structural optimization of $\text{Co}(\text{CO})_4/\text{Cu}(001)$

Table A.7.: Structural parameters for  $\text{Co}(\text{CO})_4/\text{Cu}(001)$  in  $C_{2v}$  and  $C_{4v}$  symmetry as obtained from the vdW-DF functional proposed by Dion *et al.* [234], and the vdW-DF2 functional of Langreth and Lundqvist *et al.* [240] (parentheses). Distances in Å and angles in °.

	$C_{2v}$	$C_{4v}$
$d_{\text{C1-Co}}$	1.91 (1.91)	1.85 (1.86)
$d_{\text{C2-Co}}$	1.81 (1.83)	1.85 (1.86)
$d_{\text{C1-surf.}}$	2.17 (2.23)	2.36 (2.55)
$d_{\text{C2-surf.}}$	3.12 (3.24)	2.36 (2.55)
$d_{\text{Co-surf.}}$	2.17 (2.29)	1.93 (2.16)
$\phi_{\text{C1-Co-C1}}$	179 (177)	153 (1.56)
$\phi_{\text{C2-Co-C2}}$	116 (117)	153 (1.56)

Recently several exchange–correlation functionals have been proposed to treat van der Waals interaction by adding an approximated term for long-range correlation effects [234,240,278–280]. Here, we used the vdW-DF functional developed by Dion *et al.* [234], as well as vdW-DF2 [240] for structural relaxation of  $\text{Co}(\text{CO})_4/\text{Cu}(001)$  with a fixed Cu lattice constant of 3.615 Å [206]. We found that a  $C_{2v}$  symmetry

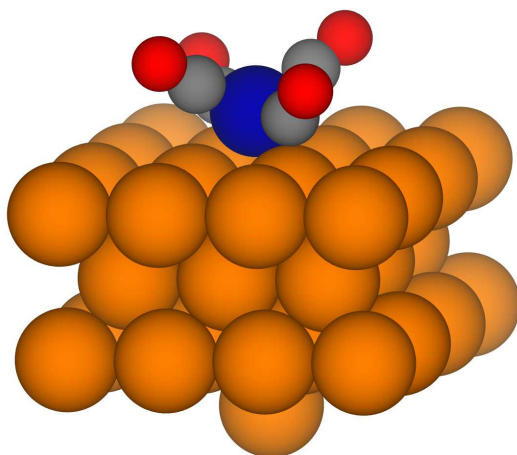


Figure A.9.: Optimized  $\text{Co}(\text{CO})_4/\text{Cu}(001)$  as obtained from a truncated cluster approach. The optimization was done with PBE-D3/def2-TZVP.

is favored by about 70 kJ/mol (vdW-DF) and 73 kJ/mol (vdW-DF2) over a  $C_{4v}$  of  $\text{Co}(\text{CO})_4/\text{Cu}(001)$ . Furthermore, the electronic structure of  $\text{Co}(\text{CO})_4/\text{Cu}(001)$  converges for both symmetries to a closed-shell solution, with both vdW-DF and vdW-DF2 functionals (i.e. there is no spin-polarization on the adsorbate).

To summarize, both the atomistic and electronic structure as obtained from DFT (vdW-DF and vdW-DF2) are in agreement with the data reported in the main article, suggesting that there is no further improvement compared to the reported optimization protocols, with respect to the experimentally observed  $C_{4v}$  symmetry and spin state.

### A.3.3. Ligand flipping in $\text{Co}(\text{CO})_4/\text{Cu}(001)$ ( $C_{2v}$ )

A hypothetical mechanism for  $\text{Co}(\text{CO})_4/\text{Cu}(001)$  ( $C_{2v}$ ) to mimic the four-fold symmetry in the experimentally observed STM [1], is a flipping of the CO ligands as depicted in Figure A.10. The energy barrier<sup>1</sup> is, however, too large for being reasonable at the low temperatures applied in the STM experiment.

---

<sup>1</sup>The calculations are based on the BLYP+ $U$  optimized structure as explained in Section 8.3. The single point calculations were done with BLYP+ $U$ .

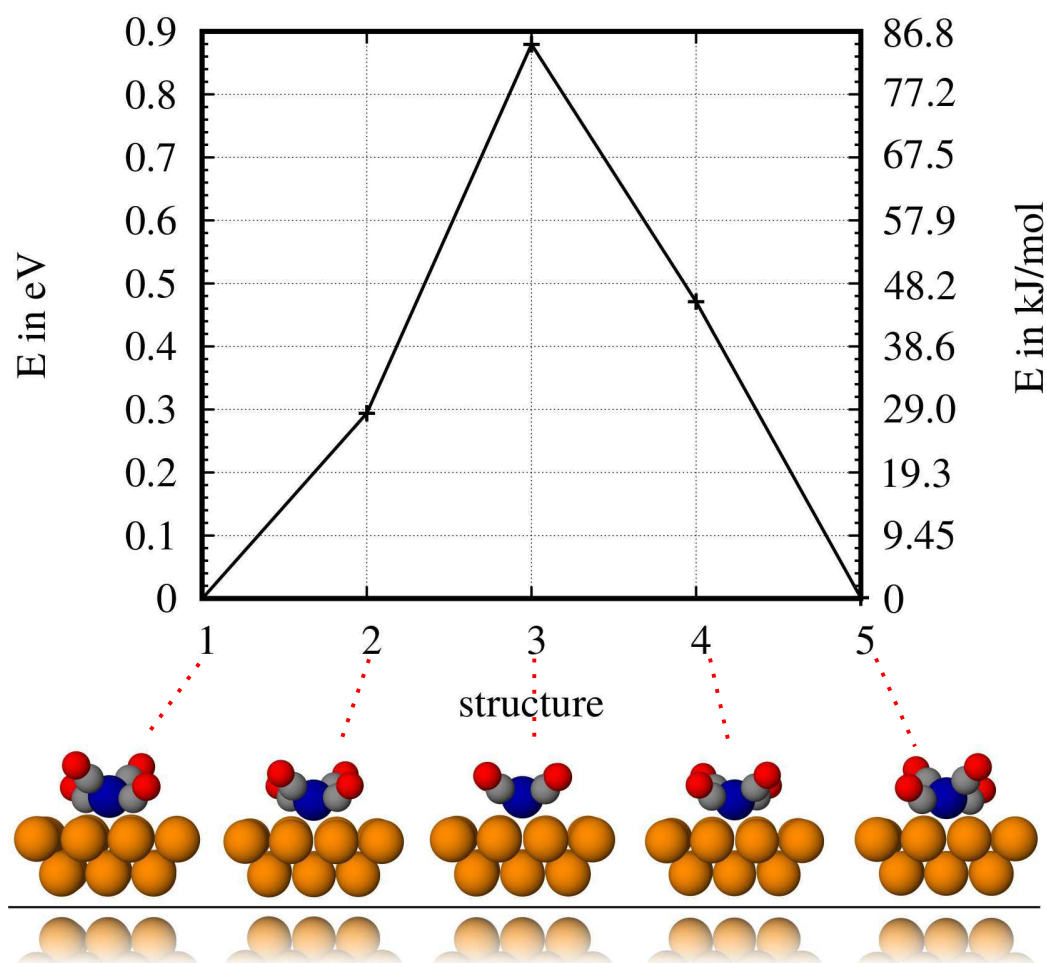


Figure A.10.: Potential energy surface for CO flipping in  $\text{Co}(\text{CO})_4/\text{Cu}(001)$  ( $C_{2v}$ ).

### A.3.4. Spectral properties of $\text{Co}(\text{CO})_3/\text{Cu}(001)$ and $\text{Co}(\text{CO})_4/\text{Cu}(001)$ in $C_{2v}$ symmetry

For  $\text{Co}(\text{CO})_3/\text{Cu}(001)$ , none of the Co  $3d$  orbitals exhibit a sharp feature at the Fermi energy in the spectral function (Figure A.11 a)). For  $\text{Co}(\text{CO})_4/\text{Cu}(001)$  in  $C_{2v}$  symmetry (Figure A.11 b)), there is a small feature for the Co  $3d_{xz}$  orbital at the Fermi energy, but this is already present in the case of  $U = 0.0$  eV (see Figure A.11 b)). For this reason, this feature is not due to a Kondo effect, as discussed in Section A.3.5 in more detail.

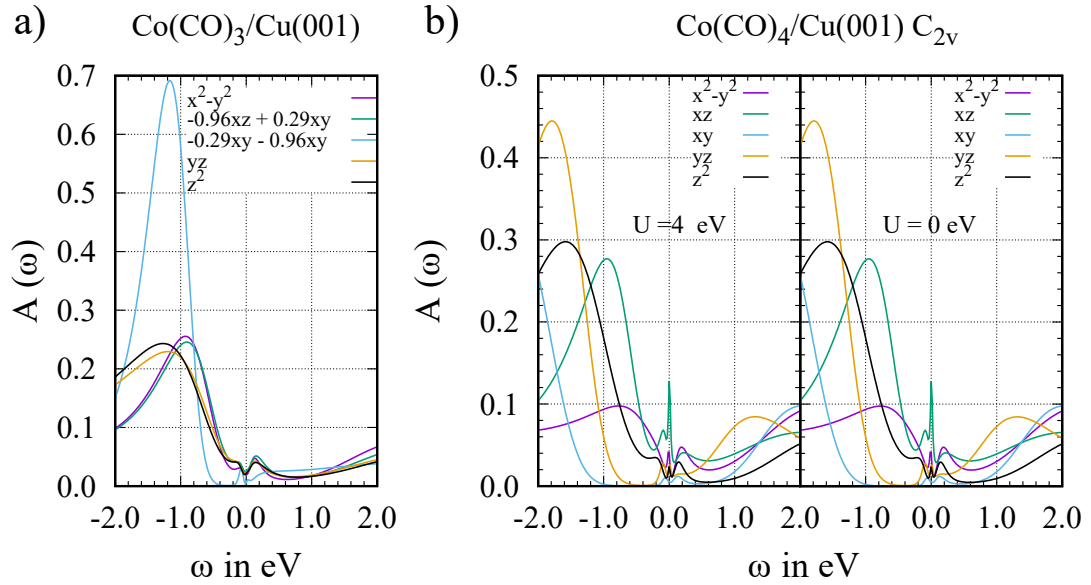


Figure A.11.: Spectral functions as obtained from PBE++ for a)  $\text{Co}(\text{CO})_3$ , b)  $\text{Co}(\text{CO})_4$  in  $C_{2v}$  symmetry on  $\text{Cu}(100)$  at  $\beta = 100 \text{ eV}^{-1}$  ( $T = 116 \text{ K}$ ). Here the fully localized limit was used with  $U = 4.0 \text{ eV}$  and  $J = 0.9 \text{ eV}$ . In case of  $\text{Co}(\text{CO})_4$  in  $C_{2v}$  symmetry the spectral function obtained with  $U = 0.0 \text{ eV}$  is shown, too.

### A.3.5. High temperature spin–spin correlation of $\text{Co}(\text{CO})_3/\text{Cu}(001)$ and $\text{Co}(\text{CO})_4/\text{Cu}(001)$ in $C_{2v}$ symmetry

For  $\text{Co}(\text{CO})_3/\text{Cu}(001)$ ,  $\chi(\tau)$  rapidly drops to zero for all Co  $3d$  orbitals (Figure A.12), proving the lack of a localized magnetic moment which could potentially be screened due to a Kondo effect. This suggests a rather closed-shell character on this adsorbate, which could be caused by a too strong interaction with the CO ligands. A related effect can be observed by stretching the bond of a  $\text{H}_2$  molecule, that shows a transition from a closed to an open-shell singlet character at a larger bond distance (i.e., this reduces the interaction of both  $1s$  orbitals which each other).

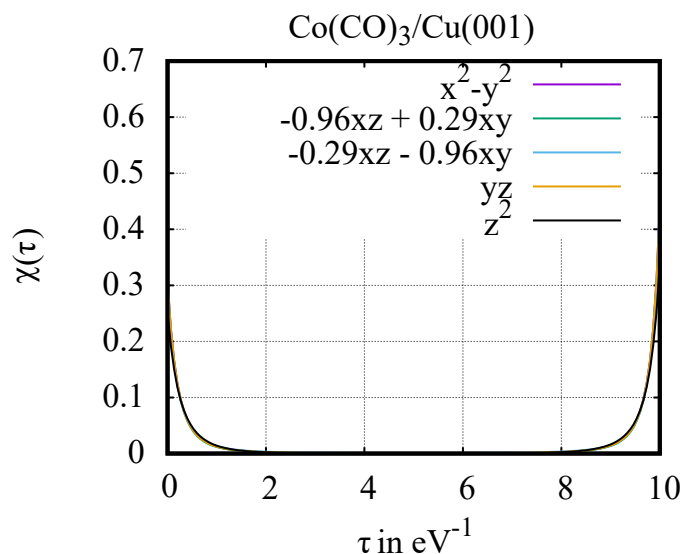


Figure A.12.: Spin–spin correlation function  $\chi(\tau)$  as obtained from PBE++ at  $\beta = 10 \text{ eV}^{-1}$  ( $T = 1160 \text{ K}$ ) of  $\text{Co}(\text{CO})_3/\text{Cu}(001)$  (based on the BLYP-D3+ $U$  optimized structure). The PBE++ calculation was done with  $U = 4.0 \text{ eV}$ ,  $J = 0.9 \text{ eV}$ , and using the fully localized limit for estimation the double-counting correction.

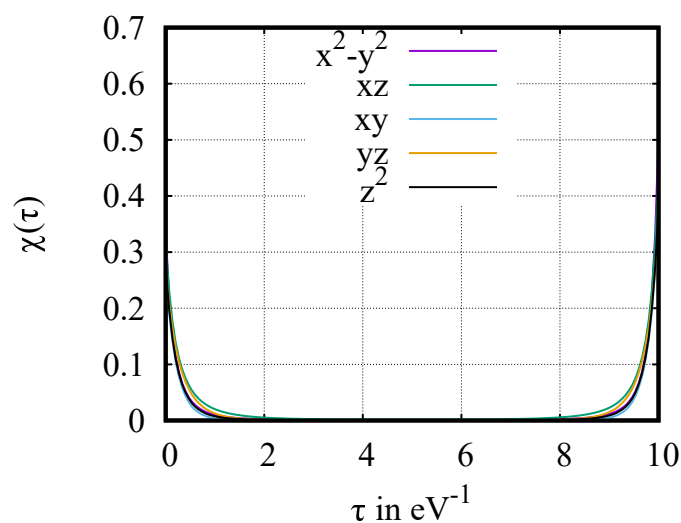


Figure A.13.: Spin–spin correlation function  $\chi(\tau)$  as obtained from PBE++ at  $\beta = 10 \text{ eV}^{-1}$  ( $T = 1160 \text{ K}$ ) of  $\text{Co}(\text{CO})_4/\text{Cu}(001)$  in  $C_{2v}$  symmetry (based on the BLYP-D3+ $U$  optimized structure). The PBE++ calculation was done with  $U = 4.0 \text{ eV}$ ,  $J = 0.9 \text{ eV}$ , and using the fully localized limit for estimation the double-counting correction.

he spin–spin correlation function at  $T = 1160$  K is shown in Figure A.13 for  $\text{Co}(\text{CO})_4/\text{Cu}(001)$  in  $C_{2v}$  symmetry, and reveals that there is no stable local moment at high temperatures ( $\chi(\beta/2)$  is zero for all Co 3d orbitals), which makes an interpretation in terms of a low temperature screening due to a Kondo effect impossible.

### A.3.6. Dependence of the spin–spin correlation function on $U$ and $J$

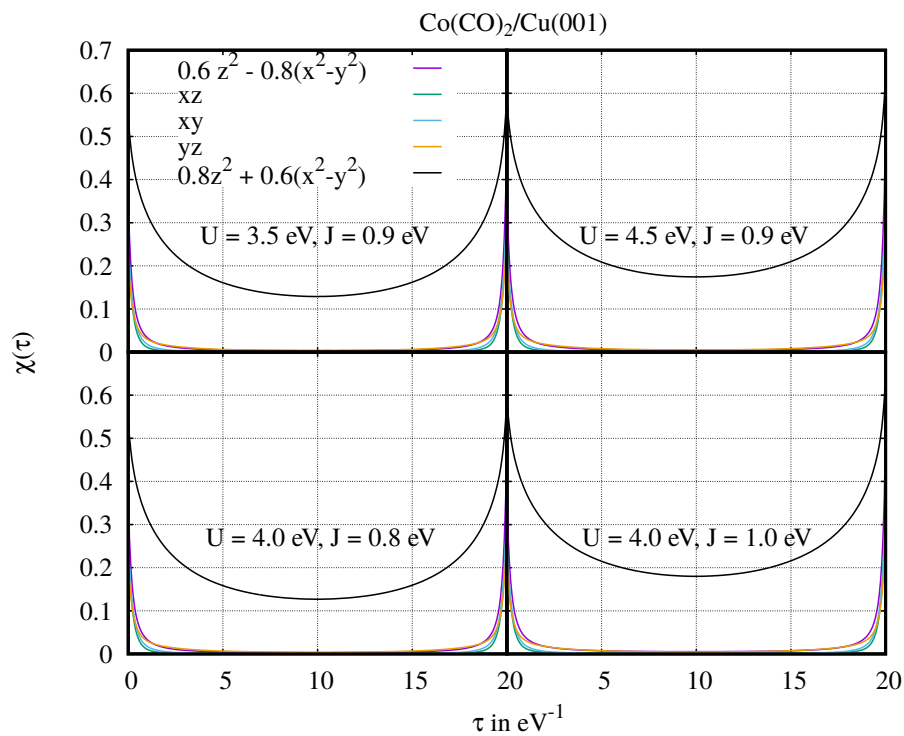


Figure A.14.: Spin–spin correlation function of the Co 3d orbitals at  $T = 580$  K, as obtained from PBE++ for a dicarbonyl complex on Cu(001) with different combinations of  $U$  and  $J$ .

Properties obtained from a DFT++ approach can depend delicately on the chosen values for the average Coulomb interaction  $U$  and the average exchange interaction  $J$ . For the reason that there are no first-principles values available for the carbonyl cobalt complexes on Cu(001), we have tested different combinations of  $U$  and  $J$  against changes in the spin–spin correlation function.

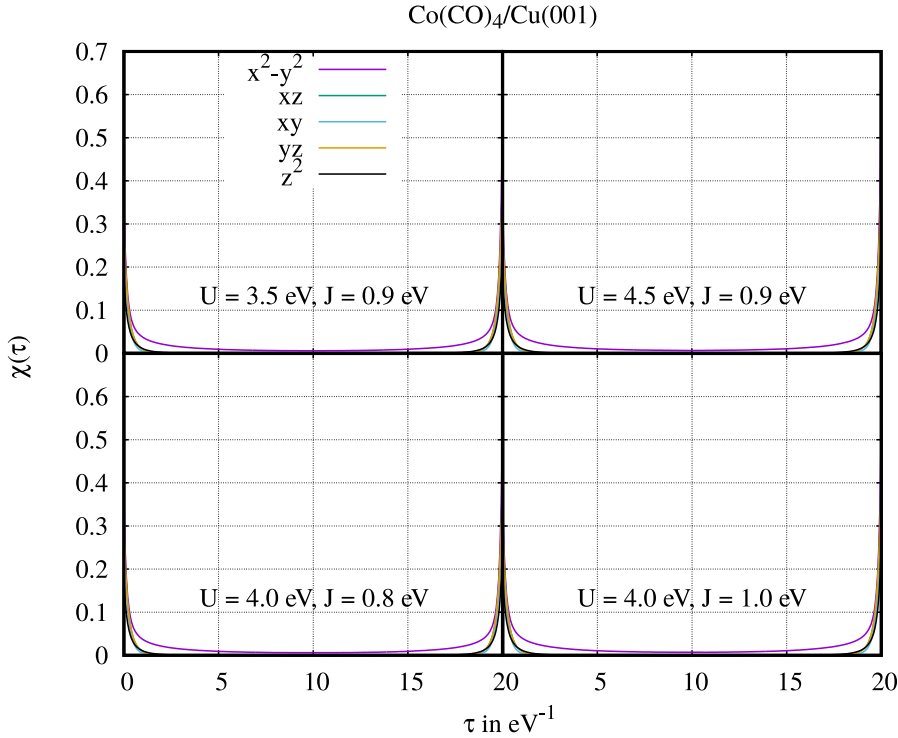


Figure A.15.: Spin–spin correlation function of the Co 3d orbitals at  $T = 580$  K, as obtained from PBE++ for a tetracarbonyl complex on Cu(001) in  $C_{4v}$  symmetry with different combinations of  $U$  and  $J$ .

For  $T = 580$  K, we provide the spin–spin correlation function of a dicarbonyl cobalt complex on Cu(001) in Figure A.14. For all Co 3d orbitals,  $\chi(\tau)$  is unaffected by changing  $U$  and  $J$ , except the Kondo relevant orbital ( $3d_{0.8z^2+0.6(x^2-y^2)}$ ). For this orbital the value of  $\chi(\beta/2)$  is slightly increased for larger values of  $U$  and  $J$ , which would potentially shift the transition to the Fermi liquid regime to lower temperatures. In case of a tetracarbonyl cobalt complex on Cu(001), the spin–spin correlation function is almost unaffected for all Co 3d orbitals (Figure A.15) upon changing  $U$ , or  $J$  within the values under consideration here.

Altogether, these data suggest that varying  $U$  and  $J$  within reasonable limits does not change the qualitative behavior reported in this work.

## A.3.7. Molecular orbital diagram of CO

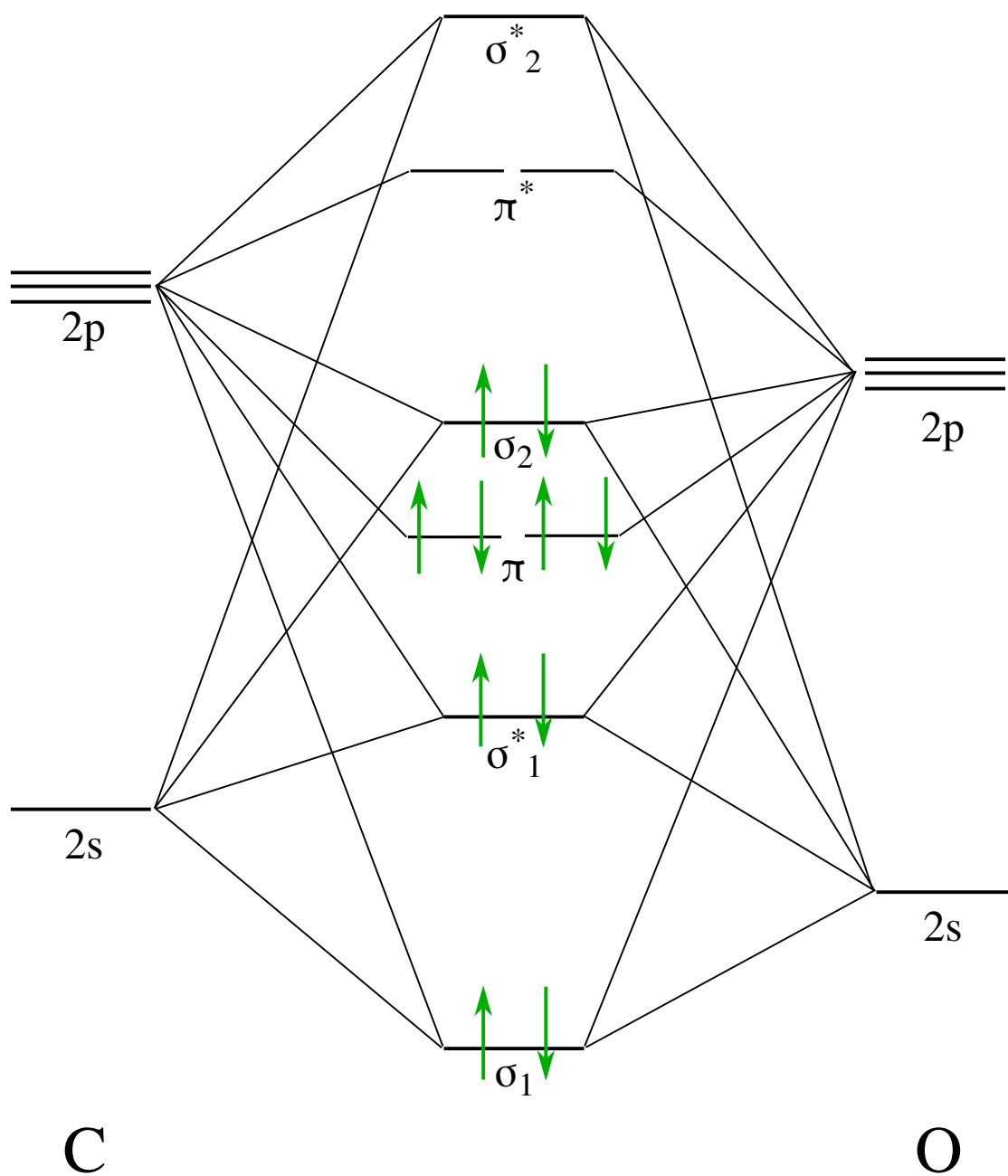


Figure A.16.: Schematic representation of a molecular orbital diagram of a CO molecule.

## B. List of publications

### B.1. Published

- [A] Marc Philipp Bahlke, Michael Karolak, and Carmen Herrmann, *Interplay between strong correlation and adsorption distances: Co on Cu(001)*, *Phys. Rev. B* **2018**, 97, 035119. (based on Chapter 5)
- [B] Marc Philipp Bahlke, Peter Wahl, Lars Diekhöner and Carmen Herrmann, *Co(CO)<sub>n</sub>/Cu(001): Towards understanding chemical control of the Kondo effect*, *J. Appl. Phys.* **2019**, 125, 142910. (based on Chapter 8)
- [C] Lynn Groß, Marc Philipp Bahlke, Torben Steenbock, Christian Klinke and Carmen Herrmann, *Modeling adsorbate-induced property changes of carbon nanotubes*, *J. Comput. Chem.* **2017**, 38, 861. (not directly related to this work)

### B.2. In preparation

- [D] Marc Philipp Bahlke, Alexander Kowalski, Michael Karolak, Angelo Valli, Carmen Herrmann and Giorgio Sangiovanni, *Kondo screening in Co/Cu(001) with full Coulomb interaction*, to be submitted. (based on Chapter 6)
- [E] Marc Philipp Bahlke and Carmen Herrmann, *Local decomposition of hybridization functions: New insights for the Kondo effect*, in preparation. (based on Chapter 4 and Chapter 9)
- [F] Marc Philipp Bahlke and Carmen Herrmann, *A general problem with approximate Coulomb interaction in DFT++? A comparative study*, in preparation. (based on Chapter 7)

## C. List of chemicals

No hazardous chemicals according to the globally harmonised system of classification and labelling of chemicals (GHS) have been used for the preparation of this thesis.

# Acknowledgement

At this point, I would like to thank the people who were directly or indirectly involved in this thesis.

First of all, I would like to thank Prof. Dr. Carmen Herrmann, who has been supervising me since my bachelor's thesis and has always taken time for professional discussions. I am indebted to her for letting me complete my dissertation in her group, and the trust she put in me. I enjoyed the time in her group a lot, and want to thank her for being such a great teacher.

I want to thank Prof. Dr. A. I. Lichtenstein for agreeing to act as the co-examiner of this work, although this being a thesis in quantum chemistry.

Furthermore, I would like to thank Prof. Dr. Gabriel Bester, and Prof. Dr. Jürgen Heck for being part of my Ph.D. committee members, and for their interest in my work.

I am very grateful for the valuable collaboration with Dr. Michael Karolak. As a physicist, he has shared the perspective onto strongly correlated systems from a different point of view with me and has helped a lot with the translation of topic related vocabulary. Furthermore, I want to thank him for sharing not only his DFT++ code with me, but also for providing me with several scripts, which have helped a lot for analyzing my data. I want to thank him also for proof reading of this thesis. As a friend, he has taken an important part in my life.

I would like to thank my other collaborators. In particular, Peter Wahl (University of St Andrews) and Lars Diekhöner (Aalborg University) for the great work on the carbonyl cobalt complexes on Cu(001). For the project about Co/Cu(001) with full Coulomb interaction, I am grateful to Alexander Kowalski and Prof. Dr. Giorgio Sangiovanni of the University of Würzburg, as well as Angelo Valli (Scuola Internazionale Superiore di Studi Avanzati of Trieste).

Though he kept me from work more often, I would like to thank Martin Sebastian Zöllner, not only for sharing his tool to extract important matrices from a TURBOMOLE calculation, but also for being a friend. Our professional discussions have

---

always given me great pleasure and inspired me. Thank you also for proofreading this thesis.

I would like to thank Dr. Lynn Groß and Dr. Torben Steenbock, who helped me a lot when I joined our group for writing my bachelor's thesis. During the last years, they were always there for technical and topic related questions, and I enjoyed working with them a lot.

In particular I want to thank Jan-Hendrik Jensen, Michael Deffner, Torben Steenbock, and Rukan Nasri for proofreading this thesis.

For valuable discussion concerning different aspects and works in theoretical chemistry, I am grateful to the Herrmann group. But I am also grateful to the people in our group for keeping things going thanks to a good organization.

I am also grateful for the people who work at "Hummel" (the high-performance computation cluster in Hamburg), for technical support. In this direction, special thanks goes to Dr. Hinnerk Stüben and Dr. Thomas Orgis for the excellent support during the time I worked at my dissertation.

For computational resources, and technical support whenever needed, I thank the people of the Norddeutscher Verbund für Hoch- und Höchstleistungsrechnen (HLRN).

Of course, all the work would have been harder without the great technical support of the IT-Service of our department, for which I am grateful.

For all administrative matters at our department and at our institute, I want to thank Ingke Klemm, Susanne Breidohr, and Beate Susemihl.

I thank my family for always being there when I need them. Without the mental support I would never have been able to reach the goal of the path I took. I am grateful to my parents and grandparents not only for the financial support that made my work so much easier, but also for how they raised me and for the things they taught me. Without them, I would not have had the strength and the trust in me to pass the way that I have chosen.

Last but not least, I want to thank the person who I am in love with. She kept me smiling and motivated during the last three and a half year. Thank you Johanna for being always at my side, and making the hard days bearable.

# Bibliography

- [1] P. Wahl, L. Diekhöner, G. Wittich, L. Vitali, M. A. Schneider, K. Kern, *Phys. Rev. Lett.* **2005**, *95*, 166601.
- [2] N. S. Hush, *Ann. N.Y. Acad. Sci.* **2003**, *1006*, 1.
- [3] M. Mitchell Waldrop, *Nature* **2016**, *530*, 144.
- [4] A. H. Flood, J. F. Stoddart, D. W. Steuerman, J. R. Heath, *Science* **2004**, *306*, 2055.
- [5] M. Ratner, *Nat. Nanotechnol.* **2013**, *8*, 378.
- [6] V. K. Joshi, *Eng. Sci. Technol. Int J.* **2016**, *19*, 1503.
- [7] A. Von Hippel, *Science* **1956**, *123*, 315.
- [8] S. Marqués-González, P. J. Low, *Aust. J. Chem.* **2016**, *69*, 244.
- [9] B. Mann, H. Kuhn, *J. Appl. Phys.* **1971**, *42*, 4398.
- [10] A. Aviram, M. A. Ratner, *Chem. Phys. Lett.* **1974**, *29*, 277.
- [11] N. F. Mott, H. Fowler, *Proc. Royal Soc. Lond. A* **1936**, *153*, 699.
- [12] G. Binasch, P. Grünberg, F. Saurenbach, W. Zinn, *Phys. Rev. B* **1989**, *39*, 4828.
- [13] M. N. Baibich, J. M. Broto, A. Fert, F. N. Van Dau, F. Petroff, P. Etienne, G. Creuzet, A. Friederich, J. Chazelas, *Phys. Rev. Lett.* **1988**, *61*, 2472.
- [14] I. McFadyen, E. Fullerton, M. Carey, *MRS Bull.* **2006**, *31*, 379.
- [15] V. Dediu, M. Murgia, F. Maticotta, C. Taliani, S. Barbanera, *Solid State Communications* **2002**, *122*, 181.
- [16] A. Rocha, V. García-Suárez, S. Bailey, C. Lambert, J. Ferrer, S. Sanvito, *Nat. Mater.* **2005**, *4*, 335-9.
- [17] A. Khajetoorians, *Science* **2011**, *332*, 1062.
- [18] J. M. Tour, *Acc. Chem. Res.* **2000**, *33*, 791.

- [19] S. Wolf, D. Awschalom, R. Buhrman, J. Daughton, S. Von Molnar, M. Roukes, A. Y. Chtchelkanova, D. Treger, *Science* **2001**, *294*, 1488.
- [20] P. Avouris, *Acc. Chem. Res.* **2002**, *35*, 1026.
- [21] R. L. Carroll, C. B. Gorman, *Angew. Chem. Int. Ed.* **2002**, *41*, 4378.
- [22] R. Hoffmann, *Solids and Surfaces: A Chemist's View of Bonding in Extended Structures*; Wiley-VCH: New York, 1989.
- [23] P. Coleman, *AIP Conf. Proc.* **2002**, *629*, 79.
- [24] G. Kotliar, D. Vollhardt, *Physics Today* **2004**, *57*, 53.
- [25] E. Morosan, D. Natelson, A. H. Nevidomskyy, Q. Si, *Adv. Mater.* **2012**, *24*, 4896.
- [26] L. Kouwenhoven, L. Glazman, *Physics World* **2001**, *14*, 33.
- [27] S. M. Cronenwett, T. H. Oosterkamp, L. P. Kouwenhoven, *Science* **1998**, *281*, 540.
- [28] T. Choi, S. Bedwani, A. Rochefort, C.-Y. Chen, A. J. Epstein, J. A. Gupta, *Nano Lett.* **2010**, *10*, 4175.
- [29] T. Choi, M. Badal, S. Loth, J.-W. Yoo, C. P. Lutz, A. J. Heinrich, A. J. Epstein, D. G. Stroud, J. A. Gupta, *Nano Lett.* **2014**, *14*, 1196.
- [30] A. Enders, R. Skomski, J. Honolka, *J. Phys.: Condens. Matter* **2010**, *22*, 433001.
- [31] B. Maughan, P. Zahl, P. Sutter, O. L. A. Monti, *J. Phys. Chem. Lett.* **2017**, *8*, 1837.
- [32] A. Zhao, Q. Li, L. Chen, H. Xiang, W. Wang, S. Pan, B. Wang, X. Xiao, J. Yang, J. G. Hou, Q. Zhu, *Science* **2005**, *309*, 1542.
- [33] R. Temirov, A. Lassise, F. Anders, F. Tautz, *Nanotechnology* **2008**, *19*, 065401.
- [34] N. Tsukahara, E. Minamitani, Y. Kim, M. Kawai, N. Takagi, *J. Chem. Phys.* **2014**, *141*, 054702.
- [35] T. Knaak, M. Gruber, C. Lindström, M.-L. Bocquet, J. Heck, R. Berndt, *Nano Lett.* **2017**, *17*, 7146.
- [36] J. Kügel, M. Karolak, A. Krönlein, D. Serrate, M. Bode, G. Sangiovanni, *npj quantum mater* **2018**, *3*, 53.

- [37] A. Lichtenstein, M. Katsnelson, *Phys. Rev. B* **1998**, *57*, 6884.
- [38] W. De Haas, J. De Boer, G. Van den Berg, *Physica* **1934**, *1*, 1115.
- [39] J. Kondo, *Prog. Theor. Phys.* **1964**, *32*, 37.
- [40] A. C. Hewson, *The Kondo Problem to Heavy Fermions*; Cambridge University Press: Cambridge, 1997.
- [41] P. Fulde, *Electron Correlations in Molecules and Solids*; Springer Series in Solid-State Science 100: Berlin, 1991.
- [42] R. D. Mattuck, *A Guide to Feynman Diagrams in the Many-Body Problem*; Dover Publications: New York, 1992.
- [43] P. Nozières, *J. Low Temp. Phys.* **1974**, *17*, 31.
- [44] P. Coleman, *Introduction to Many Body Physics*; Cambridge University Press: 2015.
- [45] J. Reinhold, *Quantentheorie der Moleküle*; Springer Spektrum: Wiesbaden, 2012.
- [46] D. K. Mok, R. Neumann, N. C. Handy, *J. Phys. Chem.* **1996**, *100*, 6225.
- [47] F. Jensen, *Introduction to Computational Chemistry*; John Wiley & Sons: West Sussex, 2011.
- [48] T. Helgaker, P. Jørgensen, J. Olsen, *Molecular Electronic Structure Theory*; John Wiley & Sons, LTD: Chichester, 2000.
- [49] P. Hohenberg, W. Kohn, *Phys. Rev.* **1964**, *136*, B864.
- [50] A. J. Cohen, P. Mori-Sánchez, W. Yang, *Chem. Rev.* **2012**, *112*, 289.
- [51] A. J. Cohen, P. Mori-Sánchez, W. Yang, *Science* **2008**, *321*, 792.
- [52] L. Noodleman, *J. Chem. Phys.* **1981**, *74*, 5737.
- [53] M. E. Ali, S. N. Datta, *J. Phys. Chem. A* **2006**, *110*, 2776.
- [54] Y. Kitagawa, T. Saito, Y. Nakanishi, Y. Kataoka, T. Matsui, T. Kawakami, M. Okumura, K. Yamaguchi, *J. Phys. Chem. A* **2009**, *113*, 15041.
- [55] J. P. Perdew, A. Savin, K. Burke, *Phys. Rev. A* **1995**, *51*, 4531.
- [56] J. A. Pople, P. M. W. Gill, N. C. Handy, *Int. J. Quantum Chem.* **1995**, *56*, 303.
- [57] E. Ruiz, J. Cano, S. Alvarez, P. Alemany, *J. Comput. Chem.* **1999**, *20*, 1391.

- [58] F. Illas, I. de P. R. Moreira, J. M. Bofill, M. Filatov, *Phys. Rev. B* **2004**, *70*, 132414.
- [59] S. Yamanaka, R. Takeda, M. Shoji, Y. Kitagawa, H. Honda, K. Yamaguchi, *Int. J. Quantum Chem.* **2005**, *105*, 605.
- [60] C. R. Jacob, M. Reiher, *Int. J. Quantum Chem.* **2012**, *112*, 3661.
- [61] S. Sinnecker, F. Neese, L. Noodleman, W. Lubitz, *J. Am. Chem. Soc.* **2004**, *126*, 2613.
- [62] C. van Wüllen, *J. Phys. Chem. A* **2009**, *113*, 11535.
- [63] N. J. Beal, T. A. Corry, P. J. O'Malley, *J. Phys. Chem. B* **2018**, *122*, 2881.
- [64] C. Caroli, R. Combescot, P. Nozieres, D. Saint-James, *J. Phys. C: Solid State Phys.* **1971**, *4*, 916.
- [65] D. N. Zubarev, *Soviet Physics Uspekhi* **1960**, *3*, 320.
- [66] J. C. Cuevas, E. Scheer, *Molecular Electronics*; WORLD SCIENTIFIC: 2010.
- [67] M. M. Odashima, B. G. Prado, E. Vernek, *Revista Brasileira de Ensino de Física* **2017**, *39*,.
- [68] P. Fulde, *Correlated Electrons in Quantum Matter*; World Scientific: Singapore, 2012.
- [69] D. Zgid, E. Gull, *New J. Phys.* **2017**, *19*, 023047.
- [70] J. Gräfenstein, E. Kraka, M. Filatov, D. Cremer, *Int. J. Mol. Sci.* **2002**, *3*, 360.
- [71] A. D. Becke, *J. Chem. Phys.* **2003**, *119*, 2972.
- [72] A. D. Becke, *J. Chem. Phys.* **2005**, *122*, 064101.
- [73] C. J. Cramer, M. Włoch, P. Piecuch, C. Puzzarini, L. Gagliardi, *J. Phys. Chem. A* **2006**, *110*, 1991.
- [74] A. D. Becke, *J. Chem. Phys.* **2013**, *138*, 074109.
- [75] J. Kong, E. Proynov, *J. Chem. Theory Comput.* **2016**, *12*, 133.
- [76] C. J. Cramer, D. G. Truhlar, *Phys. Chem. Chem. Phys.* **2009**, *11*, 10757.
- [77] L. Mattheiss, *Phys. Rev. B* **1972**, *5*, 290.
- [78] T. Bredow, A. R. Gerson, *Phys. Rev. B* **2000**, *61*, 5194.
- [79] G. A. Sawatzky, J. W. Allen, *Phys. Rev. Lett.* **1984**, *53*, 2339.

- [80] D. Jacob, S. Kurth, *Nano letters* **2018**, *18*, 2086.
- [81] J. Muscat, A. Wander, N. Harrison, *Chem. Phys. Lett.* **2001**, *342*, 397.
- [82] C. Patterson, *Int. J. Quantum Chem.* **2006**, *106*, 3383.
- [83] A. M. Ferrari, C. Pisani, F. Cinquini, L. Giordano, G. Pacchioni, *J. Chem. Phys.* **2007**, *127*, 174711.
- [84] J. Paier, M. Marsman, K. Hummer, G. Kresse, I. C. Gerber, J. G. Ángyán, *J. Chem. Phys.* **2006**, *124*, 154709.
- [85] X. Ren, I. Leonov, G. Keller, M. Kollar, I. Nekrasov, D. Vollhardt, *Phys. Rev. B* **2006**, *74*, 195114.
- [86] M. Karolak, G. Ulm, T. Wehling, V. Mazurenko, A. Poteryaev, A. Lichtenstein, *J. Electron Spectrosc. Relat. Phenom.* **2010**, *181*, 11.
- [87] M. Schüler, S. Barthel, T. Wehling, M. Karolak, A. Valli, G. Sangiovanni, *Eur. Phys. J. Spec. Top.* **2017**, *226*, 2615.
- [88] P. W. Anderson, *Phys. Rev.* **1961**, *124*, 41.
- [89] J. Hubbard, *Proc. R. Soc. Lond. A* **1963**, *276*, 238.
- [90] J. Hubbard, *Proc. R. Soc. Lond. A* **1964**, *281*, 401.
- [91] V. Anisimov, Y. Izyumov, *Electronic Structure of Strongly Correlated Materials*; Springer Series in Solid-State Sciences 163: Berlin, 2010.
- [92] J. C. Slater, *Phys. Rev.* **1929**, *34*, 1293.
- [93] F. De Groot, J. Fuggle, B. Thole, G. Sawatzky, *Phys. Rev. B* **1990**, *42*, 5459.
- [94] I. Schnell, G. Czycholl, R. Albers, *Phys. Rev. B* **2003**, *68*, 245102.
- [95] A. Hausoel, M. Karolak, E. Şaşoğlu, A. Lichtenstein, K. Held, A. Katanin, A. Toschi, G. Sangiovanni, *Nat. Commun.* **2017**, *8*, 16062.
- [96] V. Anisimov, A. Belozarov, A. Poteryaev, I. Leonov, *Phys. Rev. B* **2012**, *86*, 035152.
- [97] A. Antipov, I. Krivenko, V. Anisimov, A. Lichtenstein, A. Rubtsov, *Phys. Rev. B* **2012**, *86*, 155107.
- [98] E. Şaşoğlu, C. Friedrich, S. Blügel, *Phys. Rev. B* **2011**, *83*, 121101.
- [99] B.-C. Shih, Y. Zhang, W. Zhang, P. Zhang, *Phys. Rev. B* **2012**, *85*, 045132.
- [100] A. McMahan, R. M. Martin, S. Satpathy, *Phys. Rev. B* **1988**, *38*, 6650.

- 
- [101] M. S. Hybertsen, M. Schlüter, N. E. Christensen, *Phys. Rev. B* **1989**, *39*, 9028.
- [102] V. I. Anisimov, O. Gunnarsson, *Phys. Rev. B* **1991**, *43*, 7570.
- [103] F. Aryasetiawan, M. Imada, A. Georges, G. Kotliar, S. Biermann, A. I. Lichtenstein, *Phys. Rev. B* **2004**, *70*, 195104.
- [104] K. Nakamura, R. Arita, Y. Yoshimoto, S. Tsuneyuki, *Phys. Rev. B* **2006**, *74*, 235113.
- [105] H. Jiang, *Int. J. Quantum Chem.* **2015**, *115*, 722.
- [106] M. Cococcioni, S. de Gironcoli, *Phys. Rev. B* **2005**, *71*, 035105.
- [107] H. J. Kulik, M. Cococcioni, D. A. Scherlis, N. Marzari, *Phys. Rev. Lett.* **2006**, *97*, 103001.
- [108] M. R. Norman, *Phys. Rev. B* **1995**, *52*, 1421.
- [109] F. Bultmark, F. Cricchio, O. Grånäs, L. Nordström, *Phys. Rev. B* **2009**, *80*, 035121.
- [110] F. Aryasetiawan, K. Karlsson, O. Jepsen, U. Schönberger, *Phys. Rev. B* **2006**, *74*, 125106.
- [111] D. Jacob, *J. Phys.: Condens. Matter* **2015**, *27*, 245606.
- [112] N. J. Mosey, P. Liao, E. A. Carter, *J. Chem. Phys.* **2008**, *129*, 014103.
- [113] B. Amadon, F. Jollet, M. Torrent, *Phys. Rev. B* **2008**, *77*, 155104.
- [114] A. Lichtenstein, V. Anisimov, J. Zaanen, *Phys. Rev. B* **1995**, *52*, R5467.
- [115] G. Kresse, A. Gil, P. Sautet, *Phys. Rev. B* **2003**, *68*, 073401.
- [116] M. T. Czyżyk, G. A. Sawatzky, *Phys. Rev. B* **1994**, *49*, 14211.
- [117] V. I. Anisimov, J. Zaanen, O. K. Andersen, *Phys. Rev. B* **1991**, *44*, 943.
- [118] A. Avella, F. Mancini, *Strongly Correlated Systems*; Springer Series in Solid-State Sciences 171: Berlin, 2012.
- [119] A. Georges, G. Kotliar, W. Krauth, M. J. Rozenberg, *Rev. Mod. Phys.* **1996**, *68*, 13.
- [120] G. Kotliar, D. Vollhardt, *Phys. Today* **2004**, *57*, 53.
- [121] A. Droghetti, I. Rungger, *Phys. Rev. B* **2017**, *95*, 085131.

- [122] J. C. Slater, *Quantum Theory of Atomic Structure*; McGraw-Hill, New York: 1960.
- [123] M. K. E. L. Planck, *Verhandl. Dtsch. Phys. Ges.* **1900**, 2, 237.
- [124] A. Einstein, *Annalen der Physik* **1905**, 322, 132.
- [125] J. Kügel, M. Karolak, A. Krönlein, J. Senkpiel, G. Sangiovanni, M. Bode, *Phys. Rev. B* **2015**, 235130.
- [126] D. Meyer, T. Wegner, M. Potthoff, W. Nolting, *Physica B* **1999**, 270, 225.
- [127] F. Lechermann, A. Georges, A. Poteryaev, S. Biermann, M. Posternak, A. Yamasaki, O. Andersen, *Phys. Rev. B* **2006**, 74, 125120.
- [128] B. Amadon, *J. Phys.: Condens. Matter* **2012**, 24, 075604.
- [129] I. Souza, N. Marzari, D. Vanderbilt, *Phys. Rev. B* **2001**, 65, 035109.
- [130] N. V. Prokof'ev, B. V. Svistunov, I. S. Tupitsyn, *J. Exp. Theor. Phys. Lett.* **1996**, 12, 911.
- [131] B. B. Beard, U.-J. Wiese, *Phys. Rev. Lett.* **1996**, 77, 5130.
- [132] A. N. Rubtsov, A. I. Lichtenstein, *J. Exp. Theor. Phys. Lett.* **2004**, 80, 61.
- [133] A. N. Rubtsov, V. V. Savkin, A. I. Lichtenstein, *Phys. Rev. B* **2005**, 72, 035122.
- [134] P. Werner, A. J. Millis, *Phys. Rev. B* **2006**, 74, 155107.
- [135] E. Pavarini, E. Koch, D. Vollhardt, A. I. Lichtenstein, *The LDA+DMFT approach to strongly correlated materials*; Forschungszentrum Jülich: Jülich, 2011.
- [136] E. Gull, A. J. Millis, A. I. Lichtenstein, A. N. Rubtsov, M. Troyer, P. Werner, *Rev. Mod. Phys.* **2011**, 83, 349.
- [137] H. Bruus, K. Flensberg, *Many-Body Quantum Theory in Condensed Matter Physics: An Introduction*; Oxford University Press: New York, 2004.
- [138] P. Werner, A. Comanac, L. de' Medici, M. Troyer, A. J. Millis, *Phys. Rev. Lett.* **2006**, 97, 076405.
- [139] L. Huang, . Wang, Z. Y. Meng, L. Du, P. Werner, X. Dai, *Comput. Phys. Commun.* **2015**, 195, 140.
- [140] X. Gonze, *et al.* *Comput. Phys. Commun.* **2009**, 180, 2582.
- [141] M. Heyl, S. Kehrein, *Phys. Rev. B* **2010**, 81, 144301.

- 
- [142] A. Lichtenstein, M. Katsnelson, G. Kotliar, *Phys. Rev. Lett.* **2001**, 87, 067205.
- [143] P. Werner, E. Gull, M. Troyer, A. J. Millis, *Phys. Rev. Lett.* **2008**, 101, 166405.
- [144] B. Surer, M. Troyer, P. Werner, T. O. Wehling, A. M. Läuchli, A. Wilhelm, A. I. Lichtenstein, *Phys. Rev. B* **2012**, 85, 085114.
- [145] A. V. Chubukov, D. L. Maslov, *Phys. Rev. B* **2012**, 86, 155136.
- [146] L. Huang, T. O. Wehling, P. Werner, *Phys. Rev. B* **2014**, 89, 245104.
- [147] M. Jarrell, J. E. Gubernatis, *Phys. Rep.* **1996**, 269, 133.
- [148] C. E. Shannon, *Bell Syst. Tech. J.* **1948**, 27, 379.
- [149] M. Jarrell, *Numerical Methods for Lattice Quantum Many-Body Problems*, Addison Wesley, Reading **1997**, .
- [150] R. Bryan, *Eur. Biophys. J.* **1990**, 18, 165.
- [151] J. E. Hirsch, R. M. Fye, *Phys. Rev. Lett.* **1986**, 56, 2521.
- [152] R. M. Fye, J. E. Hirsch, *Phys. Rev. B* **1989**, 40, 4780.
- [153] G. Kotliar, S. Y. Savrasov, K. Haule, V. S. Oudovenko, O. Parcollet, C. Marianetti, *Rev. Mod. Phys.* **2006**, 78, 865.
- [154] N. Blümer, *Phys. Rev. B* **2007**, 76, 205120.
- [155] E. Gull, P. Werner, A. Millis, M. Troyer, *Phys. Rev. B* **2007**, 76, 235123.
- [156] J. Yoo, S. Chandrasekharan, R. K. Kaul, D. Ullmo, H. U. Baranger, *J. Phys. A: Math. Gen.* **2005**, 38, 10307.
- [157] A. Flesch, E. Gorelov, E. Koch, E. Pavarini, *Phys. Rev. B* **2013**, 87, 195141.
- [158] M. Schiró, M. Fabrizio, *Phys. Rev. B* **2009**, 79, 153302.
- [159] L. Mühlbacher, E. Rabani, *Phys. Rev. Lett.* **2008**, 100, 176403.
- [160] P. Werner, T. Oka, M. Eckstein, A. J. Millis, *Phys. Rev. B* **2010**, 81, 035108.
- [161] W. B. Thimm, J. Kroha, J. von Delft, *Phys. Rev. Lett.* **1999**, 82, 2143.
- [162] T. Hand, J. Kroha, H. Monien, *Phys. Rev. Lett.* **2006**, 97, 136604.
- [163] Y. Bomze, I. Borzenets, H. Mebrahtu, A. Makarovski, H. Baranger, G. Finkelstein, *Phys. Rev. B* **2010**, 82, 161411.

- [164] C. Neumann, P. Fulde, *Z. Phys. B* **1989**, *74*, 277.
- [165] M. Dolg, P. Fulde, W. Küchle, C. Neumann, H. Stoll, *J. Chem. Phys* **1991**, *94*, 3011.
- [166] M. Dolg, P. Fulde, H. Stoll, H. Preuss, A. Chang, R. Pitzer, *Chem. Phys.* **1995**, *195*, 71.
- [167] C. H. Booth, M. D. Walter, M. Daniel, W. W. Lukens, R. A. Andersen, *Phys. Rev. Lett.* **2005**, *95*, 267202.
- [168] N. Marzari, D. Vanderbilt, *Phys. Rev. B* **1997**, *56*, 12847.
- [169] R. Sakuma, *Phys. Rev. B* **2013**, *87*, 235109.
- [170] A. Bakhta, E. Cancès, P. Cazeaux, S. Fang, E. Kaxiras, *Comput. Phys. Commun.* **2018**, *27*.
- [171] S. Bhandary, M. Schüler, P. Thunström, I. di Marco, B. Brena, O. Eriksson, T. Wehling, B. Sanyal, *Phys. Rev. B* **2016**, *93*, 155158.
- [172] I. Mayer, *Int. J. Quantum Chem.* **2002**, *90*, 63.
- [173] B. Amadon, F. Lechermann, A. Georges, F. Jollet, T. O. Wehling, A. I. Lichtenstein, *Phys. Rev. B* **2008**, *77*, 205112.
- [174] G. Kresse, J. Furthmüller, *Phys. Rev. B* **1996**, *54*, 11169.
- [175] G. Kresse, D. Joubert, *Phys. Rev. B* **1999**, *59*, 1758.
- [176] M. Karolak, T. Wehling, F. Lechermann, A. Lichtenstein, *J. Phys.: Condens. Matter* **2011**, *23*, 085601.
- [177] B. W. Heinrich, L. Braun, J. I. Pascual, K. J. Franke, *Nano Letters* **2015**, *15*, 4024 PMID: 25942560.
- [178] W. Wang, R. Pang, G. Kuang, X. Shi, X. Shang, P. N. Liu, N. Lin, *Phys. Rev. B* **2015**, *91*, 045440.
- [179] D. P. Miller, J. Hooper, S. Simpson, P. S. Costa, N. Tymieńska, S. M. McDonnell, J. A. Bennett, A. Enders, E. Zurek, *J. Phys. Chem. C* **2016**, *120*, 29173.
- [180] G. Kuang, Q. Zhang, T. Lin, R. Pang, X. Shi, H. Xu, N. Lin, *ACS Nano* **2017**, *11*, 6295.

- [181] “TURBOMOLE V7.1 2016, a development of University of Karlsruhe and Forschungszentrum Karlsruhe GmbH, 1989-2007, TURBOMOLE GmbH, since 2007; available from <http://www.turbomole.com>”, .
- [182] J. P. Perdew, Y. Wang, *Phys. Rev. B* **1992**, *45*, 13244.
- [183] J. P. Perdew, K. Burke, M. Ernzerhof, *Phys. Rev. Lett.* **1996**, *77*, 3865.
- [184] F. Weigend, R. Ahlrichs, *Phys. Chem. Chem. Phys.* **2005**, *7*, 3297.
- [185] A. Hellweg, C. Hättig, S. Höfener, W. Klopper, *Theor. Chem. Acc.* **2007**, *117*, 587.
- [186] A. R. Groenhof, M. Swart, A. W. Ehlers, K. Lammertsma, *J. Phys. Chem. A* **2005**, *109*, 3411.
- [187] C. Rovira, K. Kunc, J. Hutter, P. Ballone, M. Parrinello, *J. Phys. Chem. A* **1997**, *101*, 8914.
- [188] M. E. Ali, B. Sanyal, P. M. Oppeneer, *J. Phys. Chem. B* **2012**, *116*, 5849.
- [189] E. Riedel, H.-J. Meyer, *Allgemeine und Anorganische Chemie*; De Gruyter: Berlin, 2018.
- [190] G. L. Miessler, D. A. Tarr, *Inorganic Chemistry*; Pearson Prentice Hall: New Jersey, 3rd ed.; 2004.
- [191] P. A. M. Dirac, *Proc. R. Soc. London, Ser. A* **1929**, *123*, 714.
- [192] J. C. Slater, *Phys. Rev.* **1951**, *81*, 385.
- [193] S. H. Vosko, L. Wilk, M. Nusair, *Can. J. Phys.* **1980**, *58*, 1200.
- [194] A. D. Becke, *Phys. Rev. A* **1988**, *38*, 3098.
- [195] J. P. Perdew, *Phys. Rev. B* **1986**, *33*, 8822.
- [196] A. Szabo, N. S. Ostlund, *Modern Quantum Chemistry: Introduction to Advanced Electronic Structure Theory*; Dover Publications, Inc.: Mineola, First ed.; 1996.
- [197] W. J. Hehre, R. F. Stewart, J. A. Pople, *J. Chem. Phys.* **1969**, *51*, 2657.
- [198] N. Néel, J. Kröger, R. Berndt, *Phys. Rev. B* **2010**, *82*, 233401.
- [199] P. P. Baruselli, R. Requist, A. Smogunov, M. Fabrizio, E. Tosatti, *Phys. Rev. B* **2015**, *92*, 045119.

- [200] N. Knorr, M. A. Schneider, L. Diekhöner, P. Wahl, K. Kern, *Phys. Rev. Lett.* **2002**, *88*, 096804-1.
- [201] P. Wahl, L. Diekhöner, M. A. Schneider, L. Vitali, G. Wittich, K. Kern, *Phys. Rev. Lett.* **2004**, *93*, 176603.
- [202] P. Wahl, A. P. Seitsonen, L. Diekhöner, M. A. Schneider, K. Kern, *New J. Phys.* **2009**, *11*, 2009.
- [203] N. Néel, J. Kröger, L. Limot, K. Palotas, W. A. Hofer, R. Berndt, *Phys. Rev. Lett.* **2007**, *98*, 016801.
- [204] M. P. Bahlke, M. Karolak, C. Herrmann, *Phys. Rev. B* **2018**, *97*, 035119.
- [205] M. P. Bahlke, *The effect of strong correlation on potential energy surfaces* (master's thesis); University of Hamburg: Hamburg, 2015.
- [206] R. W. G. Wyckoff, *Crystal Structures*; Interscience Publishers: New York, 1963.
- [207] P. E. Blöchl, *Phys. Rev. B* **1994**, *50*, 17953.
- [208] M. Torrent, F. Jollet, F. Bottin, G. Zérah, X. Gonze, *Comput. Mat. Science* **2008**, *42*, 337.
- [209] J. Perdew, A. Zunger, *Phys. Rev. B* **1981**, *23*, 5048.
- [210] D. M. Ceperly, B. J. Alder, *Phys. Rev. Lett.* **1980**, *45*, 566.
- [211] K. Haule, *Phys. Rev. Lett.* **2015**, *115*, 196403.
- [212] J. Kügel, M. Karolak, J. Senkpiel, P.-J. Hsu, G. Sangiovanni, M. Bode, *Nano Lett.* **2014**, *14*, 3895.
- [213] G. Painter, F. Averill, *Phys. Rev. B* **1982**, *26*, 1781.
- [214] J. C. Grossman, L. Mitáš, *Phys. Rev. Lett.* **1995**, *74*, 1323.
- [215] M. J. Mayor-Lopez, J. Weber, *Chem. Phys. Lett.* **1997**, *281*, 226.
- [216] P. Huang, E. A. Carter, *Nano Lett.* **2008**, *8*, 1265.
- [217] J. Heyd, G. E. Scuseria, *J. Chem. Phys.* **2004**, *121*, 1187.
- [218] Z. Wu, R. E. Cohen, *Phys. Rev. B* **2006**, *73*, 235116.
- [219] J. Ma, A. Michaelides, D. Alfe, L. Schimka, G. Kresse, E. Wang, *Phys. Rev. B* **2011**, *84*, 033402.

- 
- [220] V. Madhavan, W. Chen, T. Jamneala, M. Crommie, N. Wingreen, *Science* **1998**, *280*, 567.
- [221] V. Madhavan, W. Chen, T. Jamneala, M. Crommie, N. S. Wingreen, *Phys. Rev. B* **2001**, *64*, 165412.
- [222] N. Parragh, A. Toschi, K. Held, G. Sangiovanni, *Phys. Rev. B* **2012**, *86*, 155158.
- [223] M. Wallerberger, A. Hausoel, P. Gunacker, A. Kowalski, N. Parragh, F. Goth, K. Held, G. Sangiovanni, *Comput. Phys. Commun.* **2019**, *235*, 388.
- [224] E. Gorelov, T. O. Wehling, A. N. Rubtsov, M. I. Katsnelson, A. I. Lichtenstein, *Phys. Rev. B* **2009**, *80*, 155132.
- [225] S. Gardonio, M. Karolak, T. Wehling, L. Petaccia, S. Lizzit, A. Goldoni, A. Lichtenstein, C. Carbone, *Phys. Rev. Lett.* **2013**, *110*, 186404.
- [226] J. Bieder, B. Amadon, *Phys. Rev. B* **2014**, *89*, 195132.
- [227] M. Karolak, M. Izquierdo, S. L. Molodtsov, A. I. Lichtenstein, *Phys. Rev. Lett.* **2015**, *115*, 046401.
- [228] Y. Nagai, S. Hoshino, Y. Ota, *Phys. Rev. B* **2016**, *93*, 220505.
- [229] P. J. Feibelman, B. Hammer, J. K. Nørskov, F. Wagner, M. Scheffler, R. Stumpf, R. Watwe, J. Dumesic, *J. Phys. Chem. B* **2001**, *105*, 4018.
- [230] S. E. Mason, I. Grinberg, A. M. Rappe, *Phys. Rev. B* **2004**, *69*, 161401.
- [231] M. Alaei, H. Akbarzadeh, H. Gholizadeh, S. de Gironcoli, *Phys. Rev. B* **2008**, *77*, 085414.
- [232] F. Favot, A. Dal Corso, A. Baldereschi, *J. Chem. Phys.* **2001**, *114*, 483.
- [233] P. Lazić, M. Alaei, N. Atodiresei, V. Caciuc, R. Brako, S. Blügel, *Phys. Rev. B* **2010**, *81*, 045401.
- [234] M. Dion, H. Rydberg, E. Schröder, D. C. Langreth, B. I. Lundqvist, *Phys. Rev. Lett.* **2004**, *92*, 246401.
- [235] O. A. Vydrov, T. V. Voorhis, *Phys. Rev. Lett.* **2009**, *103*, 063004.
- [236] M. Obata, M. Nakamura, I. Hamada, T. Oda, page 093701.
- [237] P. Janthon, F. Viñes, J. Sirijaraensre, J. Limtrakul, F. Illas, *J. Phys. Chem. C* **2017**, *121*, 3970.

- [238] S. Grimme, J. Antony, S. Ehrlich, H. Krieg, *J. Chem. Phys.* **2010**, *132*, 154104.
- [239] S. Grimme, S. Ehrlich, L. Goerigk, *J. Comput. Chem.* **2011**, *32*, 1456.
- [240] K. Lee, E. D. Murray, L. Kong, B. I. Lundqvist, D. C. Langreth, *Phys. Rev. B* **2010**, *82*, 081101.
- [241] M. Karolak, D. Jacob, A. Lichtenstein, *Phys. Rev. Lett.* **2011**, *107*, 146604.
- [242] T. A. Halgren, W. N. Lipscomb, *Chem. Phys. Lett.* **1977**, *49*, 225.
- [243] S. Lubber, S. Leung, C. Herrmann, W. H. Du, L. Noodleman, V. S. Batista, *Dalton Trans.* **2014**, *43*, 576.
- [244] M. Head-Gordon, J. C. Tully, *Phys. Rev. B* **1992**, *46*, 1853.
- [245] R. van Santen, *J. Mol. Catal. A: Chem.* **1997**, *115*, 405.
- [246] W. B. Schneider, U. Benedikt, A. A. Auer, *ChemPhysChem* **2013**, *14*, 2984.
- [247] O. Tsendra, A. M. Scott, L. Gorb, A. D. Boese, F. C. Hill, M. M. Ilchenko, D. Leszczynska, J. Leszczynski, *J. Phys. Chem. C* **2014**, *118*, 3023.
- [248] R. J. Maurer, M. Askerka, V. S. Batista, J. C. Tully, *Phys. Rev. B* **2016**, *94*, 115432.
- [249] L. Groß, M. P. Bahlke, T. Steenbock, C. Klinke, C. Herrmann, *J. Comput. Chem.* **2017**, *38*, 861.
- [250] J. Banerjee, S. Behnle, M. C. E. Galbraith, V. Settels, B. Engels, R. Tonner, R. F. Fink, *J. Comput. Chem.* **2018**, *39*, 844.
- [251] S. N. Yaliraki, A. E. Roitberg, C. Gonzalez, V. Mujica, M. A. Ratner, *J. Chem. Phys.* **1999**, *111*, 6997.
- [252] Y. Luo, C.-K. Wang, Y. Fu, *J. Chem. Phys.* **2002**, *117*, 10283.
- [253] A. Nitzan, M. A. Ratner, *Science* **2003**, *300*, 1384.
- [254] C. Herrmann, G. C. Solomon, M. A. Ratner, *J. Am. Chem. Soc.* **2010**, *132*, 3682-3684.
- [255] R. Hayakawa, M. A. Karimi, J. Wolf, T. Huhn, M. S. Zöllner, C. Herrmann, E. Scheer, *Nano Lett.* **2016**, *16*, 4960.
- [256] G. Knizia, *J. Chem. Theory Comput.* **2013**, *9*, 4834.
- [257] J. P. Perdew, M. Ernzerhof, K. Burke, *J. Chem. Phys.* **1996**, *105*, 9982.

- [258] J. Tao, J. P. Perdew, V. N. Staroverov, G. E. Scuseria, *Phys. Rev. Lett.* **2003**, *91*, 146401.
- [259] S. Grimme, J. G. Brandenburg, C. Bannwarth, A. Hansen, *J. Chem. Phys.* **2015**, *143*, 054107.
- [260] W. Gao, T. A. Abtew, T. Cai, Y.-Y. Sun, S. Zhang, P. Zhang, *Solid State Commun.* **2016**, *234*, 10.
- [261] W. Kohn, A. E. Mattsson, *Phys. Rev. Lett.* **1998**, *81*, 3487.
- [262] A. E. Mattsson, W. Kohn, *J. Chem. Phys.* **2001**, *115*, 3441.
- [263] R. Armiento, A. E. Mattsson, *Phys. Rev. B* **2002**, *66*, 165117.
- [264] C. R. Jacob, J. Neugebauer, L. Visscher, *J. Comput. Chem.* **2008**, *29*, 1011.
- [265] C. R. Jacob, J. Neugebauer, *Wiley Interdiscip. Rev.-Comput. Mol. Sci.* **2014**, *4*, 325.
- [266] H. Bahmann, M. Kaupp, *J. Chem. Theory Comput.* **2015**, *11*, 1540 PMID: 26574364.
- [267] T. M. Maier, H. Bahmann, M. Kaupp, *J. Chem. Theory Comput.* **2015**, *11*, 4226 PMID: 26575918.
- [268] J. Sun, A. Ruzsinszky, J. P. Perdew, *Phys. Rev. Lett.* **2015**, *115*, 036402.
- [269] Y. Zhao, D. G. Truhlar, *Theor. Chem. Acc.* **2008**, *120*, 215.
- [270] Y.-S. Fu, *et al. Phys. Rev. Lett.* **2007**, *99*, 256601.
- [271] V. Iancu, A. Deshpande, S.-W. Hla, *Nano Lett.* **2006**, *6*, 820.
- [272] J. Parks, *et al. Science* **2010**, *328*, 1370.
- [273] P.-O. Löwdin, *J. Chem. Phys.* **1950**, *18*, 365.
- [274] P.-O. Löwdin, *Adv. Quantum. Chem.* **1970**, *5*, 185.
- [275] R. Korytár, N. Lorente, *J. Phys.: Condens. Matter* **2011**, *23*, 355009.
- [276] M. Schüler, S. Barthel, M. Karolak, A. I. Poteryaev, A. I. Lichtenstein, M. I. Katsnelson, G. Sangiovanni, T. O. Wehling, *Phys. Rev. B* **2016**, *93*, 195115.
- [277] M. J. Frisch, *et al.* "Gaussian 09 Revision E.01", Gaussian Inc. Wallingford CT 2009.
- [278] O. A. Vydrov, T. Van Voorhis, *J. Chem. Phys.* **2010**, *133*, 244103.
- [279] R. Sabatini, T. Gorni, S. de Gironcoli, *Phys. Rev. B* **2013**, *87*, 041108.

[280] H. Peng, J. P. Perdew, *Phys. Rev. B* **2017**, *95*, 081105.



## Declaration on Oath

I hereby declare, on oath, that I have written the present dissertation by my own and have not used other than the acknowledged resources and aids. The written version submitted corresponds to that on the electronic storage medium. I hereby declare that I have not previously applied or pursued for a doctorate (Ph.D. studies) with this thesis.

Hiermit versichere ich an Eides statt, dass die vorliegende Arbeit von mir selbständig verfasst wurde und ich keine anderen als die angegebenen Hilfsmittel benutzt habe. Die eingereichte schriftliche Fassung entspricht der auf dem elektronischen Speichermedium. Ich versichere, dass diese Dissertation nicht in einem früheren Promotionsverfahren eingereicht wurde.

Hamburg, 14.02.2019

---

Marc Philipp Bahlke